Universitat Autònoma de Barcelona

COLLOIDAL COORDINATION POLYMER NANOSTRUCTURES: NOVEL THERMOCHROMIC AND BIOIMAGING PROBES

Salvio Suárez García

Universitat Autònoma de Barcelona

Departament de Química

Facultat de Ciències

COLLOIDAL COORDINATION POLYMER NANOSTRUCTURES: NOVEL THERMOCHROMIC AND BIOIMAGING PROBES

Salvio Suárez García

Ph.D. Thesis

Ph.D. in Materials Science

2019

Supervisors:

Dr. Daniel Ruiz Molina

Dr. Fernando Novio Vázquez

Tutor:

Dr. Jordi Hernando Campos

Memòria presentada per aspirar al Grau de Doctor per Salvio Suárez García.

Salvio Suárez García

Vist i plau,

Dr. Daniel Ruiz Molina (Director)

Dr. Fernando Novio Vázquez (Director)

Dr. Jordi Hernando Campos (Tutor)

Bellaterra, 25 de Setembre del 2019

ABSTRACT

Coordination polymers and its rational design let the formation of nanostructured materials with a broad variety of properties. The multiple combinations between metal ions and organic ligands as precursors of self-assembled materials have fascinated scientists for decades. The application of coordination chemistry at the nanoscale is considered one of the most versatile approaches for the development of new nanostructured materials due to the infinite possibilities for reaching unprecedented properties. Furthermore, the development of metal-organic systems has aroused in a plethora of examples for their use in a wide range of applications.

In this Thesis we have been particularly interested in the fine tune of the properties of nanostructured materials based on coordination polymers whose were obtained through different synthetic routes. The method of synthesis, the properly selection of precursors and the study of the final properties has centred the work carried out. Additionally, the formation of water-stable colloidal suspensions was stablished as a main requirement for their potential application. For that, a multidisciplinary synergy was necessary with the aim to pursue the final application of the novel nanostructured materials developed. Achieving this objective was possible thanks to a properly design of the strategy followed together with complete characterisation of the nanostructures prepared.

In a first part of this Thesis, the nanostructuration of Fe(II)-based switchable systems with spin crossover behaviour was achieved by following two different strategies. On the one hand, a top-down methodology based on liquid-phase exfoliation was applied for the isolation of 2D flakes from the bulk crystal. On the other hand, through a bottom-up approach, the synthesis of novel nanoparticles was possible by modulating the reaction diffusion using microfluidic based methodologies. In both cases, the nanostructured materials were integrated in polymeric matrices to evaluate their potential application as proof-of-concept thermochromic films. In the second part of the Thesis, a novel family of nanoscale coordination polymers (NCPs) based on Fe(III), Gd(III), Mn(II), In(III) and Cu(II) was stablished through its rational synthesis by using one-pot reaction. The nanoparticles obtained were validated by pre-clinical *in vivo* tests showing interesting performance as potential theranostic agents for imaging (Magnetic resonance imaging, positron emission tomography and single-photon emission computed tomography) and potential pre-treatment of glioblastoma and lung diseases.

LIST OF ABBREVIATIONS

AFM	Atomic force microscopy
BBB	Blood-brain barrier
BP	Black phosphorous
BSA	Bovine serum albumin
CA(s)	Contrast agents(s)
CP(s)	Coordination polymer(s)
CPP	Coordination polymer particle(s)
CN(s)	Coordination network(s)
CNS	Central nervous system
COF(s)	Covalent-organic framework(s)
CONASH(s)	Coordination nanosheet(s)
CT	Computed tomography
CVD	Chemical vapour deposition
DFT	Density functional theory
DLS	Dynamic light scattering
DMCA(s)	Dual-mode contrast agents(s)
DMF	Dimethylformamide
DSC	Differential scanning calorimetry
EDX	Elemental energy dispersive X-ray
EPR	Enhanced permeability and retention
EtOH	Ethanol
FR	Folate receptor
FRR(s)	Flow rate ratio(s)
GBCA(s)	Gadolinium-based contrast agent(s)
HS	High Spin
ICP(s)	Infinite coordination polymer(s)
ICP-MS	Inductively coupled plasma - Mass spectroscopy
i.v.	Intravenous
LB	Langmuir-Blodgett
LDH(s)	Layered double hydroxide(s)
LPE	Liquid-phase exfoliation
LS	Low spin
LTDDS(s)	Lung-targeted drug delivery system(s)
MeOH	Methanol
MI	Molecular imaging
MPS	Mononuclear phagocytic system
MOF(s)	Metal-organic framework(s)
MRI	Magnetic resonance imaging
MSA	Mouse serum albumin
NCP(s)	Nanoscale coordination polymer(s
NMOF(s)	Nanostructured MOF(s)
NMR	Nuclear magnetic resonance
NSF	Nephrogenic system fibrosis
OI	Optical imaging
OM	Optical microscopy
PBS	Phosphate buffer saline
PDA	Polydopamine
PDI	Polydispersity index
PDOS	Projected densities of states
PEG	Poly(ethylene glycol)
PET	Positron emission tomography
p.i.	Post-injection
PXRD	Powder X-ray diffraction
PVA	Poly(vinyl alcohol)
PVD	Physical vapour deposition
r_1	Longitudinal relaxivity value
r_2	Transversal relaxivity value
RCE	Relative contrast enhancement
RCY	Radiochemistry yield
RD	Reaction-diffusion
RES	Reticuloendothelial system
RF	Radiofrequency
ROI	Region of interest
ROS	Reactive oxygen species
SAXS	Small-angle X-ray scattering
SCO	Spin crossover
SEM	Scanning electron microscopy
SPECT	Single-photon emission computed tomography
SPIONs	Superparamagnetic iron oxide nanoparticles
SQUID	Superconducting quantum interference device
ST	Spin transition
STM	Scanning tunnelling microscopy
SUV(s)	Standardised uptake value(s)
SXRD	Single X-ray diffraction
T_1	Longitudinal relaxation time
T_2	Transversal relaxation time
TEM	Transmission electron microscopy
TGA	Thermogravimetric analysis
THF	Tetrahydrofuran
TMD	Transition metal dichalcogenides
XPS	X-ray photoelectron spectroscopy
χ_M	Magnetic molar fraction
XRD	X-ray diffraction
WAXS	Wide-angle X-ray scattering

LIST OF MOLECULES

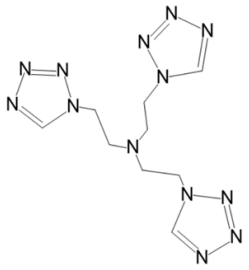

(**L1**, t3z)
(tris[2-(1H-tetrazol-1-yl)ethyl]amine)

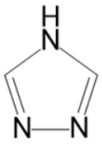

(**H-L2**)
(1,2,4-traizole)

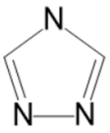

(**L2**)
(1,2,4-traizolato)

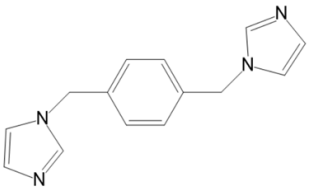

(**L3**, Bix)
(1,4-Bis(imidazol-1-ylmethyl)benzene)

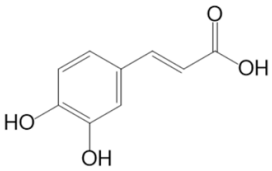

(**L4**, dhc)
(3,4-dihydroxycinnamic acid)

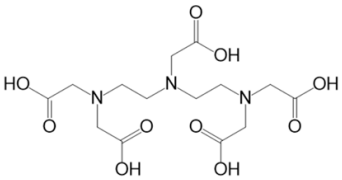

(**L5**, DTPA)
(diethylenetriaminepentaacetic acid)

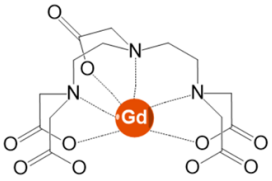

(**Gd-L5**, GdDTPA)
(Gadopentate dimeglumine)

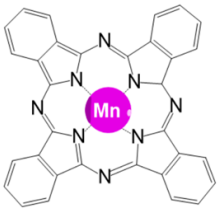

(**Mn-L6**, MnDPD)
(Mangafodipir trisodium)

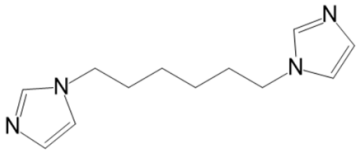

(**L7**)
(1,6-Bis(imidazol-1-yl)hexane)

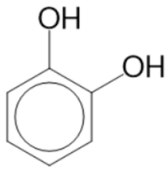

(**L8**, cat)
(Pyrocatechol)

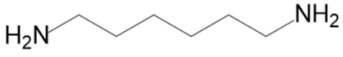

(**L9**, HMDA)
(Hexamethylenediamine)

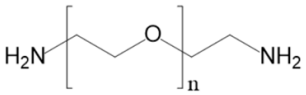

(**L10**, PEG)
(poly(ethylene glycol)bis(amine))

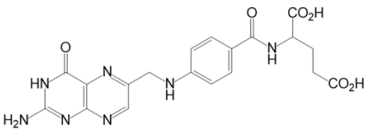

(**L11**, FA)
(folic acid)

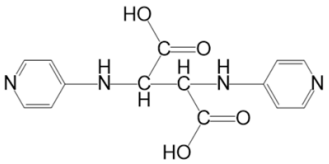

(**L12**)
(1,6-Bis(imidazole-1-ylmethil)-hexane)

The results reported in this Thesis have been partially described in the following publications:

Chapter 3:

(1) **"Spin Crossover in an Exfoliated 2–D Coordination Polymer and its Implementation in Thermochromic Films."** Salvio Suárez-García, Narayanan Narayasseri Adarsh, Gabor Molnár, Azzedine Bousseksou, Yann Garcia, Marinela M. Dîrtu, Javier Saiz-Poseu, Roberto Robles, Pablo Ordejón, Daniel Ruiz-Molina. ACS Appl. Nano Mater. **2018**, 1 (6). doi: 10.1021/acsanm.8b00341.

(2) **"Pathway Selection as a Tool for Crystal Defect Engineering."** Afshin Abrishamkar^, Salvio Suárez–García^, Semih Sevim^, Alessando Sorrenti, Ramon Pons, Shi-Xia Liu, Silvio Decurtins, Guillem Aromí, David Aguilà, Salvador Pané, Andrew J. deMello, Aurelian Rotaru, Daniel Ruiz–Molina, Josep Puigmartí-Luis. ^Equal contribution. (Submitted)

Chapter 4:

(1) **"Dual T1/T2 Nanoscale Coordination Polymers as Novel Contrast Agents for MRI: A Preclinical Study for Brain Tumor.**" Salvio Suárez-García, Nuria Arias-Ramos, Carolina Frias, Ana Paula Candiota, Carles Arús, Julia Lorenzo, Daniel Ruiz-Molina, Fernando Novio. ACS Appl. Mater. Interfaces **2018**, 10 (45), 38819–38832. doi: 10.1021/acsami.8b15594.

(2) **"Copolymerization of a Catechol and a Diamine as a Versatile Polydopamine-Like Platform for Surface Functionalization: The Case of a Hydrophobic Coating".** Salvio Suárez-García, Josep Sedó, Javier Saiz-Poseu, Daniel Ruiz-Molina. Biomimetics **2017**, 2, 22. doi: 10.3390/biomimetics2040022.

(3) **"Molecular Assembly of Radiolabelled Catechol-Based Nanostructured Coordination Polymers for Lung Targeting."** Salvio Suárez-García, Tullio Espósito, Jenna Neufeld-Peters, Marta Bergamo, Jeppe Harboe, Pedro L. Esquinas, Katayoun Saatchi, Urs Häfeli, Daniel Ruiz-Molina, C. Rodríguez-Rodríguez, Fernando Novio. (Submitted)

Table of contents

4. Chapter 4: Design of Novel Nanostructured Coordination polymers for its use in Bioimaging

Chapter 1

Introduction

Traditional polymers are long molecules or macromolecules produced from the polymerization of simple small chemical components or monomers. This description was established in the early 1920s by the hand of Herman Staudinger who found wide opposition from the scientific community of that time.[1] Since then, and after almost a century, polymer chemistry has radically revolutionised the chemical synthesis, structure, physicochemical properties of polymers and macromolecules. Both synthetic and natural polymers, from plastics to DNA, have allowed spreading the progress in different areas of science. These macromolecule structures are part of any system that we can think of, thus conferring unique properties that have allowed us to develop a vast knowledge that continues to grow today. As far as Nanoscience and Nanotechnology is concerned, polymers are playing a transcendental role allowing the creation of mouldable structures under design with properties and functionalities never observed before. Specifically, coordination chemistry, where metal-to-ligand bonds become relevant, offers a very powerful tool for the architect of new structures with potential applications in the nanomaterials science, from electronics to medicine.

In this Chapter, a detailed discussion on the use of coordination chemistry in nanoscience has been addressed. Special emphasis is given to those systems which presents colloidal-sized stability in water as a main condition for their potential application in different technological or biomedical areas. Furthermore, the different synthetic routes for the synthesis of coordination polymers are described. At the end of this chapter, the scope of this Thesis is presented.

1. Introduction. Rational design of functional nanostructured coordination polymers

The assembly of units at the nanoscale includes a series of processes that do not occur in other types of manufacturing processes. As the material size is reduced to the nanoscale, the parameters that influence its synthesis require specific control to avoid, for example, the uncontrolled interaction of the different components or building blocks. Based on this, for the fabrication and processing of functional materials at the nanoscale it is necessary to consider the processes that simultaneously take place such as i) self-assembly of components, ii) atomic and molecular manipulation, iii) reaction conditions (concentration, pH, solvent, etc.), iv) the application of physical external stimuli (temperature, pressure, agitation, etc.) and v) stability of the final product. Recently, the term nanoarchitectonic has been established with the aim of harmonizing these parameters and identifying the more influential agents.[2-4] According to the founders of this terminology, nanoarchitecture supposes[5]:

i. Organization of components at the nanoscale for the production of reliable nanomaterials and nanosystems
ii. Development of novel and unexpected functionalities
iii. Exploration of the new phenomena based on new theoretical approximations

Based on this rationale, coordination chemistry appears in this scenario as a potential and attractive tool for the nanoarchitectonics processes. The formation of coordination polymers (CPs) at the nanoscale begins with the association of their components consisting on the reaction of ionic metals with multi-anchoring organic ligands via coordination bonds. The main characteristic of this type of systems is the chemical versatility and flexibility of coordination complexes, which allows the rational design of novel functional materials. The control over the parameters involved in the synthesis processes and the rational selection of its components according to the desired properties and applications, allows the elaboration of a wide range of promising functional nanostructures based on coordination chemistry.

1.1 Dimensionality, classification and properties

1.1.1 Dimensionality

Since the late 1950s when the concept of CPs began to be used a lot of examples have been reported covering different fields. Metal-to-ligand bonds exhibit precise directional interactions, which may modulate the dimensionality of the resulting system. This dimensionality can be

systematically controlled and tuned by the rationale selection of metals and ligands, which define the coordination sphere and binding sites, respectively. Additionally, by changing the dynamic equilibrium of the processes involved and the miniaturization to nanometre scale, it is possible to influence the resulting extended structure.

The range of metal ions and their coordination modes have been studied and detailed for many years. For this reason, a wide research and big effort are being focused on the design of organic ligands for the formation of CPs.[6] Organic ligands can be tuned by modifying their structural features (spacers, substituents, functional groups, etc.) allowing the accurate adjustment of the different coordination framework (Figure 1.1).

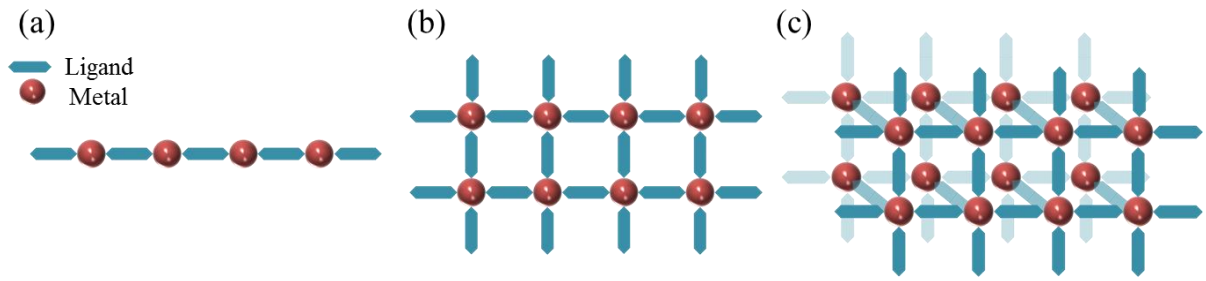

Figure 1.1 Schematic illustration of the different dimensionalities through the coordination between metals and ligands: (a) 1D, (b) 2D and (c) 3D.

Besides the metal ion coordination, which acts as a driving force, different non-covalent intermolecular interactions take relevance during the polymer assembly: i) hydrogen bonding, ii) π-π stacking and iii) van der Waals forces. These interactions are decisive for the final formation of the CPs in a specific coordination network (CN). The CNs consisted on the extension of a coordination compound through the repetition of its coordination entities. This extension can take place in 1D within cross-links between two or more individual chains or through the repetition of coordination entities in 2D or 3D. Particularly, when the network formed has potential voids with specific porous sizes, the resulting system obtained is called metal-organic framework (MOF).[7]

1.1.2 Classification

By definition, a coordination polymer stands for an extended polymeric structure generated by the bridging ligands connecting metal ion nodes. The most used classification for different types of coordination polymers is based on their crystallinity and porosity. Thus, as detailed previously, the crystalline and porous coordination polymers are named as metal-organic frameworks (MOFs). MOFs can have different dimensionalities and morphologies depending on the synthetic route and the nature

of the intrinsic components. Other interesting varieties are related with covalent-organic frameworks (COFs) were in this case, a covalent bond is formed. On the other hand, coordination polymer particles (CPPs) have recently emerged as an alternative to MOFs. Although CPPs are not hollow or open-framework structures, and normally exhibit an amorphous structure, they showed an interesting tuneable matrix composition that facilitates the modification of their properties to adapt these materials to cutting-edge technological uses. With the irruption of nanoscience, the terminologies for these materials have been modified. When the dimensionalities are at the nanoscale, the most recent terminology differentiate the crystalline or amorphous nature of the nanomaterials and divide them into two main classes based on their structural regularity and crystallinity: i) the amorphous systems that can be either porous or nonporous which are denoted as Nanostructured Coordination Polymers (NCPs) and ii) the crystalline and porous materials which are known as nanoscale metal-organic frameworks (NMOFs or nanoMOFs). Although the main differences are found in their morphology and structure, NMOFs/NCPs possess several potential advantages over existing nanoplatforms in different technological or biomedical applications: i) compositional and structural tuneability allows for the synthesis of NMOFs/NCPs with different compositions, shapes, sizes, and chemical properties; ii) highly porous and oriented structures accommodate efficient loading of diverse functional cargoes; and ii) they are intrinsically (bio)degradable due to the relatively labile metal−ligand bonds.

NMOFs are a specific type of hybrid inorganic–organic solids, built up from the assembly of inorganic secondary building units, and easily tuneable polycomplexant organic linkers, which present permanent pores in their structure. Their composition and structure allow control over the release cargo via modification of tuneable pores with an exceptionally high surface area and therefore loading capacity. The crystalline nature of NMOFs facilitates analyses of host–guest interactions and systematic drug encapsulation and release studies, as well as theoretical models. These materials represent the most CP studied for technological or medical applications and extensive studies and reviews have been published.[8]

However, NCPs have recently emerged as an alternative to NMOFs. The first allusion of NCPs was reported in 2005[9,10] and the number of publications is exponentially increasing in the recent years foreseeing their potential interest in biomedical application. Unlike conventional MOFs, these NCPs exhibit a higher level of structural tailorability, including size- and morphology-dependent properties. A variety of methods now exist for making numerous compositions, with modest control over particle size and shape. These structures can exhibit microporosity, tuneable fluorescence, magnetic susceptibility, and unusual catalytic activity and selectivity.[11] Interestingly, many of these NCP structures can be depolymerized much faster and under milder conditions than MOFs, which makes them attractive for a variety of biomedical applications such as drug delivery or bioimaging. One of the main advantages of NCPs is concerning the synthetic methodology. Normally, NCPs are synthesized by a low-cost and scalable room-temperature nanoscale precipitation method, taking

advantage of the insolubility of the formed particles in a given solvent system where the individual precursors remain soluble. Although this strategy was used to synthesize a wide range of NCPs, various preparation methods of micro- and nano-sized particles made from CPs have been reported. This aspect will be revised in the following sections.

1.1.3 Synthetic routes

As explained in previous sections, the formation of CPs depends on several crucial factors to be considered. Certainly, due to the expansion in the research and the development of new functional nanostructured systems, different synthetic processes and routes have been developed. As molecular nanomaterials, NMOFs and NCPs can be synthesized with an infinite array of metal/metal cluster and bridging ligands. Overall approaches, the most used methods for their synthesis can be classified mainly into: solvent-induced precipitation, hydro-/solvothermal, surfactant-templated, and reverse microemulsion.[12] The first method generally yields amorphous materials, while the latter three methods could produce both amorphous and crystalline materials. These synthetic approaches can be classified in different groups together with other alternatives. In this section, some of the conventional and non-conventional used methods for the synthesis of CPs are briefly discussed. Furthermore, new methodologies still in development are described.

1.1.3.1 Conventional methods

a) Solvent-induced precipitation. This methodology (also called as nanoprecipitation or one-pot solution reaction) is the most common process for the synthesis of CPs. A schematic illustration is shown in Figure 1.2. Basically, the different ligands and metal salts are mixed together in a solvent for the formation of the functional systems.

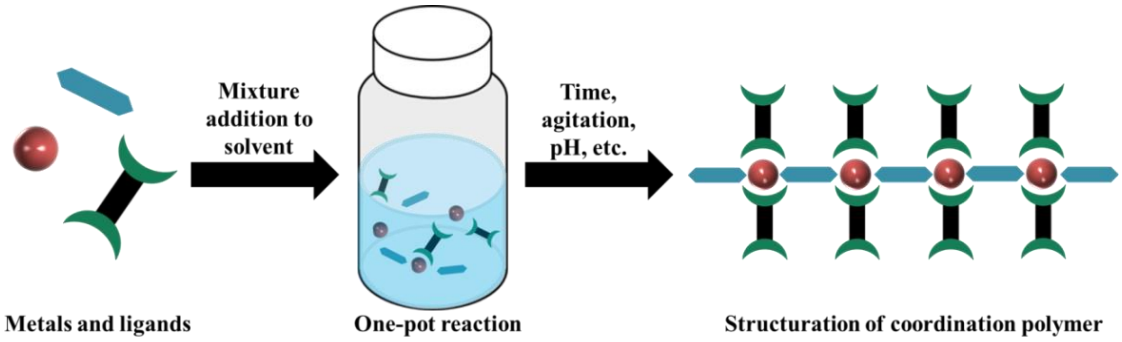

Figure 2.2 Schematic illustration of a one-pot synthesis reaction for the formation of CPs.

There are different modifications that can modulate the synthesis process and tune the final properties. For example, the addition of solvent mixtures (biphasic synthesis) can promote the formation of determined structures from nanoparticles to crystals (e.g. co-precipitation).[13-15] Moreover, the use of external inputs such as vigorous magnetic stirring for the correct mixing of the components may modulate the size of the final CPs.[16] Depending on the reaction conditions (e. g. temperature and time, among others) and the nature of the building components, this methodology let the formation of amorphous and crystalline CPs, as it allows to slow down the reaction time between reactants.[17] In general, the most used approach for the synthesis of nanoparticles was described by Mirkin and co-workers.[9,18] This approach consists on the addition of a poor solvent into the solution containing the precursors inducing the formation of an insoluble product which precipitates and can be easily isolated.

b) *Reaction diffusion.* This synthetic route is usually employed for the growth of crystals. In this case, the coordination reaction is slowed down, allowing the controlled diffusion of the separated components into the selected solvents with different densities through a test tube (Figure 1.3). The diffusion reaction becomes useful for the growing of good-shaped and quality single crystals.[19,20] Parameters such slow evaporation of the solvents may be adjusted to favour the nucleation growth. Additionally, an interlayer between the different solvents can be created with a third solvent for the correct crystallization of the metal-organic compounds.[21,22]

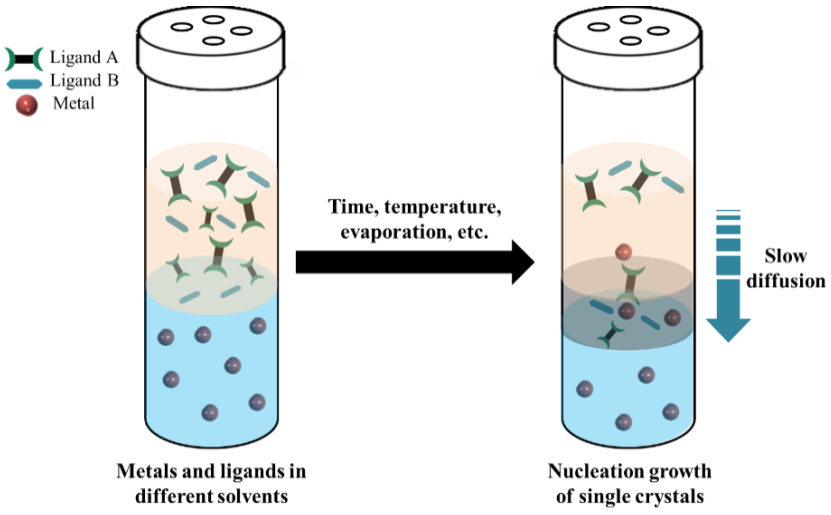

Figure 3.3 Schematic illustration of a diffusion reaction for the formation of CPs.

c) *Mechanochemistry.* This powerful methodology lets to the synthesis of CPs in rapid, clean and environmental conditions,[23] avoiding solvolysis and solvent complexation processes.[24] Fundamentally, a mechanochemistry reaction is induced by the direct absorption of

mechanical energy, mainly by grinding or milling. This procedure can be applied on different fields such as inorganic materials, organic synthesis, co-crystallisation, metal complexes and supramolecular aspects, among others.[25] During the last years, the synthesis of CPs (especially in the case of MOFs) based on mechanochemical reactions have been reported.[26-28] The molecular self-assembly of metal and ligands is accessible through, for example, the liquid-assisted grinding.[29]

d) *Controlled atmosphere*. In some cases, the CPs formation needs the presence of inert atmospheres (N_2, Ar) or specific gases for the properly polymerization reaction. Thereby, several oxidation processes or secondary reactions can be avoided. In order to produce functional materials out of ambient atmosphere, some common lab equipment can be used, as for example, the Schlenk, which is widely used in inorganic, organic and bioinorganic chemistry. Based on this, the air-sensitive systems are maintained in controlled atmospheres during the whole coordination reaction, from the starting materials to the final product.[30-33]

1.1.3.2 Non-conventional methods

a) *Hydro-/solvothermal method*. The synthesis of CPs by hydro-/solvothermal methods allows the formation of crystalline structures (Figure 1.4). In this case, it is common to mix the building blocks with aqueous or organic solvents.[34] The reaction usually takes place in a heated sealed container, reactor, autoclave or bomb (made of Teflon and steel). The temperatures used are in the range of 100–250 ºC and the creation of internal pressures allows the nucleation of good-sized and high-quality crystals. This methodology is widely used for the formation of crystals of different dimensionality and/or porosity.[35-37]

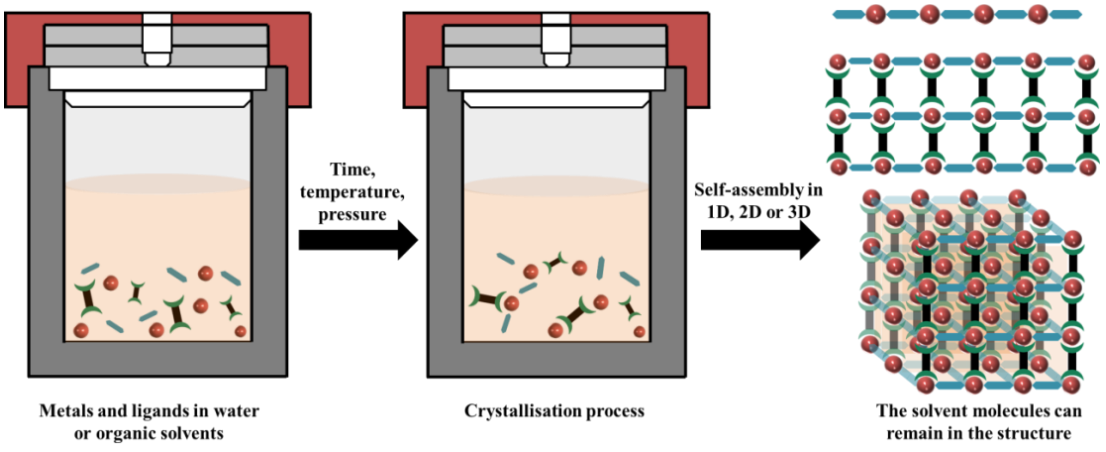

Figure 4.4 Schematic illustration of a hydro-/solvothermal approach for the formation of 1D, 2D and 3D CPs.

b) *In situ metal/ligand reaction*. In this approach, the formation of the needed ligand for the coordination bonds with the metal is synthesized *in situ* prior to the polymerization of the final functional complex.[38] The use of this hydro-/solvothermal metal/ligand reaction has been increased during the last years for the synthesis of CPs confirming the high effectiveness, simplicity and low environmental impact.[39-40] Some *in situ* ligand reactions like cycloaddition or carbon-carbon bond formation, are needed before the polymerization reaction. The whole process is carried out in the same set up and the combination with other approaches like diffusion[41] or solvothermal[42] could be necessary for the structuration of the CP.

1.1.3.3 Emerging approaches

The methodologies described above are useful for the formation of both crystals and amorphous CPs. Additionally, during the last years, other approaches have been implemented aiming to overcome one of the major challenges in this field: having nanostructures with fine-tuned properties by controlling the self-assembly of the components. Some examples of these emerging methodologies are described.

a) *Lab-on-a-chip*. The use of platforms with microfluidics features is showing their potential for the synthesis of novel materials with unprecedented properties.[43-45] Microfluidics, which is based on flow chemistry,[46] consisted on the fine control of the mass transport thanks to the sub-millimetre dimensions where the reaction is taken place (Figure 1.6).[47] The conditions reached in the microfluidic approach are completely different from the classical bulk synthesis. This is especially relevant for the formation of crystalline structures since the key parameters for their formation such as diffusion, mixing and heat transport are finely controlled.

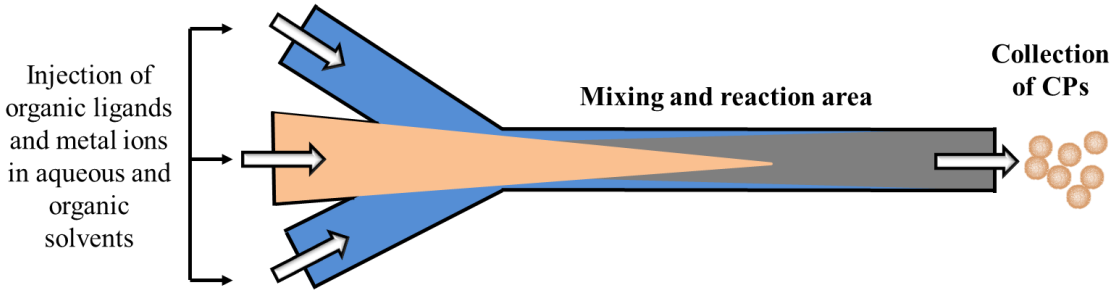

Figure 1.6 Schematic illustration of the laminar flow regime operating in a continuous flow platform.

b) *Direct synthesis on surfaces*. The direct growth of functional metal-organic nanostructures directly on surfaces is one of the approaches with special relevance due to the amount of potential applications that may arises upon their integration into functional hybrid devices.[48] Different technologies have been developed for the specific control of the synthesis on the surfaces of different substrates. In this sense, Dip-Pen Nanolithography (DPN, also named as direct-write atomic-force microscopy (AFM)-assisted lithography) allows the precise deposition of precursors (organic ligands and metal ions) in specific areas on the surfaces through the delivery of small volumes (femtolitre scale synthesis) by using the tip (Figure 1.5).[49]

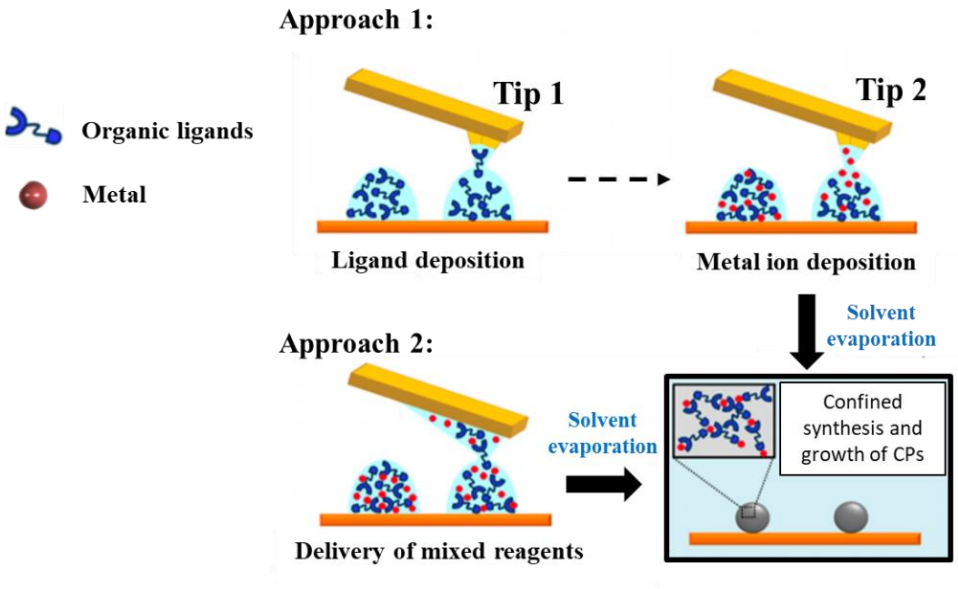

Figure 1.5 Schematic representation of two possible approaches for the direct synthesis of metal-organic nanostructures on surfaces. The synthesis can be done in femtolitre scale by using the tip of an AFM. Approach 1: two different AFM tips can be functionalized with ligands (Tip 1) and the metal salt (Tip 2); then both are mixed directly on the surface by sequentially delivering each one of the solutions. Approach 2: both ligand and metal ions can be mixed in the cantilever array and transferred to the surface where the reaction takes place. Adapted from ref. 49.

c) *Atomization*. The atomization of solutions containing the precursors in colloidal suspension let the formation of droplets which act as microreactors, allowing the formation and confined crystallization of several functional structures. The use of spray technique for the development of CPs have been reported previously.[50,51] This technique consisted on the atomization in droplets to confine the synthesis and self-assembly of the precursors forming the CPs (Figure 1.6)

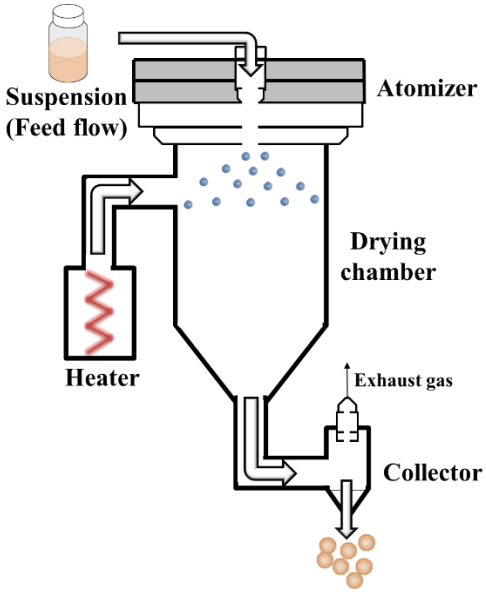

Figure 1.6 Scheme of a spray-drying set up for the formation of CPs.

d) External stimuli. Some external stimuli such as microwave or ultrasounds can be applied during the synthesis reaction in order to generate extreme conditions. The heating effect, due to the application of microwaves, accelerates the reaction times compared with the conventional reactions (Figure 1.7a).[52,53] In the other case, the ultrasounds-assisted or sonochemistry reactions promotes the creation of acoustic cavitation followed by a local temperature and pressure increase.[54] The application of ultrasounds promotes the formation of bubbles that collapse reaching high temperature and pressure values (Figure 1.7b).

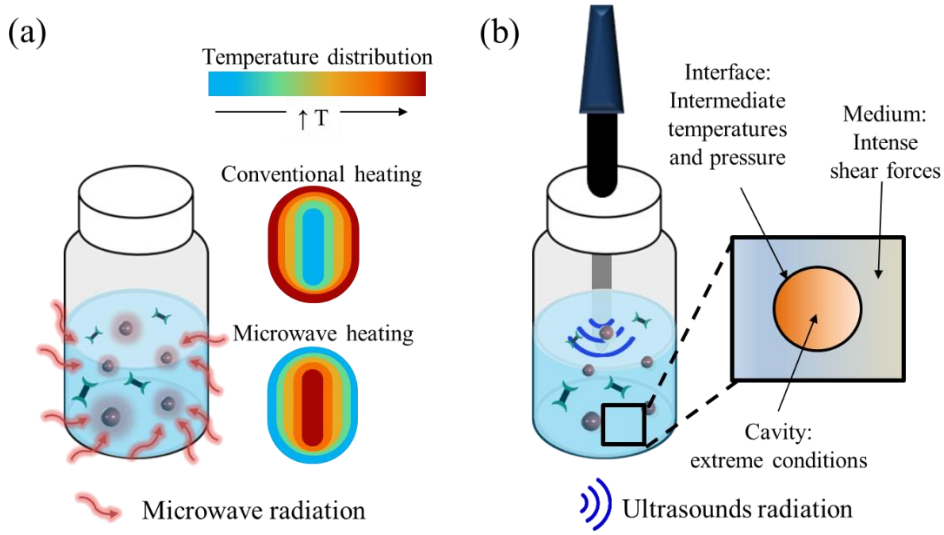

Figure 1.7 Schematic illustration of external stimuli synthetic methods. (a) Microwave radiation directly heats the reaction mixture due to its interaction with the molecules involved. This allows to locally increase the temperature with low dissipation. (b) The energy received from ultrasounds radiation let the formation of acoustic cavitation which generates a localized increase of temperature and pressure arousing in extreme conditions.

e) Nano- and microemulsion. Some examples in the literature use the nano-/microemulsion for the synthesis of nanoparticles. In this case, the systems are generated through water-in-oil emulsion strategy which allows the formation of crystalline particles.[55-58] Water-in-oil, or reverse (oil-in-water), microemulsions are highly tailorable thanks to the tune of the nanometre-sized water droplets stabilized with surfactants. The size and morphology of the resulting particles can be modulated by varying the water to surfactant ratio. The micelles formed during the emulsions can act as nanoreactors which controls the nucleation and growth of the nano-/micro particles. The use of this methodology is mainly reported for the formation of NMOFs due to the crystalline nature of the products generated in this synthetic route.

Worth to mention, depending on the design and chemical nature of the starting materials, the synthetic procedures can be done with a combination of approaches adapting each one to the specific needs. Most of the synthetic routes presented are based on out-of-equilibrium approaches were the reaction conditions can be tuned to get the self-assembly of functional materials with new and interesting physicochemical properties. The exploration of molecular self-assembly occurred out of chemical equilibrium let to generate chemical states that can be properly isolated showing relevant features. The rational combination of self-assembly processes, out-of-equilibrium conditions and confined environments can promote the formation of unprecedented nanoscale systems with revolutionary properties applicable in different technological areas.

1.1.4 Properties and applications

As detailed in the previous section, many approaches can be used for obtaining functional CPs with a wide range of morphologies and structures. These CP-based materials have demonstrated exceptional intrinsic features that make them especially interesting for multitude of applications. The most important ones are:

i. The rational design through the selection of ligands and metals allows suitable modifications to enhance interaction ligand-metal and addition of other functionalities.
ii. The dimensionality can be systematically modified by the presence of metal-ligand bonds, which exhibits directional interactions.
iii. The metals provide the final functional properties of CPs, which can be used for magnetic, electronic, optical, catalytic and biological applications, among others.

An extensive interest in the development of new nanostructured CPs is related with their novel encouraging and high impact applications, especially in such areas as, gas adsorption and separation processes,[13,31,59-61] theranostics (i.e. diagnosis and drug delivery),[11,12,34,62-64] sensor devices,[65,66] heterogeneous and biomimetic catalysis,[33,67,68] photoluminescence,[23,31,33,39,70] energy and electronics (e.g. energy harvesting, conductivity),[17,18,38,71-73] among others.

In many of these applications, nanostructuration has become essential in such it allows for the exploitation of novel and unprecedented properties. This allows for the development of sustainable processes that respect the environment by avoiding the use of harmful solvents. Furthermore, recent progress showed that CPs with nano-sized dimensions can overcome the limitation of solubility. The reduction to nanoscale can promotes the formation of stable colloidal dispersions in water. This fact can favour the development of novel functional CPs for their application in different fields.

1.2 Colloidal-sized CPs

1.2.1 The role of water stability

As mentioned above, there is a tendency to use more and more synthetic routes and methodologies that meet the requirements of the so-called Green chemistry (no use of organic solvents, eco-friendly methods, etc.). This is a key parameter when designing new nanostructured CPs which no longer only must fulfil a series of structural and functional characteristics, but at the same time must be environmentally friendly and sustainable. It is therefore essential to create new functional nanostructured systems that are chemically stable in aqueous media and whose properties remain intact.

At this point, one must distinguish between soluble and colloidal systems in water. The solubility of the coordination polymer formed will determine its stability in water and therefore its use in applications that require the use of this solvent. Soluble CPs has recently attracted increasing interest.[74] The metal ion induces self-assembly of polytopic ligands can be employed to make macromolecular assemblies in solution. This new class of CPs can be formed by carefully adjusting the boundary conditions of self-assembly. The final strength of the binding constants between metal ions and ligands will determine the formation of soluble CPs, since, if the interaction is very weak macromolecular species will not be form, but if it is too strong, precipitation may occur. For this reason, intermediate binding constants imply a facile exchange of ligands, forming soluble CPs which are generally dynamic equilibrium systems. However, this dynamic nature poses a great challenge for characterization because structure and property depend on external conditions. For this reason, the

study and formation of soluble CPs has motivated its use mainly in fundamental research to address questions concerning self-assembly thermodynamics and kinetics.

In other context, forcing systems to react in out-of-equilibrium conditions, induce the generation of non-covalent interactions during the self-assembly of its constituents allowing the formation of insoluble nanometre-scale aggregates that respond to environmental changes, and can thus become adaptable and start to display emergent properties characteristic of living systems. Furthermore, thanks to the possibility of the isolation of the obtained self-assembled nanostructures, they can be characterized in a wide range of techniques. The solubility of these kind of systems, especially in water, is highly dependent on the intrinsic properties. Nevertheless, for many potential applications, the water stability of the synthesized nanostructured materials becomes essential.

1.2.2 Colloidal nanostructured CPs in water

Water is often unavoidable, and even desirable, in common applications of colloidal chemistry. Instead of design and synthesize soluble CPs, another strategy is to form CPs that are stable in the form of colloidal solutions by controlling their properties such as size, exposed functional groups and surface charge, among others. The main challenges to overcome in terms of colloidal stability in water, can be classified in two issues:

i. Physically: formation of aggregates and consequent sedimentation of the CP
ii. Chemically: loss of chemical structure (degradation)

Both issues can end up affecting the properties of the CPs and therefore invalidating its use in the desired application. In this scenario, nanoscience plays an important role in the formation of nanostructured CPs that are colloidal systems in water and maintain the necessary physical and chemical stability during the time necessary for their application. The system must not be only colloidal-stable in water for the time necessary to make use of its properties, but also its inevitable degradability over time must generate compounds that do not affect the environment in which they have been applied. This fact is critical especially in those applications related to medicine, where the requirements are much stricter due to their final use in patients.

The control of the reaction parameters for the formation of CPs and their versatility when choosing ligands and metals, allows the formation of nanostructured systems that can be redispersed in water to form colloidal solutions. However, if the CPs formed does not present colloidal stability, there are different strategies that can improve it, such as: i) mechanical dispersing tools (e. g. ultrasounds), ii)

surface coating (e. g. use of poly(ethylene glycol) - PEGylation) and iii) viscosity increase (e. g. surfactants) (Figure 1.8 and Table 1).

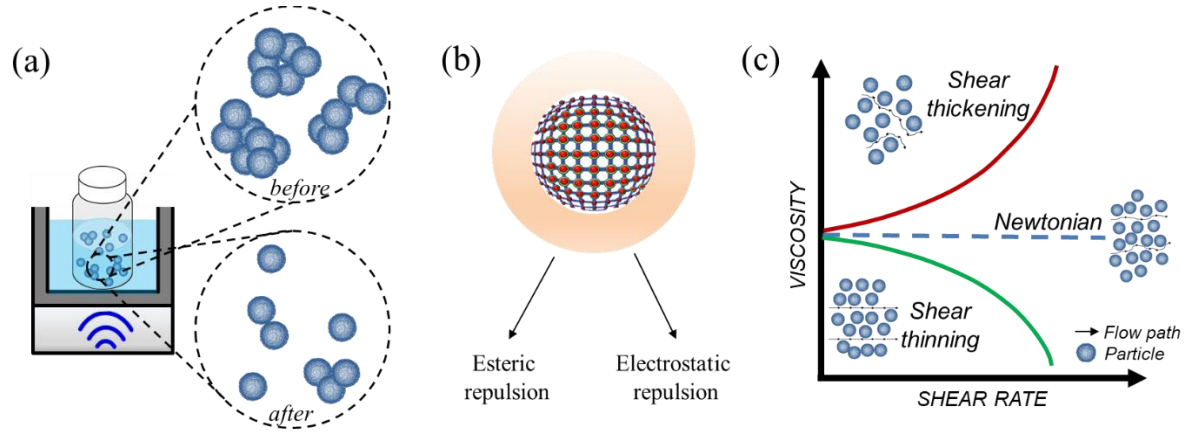

Figure 1.8 Main strategies for the obtaining of colloidal dispersions of nanostructured materials. (a) Mechanical dispersing tools such as ultrasounds let the separation of big aggregates avoiding the sedimentation. (b) The formation of core-shell systems through the coating of, for example, nanoparticles let to change the properties of the surface inducing repulsion between the nanostructured materials. (c) The change of the viscosity of the medium containing the nanostructured materials can promote a better colloidal dispersion of the systems changing the interaction between them.

Table 1.1 Main strategies for the improvement of the colloidal dispersions containing nanostructured materials.

Strategy	Method	Characteristics
Mechanical dispersing tools	Sonication	Use of ultrasounds energy for the separation of aggregates
Surface coating	Core-shell systems	Use of polymers (e.g. poly(ethylene glycol) - PEG), which change the surface of the CPs
Viscosity increment	Gelation	Use of substances (e.g. sugars, surfactants), which increase the viscosity of the solvent

The water colloidal stability is mainly determined by the inter-particle interaction resulting from the intermolecular and surface forces involved such as van der Waals or repulsive electrostatic forces, among others. The balance between these forces would determine the stability of nanostructured materials in aqueous suspensions. In this sense, the rational design of coordination polymers can tune their final physical features in order to enhance their stability. For example, the exposition on the surface of specific groups with different polarity can tune the surface charge thus increasing their colloidal stability. The adsorption of charged molecules or metal ions will be involved in ionization/dissociation processes that can trigger the water stability. Furthermore, the addition of polymers or biopolymers (e.g. PEG or surfactants) can lead to steric stabilization of the colloids in water. This strategy is a powerful tool for the stabilization of nanostructures by preventing the formation of attractive forces that induces the aggregation, agglomeration and consequent

precipitation of the nanostructured materials. In this case, the homogenous coating of the surface is necessary in order to achieve steric stabilization; otherwise, non-uniform coating of the surface induces the opposite effect by introducing aggregation.[75]

The control offered by the rational design of the coordination polymers allows to finely modulating the physicochemical properties and features of the developed system. Through the correct selection of organic ligands that expose functional groups in the surface that can be protonated/deprotonated according to the interaction with the medium, as well as their functionalization with other molecules, allows to greatly improve their colloidal stability. This versatility opens their use in a very broad range of applications where the water-stable colloidal suspension is an added value for their functional implementation.

1.2.3 State-of-the-art of colloidal coordination polymers suspensions

There is a plethora of examples concerning the use of nanomaterials which its main requirement is their colloidal stability in water. This is especially applicable for those developed materials with application in medicine where the stability of the nanostructures in water and physiological conditions must be proved. For this reason, in this section some characteristic examples will be discussed classified by some of the most reported applications. Two of these applications as thermochromic materials and as bioimaging probes are the focus of this Thesis. Additionally, especial attention will be paid on the challenges to be overcome by CPs as colloidal suspensions.

a) Thermochromic materials: The case of spin crossover

Briefly spin crossover is a phenomenon whereby a material can switch between two different electronic states (from low-spin configuration to high-spin configuration) as a result of an external stimulus such as temperature or light-irradiation. The spin crossover property is highly dependent on the environment of the material. Modifications in size, surface and solvation, among others, can induce changes that may modify or even eliminate the switch behaviour of the synthesized materials. For this reason, the colloidal dispersion of these materials in water is a challenge. Their stability in water could facilitate their integration in water-soluble polymers and open their application to other many fields instead of their main focus as memory devices. However, its study as colloidal suspensions in water has not been sufficiently developed due to the fragility of the spin crossover phenomenon. For achieving this, the main objective is to generate colloidal structures in water that also retain the magnetic properties. In this sense, some examples of spin crossover nanoparticles with stability in water have been reported. The main synthetic route used for

achieving colloidal stability is the microemulsion approach by the formation of water-in-oil (or reverse micelle) droplets. In this sense, Coronado *et al.*[57] and Gaspar, Real and co-workers[76] reported the synthesis of spherical Fe(II)-based NMOFs. Nevertheless, the use of surfactant was needed for the colloidal stability in water emulsions and the small changes in the ratio, especially in the second case, induced the precipitation of the nanoparticles synthesized losing their colloidal stability.

Although the use of surfactants could facilitate the formation of colloidal dispersions, their presence can modify the magnetic properties. Ruiz-Molina and co-workers described the formation of Co(III) NCPs through a one pot reaction.[77] The nanoparticles with average diameter of 79 ± 9 nm were obtained by adding the aqueous solution of metallic salt to an ethanolic solution containing the organic ligands. The fast addition of water let the precipitation of the insoluble nanoparticles which can be collected, washed and redispersed in water showing colloidal stability (Figure 1.9). The nanoparticles showed a smooth spherical shape. Furthermore, the size of the nanoparticles in the colloidal water suspensions was modulated by the control of the addition speed of water (Figure 1.9d).

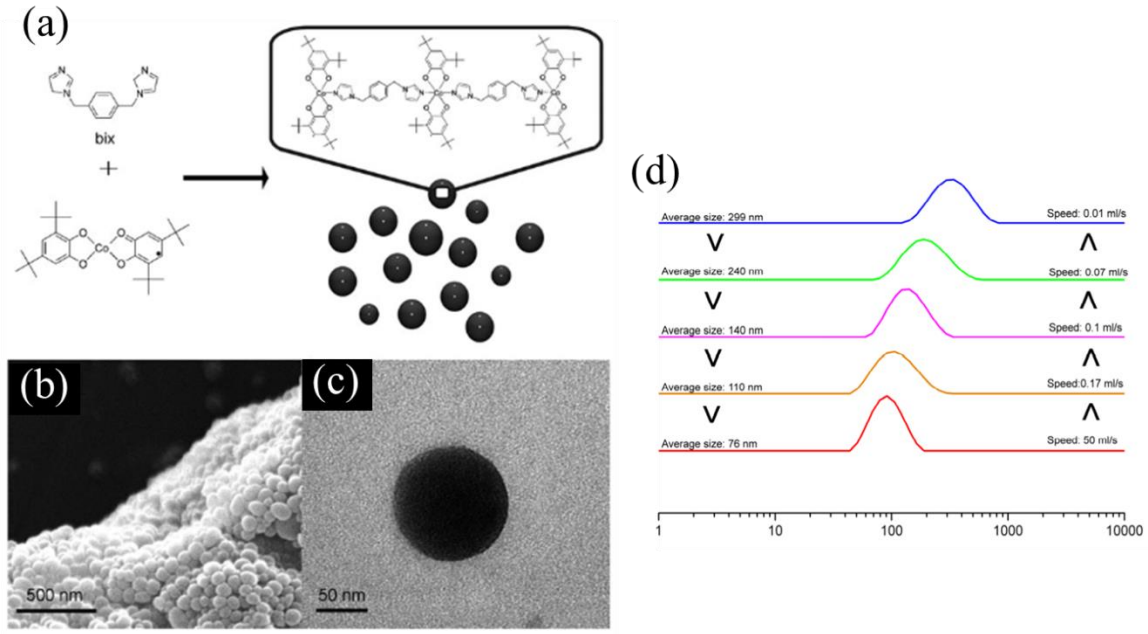

Figure 1.9 (a) Coordination polymerization used to obtain the Co(III)-based NCPs). (b) Scanning electron microscopy (SEM) image of nanoparticles created by infinite coordination polymerization. (c) High-resolution transmission electron microscopy (TEM) image of one spherical nanoparticle. (d) The modification of the water addition speed directed the final size of the colloidal nanoparticles in water. Reproduced from ref. 77.

Not many examples of water-stable colloidal suspensions of spin crossover nanoparticles are reported. One reason of this could be the high environment impact on the magnetic properties that not allow their properly dispersion in water without modifying their intrinsic properties. The exploration of the formation of nanostructured spin crossover materials by different methodologies avoiding the use of surfactants and allowing their colloidal dispersion in water is one of the most interesting challenges. This specific aspect is addressed in this Thesis.

b) Biosensing, imaging and drug delivery

In the case of the applications involved in nanomedicine, the water-stable colloidal suspension is a must. Both NMOFs and NCPs have to prove their stability in water for the needed time, avoiding aggregation and precipitation which would limit its potential clinical application. For this reason, understanding the key factors that influence the nanoparticle colloidal stability and aggregation when introduced in biological environments is important for the development of safe and effective functional nanostructures. The colloidal stability of the developed systems will determine its biodistribution, pharmacokinetics and systemic toxicity *in vivo*.[78] The physiological medium composition of an *in vivo* organism is not only formed by water but also several (bio)molecules, proteins and ions, among others, are present. This complex composition confers specific conditions to physiological medium in terms of ionic strength, concentration, pH and molecular interaction. In order to achieve colloidal stability *in vivo*, the water-stable colloidal suspension of CPs is one of the most critical points for their potential application and its complete study in real biological environment is necessary. Different approaches have been designed in order to assure the stability in such kind of environments involving electrostatic, steric and electrosteric stabilisation.[79,80] Some examples included in the aforementioned approaches are discussed next.

The electrostatic stabilisation is intimately related with the ionic strength. Ideally, by lowering the ionic strength, the particle-particle interaction is reduced. One strategy widely used is the functionalization of nanostructures with Bovine serum albumin (BSA) or similar (e.g. mouse serum albumin, MSA). The second approach consisted on the steric stabilization by introduction of natural (e. g. chitosan, alginate) or synthetic (PEG, poly(vinyl alcohol), PVA; poly(vinyl pyrrolidone) PVP) polymers. This method is the most common used for conferring stability to the nanoparticles with bioapplication. As a natural polymer, chitosan has been widely used for contributing on the stabilization of nanoparticles. In this sense Hyeon and co-workers reported the formation of Fe-based NCPs stabilized with chitosan.[81] The development of the therapeutic agent was achieved through the coordination between the dopamine-chitosan conjugate with iron metal ions in an oil-in-water reverse emulsion (Figure 1.10). The resulting nanoparticles had cubic morphology with good performance as therapeutic agent for hyperthermia. The use of chitosan, which is biocompatible and biodegradable,

allowed the improvement of the colloidal stability of the nanoparticles and enhances the *in vivo* blood circulation.

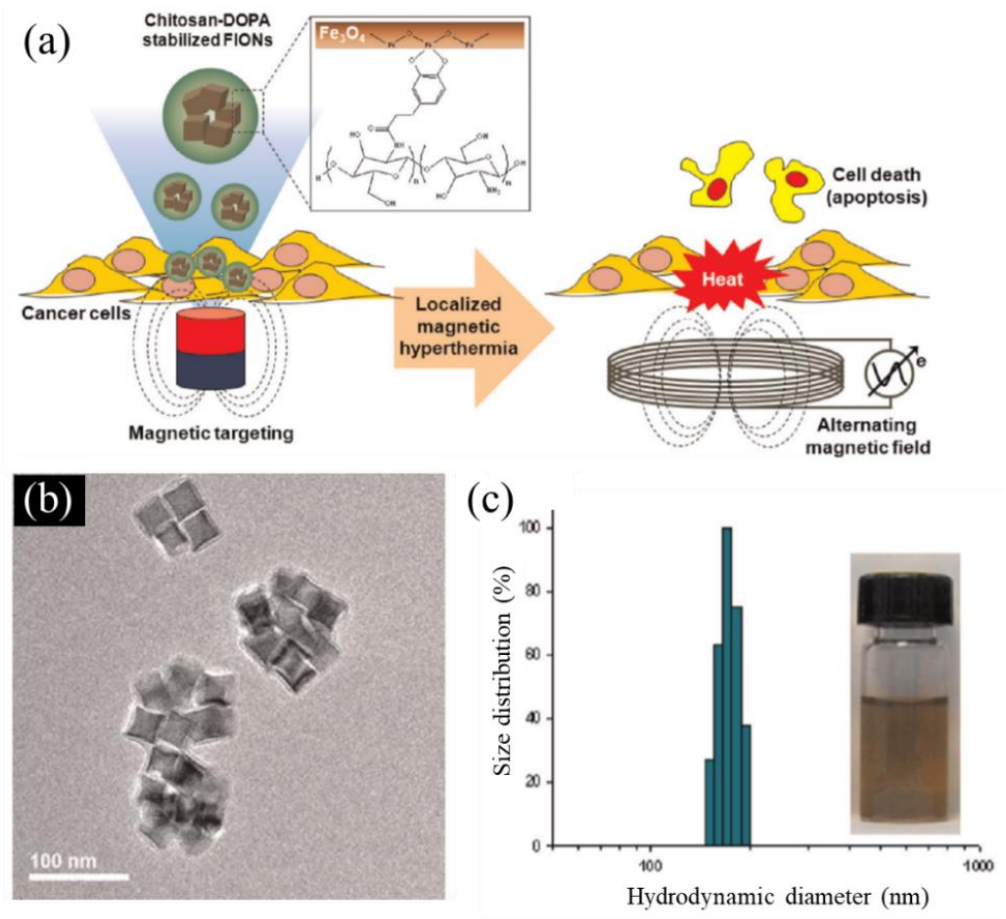

Figure 1.10 (a) Schematic illustration of Chitosan-Fe-based NCPs and their applications for the localized magnetic hyperthermia of cancer cells. (b) TEM image of Chitosan-Fe-based NCPs. (c) Hydrodynamic diameters of Chitosan-Fe-based NCPs in phosphate-buffered saline solution. Inset: Photograph showing the aqueous dispersion of Chitosan-Fe-based NCPs. Reproduced from ref. 81.

Usually, the nanoparticles are post functionalized with PEG molecules (PEGylated) in order to improve both colloidal stability and biocompatibility *in vivo*. Recently, in order to simplify the multi-step reaction processes, Chen and co-workers reported the formation of NCPs by one-pot synthesis reaction.[82] In this case the PEGylation was generated at the same time of the nanoparticle formation by the addition of poly-histidine-PEG co-polymer into the mixture of metal ions and organic ligands (Figure 1.11). Additionally, the nanoparticles synthesized were pH-responsive allowing their use as a therapeutic agent for cancer treatment by the delivery of Pt(IV) prodrug.

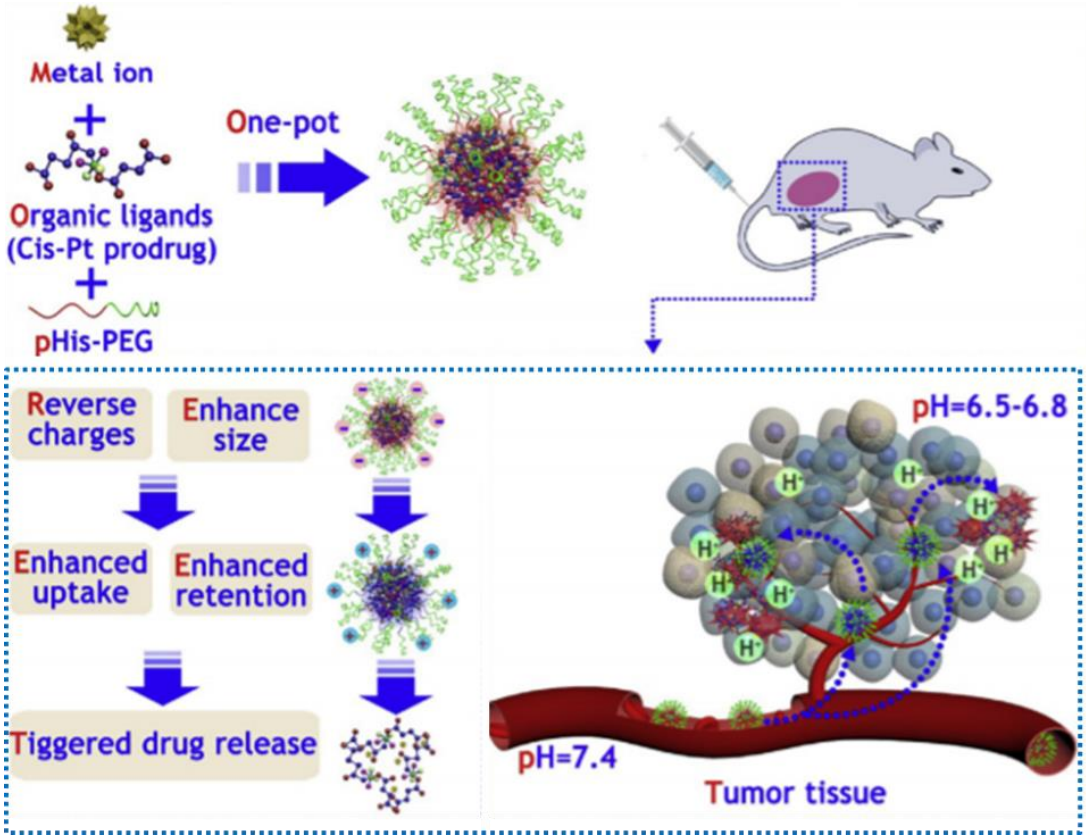

Figure 1.11 Schematic illustration of the one-pot synthesis of PEGylated NCPs and their application for responsive anticancer therapy. Reproduced from ref. 82.

There are several examples in the literature describing the use of PEG as stabilizing agent for different families of nanostructures. The use of PEG has demonstrated the reduction of protein absorption on the surfaces and the prolongation of circulation half-life *in vivo*. This is mainly due to the reduced opsonisation and increased stability of the systems in blood.[83,84] Other synthetic polymers have demonstrated its stabilizing effect. In this case, PVP has ben also widely used for the improving of colloidal stability of nanostructured materials. For example, Lin and co-workers reported the formation of NCPs from Tb(III) metal ions coordinated to Pt(IV) prodrug.[85] The PVP was added in a post-synthetic step allowing its attachment on the nanoparticles surface (Figure 1.12). This surface modification increased the colloidal stability of the nanoparticles with diameter of 52.8 ± 8.1 nm in aqueous suspensions and showed highly biodegradable nanoparticles *in vitro*.

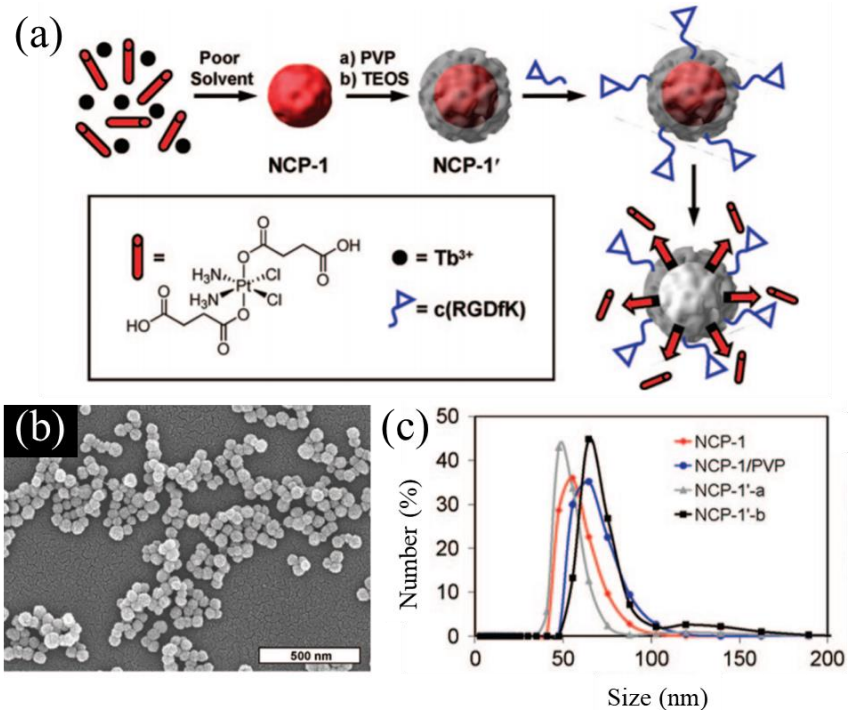

Figure 1.12 (a) NCPs constructed from Tb(III) ions and c,c,t-(diamminedichlorodisuccinato)Pt(IV) (DSCP, abbreviated for disuccinatocisplatin) bridging ligands, NCP-1, were precipitated from an aqueous solution of the components via the addition of a poor solvent. (b)TEM micrograph for as-synthesized NCP-1. (c) SEM micrographs for NCP-1. (d) Dynamic light scattering (DLS) curves for NCP-1, PVP functionalized NCP-1, and NCP-1′. Reproduced from ref. 82.

Other approach for the use of PVP consist on its *in-situ* addition during the formation of CPs. In this sense, Wang and co-workers described a one-pot methodology for the gram-scale synthesis of NCPs with highly reduced-size.[86] The coordination of Fe(III) ions with gallic acid and the addition of PVP during the synthesis let the formation nanoparticles with ultrasmall size (5.3 nm) (Figure 1.13). This reduced size allowed the renal clearance of the nanoparticles after their use in photothermal therapy.

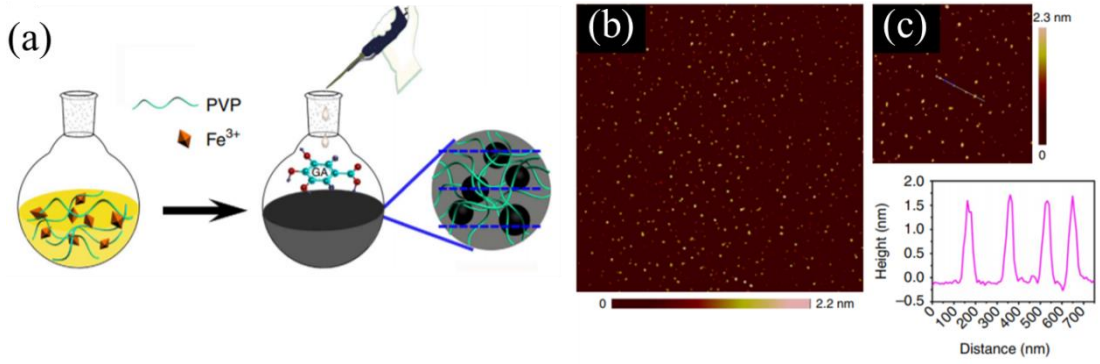

Figure 1.13 (a) Schematic illustration of the synthesis of Fe-based NCPs. (b, c) Images of Fe-based NCPs. The height profile along the line marked in the AFM image (c) is shown. Reproduced from ref. 86.

The use of PVP as stabilizer has been increased thanks to the *in vivo* proof of its non-toxicity, neutrality, long blood circulation times and low accumulation in vital organs.[87] Worth to mention that in some cases, the functionalization with natural or synthetic polymers not ensures a colloidal stability. In some systems, the polymer coating can become unstable and it can be dissociated from the surface due to the change of the conditions in the environment, resulting in the loss of the stability and thereof the precipitation of the nanostructured materials.

Finally, a third approach for the enhancement of colloidal suspensions consisted on the electrosteric stabilization through the incorporation of charged polymers as coating surfaces which induces electrostatic repulsive forces and steric hindrance which results in a combination of the both aforementioned approaches.

c) Other applications

Other applications such as catalysis in water require the properly stabilization of CPs in order to avoid its degradation.[88,89] A few examples of the use of CPs as catalysts for the photodegradation of different molecules are described. In this sense, Lang and co-workers reported the synthesis of Ag-based NCPs which exhibited good catalytic activity towards the photodegradation of nitrobenzene and other derivatives in aqueous solution under UV light irradiation.[90] In another example, Shi and co-workers described the formation of Zn(II)-based CPs for the photodegradation of different organic dyes in water.[91] Apart of catalysis, other interesting application is the use of CPs for water remediation. In this sense, MOFs and NMOFs have demonstrated their success for removing pollutants present in water. This is mainly due to the porous structure of MOFs which allows the absorption of molecules in their interstitial spaces. Their excellent performance in environmental field has generated a focus of attention for the development of MOFs and NMOFs with special attention in removing pollutants from contaminated water.[92] As an example, Li and co-workers reported a water-resistant MOF with hydrophobic nanospaces for extracting aromatic pollutants (benzene, toluene, xylene, and mixtures thereof) from water.[93]

1.3 Scope of the Thesis

The knowledge and study of the different topics reviewed here, originated this multidisciplinary thesis based on the synthesis of novel colloidal CPs for thermochromic and bioimaging probes. The structure of this Thesis is summarized in the next figure (Figure 1.16).

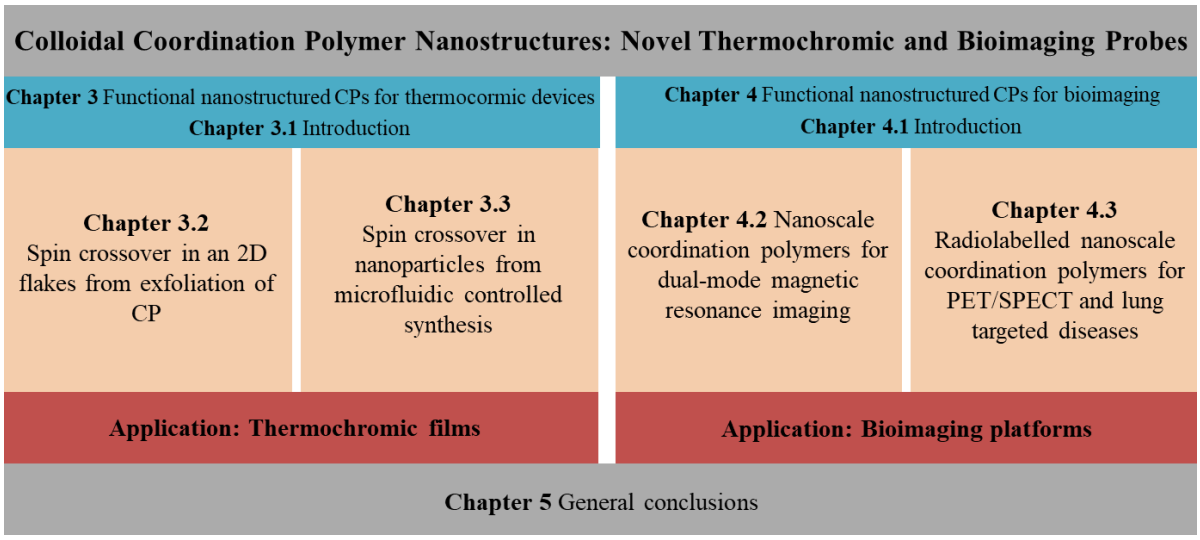

Figure 1.16 Schematic representation of the structure followed in this Thesis.

For the development of this Thesis, the work was based on two main challenges:

i. The first one consists on the **design and synthesis of novel colloidal CPs to be applied in different areas**, such as thermochromic (Chapter 3) and bioimaging (Chapter 4) probes. The rational design was based on the formation of CPs as functional nanostructured materials in out-of-equilibrium conditions. In all the cases, the synthesized nanostructures in the form of colloidal suspensions in water were explored.

   In the Chapter 3, the obtaining of functional nanostructured CPs with spin crossover behaviour useful for switchable devices was done through two different approximations that correspond to two different-sub-chapters:

   a) In Chapter 3.2, the nanoparticles were synthesized by using a lab-on-a-chip based on a microfluidic device. The synthesis of a well-known Fe(II)-based CP by controlling the reaction-diffusion conditions, let the formation of unprecedented nanoparticles with modified magnetic properties.

b) In Chapter 3.3, mono- and bilayers of a Fe(II) CP were obtained by using a top-down technique which consisted on the liquid phase exfoliation of the bulk crystals. This strategy allowed the formation of 2D flakes which retained the magnetic properties.

In the Chapter 4, the rational design offered by CPs allowed the establishment of a feasible strategy for the development of novel NCP nanoparticles based on one-pot reaction synthesis:

a) In chapter 4.2, the nanoparticles were based on metals active in magnetic resonance imaging for their use as a potential contrast agent.
b) In chapter 4.3, the nanoparticles were synthesized following the same strategy but changing the metals in order to get radiolabelled systems for radioimaging. Additionally, a polydopamine-like coating was developed for its functionalization, PEGylation for improving their colloidal stability, and targeting for specific diseases.

ii. The second challenge was related on the **validation of the developed materials in their specific applications**. In order to bring the developed technologies out of the lab to the industry, the potential applicability of the developed nanostructured materials was validated. On the one hand, the materials developed in the Chapters 3.2 and 3.3, were integrated in composites for their use as thermochromic films. On the other hand, the NCP nanoparticles synthesized in Chapters 4.2 and 4.3 were validated *in vivo* as pre-clinical step for their application as bioimaging probes.

1.4 References

1. Staudinger, H. *Ber. Dtsch. Chem. Ges*. **1920**, *53*, 1073–1085.
2. Ariga, K.; Yamauchi, Y.; Aono, M.. *APL Mater*. **2015**, *3*, 061001.
3. Ariga, K.; Ji, Q.; Nakanishi, W.; Hill, J. P.; Aono, M.. *Mater. Horiz.* **2015**, *2*, 406–413.
4. Aono, M.; Ariga, K. *Adv. Mater*. **2016**, *28*, 989–992.
5. Ariga, K.; Malgras, V.; Ji, Q.; Zakaria, M. B. *Coord. Chem. Rev*. **2016**, *320–321*, 139–152.
6. Du, M.; Li, C.-P.; Liu, C.-S.; Fang, S.-M. *Coord. Chem. Rev.* **2013**, *257*, 1282–1305.
7. Tong, M.-L; Chen, X.-M. Synthesis of Coordination Compounds and Coordination Polymers. In Modern Inorganic Synthetic Chemistry; Xu, R., Xu, Y., Eds.; Elsevier, **2017**; 2nd Edition, pp 189–217.
8. Furukawa, H.; Cordova, K. E.; O'Keeffe, M.; Yaghi, O. M. *Science* **2013**, *341*, 1230444.
9. Oh, M.; Mirkin, C. A. *Nature* **2005**, *438*, 651–654.
10. Sun, X.; Dong, S.; Wang, E. *J. Am. Chem. Soc.* **2005**, *127*, 13102–13103.

11. Spokoyny, A. M.; Kim, D.; Sumrein A.; Mirkin, C. A. *Chem. Soc. Rev*. **2009**, *38*, 1218–1227.
12. He, C.; Lin, W. Chem. Rev. 2015, 115, 11079–11108.
13. Jiang, W.-L; Fu, Q.-J.; Yao, B.-J; Ding, L.-G.; Liu, C.-X.; Dong. Y.-B. *ACS Appl. Mater. Interfaces* **2017**, *9*, 36438-36446,
14. d'Aquino, A. I.; Kean, Z. S.; Mirkin, C. A. *Chem. Mater*. **2017**, *29*, 10284–10288.
15. Adarsh, N. N.; Frias, C.; Lohidakshan, T. M. P.; Lorenzo, J.; Novio, F.; Garcia-Pardo, J.; Ruiz-Molina, D. Chem Eng J. **2018**, *340*, 94–102.
16. Novio, F.; Lorenzo, J.; Nador, F.; Wnuk, K.; Ruiz-Molina, D. *Chem. Eur. J.* **2014**, *20*, 15443–15450.
17. Wang, F.; Kusaka, S.; Hijikata, Y.; Hosono, N.; Kitagawa, S. *ACS Appl. Mater. Interfaces* **2017**, *9*, 33455–33460.
18. M. Oh,C. A. Mirkin, *Angew.Chem. Int. Ed.* **2006**, *45*, 5492 – 5494.
19. Nihei, M; Ui, M.; Yokota, M.; Han, L.; Maeda, A.; Kishida, H.; Okamoto, H.; Oshio, H. *Angew. Chem. Int. Ed*. **2005**, *44*, 6484–6487.
20. Maity, D. K.; Otake, K. ; Ghosh, S.; Kitagaw, H.; Ghoshal, D. *Inorg. Chem*. **2017**, *56*, 1581−1590.
21. Rosa, I. M. L.; Costa, M. C. S.; Vitto, B. S.; Amorim, L.; Correa, C. C.; Pinheiro, C. B.; Doriguetto, A. C. *Cryst. Growth Des.*, **2016**, *16 (3)*, 1606–1616.
22. Drath, O.; Gable, R. W.; Poneti, G.; Sorace, L.; Boskovic, C. *Cryst. Growth Des*., **2017**, *17 (6)*, 3156–3162.
23. Andersen, J.; Mack, J. *Green Chem*., **2018**, *20*, 1435–1443.
24. Howard, J. L.; Cao, Q. C.; Browne, D. L. *Chem. Sci*., **2018**, *9*, 3080–3094.
25. James, S. L.; Adams, C. J.; Bolm, C.; Braga, D.; Collier, P.; Friščić, T.; Grepioni, F.; Harris, K. D. M.; Hyett, G.; Jones, W.; Krebs, A.; Mack, J.; Maini, L.; Orpen, A. G.; Parkin, I. P.; Shearouse, W. C.; Steed, J. W.; Waddell, D. C. *Chem. Soc. Rev*., **2012**, *41*, 413–447.
26. Parmar, B.; Rachuri, Y.; Bisht, K. K.; Laiya, R.; Suresh, E. *Inorg. Chem*., **2017**, *56 (5)*, 2627–2638.
27. Barreda, O.; Taggart, G. A.; Rowland, C. A.; Yap, G. P. A.; Bloch, E. D. *Chem. Mater*., **2018**, *30 (12)*, 3975–3978.
28. Julien, P. A.; Mottillo, C.; Friščić, T. *Green Chem*., **2017**, *19*, 2729–2747.
29. Gu, J.-Z.; Liang, X.-X.; Cui, Y.-H; Wu, J.; Shi, Z.-F.; Kirillov, A. M. *CrystEngComm*, **2017**, *19*, 2570–2588.
30. Eichhöfer, A.; Lebedkin, S. *Inorg. Chem*. **2018**, *57*, 602–608.
31. Sanoja, G. E.; Schauser, N. S.; Bartels, J. M.; Evans, C. M.; Helgeson, M. E.; Seshadri, R.; Segalman, R. A. *Macromolecules* **2018**, *51*, 2017–2026.
32. Wang, H.-Y.; Cui, L.; Xie, J.-Z.; Leong, C. F.; D'Alessandro, D. M.; Zuo, J.-L. *Coord. Chem. Rev*. **2017**, *345*, 342–361.

33. Zhuge, F.; Brassinne, J.; Fustin, C.-A.; van Ruymbeke, E. Gohy, J. F. *Macromolecules* **2017**, *50*, 5165–5175.
34. Du, L.-Y.; Shi, W.-J.; Hou, L.; Wang, Y.-Y.; Shi, Q.-Z.; Zhu, Z. *Inorg. Chem.* **2013**, *52*, 14018–14027.
35. Lu, S.-Q.; Fang, K.; Liu, Y.-Y.; Li, M.-X.; Liu, S.-J.; He, X. *CrystEngComm*, **2018**, *20*, 5045–5055.
36. Cui, J.-W.; Hou, S.-X.; Li, Y.-H.; Cui, G.-H. *Dalton Trans*., **2017**, *46*, 16911–16924.
37. Chowdhuri, A. R.; Laha, D.; Chandra, S.; Karmakar, P.; Sahu, S. K. *Chem Eng J*. **2017**, *319*, 200–221.
38. Chen, X.-M.; Tong, M.-L. *Acc. Chem. Res*., **2007**, *40 (2)*, 162–170.
39. Li, Q.; Yu, M.-H.; Xu, J.; Li, A.-L; Hu, T.-L.; Bu, X.-H. *Dalton Trans*., **2017**, *46*, 3223–3228.
40. Chen, Q.-F.; Zhao, X.; Liu, Q.; Jia, J.-D.; Qui, X.-T.; Song, Y.-L.; Young, D. J.; Zhang, W.-H.; Lang, J.-P. *Inorg. Chem*., **2017**, *56 (10)*, 5669–5679.
41. Dutta, B.; Jana, R.; Sinha, C.; Ray, P. P.; Mir, M. H. *Inorg. Chem. Front*., **2018**, *5*, 1998–2005.
42. Guardingo, M.; González-Monje, P.; Novio, F.; Bellido, E.; Busqué, F.; Molnár, G.; Bousseksou, A.; Ruiz-Molina, D. *ACS Nano*, **2016**, *10 (3)*, 3206–3213.
43. Górriz-Echaide, C.; Clément, C.; Cacho-Bailo, F.; Téllez, C.; Coronas, J. *J. Mater. Chem. A*, **2018**, *6*, 5485–5506.
44. Sevim, S.; Sorrenti, A.; Franco, C.; Furukawa, S.; Pané, S.; deMello, A. J.; Puigmartí-Luis, J. *Chem. Soc. Rev*., **2018**, *47*, 3788–3803.
45. González-Estefan, J. H.; Gonidec, M.; Daro, N.; Marchivie, M.; Chastanet, G. *Chem. Commun*., **2018**, *54*, 8040–8043.
46. Puigmartí-Luis, J.; Rubio-Martínez, M.; Hartfelder, U.; Imaz, I.; Maspoch, D.; Dittrich, P. S. *J. Am. Chem. Soc*., **2011**, *133*, 4216–4219.
47. Puigmartí-Luis, J. *Chem. Soc. Rev*. **2014**, *43*, 2253–2271.
48. Molnár, G.; Cobo, S.; Real, J. A.; Carcenac, F.; Daran, E.; Vieu,́ C.; Bousseksou, A. *Adv. Mater*. **2007**, *19*, 2163−2167.
49. Gong, C.; Zhang, J.; Zeng, X.; Xie, J. *Dalton Trans*., **2017**, *46*, 25–28.
50. Li, Y.-N.; Wang, S.; Zhou, Y.: Bai, X.-J.; Song, G.-S.; Zhao, X.-Y.; Wang, Q.-T.; Qi, X.; Zhang, X.-M.; Fu, Y. *Langmuir*, **2017**, *33 (4)*, 1060–1065.
51. Carné-Sánchez, A.; Imaz, I.; Cano-Sanabria, Maspoch, D. *Nat. Chem.* **2013**, *5*, 203–211.
52. Diring, S.; Furukaw, S.; Takashima, Y.; Tsuruoka, T.; Kitagawa, S. *Chem. Mater*., **2010**, *22 (16)*, 4531–4538.
53. Liu, B.; He, Y.; Han, L.; Singh, V.; Xu, X.; Guo, T.; Meng, F.; Xu, X.; York, P.; Liu, Z.; Zhang, J. *Cryst. Growth Des*., **2017**, *17 (4)*, 1654–1660.
54. Masoomi, M. Y.; Morsali, A.; Junk, P. C.; Wang, J. *Ultrason Sonochem*. **2017**, *34*, 984–992.

55. W. J. Rieter, K. M. L. Taylor, H. An, W. Lin, W. Lin, *J. Am.Chem. Soc*. **2006**, *128*, 9024–9025.
56. K. M. L. Taylor, W. J. Rieter, W. Lin, *J. Am. Chem. Soc*. **2008**, *130*, 14358–14359.
57. E. Coronado, J. R. Galan-Mascaros, M. Monrabal-Capilla, J.Garcia-Martinez, P. Pardo-Ibanez, *Adv. Mater*. **2007**, *19*, 1359.
58. K. M. L. Taylor, A. Jin, W. Lin, *Angew. Chem. Int. Ed*. **2008**, *47*, 7722–7725.
59. Rodenas, T.; Luz, I.; Prieto, G.; Seoane B.; Miro, H.; Corma, A.; Kapteijn, F.; Llabrés-Xamena, F. X.; Gascon, J. *Nat. Mater*. **2015**, *14*, 48–55.
60. Duan, J.; Jin, W.; Kitagawa, S. *Coord. Chem. Rev*. **2017**, *332*, 48–74.
61. Samokhvalov, A. *Coord. Chem. Rev*. **2018**, 374, 236–253.
62. Novio, F.; Simmchen, J.; Vázquez-Mera, N.; Amorín-Ferré, L.; Ruiz-Molina, D. *Coord. Chem. Rev*. **2013**, *257*, 2839–2847.
63. He, C.; Liu, D.; Lin, W. *Chem. Rev*., **2015**, *115 (19)*, 11079–11108.
64. Zheng, H.; Zhang, Y.; Liu, L.; Wan, W.; Guo, P.; Nyström, A. M.; Zou, X. *J. Am. Chem. Soc*., **2016**, *138 (3)*, 962–968.
65. Campell, M. G.; Liu, S. F.; Swager, T. M.; Dincă, M. *J. Am. Chem. Soc*., **2015**, *137 (43)*, 13780–13783.
66. Chen, M.-M.; Zhou, X.; Li, H.-X.; Yang, X.-X.; Lang, J.-P. *Cryst. Growth Des*. **2015**, *15 (6)*, 2753–2760.
67. Zhang, H.; Liu, G.; Liu, H.; Wang, T.; Ye, J. *Nano Energy*, **2016**, *22*, 149–168.
68. Huang, Y.-B, Wang, Q.; Liang, J.; Wang, X.; Cao, R. *J. Am. Chem. Soc*., **2016**, *138 (32)*, 10104–10107.
69. Wang, J.; Jiang, M.; Yan, L.; Peng, R.; Huangfu, M.; Guo, X.: Li, Y.; Wu, P. *Inorg. Chem*. **2016**, *55 (24)*, 2660–12668.
70. Gu, T.-Y.; Dai, M.; Young, D. J.; Ren, Z.-G.; Lang, J.-P. *Inorg. Chem*. **2017**, *56 (8)*, 4668–4678.
71. Zhang, X.; Wang, W.; Hu, Z.; Wang, G.; Uvdal, K. *Coord. Chem. Rev*. **2015**, *284*, 206–235.
72. Sanda, S.; Biswas, S.; Konar, S. *Inorg. Chem*. **2015**, *54 (4)*, 1218–1222.
73. Guan, B. Y.; Yu, X. Y.; Wu, H. B.; Lou, X. W. *Adv. Mater*. **2017**, *29*, 1703614.
74. Friese, V. A.; Kurth, D. G. *Coord. Chem. Rev*. **2008**, *252*, 199–211.
75. Biggs, S.; Habgood, M.; Jameson, G. J.; Yan, Y.-d. *Chem. Eng. J*. **2000**, *80*, 13–22.
76. I. Boldog, A. B. Gaspar, V. Martínez, P. Pardo-Ibanez, V. Ksenofontov, A. Bhattacharjee, P. Gutlich, J. A. Real, *Angew. Chem. Int. Ed*. **2008**, *47*, 6433–6437.
77. Imaz, D. Maspoch, C. Rodriguez-Blanco, J. M. Perez-Falcon, J.Campo, D. Ruiz-Molina, *Angew. Chem. Int. Ed*. **2008**, *47*, 1857–1860.
78. Moore, T. L.; Rodriguez-Lorenzo, L.; Hirsch, V.; Balog, S.; Urban, D.; Jud, C.; Rothen-Rutishauser, B.; Lattuda, M.; Petri-Fink, A. *Chem. Soc. Rev*. **2015**, *44*, 6287–6305.

79. Jiang, X.; Weise, S.; Hafner, M.; Röcker, C.; Zhang, F.; Parak, W. J.; Nienhaus, G. U. *J. R. Soc. Interface*, **2009**, *7*, 5–13.
80. Bihari, P.; Vippola, M.; Schultes, S.; Praetner, M.; Khandoga, A.; Reichel, C.; Coester, C.; Tuomi, T.; Rehberg, M.; Krombach, F. *Part. Fibre Toxicol*. **2008**, *5*, 14.
81. Bae, K. H.; Park, M.; Do, M. J.; Lee, N.; Ryu, J. H.; Kim, G. W.; Kim, C. G.; Park, T. G.; Hyeon, T. *ACS Nano* **2012**, *6*, 5266–5273.
82. Yang, Y.; Xu, L.; Zhu, W.; Feng, L.; Liu, J.; Chen, Q.; Dong, Z.; Zhao, J.; Liu, Z.; Chen, M. *Biomaterials*, **2018**, *156*, 121–133.
83. Gref R.; Lück, M.; Quellec, P.; Marchand, M.; Dellacherie, E.; Harnisch, S.; Blunk, T.; Müller, R. H. *Colloids Surf. B* **2000**, *18*, 301–313.
84. Owens, D.E.; Peppas, N. A. *Int. J. Pharm.* **2006**, *307*, 93–102.
85. Rieter, W. J.; Pott, K. M.; Taylor, K. M. L.; Lin, W. *J. Am. Chem. Soc*. **2008**, *130*, 11584–11585.
86. Liu, F.; He, X.; Chen, H.; Zhang, J.; Zhang, H.; Wang, Z. *Nat. Commun.* **2015**, *6*, 8004.
87. Johnson, N. J. J.; Oakden, W.; Stanisz, G. J.; Prosser, R. S.; van Veggel, F.C.J.M. *Chem. Mater*. **2011**, *23*, 3714–3722.
88. Pintado, S.; Goberna-Ferrón S.; Escudero-Adán, E. C.; Galán-Mascarós, J. R. *J. Am. Chem. Soc*. **2013**, *135*, 13270−13273.
89. Li, S. -X.; Ni, C. -Y.; Chen, M. -M.; Dai, Ming, Zhang, W. -H.; Yan. W. -Y.; Qi, H. -X; Ren, Z. -G.; Lang, J. -P. CrystEngComm **2014**, *16*, 2158–2167.
90. Wu, X. -Y.; Qi, H. -X.; Ning, J. -J.; Wang, J. -F.; Ren, Z. -G.; Lang, J. -P. *Appl Catal. B-Environ*. **2015**, *168-169*, 98–104.
91. Liu, L. -L.; Yu, C. -X.; Zhou, W.; Zhang, Q. -G.; Liu, S. -M.; Shi, Y. -F. *Polymers* **2015**, *8*, 3.
92. Bian, Y.; Xiong, N.; Zhu, G. *Processes* **2018**, *6*, 122.
93. Li, J. -H.; Li, M.; Li, D. *Chem. Eur. J*.**2014**, *20*, 12004–12008.

Chapter 2

Objectives

Accordingly with the described in the introduction, the two main general objectives set for this Thesis are:

1. To design novel functional coordination polymers by using different methodologies for the formation of 2D materials and nanoparticles.

2. To validate the potential use of developed nanostructured systems thermochromic and bioimaging probes.

To achieve the first objective, the following specific objectives were set:

I. To synthesize and characterize novel 2D flakes from liquid-phase exfoliation of a Fe(II)-tetrazole based CP .

II. To synthesize and characterize novel coordination nanoparticles based on Fe(II)-triazole CP by microfluidic approach.

III. To synthesize and characterize a novel set of NCPs nanoparticles based on Fe(III), Gd(III), Mn(II), In(III) and Cu(II) by one-pot reaction.

To achieve the second objective, the following specific objectives were set:

I. To assess the water colloidal stability of all the complexes developed.

II. To study the spin crossover occurrence of obtained 2D flakes and coordination nanoparticles based on Fe(II)-tetrazole/triazole.

III. To integrate the 2D flakes and coordination nanoparticles based on Fe(II)-tetrazole/triazole into polymeric composites for its use as thermochromic films.

IV. To study the *in vitro* and *in vivo* behaviour of the set of NCPs nanoparticles based on Fe(III), Gd(III), Mn(II), In(III) and Cu(II).

V. To pre-clinical validate the set of NCPs nanoparticles based on Fe(III), Gd(III), Mn(II), In(III) and Cu(II) as bioimaging probes.

Chapter 3

Design of Novel Nanostructured Coordination Polymers with Spin Crossover Behaviour for Thermochromic Devices

Chapter 3.1

Introduction

In this section, the nanostructuration design and synthesis of Fe-tri/tetrazole based coordination polymers with spin crossover (SCO) property are described. The section includes two different subchapters that encompass two different approaches for obtaining advanced functional materials. On the one hand, in Chapter 3.2, the exfoliation of a bulk CP is used to obtain 2D layers, on the other hand, in Chapter 3.3, the formation of nanoparticles through the use of a microfluidic device is presented. Previously, a discussion on the SCO phenomenon and the state-of-the-art of SCO nanomaterials is presented.

3.1 Introduction

3.1.1 Spin crossover phenomenon: The Fe(II) complexes

The first observation of the spin crossover (SCO) phenomenon was done in 1931 by L. Cambi and co-workers.[1] The spin transition (ST) was observed in an octahedral Fe(III) dithiocarbamate complex, where the magnetic moment changed as a function of the temperature, due to an electronic reconfiguration within the Fe(III) ions. Since then, the SCO event has been associated to a reversible ST between the low spin-state (LS) and high spin-state (HS). This phenomenon, observed mainly for some of the first-row transition metal complexes of d^4-d^7 electronic configurations (Cr(II), Mn(II), Mn(III), Fe(III), Fe(II)), can be induced by external stimuli such as photoexcitation, a magnetic field, mechanical pressure or temperature. From a structural point of view, the occurrence of SCO is related with the change of the coordination sphere of the complex. Therefore, the occurrence of SCO in coordination compounds of transition-metal ions is directed by the relationship between the strength of the ligand field (the electrostatic field acting at the central metal ion) and the mean spin-pairing energy.[2,3] In other words, depending on whether the ligand field strength is weaker or stronger than the spin pairing energy, octahedral complexes of $d^{4–7}$ ions may be either HS or LS.

The most studied SCO materials are related with Fe(II) coordination complexes (d^6 configuration), with an all-nitrogen donor environment (FeN_6), inducing an intermediate ligand field. As a result, there is a change of spin from HS (S=2, $^5T_2$) with a paramagnetic behaviour at high temperatures to LS (S=0, $^1A_1$) with a diamagnetic behaviour at low temperatures (Figure 3.1).

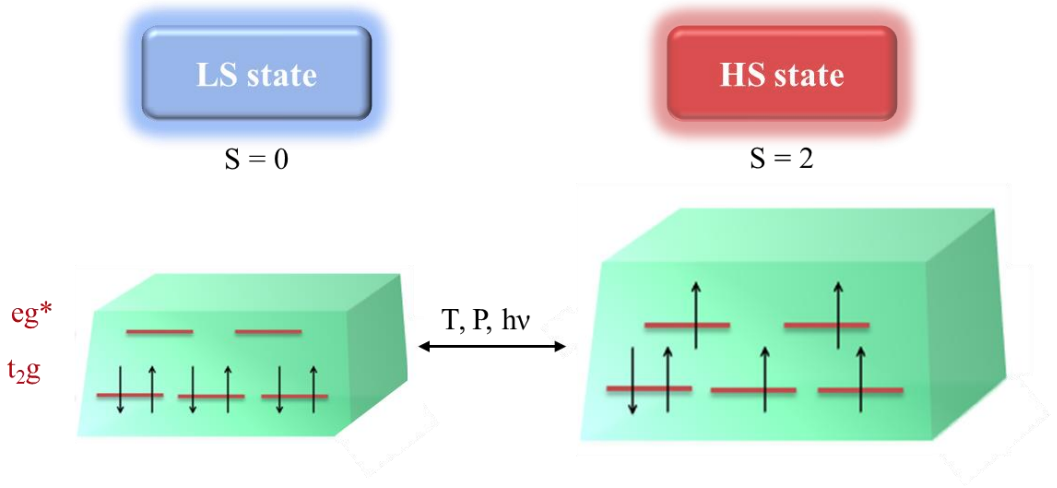

Figure 3.1 (a) Change of electron distribution between low spin (LS) and high spin (HS) states of an octahedral Fe(II) compound induced by an external stimulus. The orbitals eg* and t_2g arise from splitting of the 3d orbitals in an octahedral ligand field.

Finally, it is worth to mention that the electronic redistribution experienced by Fe(II) ions results in well-defined changes of the optical and magnetic properties of the complex. For these reasons, the SCO materials are very attractive as potential candidates for their application as electronic devices, (data and memory storage), molecular switches and sensors.[4,5]

3.1.2 Thermal spin transition: Thermochromic effect

In the case of Fe-based complexes, the occurrence of SCO is associated to a change in the bond distance between the iron atoms and the ligand (Fe-L). Specifically, the Fe-N bond length experiments a contraction during the spin transition from HS to LS, with values of approximately 2.1 and 1.9 Å for Fe(II) complexes, respectively. For a thermally induced SCO to occur, the difference in the Gibb's free energies for the two spin states involved must be on the order of thermal energy, k_BT.[6]

The ligand field strength of a complex is correlated to the metal-ligand bond length and this is true for both the HS and LS state of the same complex; consequently, it is possible to define the mean difference in metal ligand bond lengths between the HS and the LS state Δr_{HL} ($\Delta r_{HL} = r_{HS}-r_{LS}$, with r_{HS} and r_{LS} the metal-ligand bond length for the HS and the LS states, respectively, Figure 3.2).

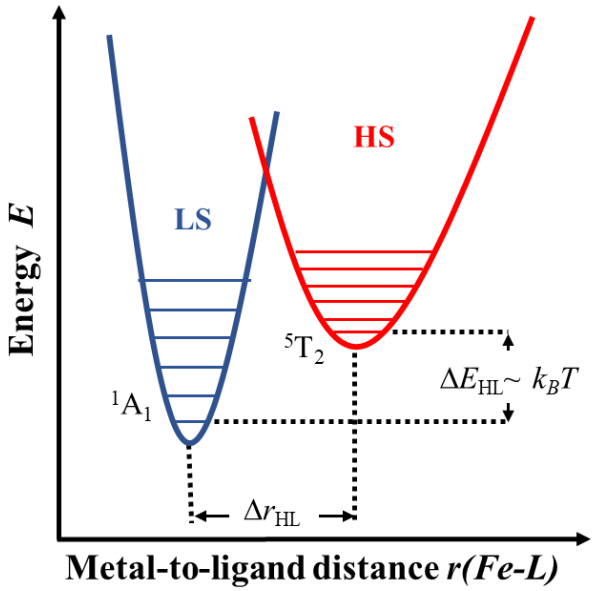

Figure 3.2 Potentials for the HS and the LS states along the most important reaction coordinate for SCO, namely the totally symmetric metal-ligand bond length denoted r(Fe-L). SCO is mostly accompanied by a colour change. The condition to fulfil in order to observe thermal SCO is $\Delta E_{HL} \approx k_BT$.

This means that in a configurational coordinate diagram (Figure 3.2), the minima of the HS and LS potential energy wells will be displaced (horizontally and vertically). In order to induce the spin transition, the zero-point energy difference between the HS and LS states (given by $\Delta E^{o}_{HL} = E^{o}_{HS} - E^{o}_{LS}$) has to be within a thermally accessible range (Figure 3.2). When this situation is satisfied, all complexes will occupy the LS state at very low temperatures, while the entropy driven population of the HS state occurs at higher temperatures (the higher entropy associated with the HS state is derived from electronic contributions from spin degeneracy and a vibrational component). In conclusion, the LS state is the ground state, but at higher temperatures, the HS state becomes the thermodynamically stable state.[7]

Furthermore, the Fe-N bond length contraction and distortion parameters accompanying the SCO from LS to HS are also correlated to a significant variation of the cell parameters and the volume of the cell, while macroscopic repercussions on the mechanical properties of the crystal are ultimately observed. In addition, these structural modifications induce modifications of the vibrational properties of the metal complex eventually impacting the optical properties of the material upon the transition.

3.1.3 Nanostructuration of spin crossover materials

Nanomaterials possess unique nanoscale, size-dependent physical and chemical properties that can be controlled in a way that is not feasible in bulk materials. So far, SCO materials have been studied as bulk powders or crystals and, more recently, as micro- and nanoscale thin films, nanoparticles or single molecules on the quest for their integration into functional devices. In this Thesis, we have been focused on the nanostructuration of SCO materials through two different approaches which consisted on the formation of i) free-standing films and ii) nanoparticles. For this reason, in this section, the main examples and some precedents of these approaches are discussed.

a) Thin films

During the last decades, an enormous effort has been carried out for the assembly of SCO thin layers and patterns on using different approaches. One of the most used consisted on the thermal evaporation of SCO systems on substrates for the formation of films. The versatility of this approach has been reported by Berndt and co-workers.[8] In their work, the authors described the formation of a densely packed layer of [Fe-$(phen)_2(NCS)_2$] and [$Fe(bpz)_2$phen] (where phen = 1,10-phenanthroline and bpz = dihydrobis(pyr-azolyl)borate) (Figure 3.3). The results reported indicated a transition between LS and HS states of the films formed on gold substrates (Figure 3.3b-d). Additionally, the

switching did not induce any instability of the ordered layer, which would limit the number of switching cycles of a given molecule.

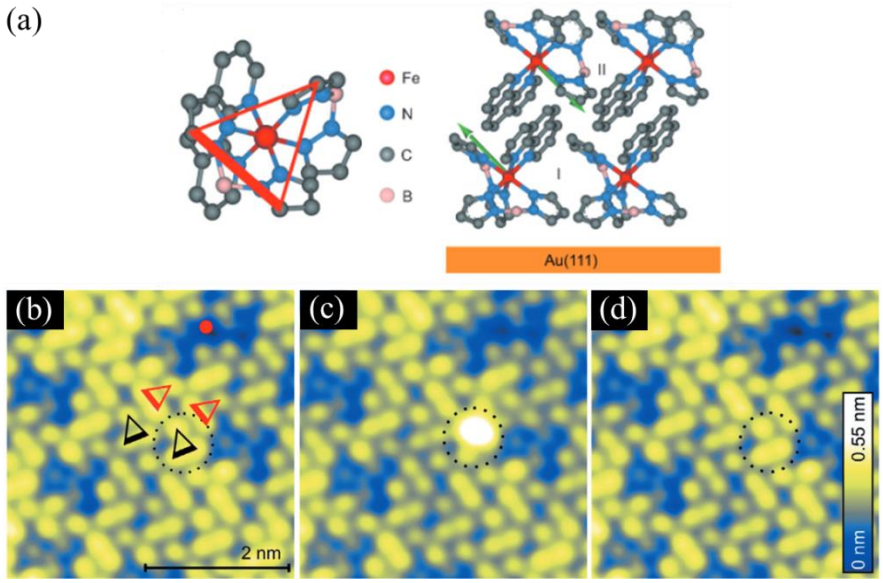

Figure 3.3 (a) Left: View of $[Fe(bpz)_2(phen)]$ along a pseudo-trigonal molecular axis. A triangle connecting three pyrazole groups is used to represent the orientation of the molecule. The thicker and shorter side indicates the two pyrazole groups of a single bpz ligand. Right: Proposed adsorption geometry on Au(111). Side view of the first two molecular layers. Green arrows depict the orientations of the dipoles of two molecules. (b-d) Constant-current scanning tunnelling microscopy (STM) topographs of a double layer of $[Fe(bpz)_2(phen)]$ on Au(111). (b-d) Sub-molecular resolution (V = -1.6 V, I = 50 pA). Triangles in (b) indicate selected molecules. Dotted circles in (b-d) indicate a molecule which is switched from LS (b) to HS (c) and back to LS (d). To switch from LS to HS, a 3 V pulse was applied with the tip positioned above the red dot in (b). HS–LS switching was obtained by pulsing directly above the HS molecule in (c). Reproduced from ref. 8.

The use of thermal evaporation allows for the formation of a wide variety of SCO-based thin films. In this sense, Tuczek and co-workers described the formation of thin films based on different analogues of the $[Fe(H_2Bpz_2)_2(phen)]$ (where H_2Bpz_2 = dihydrobis (pyrazolyl)borate) by physical vapour deposition (PVD) (Figure 3.4).[9] In all the cases, the thin films were formed on the quartz substrates showing ST with different behaviour allowing their physicochemical study.

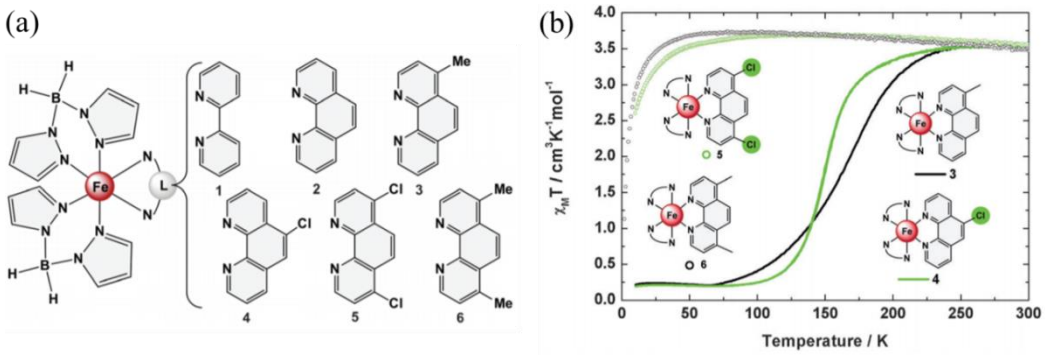

Figure 3.4 (a) The complexes $[Fe(H_2Bpz_2)_2(L)]$ investigated based on functionalized 1,10-phenanthroline ligands. (b) Molar magnetic susceptibility (χ_M) in function of temperature (T) curves of 3 (black line), 4 (green line), 5 (green circle) and 6 (black circle). Reproduced from ref. 9.

Following the same approach, Dougherty and co-workers reported the growth of films of Fe[$(H_2Bpz)_2$(bpy)] (where bpy = 2,2'-bipyridine) on Au(111) substrates.[10,11] The authors were able to growth films from bilayer to multilayer showing how the transition changed from the thinnest to the thicker films. The results showed that while bilayer system did not have evidence of temperature dependence of spin state composition, thicker films showed a transition related to changes in Fe(II) core (Figure 3.5). These differences between the thicknesses of the films grown may be related with the order-disorder degree of the films obtained, which directly affect to the spin transition. The fine tune of the packing of the SCO assemblies could allow controlling the ST behaviour compared with the bulk.

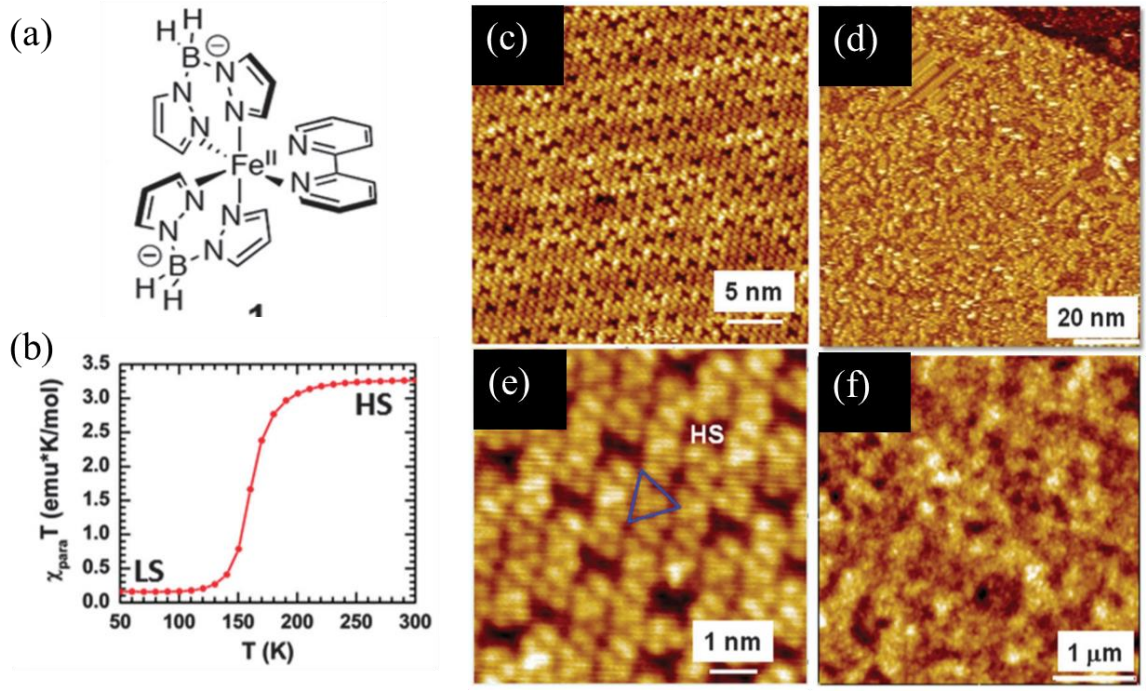

Figure 3.5 (a) Scheme of Fe[$(H_2Bpz)_2$(bpy)]. (b) Magnetometry measurements showing the χ_M vs T for the bulk powdered sample of Fe[$(H_2Bpz)_2$(bpy)] prior to film growth. (c) STM image (30 nm x 30 nm) of a bilayer film of [$H_2B(pz)_2$]Fe(II)(bpy) on Au(111). (c) small-scale STM image (7 nm x 7 nm) of bilayer film of Fe[$(H_2Bpz)_2$(bpy)] on Au(111) that shows an example of the LS molecule highlighted with a triangle and an example of an apparent depression corresponding to a HS molecule pair. (d) STM image (100 nm x100 nm) of the third layer of Fe[$(H_2Bpz)_2$(bpy)] on Au(111) showing predominantly disordered structures with only small domains of order (upper left). (e) AFM image (4 mm x 4 mm) of a 50 nm thick film of Fe[$(H_2Bpz)_2$(bpy)] on Au(111). Reproduced from ref. 10.

Most recently, Repain and co-workers reported the self–assembly of a monolayer of SCO molecules.[12] The obtained structure [Fe($(3,5\text{-}(CH_3)_2Pz)_3BH)_2$] (where Pz = pyrazolyl) was studied by scanning tunnelling microscopy (STM) and *ab initio* calculations revealing collective phenomena in 2D SCO layers (Figure 3.6). In this case, the SCO occurrence was light-induced, and it was demonstrated for the first time its propagation at the molecular scale. This example tried to overcome one of the challenges of the SCO systems which consisted on a new route for the control of bistability of individual SCO molecules ordered on a metallic substrate.

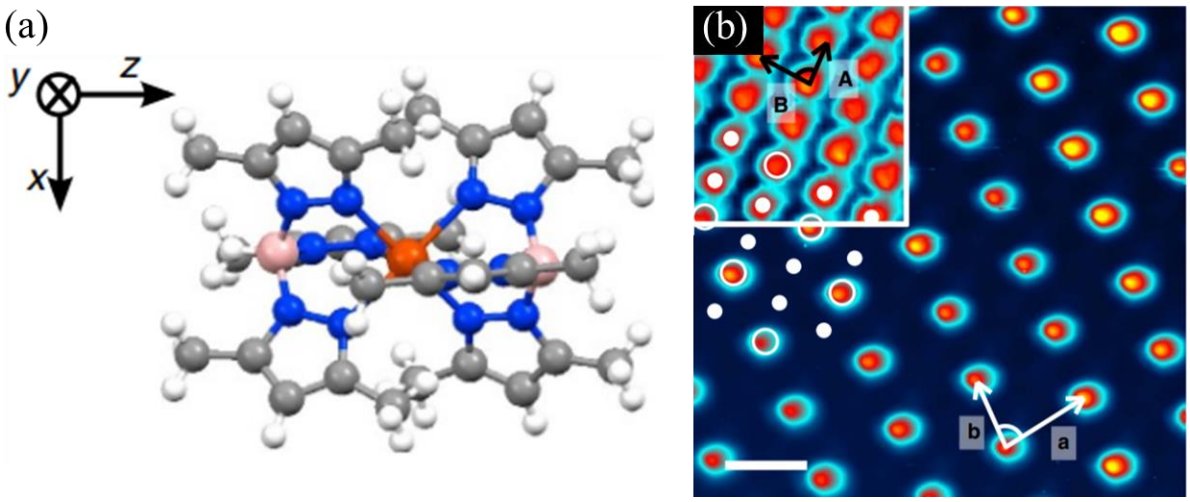

Figure 3.6. (a) Schematic of molecule [Fe((3,5-$(CH_3)_2Pz)_3BH)_2$] with the z axis along the B–Fe–B direction (grey: C atoms, blue: N atoms, pink: B atoms, red: Fe atom and white: H atoms). (b) STM image acquired at 0.3 V in constant height mode showing the mixed spin-state superstructure S1/3 (<I> = 50 pA). Inset, topographic STM image acquired at V = 1.5 V showing the full molecular crystal (I = 20 pA). The scale bar corresponds to 2 nm and is common for both images. The lattice vectors of the molecular network (A and B, black) and the S1/3 superstructure (a and b, white) are indicated. The full (empty) dots indicate the position of the dark (bright) molecules at 0.3 V. Reproduced form ref. 12.

A part of thermal evaporation, other approaches has been reported for the formation of thin films. Some of these methodologies are: Langmuir-Blodgett[13], soft lithography,[14,15] spin coating,[16] drop casting.[17], and lithographically controlled wetting.[18] Additionally to these approaches, it has been also reported several examples of the formation of hybrid thin films by embedding nanoparticles in polymeric structures, however these examples have not been considered here.

As we have seen in the previous examples, the SCO thin-films are based mainly on the integration of SCO nanostructures in substrates or matrices for the formation of films with different thickness. However, currently, there is not any example about a pure nanostructured SCO material in a free standing thin-film. This last corresponded to one of the main challenges faced in this Thesis.

The SCO phenomenon is highly dependent on the molecular environment (e.g. packing, crystallinity, anions and solvent molecules, among others), that make its occurrence critical. This fragility arouses in some major challenges associated with the use of nanotechnology to obtain functional materials owned by SCO. The main limitation is to achieve a homogeneous structure which in some cases is a requirement for the SCO applications. However, due to unwanted processes such us re-aggregation, decomposition or oxidation during the material processing, it is not possible to obtain adequate distribution on the substrate surface. Different approaches such as micro- and nanopatterning are currently investigated, however, further research is needed in order to properly develop this kind of nanostructures.[19,20]

In Chapter 3.2, we present a strategy for the direct formation of mono- and bilayers of a SCO material by a liquid phase exfoliation of the $[Fe(t3z)_2](ClO_4)_2$ complex. We hypothesized, that from multi-layered 2D CP we can obtain the layers separately for their single study. As far as we know, at the time of this Thesis, no example of a sheet–like SCO system has been described.

b) Nanoparticles

The first results concerning the synthesis of SCO nanoparticles were reported in 2004.[21,22] Létard *et al.* reported the synthesis of $[Fe(NH_2trz)_3](Br)_2 \cdot 3H_2O$, (where NH_2trz is: 4-amino-1,2,4-triazole) (Figure 3.7a).[23] The resulting nanoparticles, prepared by using the reverse micelle approach, had a mean size of 69 nm and exhibited a thermal hysteresis at room temperature (Figure 3.7b). Furthermore, the sharp ST and its hysteresis loop, were similar to the bulk powder material.

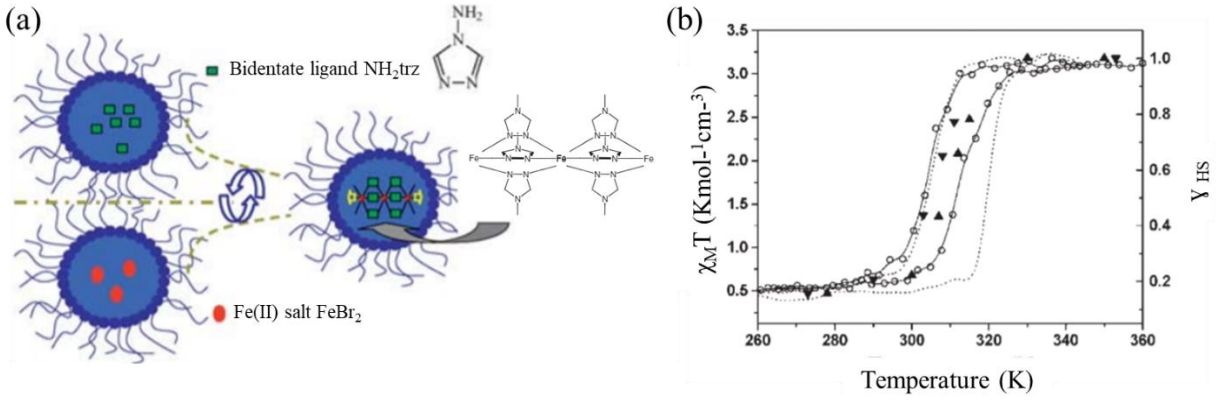

Figure 3.7 (a) Reverse micelle approach for the synthesis of the $[Fe(NH_2trz)_3](Br)_2 \cdot 3H_2O$ complex. (b) Plot of $\chi_M T$ vs. T of $[Fe(NH_2trz)_3](Br)_2 \cdot 3H_2O$ complex for nanoparticles (—) and for macroscopic particles obtained from a typical synthesis (--). The black triangles represent the calculated HS fraction obtained from the Raman spectrum at low frequency (i.e. 244 cm^{-1}), characteristic of the vibration of the inner Fe–N coordination sphere for the LS state. Reproduced form ref. 23.

In the last example, the authors reported the successful synthesis of SCO nanoparticles with controlled size and shape. In this sense, Létard and co-workers reported the synthesis of the $[Fe(NH_2trz)_3](Br)_2 \cdot 3H_2O$ complex using the reverse-micelle approach by varying the surfactant/water percentage. Through these modifications, the authors were able to prepare nanoparticles with sizes from 1.2 μm to 30 nm. However, the limit for the existence of a thermal hysteresis was at nanoparticles size around 50-30 nm. This observation demonstrated that for small particle sizes, the influence of the surface on the SCO properties and the presence of thermal bistability regime are certainly not negligible. Nevertheless, the physical limit for the SCO occurrence can vary for each different family of SCO systems.

As seen before, the reverse micelle approach has widely been used for the successful synthesis of SCO nanoparticles. As mentioned in Chapter 1, this approach consists on liquid polar droplets stabilized by surfactants in an oil phase.[24,25] With this method it is possible to modulate the final size of the nanoparticles by adjusting parameters such as water-surfactant molar ratio, stirring speed and temperature. These pioneer results have motivated the development of SCO nanoparticles by reverse-micelle approach. In this sense, Coronado *et al.* reported the synthesis of bistable SCO nanoparticles with magnetic hysteresis at room temperature.[26] The nanoparticles were based on the $[Fe(Htrz)_2(trz)](BF_4)$ (where Htrz = 1,2,4-1H-triazole and trz the deprotonated triazolato ligand) complex with a mean size of 11 ± 5 nm. The spin transition of the synthesized nanoparticles was retained almost identical to the bulk crystals with abrupt well-shaped thermal hysteresis loop of over 40 K (Figure 3.8).

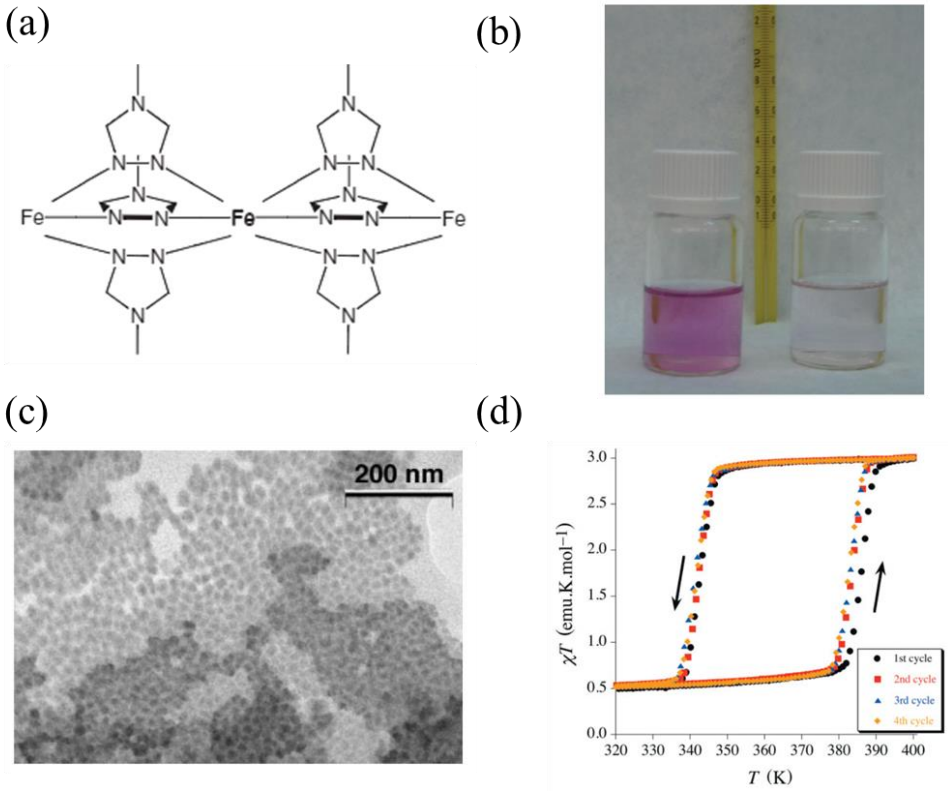

Figure 3.8 (a) Polymeric structure of the $[Fe(trz)_3]X_2$ family. (b) Bistability of a suspension of the $[Fe(Htrz)_2(trz)](BF_4)$ nanoparticles in octane: in the LS state (left) and in the HS state (right). (c) TEM image of as-prepared $[Fe(Htrz)_2(trz)](BF_4)$ nanoparticles. (d) Magnetic thermal hysteresis for as-prepared $[Fe(Htrz)_2(trz)](BF_4)$ nanoparticles (magnetic moment represented per mole of Fe). Reproduced from ref. 26.

Furthermore, the authors purposed two ways for the tuning of the nanoparticles and its SCO behaviour. On the one hand, the change of the solvent-water-surfactant ratios which directly affect the particle size and their magnetic properties and on the other hand, through the doping of the complex is possible to lower the critical temperatures. In this sense, Doudin and co-workers introduced

modifications on the synthesis of $[Fe(Htrz)_2(trz)]_n(BF_4)_n$ complex for the formation of nanoparticles with different morphology.[27] The use of a different surfactant let the formation of nanorods which exhibited similar SCO compared with its bulk counterpart (Figure 3.9). Additionally, the nanorods obtained, were positioned between Au electrodes exhibiting unexpected large conductivity with photoconductivity and photovoltaic behaviour.

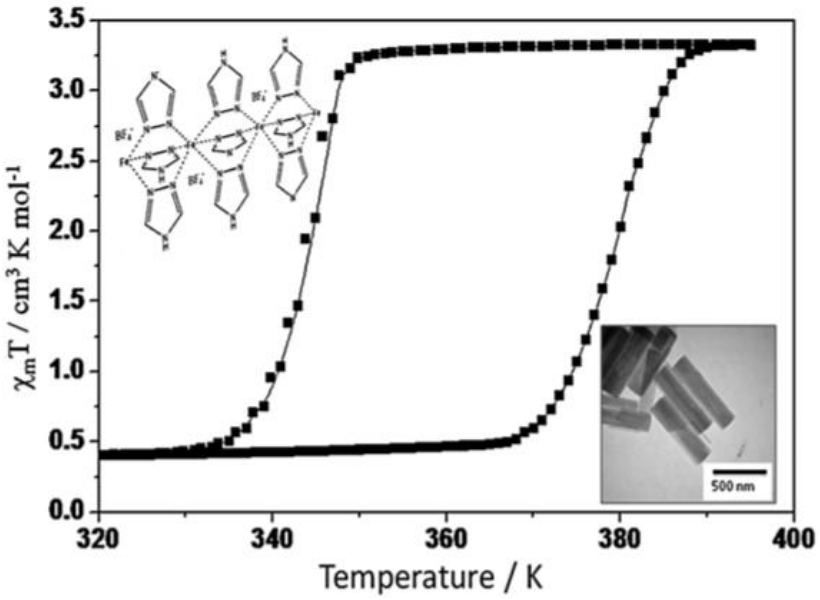

Figure 3.9 χM vs T measurements, structure representation of the $Fe(Htrz)_2(trz)](BF_4)H_2O$ polymer and TEM image of the nanoparticles prepared by a reverse micelle method. Reproduce from ref. 27.

The reduction of the nanoparticle size has been a focus of attention for the researchers. The study of the influence of the size with the SCO occurrence and the useful application of reduced-size nanoparticles in devices, make this challenge highly attractive. In this sense, in 2010 Bousseksou and co-workers reported the synthesis of 3-4 nm size SCO nanoparticles of the $[Fe(NH_2trz)_3](tos)_2$, (where tos is: p-toluene sulfonate anion)4-amino-1,2,4-triazole).[28] The nanoparticles were stabilized in colloidal suspensions by adding surfactants (Figure 3.10).

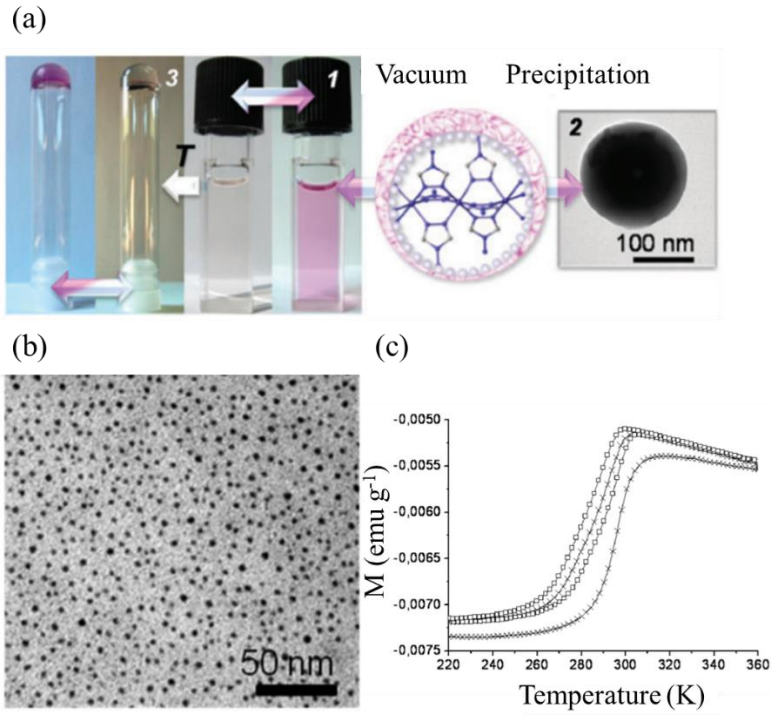

Figure 3.10 (a) Schematic representation showing the preparation procedure of SCO $[Fe(NH2trz)_3](tos)_2$ nanoparticles. A stable colloidal suspension 1 or a nanocrystalline solid 2 is obtained after vacuum treatment or solvent precipitation, respectively. Sample 3 is a transparent SCO gel obtained by thermal treatment of 1. (b) Cryo-microtomy TEM image of the 3–4 nm $[Fe(NH2trz)_3](tos)_2$ nanoparticles in a surfactant matrix (sample 1). (c) Temperature dependence of the magnetisation obtained when sample 1 goes through the first (x) and second (□) thermal cycles. After the first heating to 353 K the colloidal suspension 1 is transformed into a gel. Reproduced from ref. 28.

In this last example, the use of a non-ionic surfactant provided a useful medium for the formation and stabilization of $[Fe(NH_2trz)_3](tos)_2$ colloidal suspension. Surprisingly, although the SCO nanoparticles obtained had extremely reduced size, the system exhibited cooperative spin transitions (Figure 3.10c). These results indicated how the surfactant can influence in the SCO occurrence.

There are other approaches for the synthesis of SCO nanoparticles like polymer[29] and biopolymer stabilization (e. g. chitosan)[30] or the sol-gel technique.[31] However, all these approaches together with reverse-micelle method require the presence of stabilizers that can dramatically interact with the final product thus modifying or even cancelling the occurrence of spin transition. For this reason, there is still a need to employ a method that avoids the use of secondary materials such as polymers or surfactants for the synthesis of nanoparticles.

As we have seen in the previous examples, the nanostructuration of $[Fe(Htrz)_2(trz)]n(BF_4)_n$ in the form of nanoparticles has only been achieved through the reverse-micelle approach.[26,27] In Chapter 3.3, we present for the first time the use of a microfluidic system for the synthesis of SCO nanoparticles of the $[Fe(Htrz)_2(trz)]n(BF_4)_n$ complex as an alternative to surfactant-based approaches.

3.1.4 Spin crossover materials: the case of Fe-tri/tetrazole polymers

Since the discovery of the SCO phenomenon and during its development, multitude of materials have been obtained, grouped mainly into three groups of materials with SCO behaviour: i) mononuclear complexes with supramolecular interaction, ii) Hofmann clathrates and iii) 1D chain structure mainly based on Fe-triazole complexes with various counter anions and substituents.[32] We will focus on the last group of materials used in the present Thesis.

As we have seen in the last section, most of the examples concerning SCO materials consisted on Fe-tri/tetrazole based systems. There is a large group of SCO materials based on polymer chains containing the ligand triazole (trz) and its derivatives (tetrazole, tris-tetrazole, etc.).[33] This type of materials with general formula $[Fe(trz)_3]X_2$ (where trz is a triazole derivative and X is the counter anion) are in the form of polymeric 1D chains of triazole-bridged metal ions.[34,35] In 2011, Grosejan *et al.* reported the first single crystal based on Fe-triazole polymer: $[Fe(NH_2trz)_3]NO_3 \cdot 2H_2O$.[34] In their work, the authors described and proved the 1D polymeric nature of the crystal structure, the $[Fe(Rtrz)_3]$ chains, the anions and water implementation within the crystal structure.

The Fe-triazole based SCO materials present advantageous features compared with other type:

i) Tuneability of the SCO temperature and cooperative character by modifying the 4-substituent on the triazole ligand and the selection of the counterion
ii) High cooperativity thanks to the short Fe-Fe distances, the rigidity of the triazole ligands and its covalent connectivity.

For this thesis, the nanostructuration was performed over bulk systems based on Fe(II)-tri/tetrazole complexes. This selection allowed the discussion and comparison between the different approaches for the development of functional nanostructured SCO materials.

3.1.5 Scope of the Chapter 3

In the last section, the main examples in the literature about films and nanoparticles have been presented. At this point, it should be stressed that a reduction of the film thickness or particle size of an SCO could affect its physical properties drastically since electronic bistability depends on the collective behaviour of the SCO centres in the lattice. In recent years, efforts are focusing on the transferring of SCO phenomenon to thin layers and nanostructured materials such as thin films and nanoparticles. The need of obtaining stable materials which are able to act as SCO compounds without modifying the main properties of the bulk materials is being an important area of research. The advantages of nanotechnology applied to materials science, opens a wide range of new

applications for the development of structures with SCO phenomenon for different fields of science. This part aims to provide knowledge to help answer important still open questions such as:

i) What is the effect of the size reduction of materials on their SCO properties?
ii) It is possible to get SCO nanostructures from different novel approaches?
iii) How affect the embedment of SCO materials in polymeric films to the spin transition?
iv) Which is the role of counter anions and how can they modulate the SCO occurrence?

As aforementioned, the present Thesis has focused on the design of two different nanostructures based on Fe(II)-tri/tetrazole CPs with SCO properties. This specific property was selected due to its strong dependency with the size, morphology and chemistry of the material allowing to study the role of the nanotechnology for the design of novel nanostructures with different applications. In Chapter 3.2, we present the exfoliation of a Fe(II)-tetrazole based CP ($[Fe(t3z)_2](ClO_4)_2$, where t3z is Tris(2-(1H-tetrazol-1-yl)ethyl)-amine) for the formation of free-standing monolayers. Additionally, in Chapter 3.3, the microfluidics was used as a successful method for the synthesis of nanoparticles of a well-known Fe(II)-tetrazole CP ($[Fe(Htrz)_2(trz)]n(BF_4)n$, where Htrz stands for 1,2,4−triazole and trz for 1,2,4−triazolato). With these examples, we hypothesized that through the nanostructuration of SCO materials, we will able to fine tune its physicochemical properties by controlling its dependence with the environment and the size.

3.1.6 References

1. Cambi, L.; Cagnasso, A. Atti. Accad. Naz. *Lincei, CI. Sci. Fis., Mat. Nut., Rend* **1931**, *13*, 809.
2. Schläfer, H. L.; Gliemann, G. Einführung in die Ligandenfeldtheorie; Akademische Verlagsgesellschaft: Wiesbaden, Germany, **1980**.
3. Shriver, D. F.; Atkins, P. W.; Langford, C. H. Inorganic Chemistry, 2nd ed.; Oxford University Press: Oxford, Melbourne, Tokyo, **1994**.
4. Matsumoto, T; Newton, G. N.; Shiga, T.; Hayami, S.; Matsui, Y.; Okamoto, H.; Kumai, R.; Murakami, Y.; Oshio, H. *Nature Comm*. **2014**, *5*, 1-8.
5. Jureschi, C.-M.; Linares, J.; Boulmaali, A.; Dahoo, P. R.; 4 , Rotaru, A.; Garcia, Y. *Sensors* **2016**, *16*, 187-195.
6. Gütlich, P.; Hauser, A.; Spiering, H. *Angew. Chem., Int. Ed. Engl*. **1994**, *33*, 2024–2054.
7. Hauser, A. *Adv Polym Sci*. **2004**, *233*, 49–58.
8. Gopakumar, T. G.; Matino, F.; Naggert, H.; Bannwarth, A.; Tuczek, F.; Berndt, R. Angew. Chem. Int. Ed.2012,51, 6262 –6266.

9. Naggert, H.; Rudnik, J.; Kipgen, L.; Bernien, M.; Nickel, F.; Arruda, L.M.; Kuch, W.; Näther, C.; Tuczek, F. J. *Mater. Chem. C* **2015**, *3*, 7870–7877.
10. Pronschinske, A.; Bruce, R. C.; Lewis, G.; Chen, Y.; Calzori, A.; Buongiorno-Nardelli, M.; Shultz, D. A.; You, W.; Dougherty, D. B. *Chem. Commun*. **2013**, *49*, 10446–10452.
11. Pronschinske, A.; Chen, Y.; Lewis, G. F.; Shultz, D. A.; Calzolari, A.; Buongiorna-Nardelli, M.; Dougherty, D. B. *Nano Lett*. **2013**, *13*, 1429−1434.
12. Bairagi, K.; Iasco, O.; Bellec, Amandine, Kartsev, A.; Li, D.; Lagoute, J.; Chacon, C.; Girard, Y.; Rousset, S.; Miserque, F.; Dappe, Y. J.; Smogunov, A.; Barreteau, C.; Boillot, M. -L.; Mallah, T.; Repain, V. *Nat. Commun.* **2016**, *7*, 12212.
13. Soyer, H.; Dupart, E.; Gomez-Garcia, C. J.; Mingotaud, C.; Delhaes, P. *Adv. Mater*. **1999**, *11*, 382–384.
14. Cavallini, M.; Bergenti, I.; Milita, S.; Kengne, J.C.; Gentili, D.; Ruani, G.; Salitros, I.; Meded, V.; Ruben, M. *Langmuir* **2011**, *27*, 4076–4081.
15. Naik, A.D.; Stappers, L.; Snauwaert, J.; Fransaer, J.; Garcia, Y. *Small* **2010**, *6*, 2842–2846.
16. Tanaka, D.; Aketa, N.; Tanaka, H.; Tamaki, T.; Inose, T.; Akai, T.; Toyama, H.; Sakata, O.; Tajiri, H.; Ogawa, T. *Chem. Commun*. **2014**, *50*, 10074–10077.
17. Y. Galyametdinov, Y; Ksenofontov, V.; Prosvirin, A.; Ovchinnikov, I.; Ivanova, G.; Gutlich, P.; Haase, W. *Angew. Chem. Int. Ed*. **2001**, *40*, 4269–4271
18. Bartual-Murgui, C.; Akou, A.; Salmon, L.; Molnar, G.; Thibault, C.; Real, J.A.; Bousseksou, A. *Small* **2011**, *7*, 3385–3391.
19. Molnar, G.; Cobo, S.; Real, J.A.; Carcenac, F.; Daran, E.; Vien, C.; Bousseksou, A. *Adv. Mater*. **2007**, *19*, 2163–2167.
20. Cavallini, M. *J. Mater. Chem*. **2009**, *19*, 6085–6092
21. Létard, J. –F; Guionneau, P.; Goux-Capes, L.; Topics Curr. Chem. **2004**, *235*, 221–249.
22. Létard, J. –F.; Nguyen, O.; Daro, N. **2005**, Patent FR 0512476.
23. Forestier, T.; Mornet, S.; Daro, N.; Nishihara, T.; Mouri, S. -i.; Tanaka, K.; Fouché, O.; Freysz, E.; Létard, J. -F. *Chem. Commun*. **2008**, *36*, 4327–4329.
24. Harris, C.; Gaster, C.; Gelabert, M. C. *J. Chem. Educ.* **2019**, *96*, 565–570.
25. Ganguli, A. K.; Ganguly, A.; Vaidya, S. *Chem. Soc. Rev.* **2010**, *39*, 474-485.
26. Coronado, E.; Galán-Mascarós, J. R.; Monrabal-Capilla, M.; García-Martínez, J.; Pardo-Ibañez, P. *Adv. Mater*. **2007**, *19*, 1359–1361.
27. Etrillard, C.; Faramarzi, V.; Dayen, J. -F.; Létard, J. -F; Doudin, B. *Chem. Commun.* **2011**, *47*, 9663–9665.
28. Tokarev, A.; Salmon, L.; Guari, Y.; Nicolazzi, W.; Molnár, G.; Bousseksou, A. *Chem. Commun.* **2010**, *46*, 8011–8013.
29. Gural'skiy, I. y. A.; Quintero, C. M.; Molnár, G.; Fritsky, I. O.; Salmon, L.; Bousseksou, A. *Chem. Eur. J*. **2012**, *18*, 9946–9954.

30. Larionova, J.; Salmon, L.; Guari, Y.; Tokarev, A.; Molvinger, K.; Molnár, G.; Bousseksou, A. *Angew. Chem. Int. Ed.* **2008**, *47*, 8236–8240.
31. Faulmann, C.; Chahine, J.; Malfant, I.; de Caro, D.; Cormary, B.; Valade, L. *Dalton Trans.* **2011**, *40*, 2480–2485
32. Salmon, L.; Catala, L. *C. R. Chimie* **2018**, *21*, 1230–1269.
33. Aromi, G.; Barrios, L. A.; Roubeau, O.; Gamez, P. *Coord. Chem Rev.* **2011**, *255*, 485–546.
34. Grosejan, A.; Daro, N.; Kauffmann, B.; Kaiba, A.; Létard, J. F.; Guionneau, P. *Chem Commun*. **2011**, *47*, 12382–12384.
35. Roubeau, O.; Gomez, J. M. A.; Balskus, E.; Kolnaar, J. J. A.; Haasnoot, J. G.; Reedijk, J. *New J. Chem*. **2001**, *25*, 144–150.

Chapter 3.2

Spin Crossover in an Exfoliated 2–D Coordination Polymer and its Implementation in Thermochromic Films

In the following chapter, the obtaining of 2D flakes from the exfoliation of a Fe-based coordination polymer by a liquid-phase methodology with spin crossover (SCO) property will be described. The application of this top–down technique results in the formation of flakes with controlled thicknesses, down to 1–2 nm thick (mostly mono– and bi–layer) that retain the chemical composition and SCO interconversion of the bulk material. Moreover, these flakes can be handled as stable colloidal dispersions for many days allowing for its transfer in a controlled manner to solid substrates and the formation of thermochromic polymeric films as a proof–of–concept device. The properties of the exfoliated 2D layers obtained will be compared with its bulk counterpart to evaluate the influence of the dimensionality on the observed physicochemical properties.

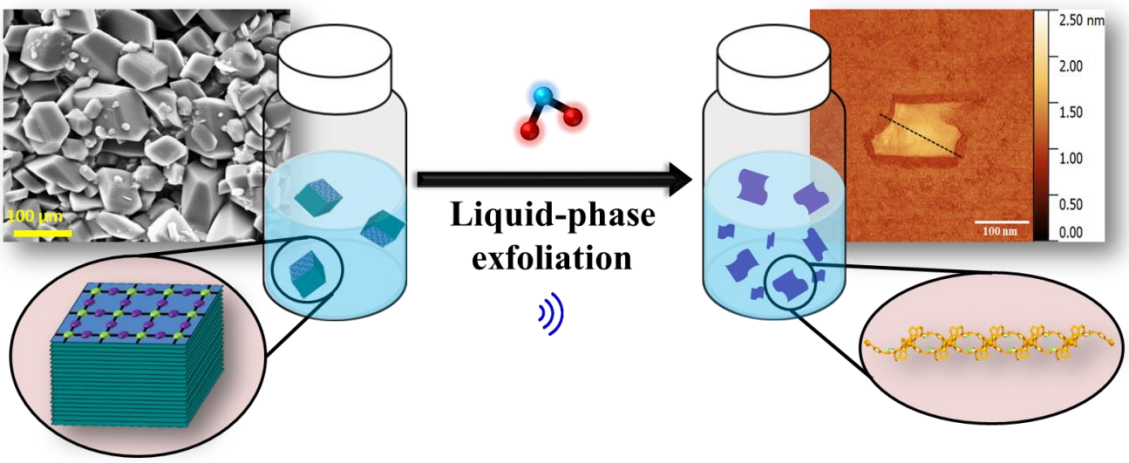

3.2.1 Introduction

Two-dimensional (2D) materials or nanosheets have gained increasing interest over the last years due to their potential applications in electronics, displays and sensors technologies.[1-4] So far, a variety of 2D nanomaterials have been reported, mainly graphene[5,6] and graphene oxide,[7] transition metal dichalcogenides (TMDs),[8,9] layered double hydroxides (LDHs),[10] metal oxides and hydroxides,[11] black phosphorous (BP),[12] boron nitride (h-BN)[13] and MXenes,[14] among others (Figure 3.11). All these materials have been shown to exhibit novel chemical and physical properties mainly originated from their ultrathin thickness and 2D morphology.[15-19] However, though successful, most of them show a limited chemical modulation and restricted functionalization capabilities.

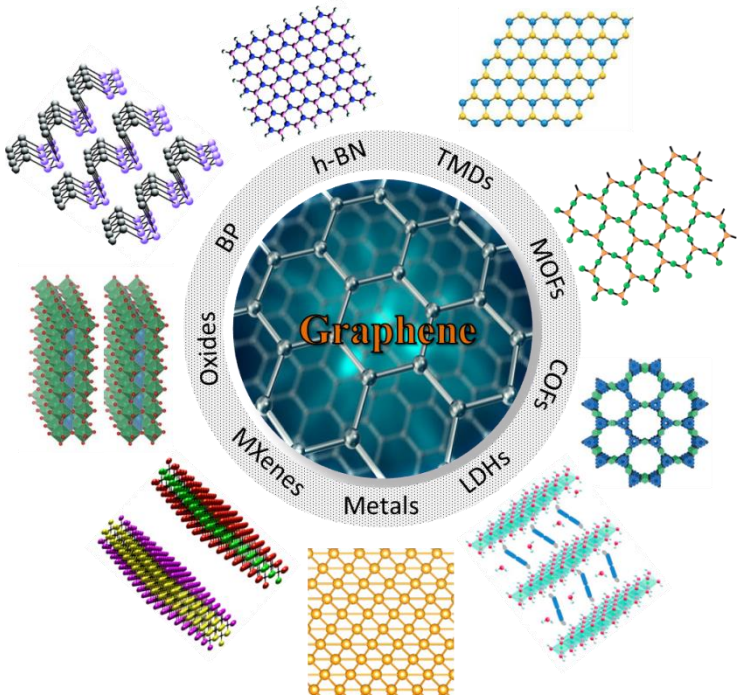

Figure 3.11 Schematic illustration of different kinds of typical ultrathin 2D nanomaterials, such as graphene, h-BN, TMDs, MOFs, COFs, MXenes, LDHs, oxides, metals, and BP. Reproduced and adapted from ref. 1.

3.2.1.1 2D coordination polymers

In this decade, the design and synthesis of novel nanosheets remain among the most actively researched areas of chemistry and physics. Up to now, the most studied nanosheets are those inorganic materials created from bulk crystalline layered materials (TMDs). Nevertheless, in the last years, an emerging alternative consisted on the molecule-based nanosheets containing organic components have been proposed. These systems arouses from the basis of coordination chemistry which let the formation of a wide variety of coordination nanosheets (also called CONASHs).[20] In this scenario, CPs have been wished over the last years as a complementary approach to graphene and related materials for the fabrication of 2D systems thanks to their rich synthetic chemistry, chemical flexibility and the presence of metal ions that add novel optical, magnetic and/or electrical

properties.[21] This has been translated in a broad research in novel 2D materials based on MOFs[21] and COFs.[22]

In fact, even though relatively new, all these premises have already crystallized in different examples of 2D CPs for several applications already described: electrochemical detection of H_2O_2,[23] thin films,[24] molecular sieve membranes,[25] polymer composites for gas separation[26] catalysis[27,28] or photoluminescence.[29,30]

3.2.1.2 Methods for obtaining monolayers of 2D coordination polymers

A CONASH is made of organic ligand molecules and metal ions/atoms/clusters which stablish coordination bonds between them forming a 2D polymeric framework. Their formation is subjected to its rationally design by selecting ligands that have three-, four- and six-fold symmetry with planar bonding directions and three, four or six reacting points to construct a hexagonal, square or triangular ordered polymeric framework (Figure 3.12). The design of novel 2D coordination layers is based on the reversibility of the coordination bonding and the affinity between the organic ligands and de metal compounds. This reversibility of the coordination bonding contributes to the formation of 2D planar structures with high quality by association/disassociation processes that let to dismiss defects and disordered structures. For the correct formation of the 2D structure, the planar bonding direction must be ensured by inducing it through the correct selection of the building blocks.

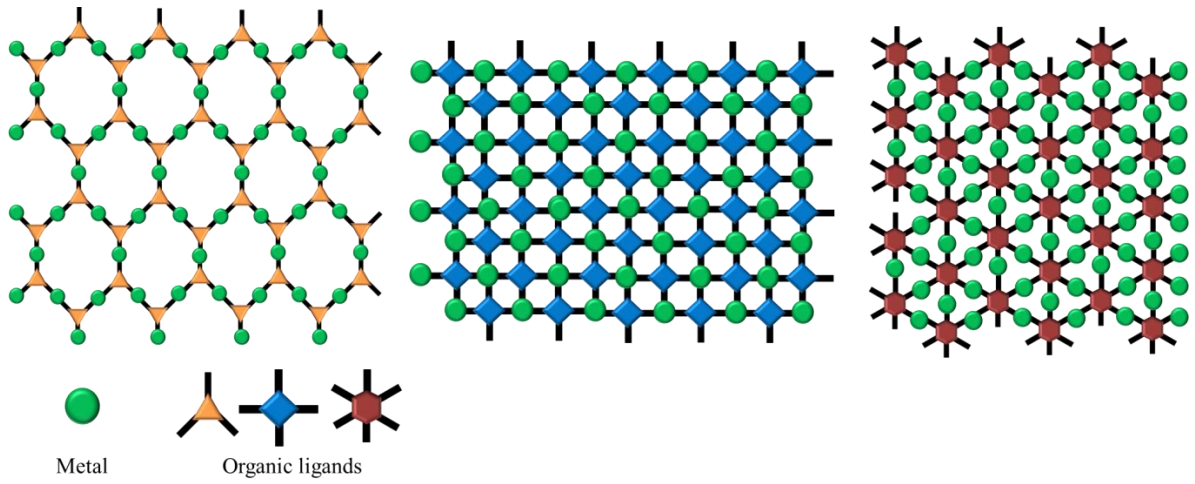

Figure 3.12 Scheme of different coordination symmetries. From left to right: 3-, 4-, and 6-fold symmetry. The metals and organic ligands are combined through a preferential planar direction for the formation of 2D coordination nanosheets.

There are different approaches for the synthesis and growth of 2D CONASHs reported in the literature. Those methodologies can be classified in two main groups: i) bottom-up and ii) top-down. In this section, the most reported techniques for the synthesis of 2D CPs in the form of mono- or few layers are described.

a) Bottom-up methodology

This approach englobes the techniques based on the formation of materials through the molecular self-assembly of its unit building blocks. During the self-assembly of the basic units, the physical forces are used for their combination allowing the formation of larger stable structures. Some examples are:

Interfacial synthesis. Two main methods are involved in this kind of techniques using interfacial systems. One of these approaches consist on the formation of a liquid/liquid interface by using solvents with different densities (Figure 3.13). Usually, an aqueous phase containing the metal ion is gently placed on an organic solution containing the ligands. If the organic solvent is less dens than the water, it becomes the upper layer. Through liquid/liquid interfacial synthesis is possible to create multi-layered nanosheets (layer-by-layer method).

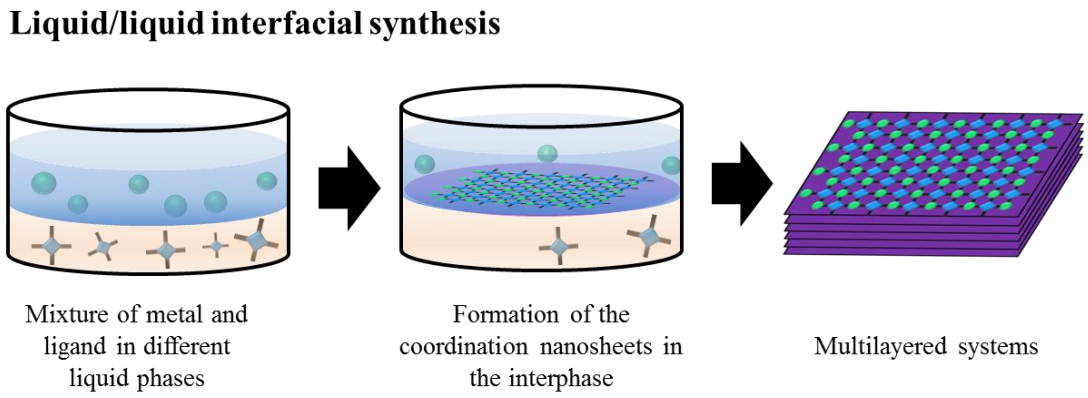

Figure 3.13 Scheme of the liquid/liquid interfacial methodology.

The second approach is based on the formation of a gas/liquid interface (Figure 3.14). In this case, the organic solution containing the ligands is spread on an aqueous solution of the metal ion. After the fast evaporation of the organic solvent, the ligand remains on the aqueous surface and the coordination reaction slowly occurs on the gas/liquid interface. The Langmuir-Blodgett (LB) technique is included in this approach. In this specific case, through a LB set up, it is possible to prepare densely packed few- or single-layer of coordination nanosheets. As a general gas/liquid approach, the receipt is filled with an aqueous solution containing the metal ions actin as a core centre. Subsequently, a small amount of organic solution containing the organic ligands is added slowly on the water surface. When the organic phase is evaporated, the coordination between the ligands and metals lead the formation of the nanosheets dispersed on the gas/liquid interface. The LB

device can be adjusted by reducing the surface and concentrating the material by increasing the density per unit area.

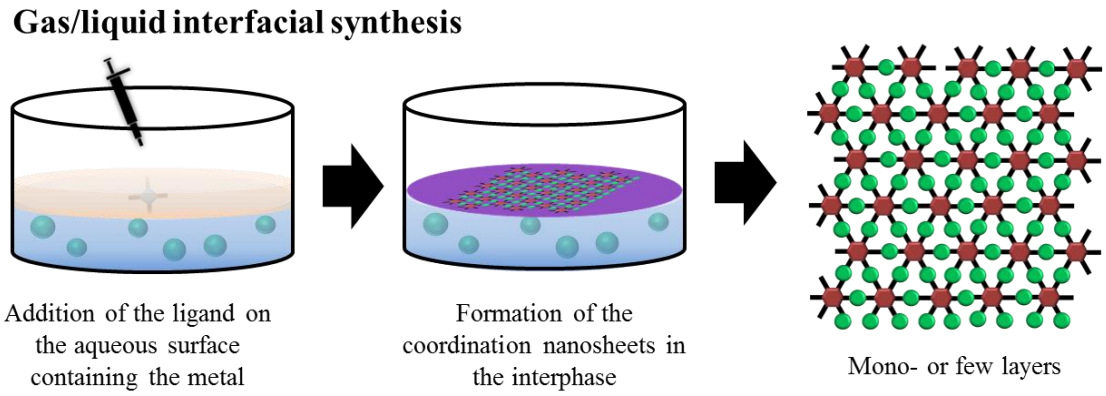

Figure 3.14 Scheme of the gas/liquid interfacial methodology.

Chemical vapour deposition (CVD). The CVD technique has been widely used for the bottom-up synthesis of several nanomaterials. In this case, is necessary to place a substrate in vacuum and subsequently evaporate the metal and ligand molecules which will be deposited on the substrate surface (Figure 3.15). Then, the nanosheet is formed directly on the substrate. Other variations can involve the use of a metallic substrate as a source of metal nodes for the coordination with the evaporated ligand molecules, without needing the evaporation of the metal part. In this approach, several parameters such as substrate, evaporation rates, and annealing temperature, play an important role for the formation of defectless CONASH.

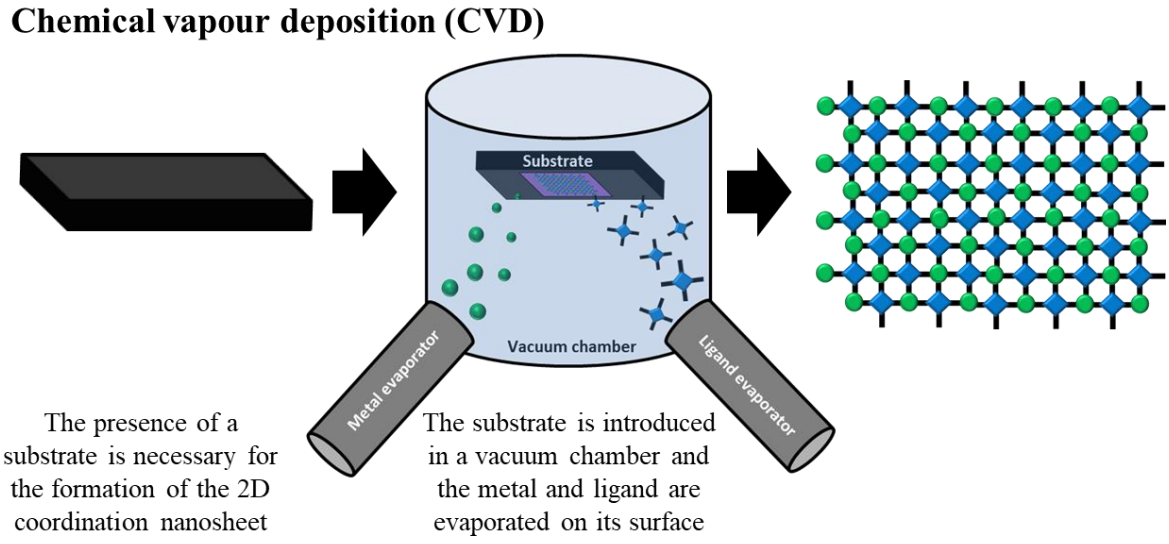

Figure 3.15 Scheme of chemical vapour deposition (CVD) methodology.

b) Top-down methodology

The techniques classified in this group are based on the miniaturization of larger (macroscopic) initial structures through externally-controlled processes. The resulting materials are similar to its counterpart but with their dimensionality drastically reduced. These methodologies are less explored for the formation of CONASH, and only the exfoliation approach has been reported for their successful synthesis.

Exfoliation. The main methodology used for the obtaining of nanosheets from a bulk layered material is the liquid-phase exfoliation (LPE). In order to get quality nanosheets, a good-shape with good crystallinity bulk material is necessary. The bulk crystal material must be formed by 2D motifs packed through weak interactions (Figure 3.16). Those weak interactions can be broken through the interference of the solvent molecules and, if necessary, with the assistance of external energy such as ultrasounds.

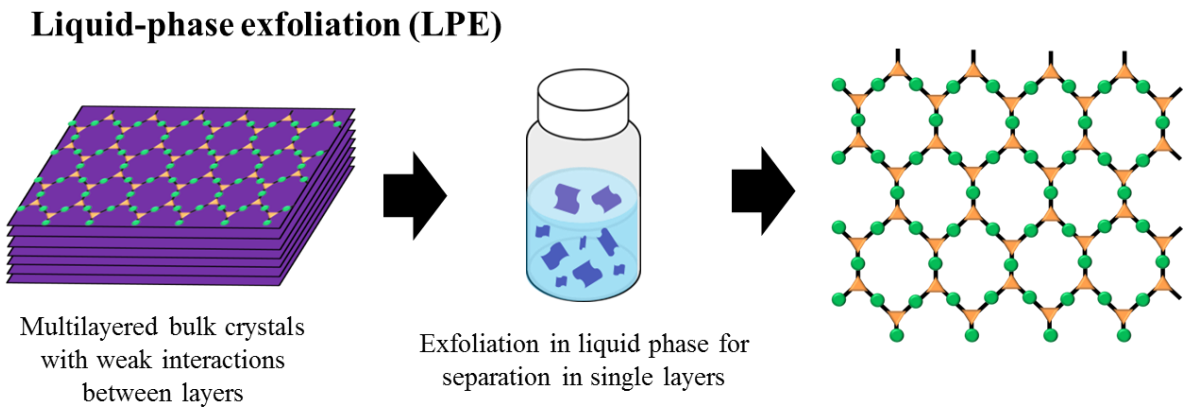

Figure 3.16 Scheme of the liquid-phase exfoliation (LPE) methodology.

All the methodologies described above represent the most reported processes in the literature for obtaining 2D layers of coordination polymers. Nevertheless, there are other alternatives that have demonstrated their effectiveness for the exfoliation of other types of 2D systems (e.g. TMDs or pure metallic systems, among others). In the literature we can find illustrative reviews about the use of alternative approaches for the obtaining of atomic-thickness layers.[31,32] Most of these strategies are mainly bottom-up techniques based on interface synthesis such as: liquid/air interface (graphene templating, salt templating, metal-directed synthesis, etc.), gas/solid or gas/vacuum interface, and photochemical synthesis, among others. There are others classified as top-down techniques that are emerging as powerful methods for the obtaining of 2D layers which are based on nanolithography.

3.2.1.3 State-of-the art of 2D coordination polymers as colloidal suspensions of 2D-layers in water

As aforementioned, in this Chapter, the top-down production of Fe(II)based nanosheets through LPE methodology is presented. For this reason, different examples of exfoliation of 2D CPs will be discussed focusing on those examples where LPE approach was used for obtaining water-stable colloidal suspensions.

The first example on the literature about the use of LPE method was reported by Zamora and co-workers.[33] In their pioneer work, a copper coordination polymer $[Cu_2Br(IN)_2]_n$ (IN=isonicotinato) was isolated as single sheets after the delamination of the bulk crystal in water (Figure 3.17).

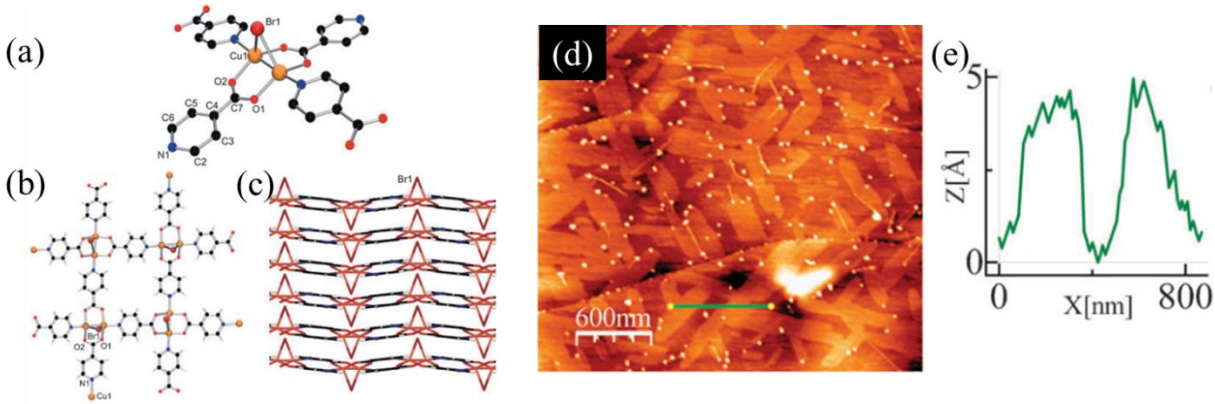

Figure 3.17 (a) Detail view of the copper environment in $[Cu_2Br(IN)_2]_n$. (b) View of a single layer framework. (c) Superposition of layers along the *a* axis. (d) AFM topography image of $[Cu_2Br(IN)_2]_n$. (e) Height profile across the green line in panel (d). Reproduced and adapted from ref. 33.

The single layers were isolated by using sonication as a mechanical force to break the interlayer interactions inspired by the widely used methodologies for the graphene isolation from graphite.[34] The layers were deposited on highly oriented pyrolytic graphite allowing their isolation with atomic-thickness of 0.5 ± 0.15 nm (Figure 3.17d,e). Additionally, due to the intrinsic electrical conductivity measured on the $[Cu_2Br(IN)_2]_n$ polymer, this system represented the first example of a potential alternative 2D material to graphene.

Following the same strategy, Zamora and co-workers reported a laminar Cu-based MOF that can be easily delaminated by immersion of the bulk crystals in water without the assistance of sonication.[35] The $[Cu(\mu\text{-}pym_2S_2)(\mu\text{-}Cl)]_n$ nY (pym_2S_2= dipyrimidinedisulfide, Y= MeOH, H_2O or 0.5EtOH) presented a crystal-to-crystal reversible transformation through its immersion in different solvents. In the case of water, after 4 days in solution, the system yielded layers with thicknesses

smaller than 2 nm. This low-energy strategy represented a soft-delamination process suitable for layered crystals with weak layer-to-layer interactions.

The examples showed before has motivated to the research community for the exploration of the LPE method for the obtaining of atomic-thickness layers. In the literature there are several examples of Cu-based materials as good metal-organic crystals for their delamination in water. In this sense, Maeda and co-workers reported the fabrication of MOF nanosheets form a layered Cu-based CP.[36] The single crystals of $[Cu(bpy)_2(OTf)_2]$ (bpy = 4,4'-bipyridine, OTf = trifluoromethanesulfonate), also formed from a N-donor type bridging ligand, were delaminated in water. The presence of hydrogen bonds involved in the stacking of the layers, made possible to obtain colloidal dispersions of exfoliated layers after shaken the bulk crystals in water for 10 h. The AFM showed the delamination of layers with thickness around 1.4-1.5 nm.

In another example, Zheng and co-workers described the exfoliation of a layered copper-phosphonate-based CP $[Cu(H_2O)(2\text{-BTP})]$ (BTP = 5-(2-bromothienyl)phosphonic acid) (Figure 3.18 a,b).[37] In this case, the weak interlayer interactions allowed the exfoliation of the bulk crystals after 2 h of LPE assisted with ultrasounds in water. The AFM revealed the formation of layers with 3.2-3.4 nm in thickness which corresponded to approximately two-layer overlapped (3.12 nm) (Figure 3.18f). Additionally, the authors showed the enhanced ability of the exfoliated system for the binding of Pb(II) metal ions with applicability in, for example, water remediation.

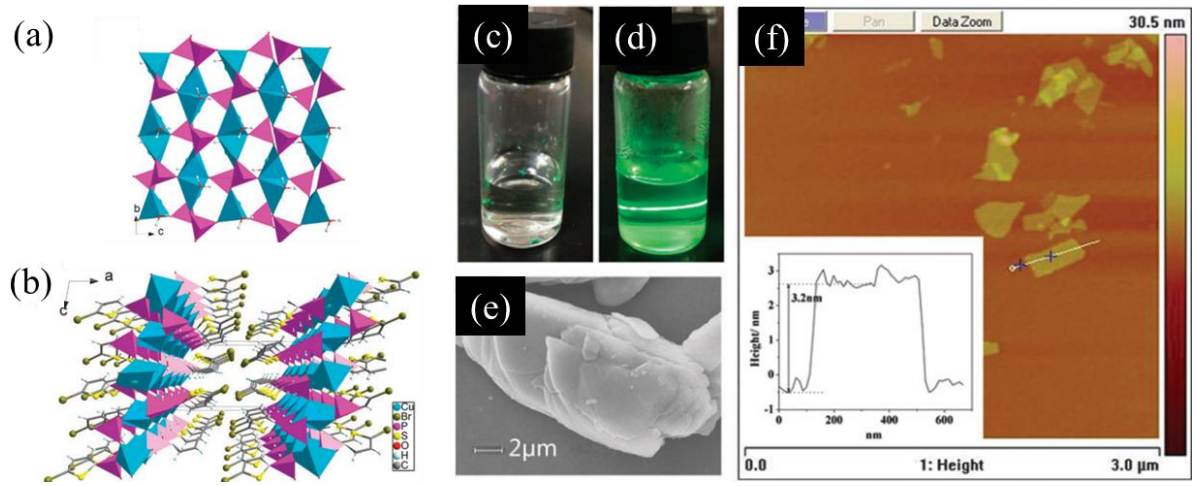

Figure 3.18 (a) Inorganic layer of $[Cu(H_2O)(2\text{-BTP})]$ viewed along the *a* axis. (b) Packing diagram of $[Cu(H_2O)(2\text{-BTP})]$ viewed along the *b* axis. The Tyndall effect of the supernatant in water before (c) and after ultrasonication (d). (e) SEM image of the precipitate after ultrasonication. (f) AFM images and the corresponding thickness of nanosheets of $[Cu(H_2O)(2\text{-BTP})]$. Reproduced and adapted from ref. 37.

Occasionally, the use of water in crystal exfoliation may involve undesired chemical processes (e.g. oxidation, solvent exchange, degradation, etc.) affecting the systems and therefore inducing structural changes that can irreversibly alter the properties of the complex. In order to avoid such modifications, one alternative strategy could consist on the exfoliation of the crystal in a crystal-stable solvent or mixture of solvents and subsequently redisperse the obtained layers in water for their colloidal suspension. Based on this rationale, Cheetham and co-workers reported the functionalization of a Cu-based MOF with alkyl-ether linkages for its successful dispersion in aqueous suspensions.[38] In their work, the authors described the exfoliation of the Cu-MOF in DMF which easily exchange the DMF solvent molecules with water yielding a new crystalline phase which retained the same topology. Furthermore, the Cu-MOF was exfoliated in DMF-water mixtures showing the interchange of solvent molecules with reversibility between crystalline phases. Additionally, the layers in aqueous suspensions were exploited to act as sensors for the detection of pyridine as a model guest compound.

Following this last strategy, Qian and co-workers reported the delamination of a Ti-based MOF by LPE in isopropanol.[39] The powder of layers yielded from the ultrasounds-assisted exfoliation of the CP $[Ti_2(HDOBDC)_2(H_2DOBDC)]$ (H_2DOBDC = 2,5-dihydroxyterephtalic acid) was properly resuspended as colloidal suspension in water showing good stability (Figure 3.19).

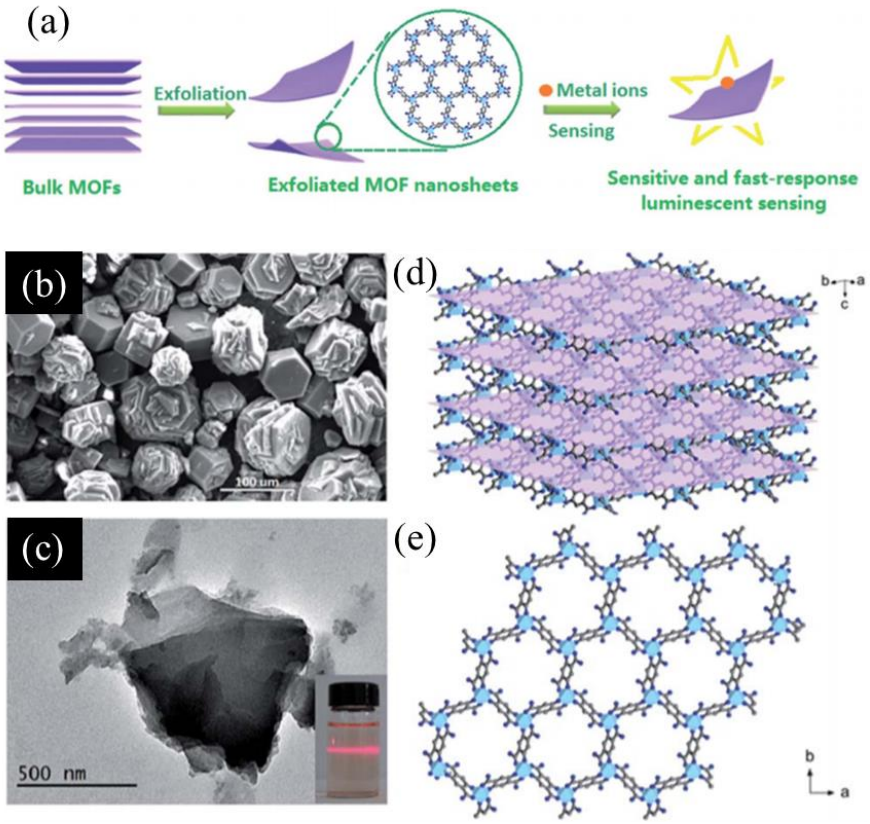

Figure 3.19 (a) Schematic illustration for the fabrication of the nanosheets (b) SEM image of Ti-MOF crystals. (c) TEM image. Inset shows the Tyndall effect of a colloidal suspension. (d) Architecture of the layered MOF precursor. The ab planes are highlighted in purple to better illustrate the layered structure. (e) Illustration of the honey-comb like layered structure of the Ti-MOF. Reproduced from ref. 39.

Furthermore, the product obtained was successfully tested in luminescent sensing of Fe(III) ions in water. The response generated by the exfoliated coordination nanosheets was faster enhancing the performing of its bulk counterpart.

As we have seen in the previous examples, the layers obtained from the LPE approach have demonstrated enough effectiveness for their applicability in different areas, especially for the sensing of specific metals or compounds. In this sense, Gu and co-workers described the applicability of water-stable nanosheets based on Zn-MOF ($Zn_2(bim)_4$, where bim = benzimidazole) as matrices for Matrix-Assisted Laser Desorption/Ionization (MALDI-TOF) analysis (Figure 3.20a).[40]

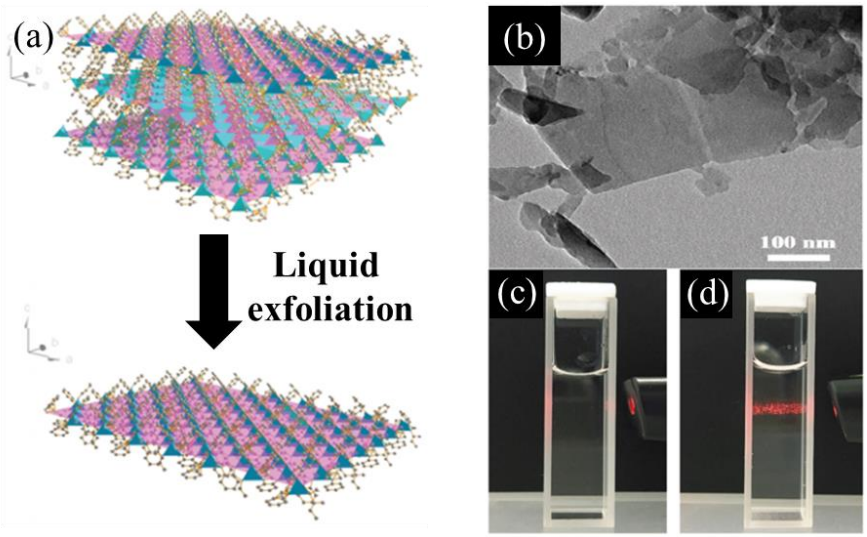

Figure 3.20 (a) Scheme of the LPE. (b) TEM image of 2D MOF nanosheets. (c) Photograph of pristine $Zn_2(bim)_4$ MOF aqueous suspension. (d) Photograph of 2D MOF nanosheet colloidal suspension. Reproduced and adapted from ref. 40

The nanosheets obtained had a thickness of ~1 nm with high stability once dispersed in water (Figure 3.19b-d). Their performance demonstrated its efficient photon absorption and target ionization making them a potential candidate for MALDI-TOF matrix.

As we have seen with these examples, the use of LPE as a methodology for obtaining delaminated layers from bulk 2D crystals is a good strategy. However, other methods have demonstrated enough efficiency for the development of atomic-thickness layers such as liquid/liquid interface or[41] air/liquid interface[42] which involve bottom-up processes for the self-assembling of atomic layers.

3.2.1.4 Present challenges

Despite the recent progress in the study and production of atomic-thickness layers, there are some critical issues to be addressed. In general, the synthesis and characterisation of molecule-based nanosheets have been difficult, which has hampered their realisation and therefore its application. More specifically, some of these challenges are:

i. Size-control of the 2D layers
ii. Retain the chemical stability from its bulk counterpart
iii. Produce water-stable colloidal suspensions
iv. Detailed structural characterization of the obtained 2D layers
v. Maintain the desired properties for its applicability
vi. Transfer 2D materials to different substrates
vii. Proof of their final use as device

The physicochemical properties of 2D materials are highly dependent on their structural features. For this reason the correct selection of the materials and their constituents is crucial. Through the rational design of the materials and methods for the obtaining of 2D systems, arouses the possibility to develop functional systems which is essential for bringing such materials in practical devices or industry products. In this scenario, CPs-based systems become an excellent candidate for their use in the design of 2D materials as they have already demonstrated its potentiality.

3.2.1.5 Our choice

Despite the pioneering examples in the literature, control over the synthesis and applications of 2D materials based on CPs still remains a significant research challenge. This is especially applicable for switchable systems, whose ability to interconvert between two different states under an external perturbation is envisaged as a promising alternative to classical inorganic materials in information processing and sensing. In this work we studied CP based on Fe(II)-tetrazole with SCO behaviour: $[Fe(t3z)_2]_n(ClO_4)_n$ (**1**) (where t3z = tris-[2-(1H-tetra-zol-1-yl)eth-yl]amine, **L1**) (Figure 3.21).

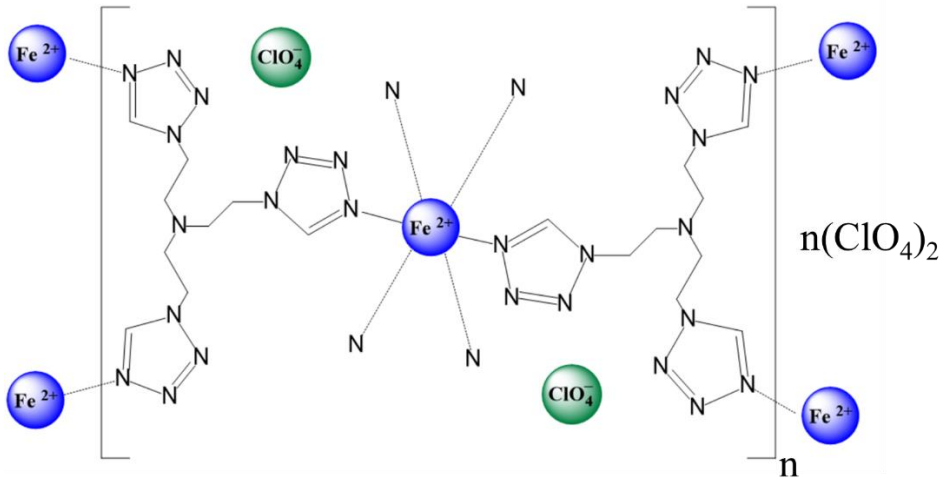

Figure 3.21 Chemical structure of complex (**1**).

The SCO occurrence of the (**1**) crystals have been already studied.[43,44] The system consisted on the packing of 2D layers through weak interactions between them. For this reason, we hypothesized that through the LPE strategy we can obtain the delaminated 2D layers for their study as a colloidal suspension of flakes in water.

3.2.1.6 Objectives

With the aim to overcome the challenges described in the previous section, different objectives were proposed derived from a main goal:

- Use of LPE method for the delamination of the bulk $[Fe(t3z)_2]_n(ClO_4)_n$ (**1**) CP for the study of the SCO property on the 2D atomic-thickens layers.

The steps followed for the achievement of the main goal were the following:

i. Synthesis of complex (**1**) using a solvothermal method
ii. Complete the crystal characterization of complex (**1**)
iii. Delamination of the layered (**1**) crystals by LPE methodology
iv. Complete physicochemical characterization of the resulting 2D materials
v. Study of the water-stability colloidal suspensions containing the 2D layers
vi. Comparison of the SCO property with its bulk counterpart
vii. Study of the integration of the 2D layers in a device

In this work, we show a successful approach for the delamination of 2D bulk SCO crystals which yield unprecedented SCO flakes.

3.2.2 Results and discussion

3.2.2.1 Synthesis and characterization of complex (1)

The synthesis of complex (**1**) was previously reported in the literature.[43,44] Nevertheless, no crystallographic characterization was done at that time. Since the structure is intimately related to the interaction between the 2D layers, a detailed crystal study is crucial for understanding the process involved during the delamination of the crystal. For this reason and due to the relevance for this work, the synthesis of complex (**1**) and a complete characterization of it were performed.

The reaction between the $Fe(ClO_4)_2 \cdot xH_2O$ metal salt and the tris–tetrazole ligand (**L1**) in acetonitrile (CH_3CN) was done in ambient conditions. After slow evaporation of the solvent, yellowish crystals of complex (**1**) were yielded (Figure 3.22).

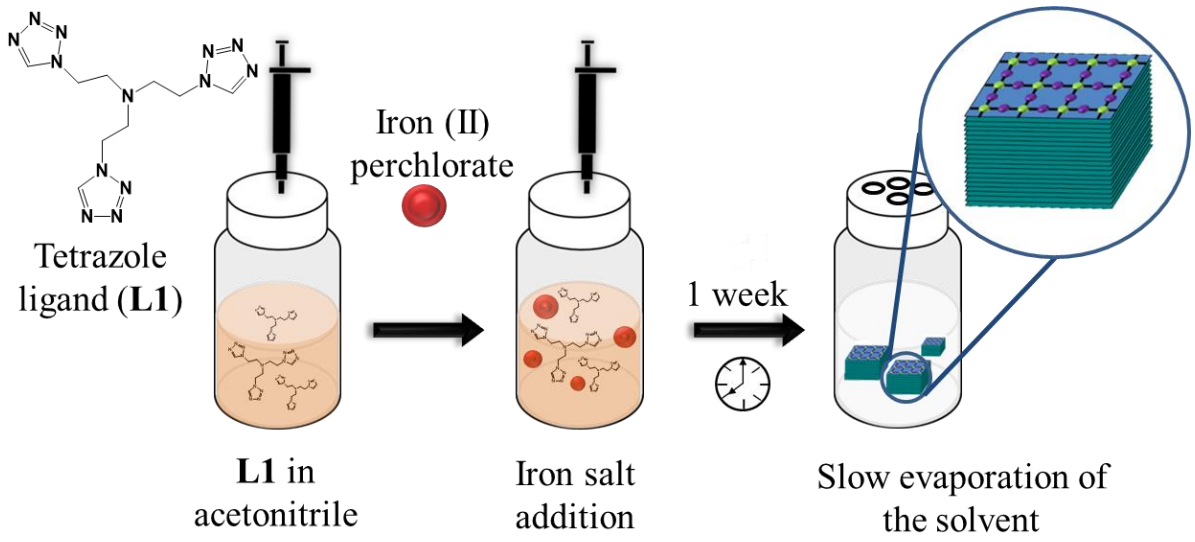

Figure 3.22 Schematic illustration for the synthesis of complex (**1**).

The sizes of the crystals obtained were measured by optical microscopy (OM) and scanning electron microscopy (SEM), resulting in an average of 0.8 ± 0.3 mm (Figure 3.23).

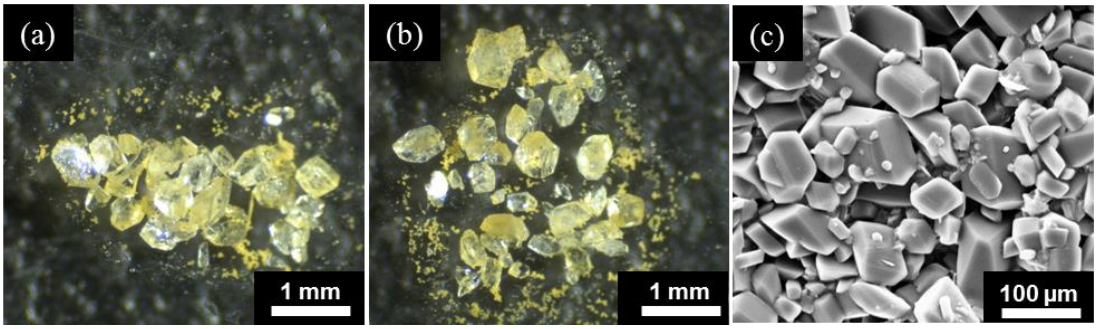

Figure 3.23 Morphology of the synthesized crystals of complex (1). (a, b) Optical microscopy (OM) and (c) Scanning electron microscopy (SEM) images of complex (**1**).

The crystallographic measurements were done at different temperatures since the Fe-N distance is modified with the variation of the temperature (Table 3.1).

Table 3.1 Crystal data of (**1**) at different temperatures

Crystal data	**(1)-250K**	**(1)-150K**	**(1)-110K**
CCDC	1534951	1534952	1534953
Empirical formula	$C_{18}H_{30}Cl_2FeN_{26}O_8$	$C_{18}H_{30}Cl_2FeN_{26}O_8$	$C_{18}H_{30}Cl_2FeN_{26}O_8$
Formula weight [g·mol^{-1}]	865.43	865.43	865.43
Crystal size [mm]	0.25 x 0.25 x 0.15	0.25 x 0.25 x 0.15	0.25 x 0.25 x 0.15
Crystal system	Triclinic	Triclinic	Triclinic
Space group	$P\bar{1}$	$P\bar{1}$	$P\bar{1}$
a [Å]	8.7163(18)	8.5142(10)	8.4978(12)
b [Å]	9.5250(16)	9.7903(10)	9.7837(7)
c [Å]	12.019(4)	11.4132(4)	11.4156(12)
α [°]	67.88(2)	65.392(9)	65.337(9)
β [°]	86.35(2)	74.695(8)	74.788(10)
γ [°]	69.314(17)	72.179(10)	72.107(10)
Volume [Å^3]	862.1(4)	813.15(13)	810.85(15)
Z	1	1	1
Dcalc.[g·cm^{-3}]	1.667	1.767	1.772
F(000)	444	444	444
μ MoKα [mm^{-1}]	0.678	0.718	0.720
Temperature [K]	250(2)	150(2)	110(2)
Range of h, k, l	–9/9, –10/9, –12/12	–10/10, –11/11, –12/12	-10/10, -11/11, -13/13
θ min/max	2.94/21.97	2.97/25.35	2.88/25.35
Reflections collected/unique/observed	3641/1945/1496	6553/2774/2229	5925/2781/2340
Data/restraints/parameters	1945/0/250	2774/0/250	2781/0/250
Goodness of fit on F^2	1.080	1.114	1.040
Final R indices [I>2σ(I)]	R_1 = 0.0658	R_1 = 0.0596	R_1 = 0.0426
	wR_2 = 0.1762	wR_2 = 0.1177	wR_2 = 0.1097
R indices (all data)	R_1 = 0.0833	R_1 = 0.0819	R_1 = 0.0526
	wR_2 = 0.1905	wR_2 = 0.1260	wR_2 = 0.1160

The single crystals of complex (**1**) were carefully grown and the good-quality shaped ones were selected for its analysis by single x-ray diffraction (SXRD). The results showed that complex (**1**) crystallizes in a triclinic Pī space group with an asymmetric unit comprising one Fe(II) metal node (located in the centre of inversion), one molecule of tetrazole ligand **L1**, and one perchlorate counter anion (Figure 3.24).

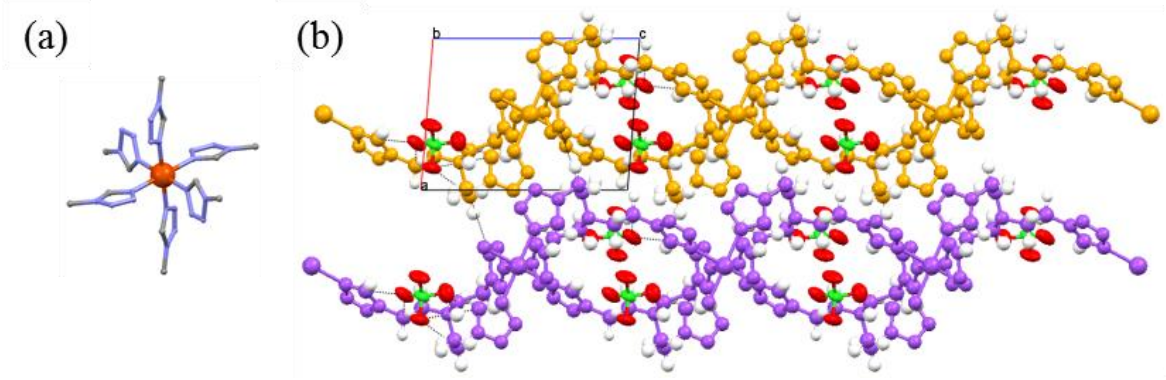

Figure 3.24 Crystallographic structure of the complex (**1**). (a) FeN_6 chromophore (the Fe(II) is represented in red). (b) Offset packing of complex (**1**). The unit cell is shown. The perchlorate counter anions are represented in green (Cl) and red (O). Each layer is represented in different colour (orange and purple).

The resulting repetitive unit of FeN_6 (Figure 3.24a) (perchlorate remains uncoordinated) undergo extended coordination leading to the formation of a 2D–corrugated sheet coordination polymer architecture (Figure 3.25a), which is packed on top of each other in an offset manner (Figure 3.25b).

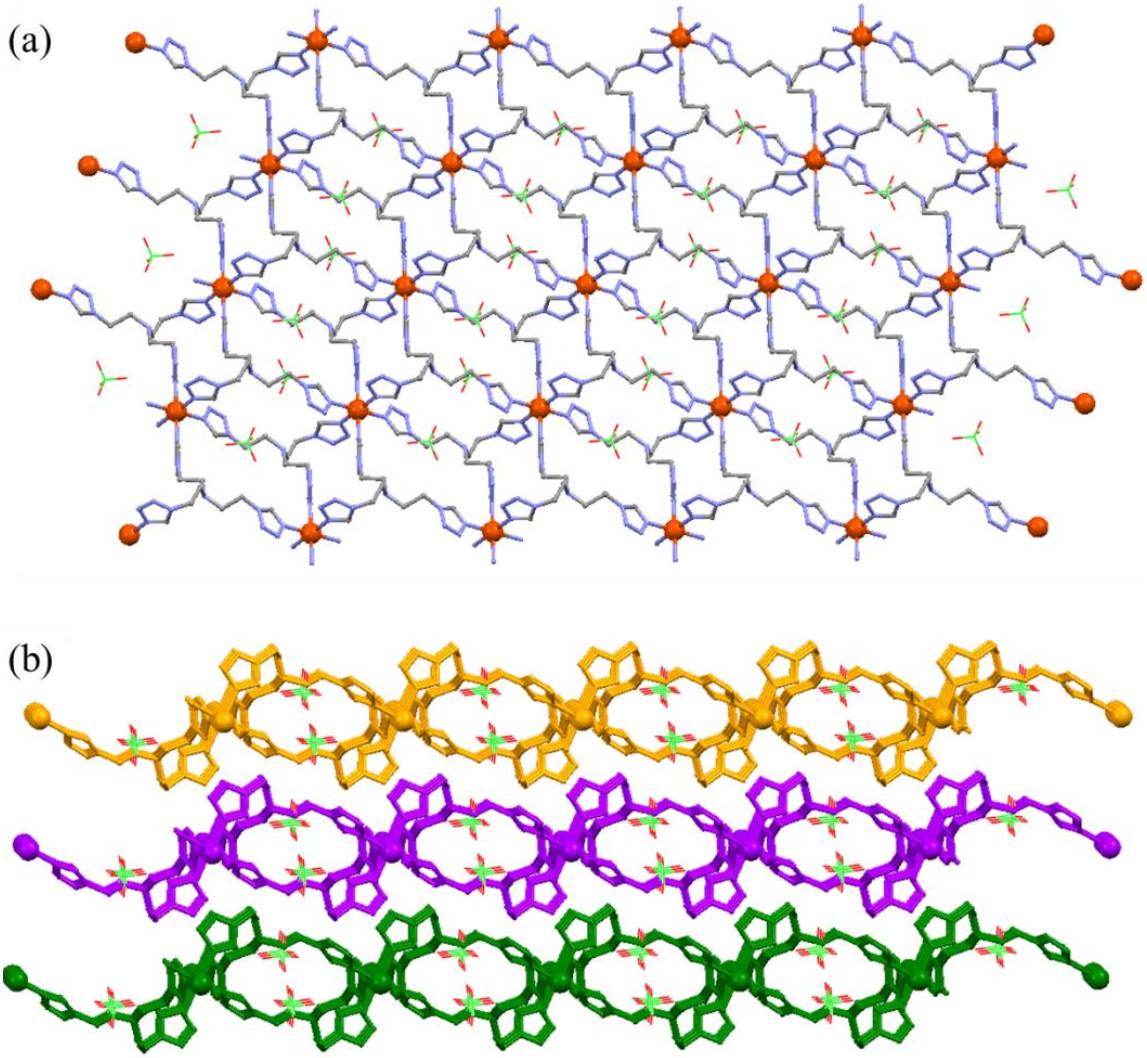

Figure 3.25 (a) TOPOS software view of crystal structure illustration of (**1**). The Fe(II) metal node exhibits a slightly distorted octahedral geometry at 250 K [N–Fe–N = 88.87(19)-91.13(19)°] with the equatorial and apical positions of the Fe(II) coordinated by the tetrazole moieties of **L1** (the repetitive unit is FeN_6, perchlorate remains uncoordinated). Each **L1** ligand bridges three Fe(II) ions and, simultaneously, six **L1** ligands are coordinated to one central atom. The extended coordination of such FeN_6 chromophore leads to the formation of a 2D-corrugated sheet coordination polymer packed on top of each other in an offset manner supported by various supramolecular interactions. (b) Packing of 2D-corrugated sheets along the *b* axis displaying the occlusion of perchlorate anions within the interstitial space (adjacent sheets are shown with orange, purple and green), which are involved in hydrogen bonding and other weak interactions with the tetrazole rings of different layers (the unit cell contains no voids accessible for the solvent molecules).

More in detail, the supramolecular interactions involved in the 2D packing are shown in Figure 3.26.

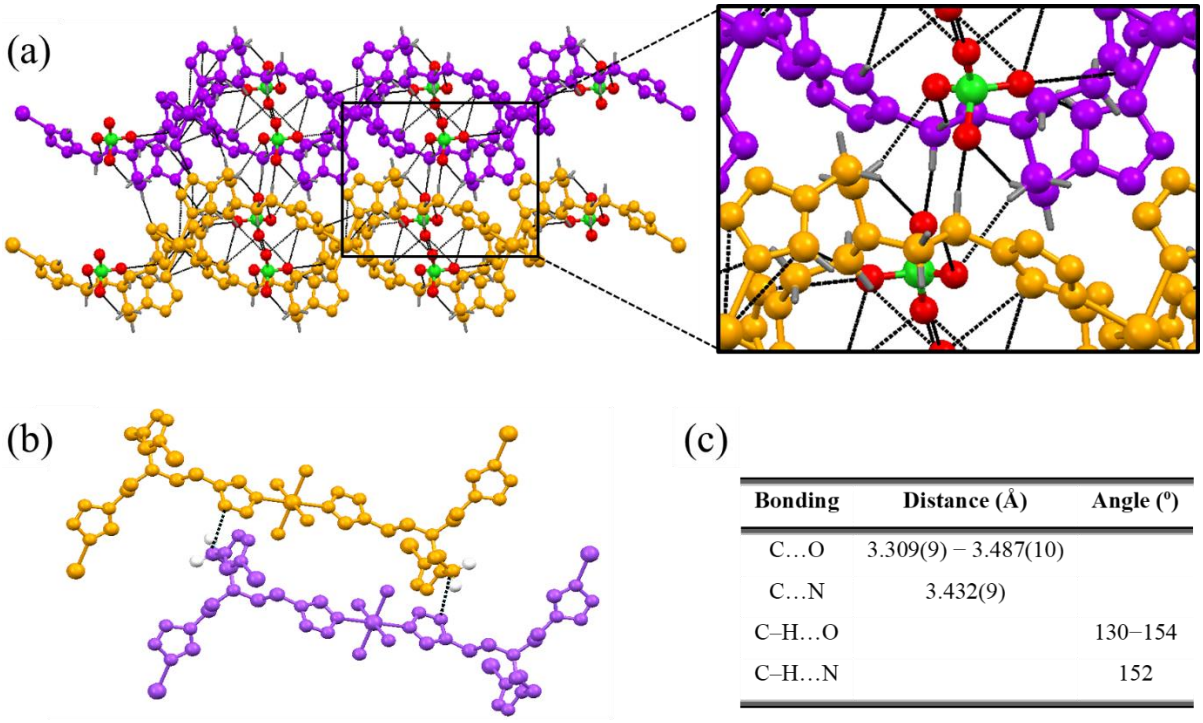

Bonding	Distance (Å)	Angle (°)
C…O	3.309(9) – 3.487(10)	
C…N	3.432(9)	
C–H…O		130–154
C–H…N		152

Figure 3.26 (a) C−H…O interaction involving the **L1** ligand and perchlorate counter anion. The detailed zone is amplified. (b) Interaction between layers by C−H…N hydrogen bonding involving C−H of $-CH_2-$ group and tetrazole N atom from **L1**. (c) Distance and angle between different bonding environments. Adjacent layers are shown in orange and purple colour, perchlorate is shown in red (O) and green (Cl) colour.

The occurrence of the SCO in the complex (**1**) was previously studied and reported.[43] For comparison purposes, a brief description of the SCO characterization is provided. This description is necessary for the properly discussion compared with the SCO behaviour of the exfoliated 2D coordination nanosheets.

The complex (**1**) showed a ST when cooling the crystals changing form the HS to the LS accompanied with a notable colour change from yellowish to purple (Figure 3.26a). First of all, the variable-temperature magnetization data ($\chi_M T$ *vs.* T) was obtained by a superconducting quantum interference device (SQUID). For the complex (**1**), the results highlighted the good bistability of the bulk crystal. At 250 K, the $\chi_M T$ value was equal to 3.7 cm^3 mol^{-1} K, in agreement with a full fraction of Fe(II) ions in the HS state. As T was lowered, $\chi_M T$ first decreases abruptly upon the spin transition (Figure 3.26b). As the temperature was increased back, $\chi_M T$ follows the same behaviour except for a hysteresis loop (width ~ 22 K) centred at 160 K. The transition temperatures (the temperatures at which 50% of active LS and HS molecules are present) in the cooling and warming modes, respectively, were $T_c^{\downarrow}$ = 148 K and $T_c^{\uparrow}$ = 170 K. Additionally, the hysteresis was retained over

successive cooling and heating thermal cycles. The transition temperatures, on warming and cooling, were $T_c^{\uparrow}$ = 170 K and $T_c^{\downarrow}$ = 149 K, respectively. At 78 K, the spectrum of complex (**1**) consisted on a single quadrupole doublet corresponding to a LS Fe(II) ion, with an isomer shift δ^{LS} = 0.59 mm s^{-1} and a low quadrupole splitting $\Delta E_Q{}^{LS}$=0.21 mm s^{-1} (Figure 3.26c). This quadrupole splitting is characteristic for a lattice contribution to the electric field gradient which indicates a distortion of the LS octahedron. Upon warming up to 135 K, no change was observed in the spectra but at 140 K, a new quadrupole doublet characteristics of a HS Fe(II) ion was detected, indicating the onset of a spin state crossover from LS to HS, which progresses further at 175 K. Indeed, at 250 K, no fraction of LS Fe(II) ions was detected in agreement with the yellowish colour of the powder. At 298 K, a single HS quadrupole doublet was observed, with δ^{HS} = 1.07 mm s^{-1} and $\Delta E_Q{}^{HS}$ = 1.46 mm s^{-1}, indicating a complete and abrupt SCO. On cooling, a hysteretic behaviour was clearly revealed, by comparing Mössbauer spectra recorded at 160 K. Isomer shifts and quadrupole splittings for both LS and HS species were typical of a Fe(II)N_6 core.

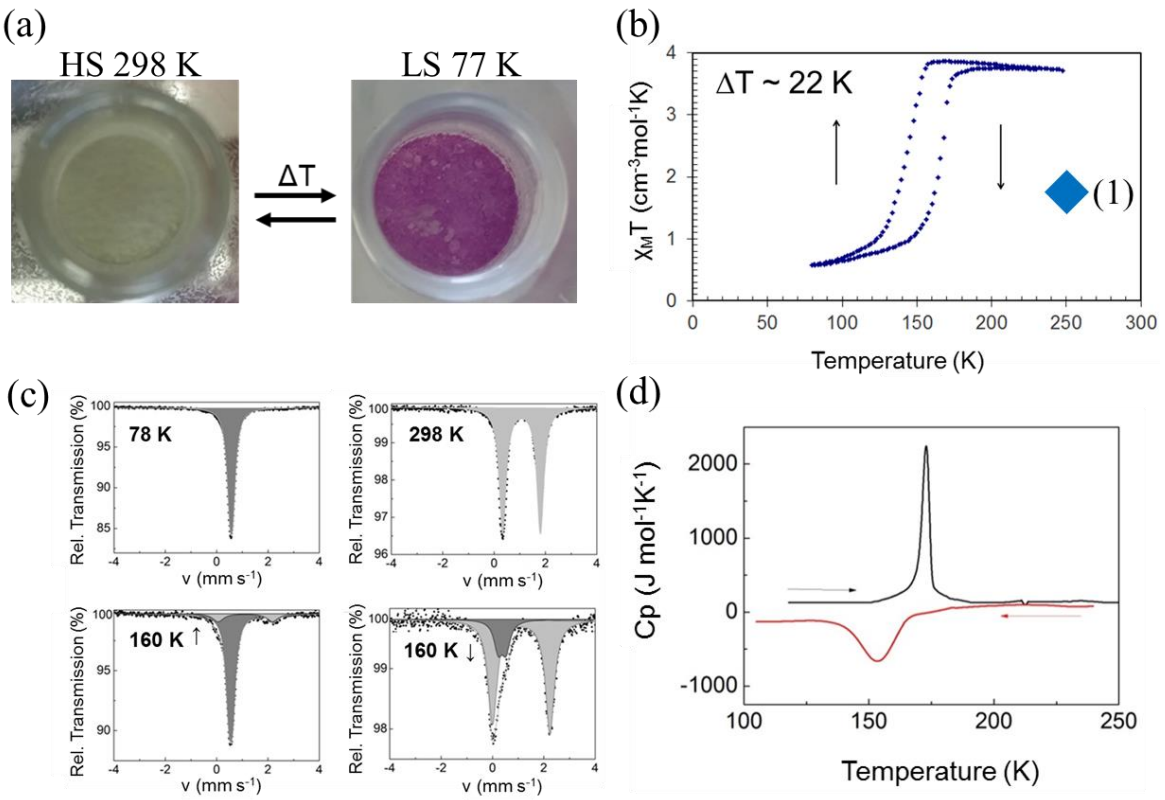

Figure 3.26 (a) Colour change of complex (**1**) at two different temperatures. (b) Temperature dependence of χ_MT vs. T after consecutive heating and cooling cycle. (c) Selected ^{57}Fe Mössbauer spectra for (**1**). Grey and dark grey correspond to the HS and LS doublets, respectively. (d) Plot of heat capacities (Cp) vs. T for complex (**1**) on warming and cooling at 10 K min^{-1} over the temperature range 108-250 K.

Complex (**1**) was also investigated by differential scanning calorimetry (DSC) over the temperature range 108 - 300 K, at 10 K min^{-1}, in cooling and heating modes (Figure 3.26d). An

endothermic peak was observed on warming (**1**) at $T_{max}^{\uparrow}$ = 171 K and an exothermic peak was recorded on cooling at $T_{max}^{\downarrow}$ = 151 K. These peaks corresponded to a first-order phase transition associated to the ST behaviour of (**1**). The hysteresis loop width of 20 K was in agreement with the one found by ^{57}Fe Mössbauer spectroscopy and SQUID magnetometry. The enthalpy and entropy associated to the ST were derived: ΔH_{HL} = 10.5 kJ.mol^{-1} and ΔS_{HL} = 65.5 J.mol^{-1}K^{-1}. The slight temperature shift between the different measurements was related to the difference of thermalisation conditions (heating rates, etc.).

3.2.2.2 Exfoliation of complex (1)

Before delamination, good–shaped crystals (average size 8.2 ± 1.2 μm) were manually picked–up from the bulk sample (Figure 3.23 a,b). After the selection, the LPE methodology was applied in order to perform the delamination of the complex (**1**) (Figure 3.27). First of all, the selection of the proper solvent for the correct delamination of the crystals was performed. In a standard procedure, the crystals were dispersed on several solvents with different polarity under sonication at room temperature for different times.

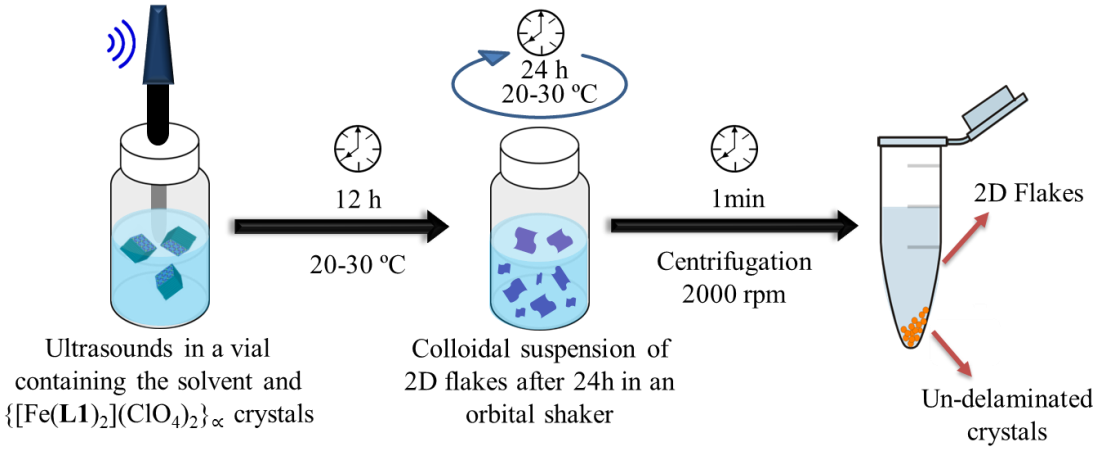

Figure 3.27 Schematic illustration of the liquid-phase exfoliation (LPE) process. The complex (**1**) was exfoliated in different solvents by applying ultrasounds in order to provide enough energy for breaking the weak interactions between layers. A final step consisted on the centrifugation of the resulting material was done in order to remove the un-delaminated crystals.

Organic solvents such as dimethylformamide (DMF), acetone ($(CH_3)_2CO$), chloroform ($CHCl_3$), toluene (Tol) or tetrahydrofuran (THF) induced the chemical decomposition of the sample as FT–IR spectroscopy confirmed (Figure 3.28).

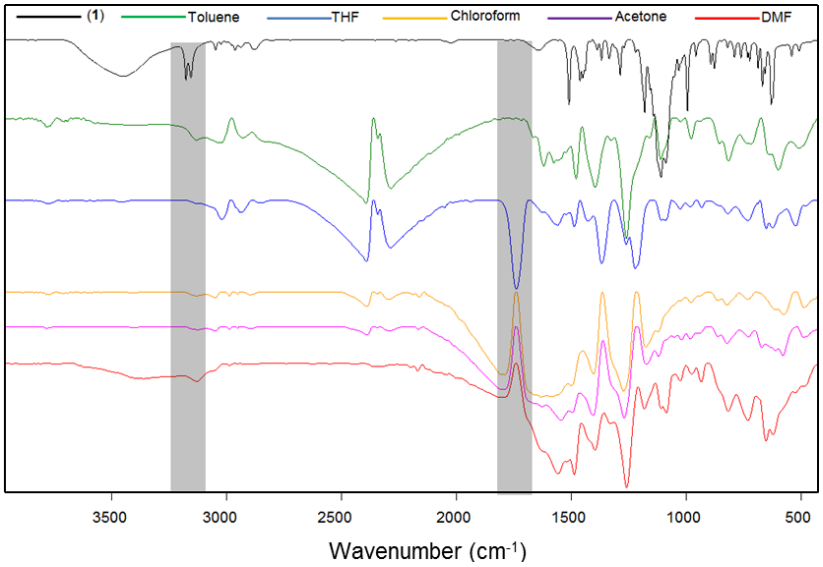

Figure 3.28 FT-IR spectra recorded from the different products after the sonication with different solvents. The comparison with the spectrum of the pure material (bulk crystals of **1**) (black line) corroborated the chemical degradation of the material when is mixed with organic solvents.

The major changes observed in the FT-IR spectra, appeared in those bands corresponding to the ligand where the stretching vibrational band of the N–H bond is involved. This bond is highly affected due to its role as coordinating point for the Fe(II) metal ions. The organic solvents tested may induce oxidative process which affects the crystalline structure promoting the chemical degradation of the complex (**1**). This chemical degradation was accompanied with a progressive fragmentation of the crystals through the exfoliation process (Figure 3.29), resulting in the formation of small fragments of the complex (**1**) without colloidal stability.

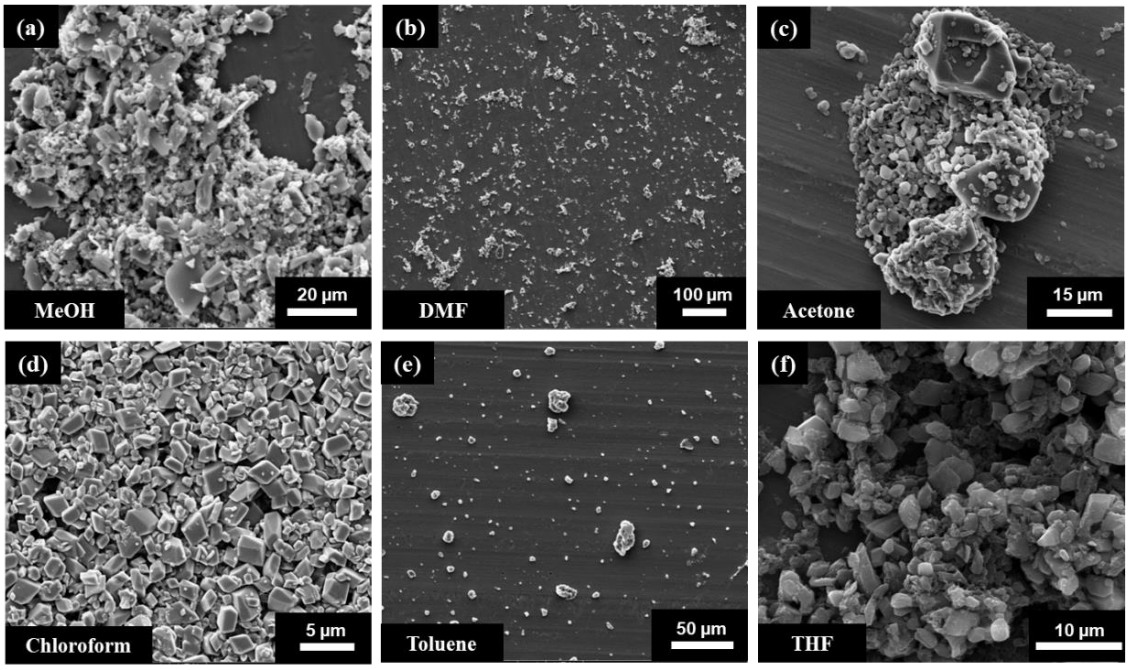

Figure 3.29 SEM images corresponding to samples sonicated in different solvents. The images were taken after 12 h of sonication.

In polar organic solvents such as methanol (MeOH) and ethanol (EtOH) the crystals were chemically stable although no flakes were found upon sonication. Overall, water turned out to be the most suitable solvent for the exfoliation process as i) bulk crystals of complex (**1**) were stable in water at least for a week (up to several months under N_2 atmosphere) and ii) the sonication methodology allowed a proper delamination of the crystals. The formation of colloidal suspensions containing exfoliated 2D flakes was at first optically confirmed by the observation of a Tyndall effect (Figure 3.30).

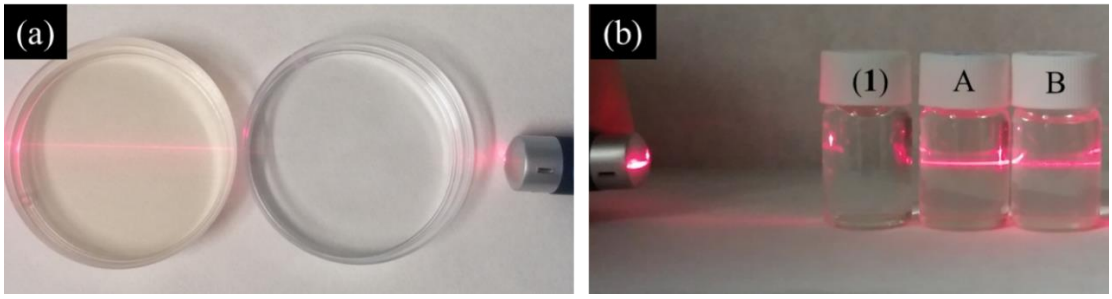

Figure 3.30 Tyndall effect observation through the exfoliated 2D crystals of complex (**1**) in water. (a) Comparison between exfoliated 2D crystals (left) and water as a blank (right). (b) From left to right: The red laser beam remains invisible through the solution with the complex (**1**) before exfoliation process, after 12 h of sonication (A) the presence of flakes in colloidal suspension allows to visualize the laser beam due to scattering phenomena which remains constant after few weeks (B) without precipitation or colour changes in a colloidal suspension containing water.

The laser beam could be observed trough the suspensions indicating the scattering due to the formation of aqueous colloidal suspensions of flakes (Figure 3.30a) which was maintained after few weeks (Figure 3.30b). Nevertheless, at this stage no control over the degree of delamination was achieved. With this aim, a time-dependent exfoliation experiment in water was carried out and followed by combined dynamic light scattering (DLS) and atomic force microscopy (AFM) at three different sonication periods of 4, 6 and 12 h. The DLS measurements taken from samples at 4 and 6 h showed mean size diameters of 347 ± 6 nm and 141 ± 9 nm, respectively (Figure 3.31).

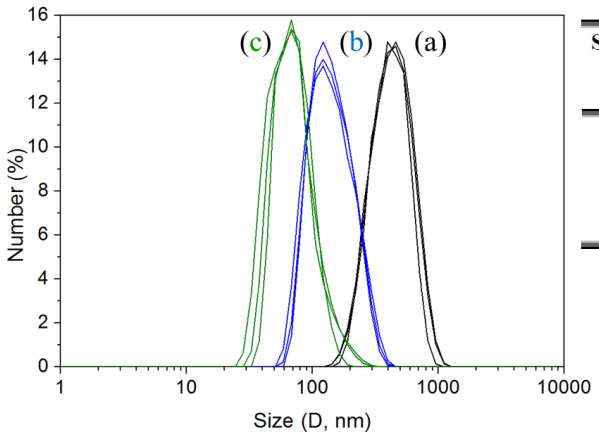

Sonication time (h)		Size (D, nm)
a	4	347 ± 6
b	6	141 ± 9
c	12	86 ± 7

Figure 3.31 Dynamic light scattering (DLS) measurements in water after different sonication times. The mean size was decreased after (a) 4 h, (b) 6 h and (c) 12 h of sonication. The mean sizes are summarized in the table (right).

Complementary AFM measurements of the same thin–films upon deposition by spin coating on silicon surfaces (Figure 3.32a) revealed average thicknesses 200 nm and 25 nm, respectively (Figure 3.32b-d). This would be in agreement with the obtaining of flakes a few hundreds and a few tens of layers, for 4 and 6 h, respectively.

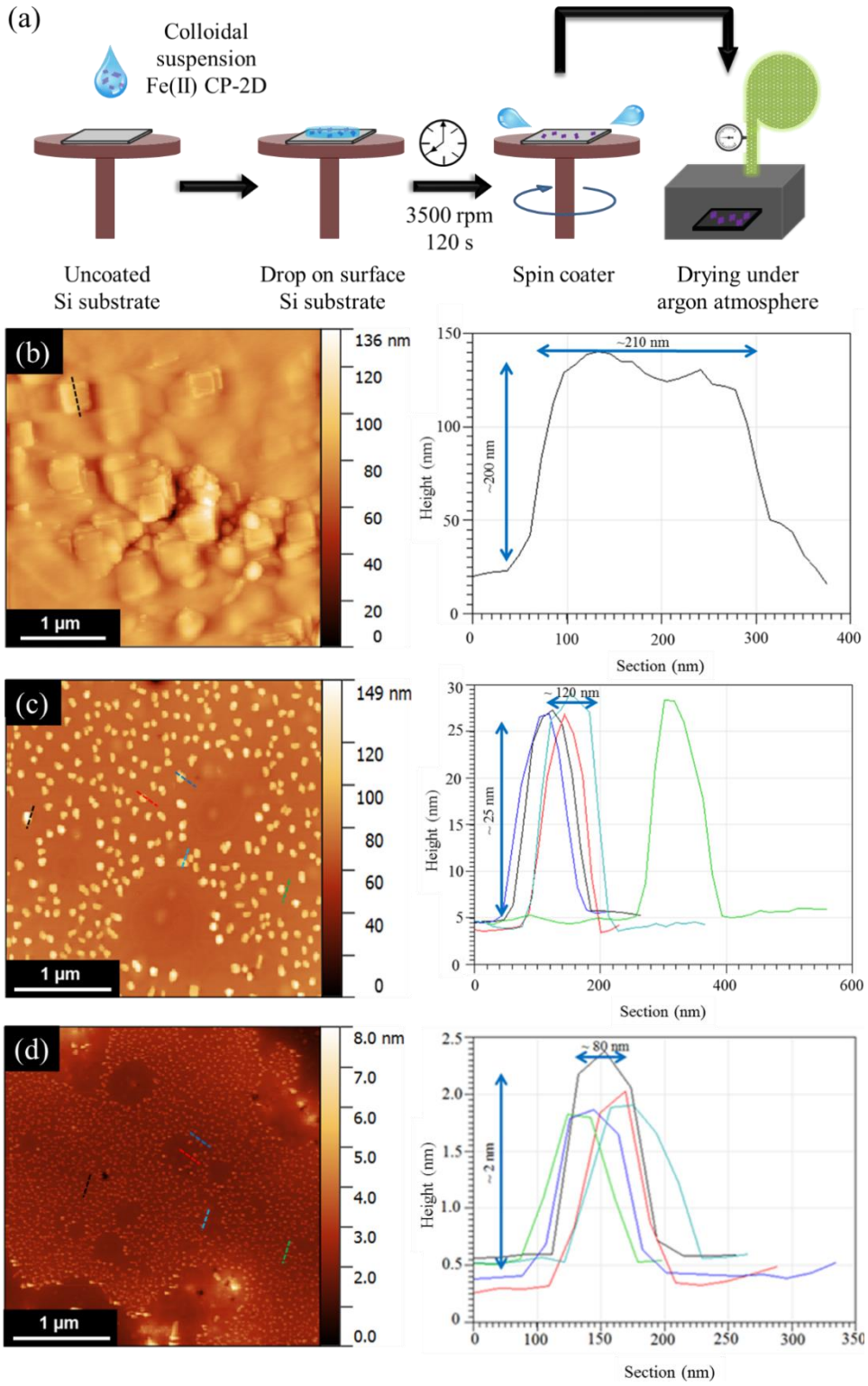

Figure 3.32 (a) Schematic procedure for the sample preparation by spin coating. The AFM images were obtained at different sonication times for (b) 4 h, (c) 6 h and (d) 12 h. Next to each image the corresponding topographic profiles taken at different sonication time is showed.

Sonication for a longer period of 12 h finally allowed for the formation of the desired flakes with average diameters of 86 ± 7 nm (Figure 3.32c) and a narrow 1–3 nm peak thickness distribution as confirmed by AFM. This would be in agreement with the presence of mostly mono– and bi–layer flakes. The 2D coordination nanosheets obtained after a complete cycle of LPE were studied in deep through AFM and transmission electron microscopy (TEM). Representative AFM images of one of the 2D flakes obtained after 12 h of sonication are shown in Figure 3.33.

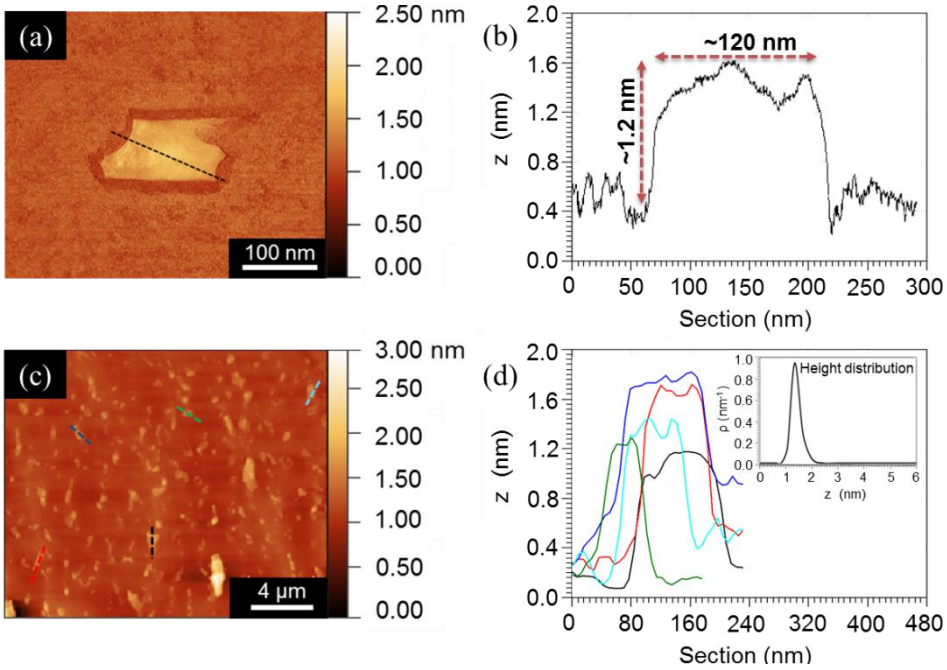

Figure 3.33. Morphological characterization of the exfoliated 2D coordination nanosheets. (a) Tapping mode AFM topography (in ambient air) of a layer on silicon substrate. (b) Height profile corresponding to the dashed line in panel (a). (c) General view of tapping mode AFM topography (in ambient air) after the redispersion in water of the exfoliated flakes. (d) Different height profiles corresponding to the dashed lines in panel (c). Inset graph: Height profile distribution corresponding to the image showed in panel (c).

Additionally, TEM imaging allowed the observation of a single layer of the exfoliated 2D complex (**1**) confirming the success of the applied LPE method (Figure 3.34).

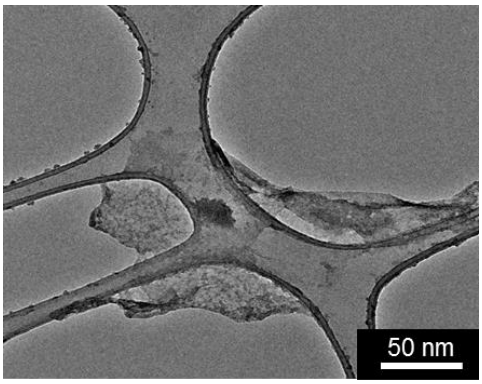

Figure 3.34 Transmission electron microscopy (TEM) image of a single flake, a few hundred nanometres width, obtained after transferring a drop of the colloidal suspension containing the exfoliated 2D CONASHs.

3.2.2.3 Chemical characterization of the exfoliated 2D coordination nanosheets

The previous results demonstrated the optimized LPE method for the obtaining of 2D coordination nanosheets with nanometre sizes close to the monolayer forming the bulk 2D complex (**1**). At this point, it was necessary to confirm the chemical stability of the flakes after a complete cycle of exfoliation. In this sense, a complete chemical characterization of the flakes after 12 h of sonication was performed by different spectroscopies (Raman, FT-IR and X-ray photoelectron spectroscopy (XPS), X-ray diffraction (XRD) and UV-vis). First of all, the exfoliated flakes from the complex (**1**) used for its study by the aforementioned spectroscopies, were redispersed in water in order to assure the formation of the colloidal dispersion avoiding irreversible aggregation between flakes. The 2D coordination nanosheets were analysed by DLS (Figure 3.35).

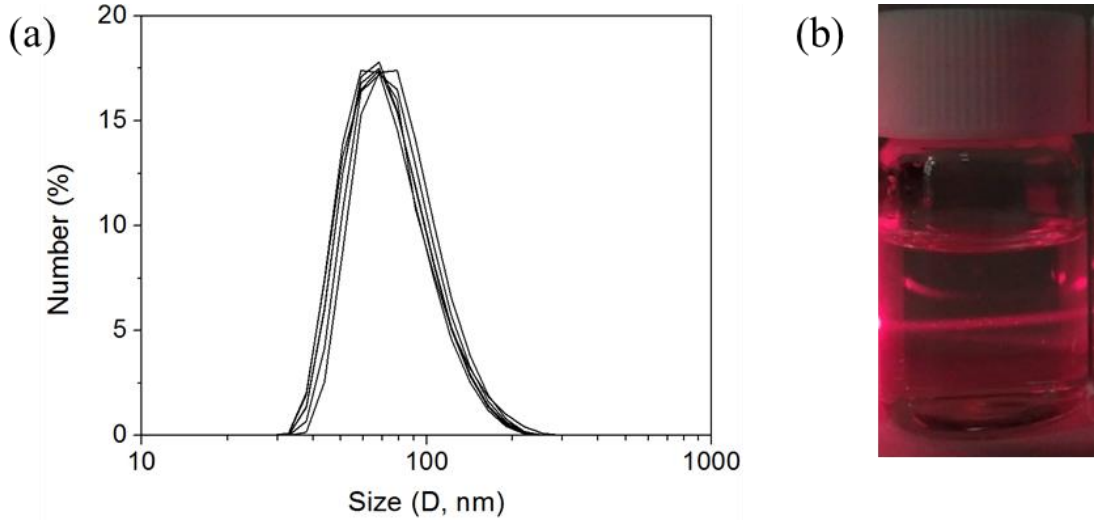

Figure 3.35 (a) DLS measurements of the colloidal dispersions obtained after redispersing the dried flakes in water (b) Redispersed 2D coordination nanosheets in water after they complete drying forming a colloidal suspension.

The results demonstrated a good redispersion of the flakes in water obtaining stable colloidal dispersions with average size of 79 ± 12 nm. These results confirmed that the flakes can be redispersed after being completely dried. The aggregation of the layers can affect their properties and therefore the spectroscopy characterization may vary depending on whether a single monolayer or several non-delaminated or aggregated layers are measured after evaporation of the solvent. However, these preliminary results ensure that the layers can be redispersed once the solvent has been evaporated.

Different drops of the colloidal suspension obtained were deposited on Si substrates by drop casting (Figure 3.36a) and consequently analysed by AFM in order to study the topography and average thickness of the layers after redispersion (Figure 3.36b-d).

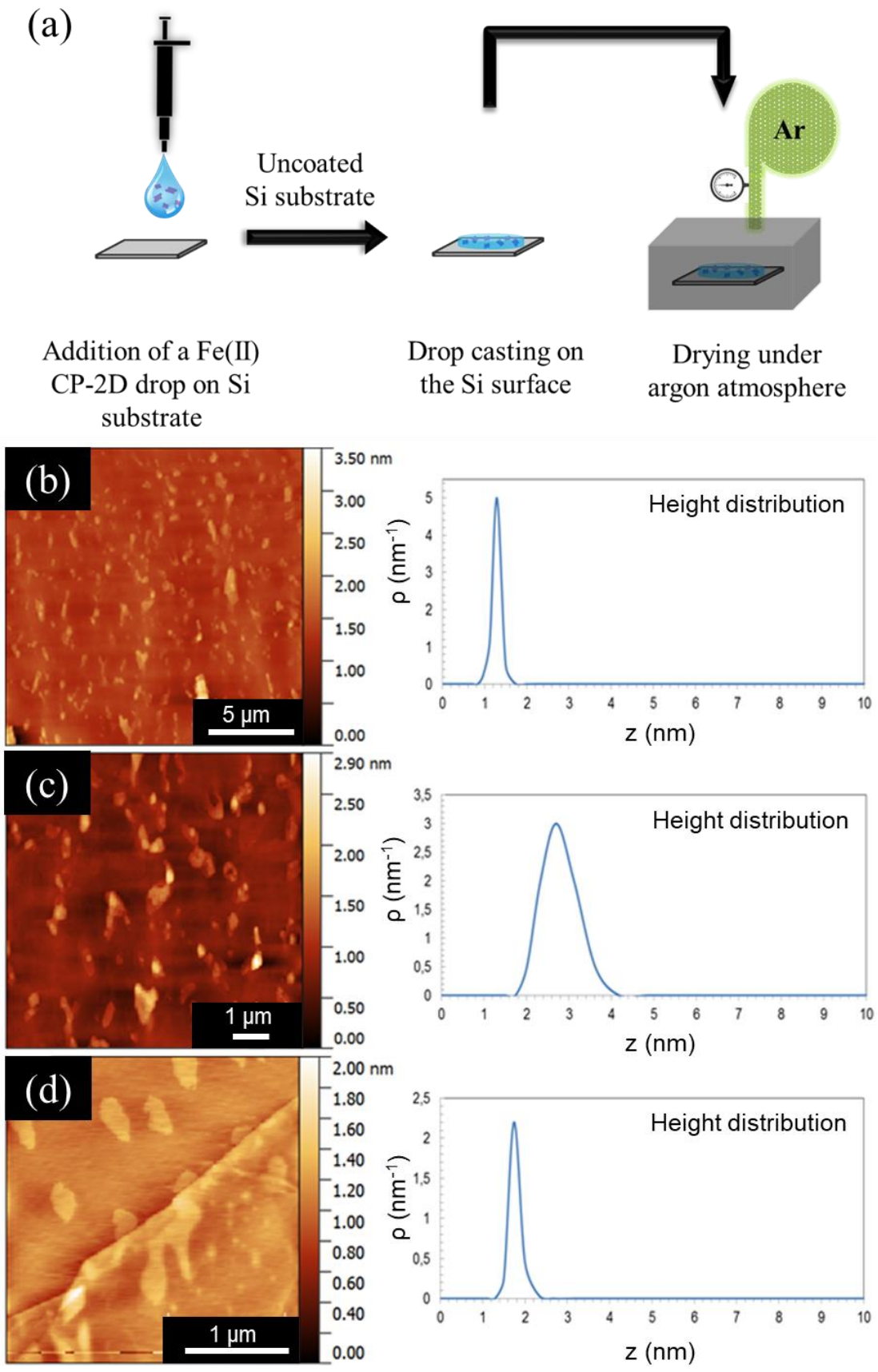

Figure 3.36 (a) Schematic procedure for the sample preparation by drop casting. (b-d) The topographic AFM images and their corresponding height distribution profiles were acquired in different silicon substrates by addition of the same volume of the same sample containing exfoliated flakes (measured in Raman spectroscopy, FT-IR, XRD and UV-vis measurements). The deposition of the flakes was done by drop casting method after the redispersion of the exfoliated flakes in water. Three different substrates where analysed by around 30 scans in different zones.

The images obtained from the AFM showed the deposition of flakes on the Si surface with similar morphology observed before the redispersion in water. The height distribution performed on the AFM topographic images resulted on a layer average thickness of 1.2 – 3 nm thus indicating the retention mainly of mono- and bi-layers once the flakes were redispersed in water after a complete cycle of LPE.

The flakes exfoliated in water after 12 h in the ultrasounds bath, were deposited by crop casting on silicon substrates and fully characterized. The FT-IR spectroscopy showed the retention of the main bands corresponding to the coordination polymer (**1**) (Figure 3.37).

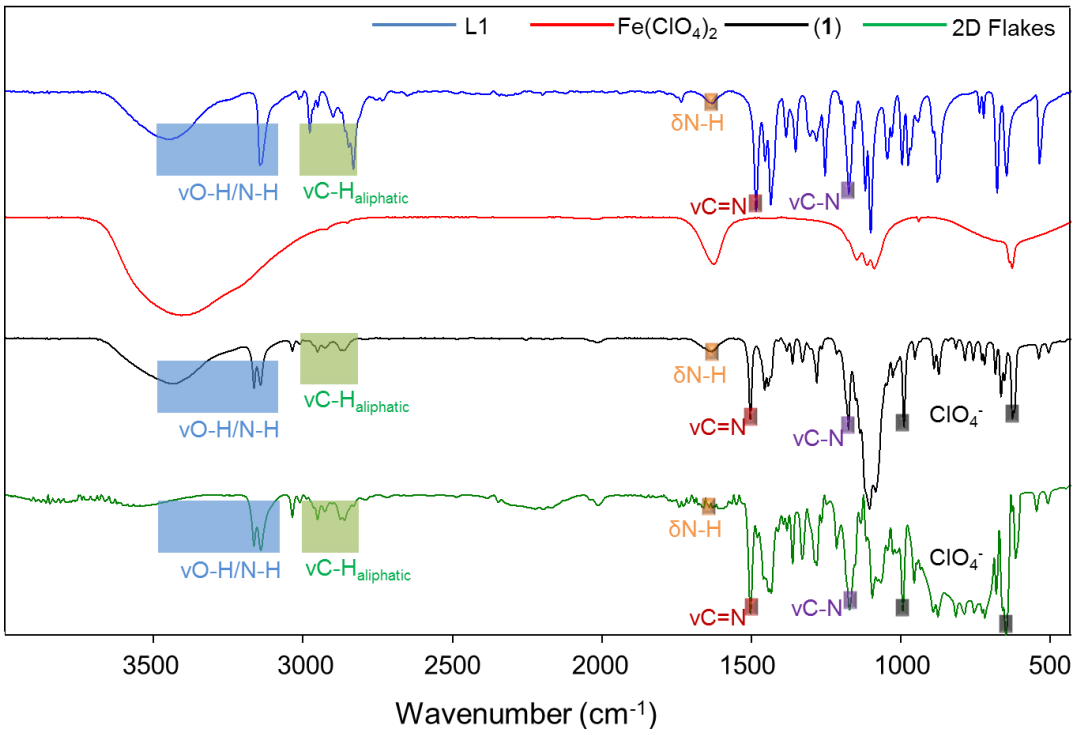

Figure 3.37 FT-IR spectra of the complex (**1**) (black) and the exfoliated material deposited on silicon substrate by drop-casting transfer method (green). In the graph the spectra of starting materials: **L1** (blue) and iron perchlorate (II) (red), are shown.

The main peaks of the 2D flakes were in agreement with those obtained for the bulk samples. If both spectra of 2D flakes and complex (**1**) are compared, a small shift is observed which is typical when decreasing the size of a material. However, all the bands from the complex (**1**) were found in the spectrum of the exfoliated flakes thus indicating the chemical stability after the delamination process. The presence of characteristic peaks coming from the **L1** ligand (the strong band around $\nu = 3142$ cm^{-1} assigned to coordination of Fe(II)), and the peaks attributed to the stretching and bending of Cl–O bond of perchlorate counter anion ($\nu = 1071$ and 612 cm^{-1}) were present. These results indicated the need of the counter anion for the stabilization of the structure even after the exfoliation process.

In order to determine the chemical environment of the synthesized materials, XPS was used to confirm the chemical bonding of both bulk complex (**1**) and 2D exfoliated flakes samples. As

expected, both spectra were in excellent agreement with the C1s and N1s peaks appearing in very close positions (Figure 3.38).

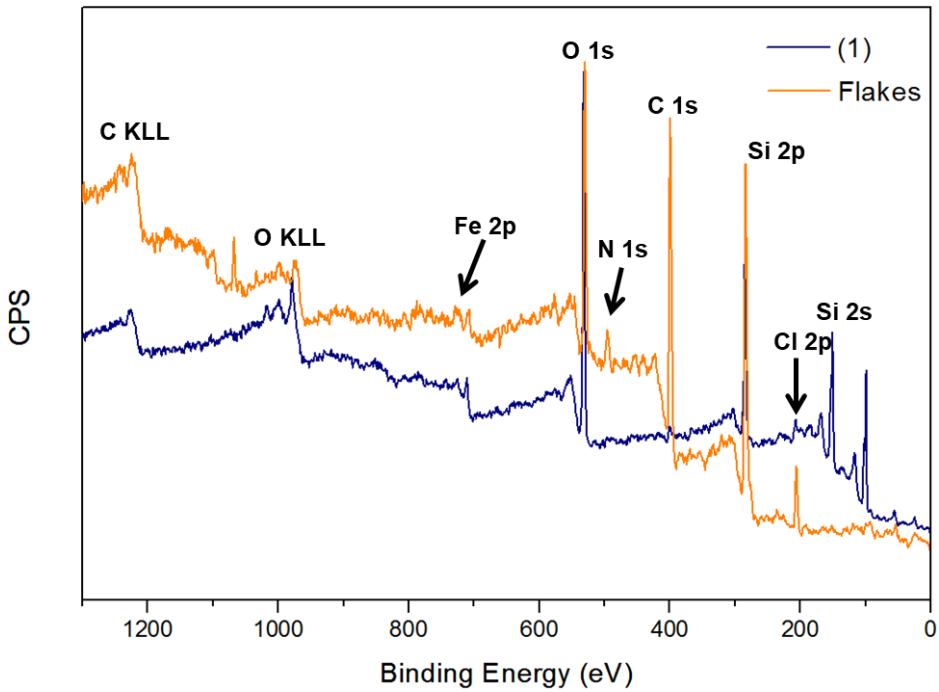

Figure 3.38 Full spectra of X-ray photoelectron spectroscopy (XPS) measurements recorded at room temperature (298 K) of complex (1) (blue) and 2D exfoliated coordination sheets (orange). The peaks corresponding to Si 2p and O1s are due to the silicon substrates used for the deposition of the samples. CPS: Counts per second.

Furthermore, the presence of Cl^- was confirmed by the appearance of the corresponding bands for 2p Cl atoms at ~200 eV. To study in detail the bonding environment of Fe(II) within the complexes deposited on SiO_2, high-resolution XPS curve-fitting was performed. Three different peaks for the C1s spectra of both complex (**1**) and 2D flakes have been properly fitted, corresponding to their three different chemical environments within the Fe(II) complexes (Figure 3.39a,d). The fitted peaks were attributed to the aliphatic C–C, the aromatic single C–N and double C=N bindings appeared at 283.07, 284.7 and 286.3 eV, respectively. Regarding the N1s spectra (Figure 3.39b,e), two peaks were fitted corresponding to the single and double bond between N and C at 397.7 and 399.7 eV, respectively. A third additional peak was attributed to the contribution of the FeN_6 chromophore. Finally, XPS measurements confirm that the Fe(II) nodes retain their oxidation state along the LPE process (Figure 3.39c,f). The spectra corresponding to the Fe 2p corresponded to the oxidation state expected, thus demonstrating that no oxidative processes were induced during the exfoliation of the complex (**1**) in water.

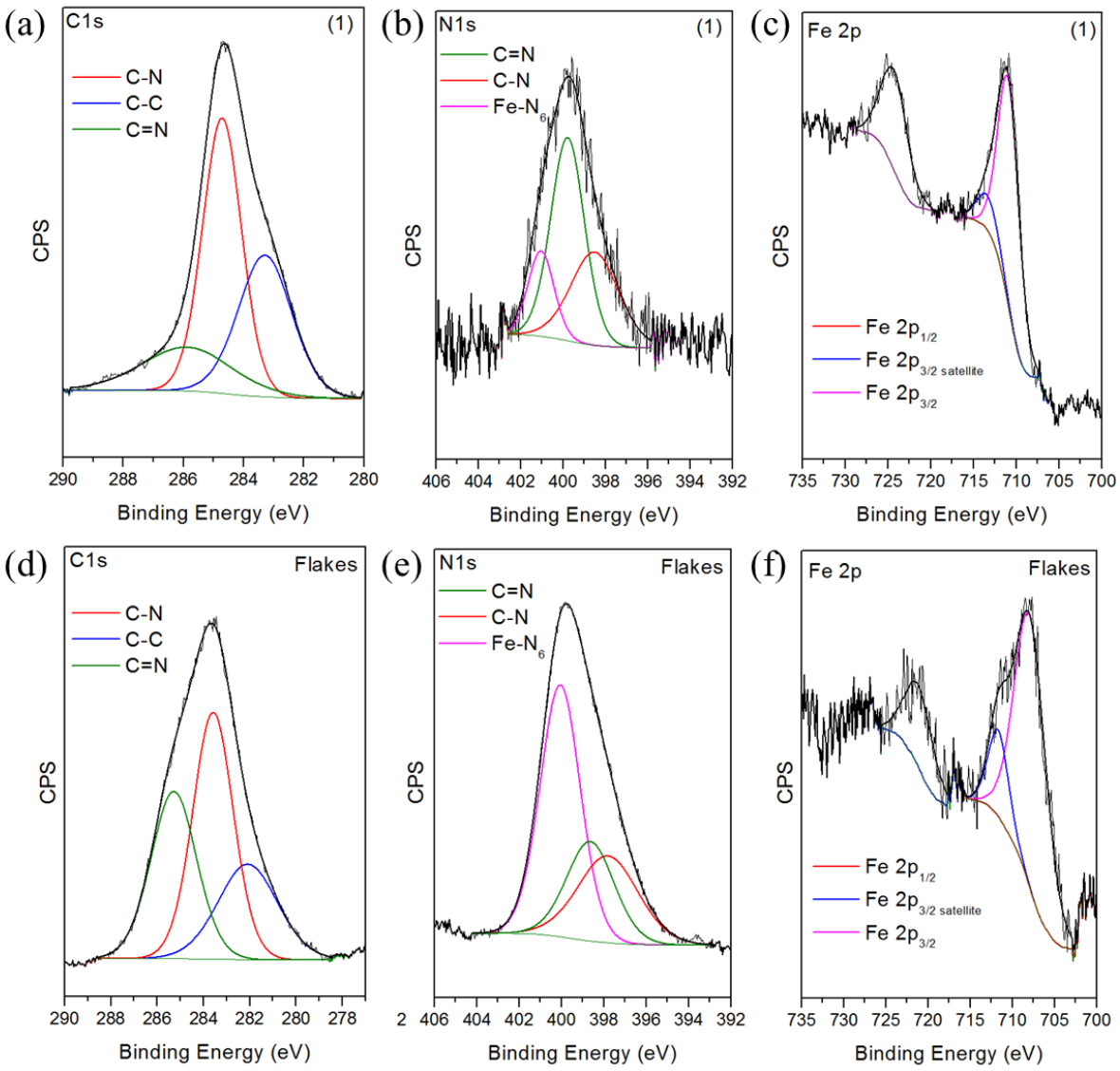

Figure 3.39 Curve-fitting results for C1s, N1s and Fe 2p high-resolution XPS spectra for complex (**1**) (top) and exfoliated 2D flakes (bottom) and the corresponding deconvolution. CPS: Counts per second.

In order to shed more light in the chemical structure between the exfoliated sheets and its bulk counterpart, Raman spectroscopy was carried out. These experiments were performed in collaboration with the *Switchable Molecular Materials* research group led by Prof. Azzedine Bousseksou at *Laboratoire de Chimie de Coordination* (LCC-CNRS, Toulouse, France) under the supervision of Dr Gábor Molnár. Raman spectroscopy is a non-destructive method allowing the characterization of the molecular composition and structure of a material. Briefly, the Raman signal comes from the interaction between the light and the matter detecting the molecular and crystalline vibrations (phonons). This technique complemented the information coming from the FT-IR spectroscopy, which also can determine the vibration modes of the matter. In this work Raman spectroscopy was used for the chemical characterization and also for the study of the changes induced by the SCO occurrence, *vide infra*.

In a first analysis at room temperature, the spectra closely matched for both bulk and flakes, except some changes of relative peak intensities (Figure 3.40).

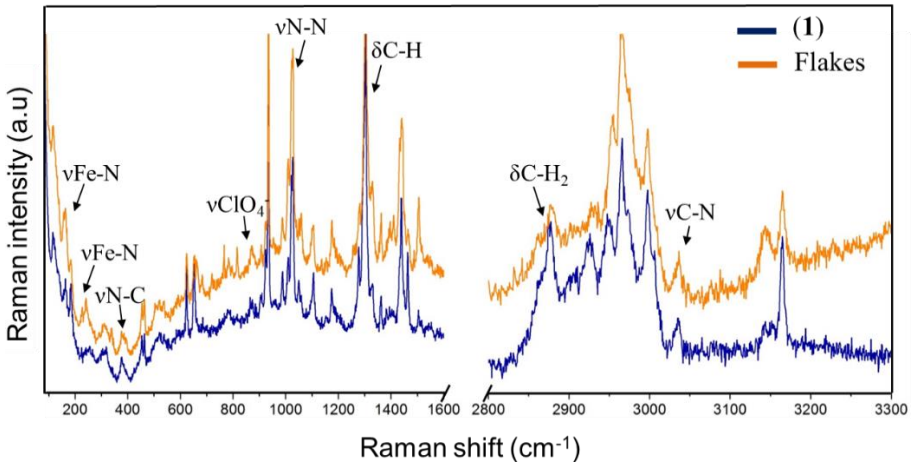

Figure 3.40 Room temperature Raman spectra (excited at 532 nm) of the exfoliated flakes (orange) and bulk crystals of complex (**1**) (blue).

The Raman spectra were in agreement with the FT-IR analysis thus confirming the chemical stability after the exfoliation of the complex (**1**) without oxidation processes and retaining the main bindings. Some of the signals appeared in the range between 700-1600 cm^{-1} can be attributed to the vibrational modes coming from the bonds of the ligand. The peak around 1190 cm^{-1} can be assigned to the bending mode of the δC–H bond in the aromatic rings and the corresponding peak at 1330 cm^{-1} to the stretching of the aromatic C–C bonds. Additionally, the presence of perchlorate counter anion (ClO_4^-) was confirmed with the observation of a peak at 879 cm^{-1}.

On the other hand, the exfoliated flakes were analysed by XRD. The exfoliated coordination nanosheets were analysed in their form as powder and after their deposition on Si substrates (Figure 3.41).

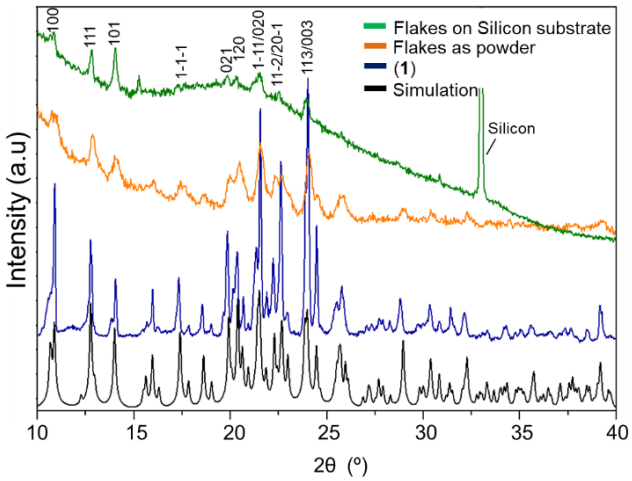

Figure 3.41 Room temperature XRD measurements for bulk crystals (blue), flakes deposited by drop casting on silicon substrate (green), flakes as powder (orange) and the simulation of complex (**1**) (black). a.u: Arbitrary units.

Results showed a remarkable decrease of the diffraction peak intensities (some of them even disappeared) and their concomitant broadening, as expected upon reduction of the dimensionality. Although some peaks were properly identified, their relative intensities did not reveal any remarkable orientation. These results indicated that the exfoliation of the complex (**1**) was not done through a preferential direction. However, in order to study in deep the crystallinity of the flakes, it would be interesting to perform studies by using Synchrotron equipment for the characterization of the single-exfoliated flakes. Additionally, some differences were observed between the spectra corresponding to the flakes as powder and after their deposition on Si substrates. Thus, could be related with flake-substrate interactions which would be interesting to deeply study by the deposition of the exfoliated flakes on different substrates (silicon, gold and graphene, among others).

3.2.2.4 Study of the spin transition occurrence

3.2.2.4.1 UV-vis spectroscopy

Once the chemical stability of complex (**1**) after the delamination process was demonstrated, the SCO behaviour was studied for both bulk crystals and 2D flakes by means of UV–vis spectroscopy under different thermal cycles: cooling (298 K to 73 K) (Figure 3.42a,b) and heating (73 K to 298 K) (Figure 3.42c,d).

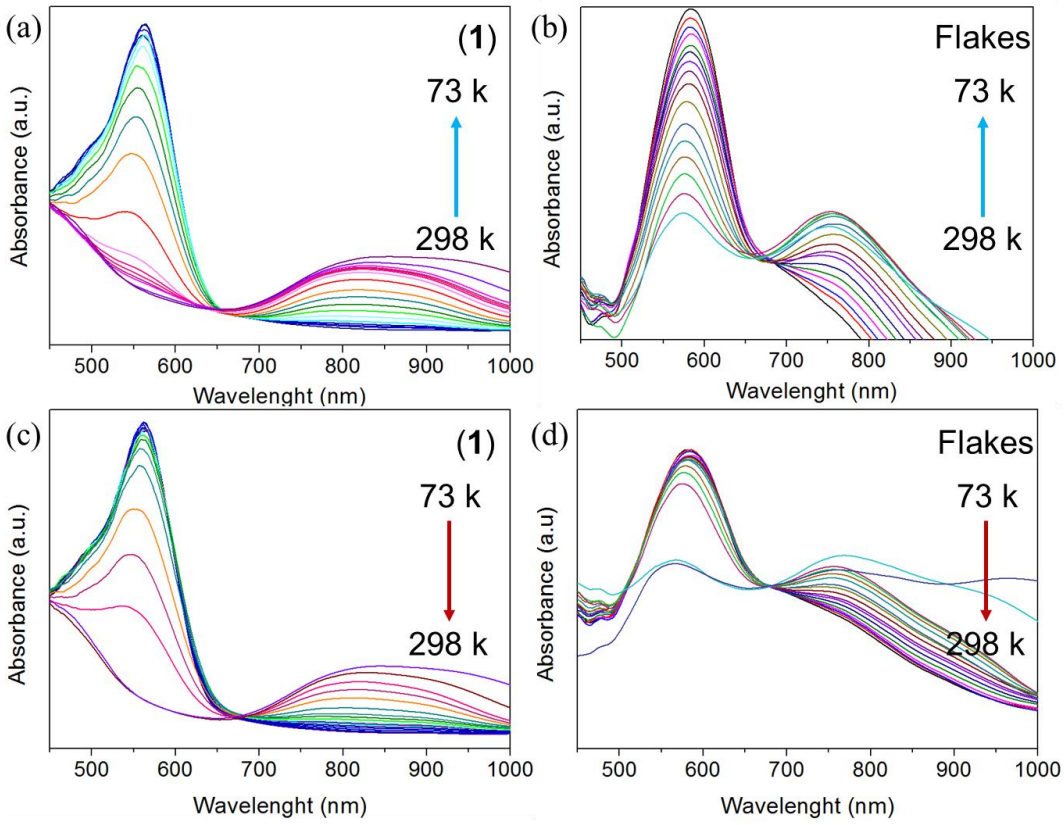

Figure 3.42 Variable–temperature absorption spectra for (a,c) the bulk crystals and (b,d) flakes over the 73–298 K temperature range. a.u: Arbitrary units.

At 73 K, (with a complete LS state) the maximum absorbance of the crystals was at λ = 560 nm. In the case of exfoliated flakes, a red shift to lower energies was observed. A new maximum at λ = 585 nm was now observed, presumably due to enhanced light scattering. This absorption band is characteristic of the LS isomer which corresponds to $^1A_1 \rightarrow {}^1T_1$ ligand field transition of the LS Fe(II).[45-47] This transition was accompanied by visible thermochromism, which changed from colourless (HS) to pink-violet (LS). An increase of the temperature induced a decrease of this LS absorption band until it almost disappeared while a HS band appeared and increased in intensity in the near-infrared region between 750-850 nm. This band can be attributed to the characteristic spin-allowed $^5T_{2g} \rightarrow {}^5E_g$ transition corresponding to HS state which reached the maximum intensity at 298 K.[47-48] When the maximum absorbance of the LS peak was plotted for a whole temperature cycle (heating-cooling), hysteresis loops appeared for both bulk crystals and flakes (Figure 3.43). For the bulk complex (**1**), the absorbance abruptly decreased around 150 K (during the heating process) and abruptly increased again upon cooling around 130 K, with a hysteresis of ~20 K. In the case of the exfoliated flakes, the hysteresis changes being this wider (~50 K) compared with the bulk crystals.

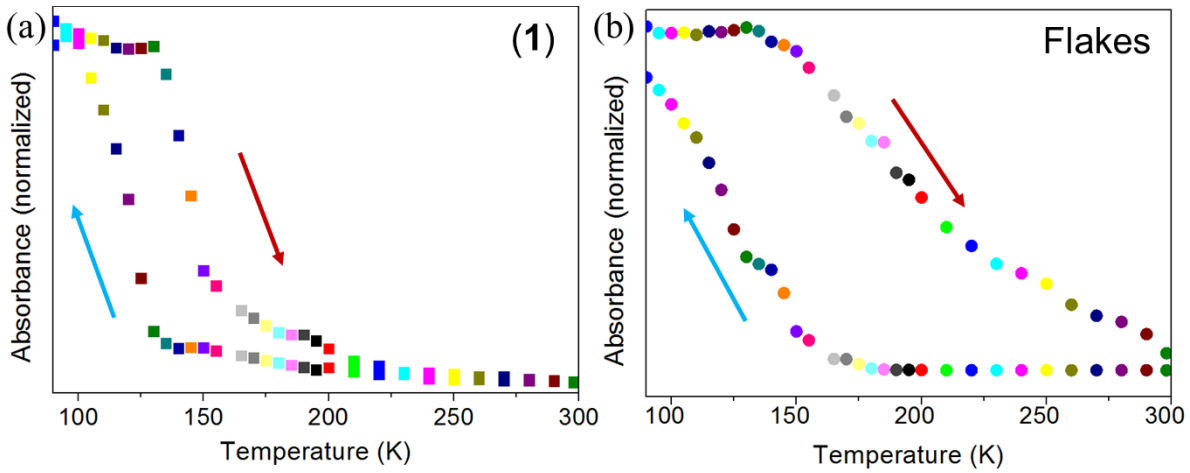

Figure 3.43 Hysteresis loops obtained from temperature–depending absorbance spectra of a) complex (**1**) and b) for 2D flakes on cooling (298 K to 73 K) and heating (73 K to 298 K) cycles. The spectra demonstrate the presence of hysteresis in both systems and the SCO occurrence. The temperatures recorded where from 73-80 K to 200 K (every 5 K) and from 200 K to 298 K (every 10 K). The blue arrow indicates the cooling process and the red arrow indicates the heating process.

Regarding 2D flakes, two main differences were observed for the heating-cooling cycles: i) the transition was not so abrupt but rather progressive over a broad range of temperatures, as expected considering the strong phononic dependence of SCO systems and ii) a broader hysteresis associated to the smoother interconversion process was observed (Figure 3.43b). Finally, for both samples consecutive fully reversible cooling–heating cycles were done thus confirming the stability and reproducibility of the SCO interconversion (Figure 3.44).

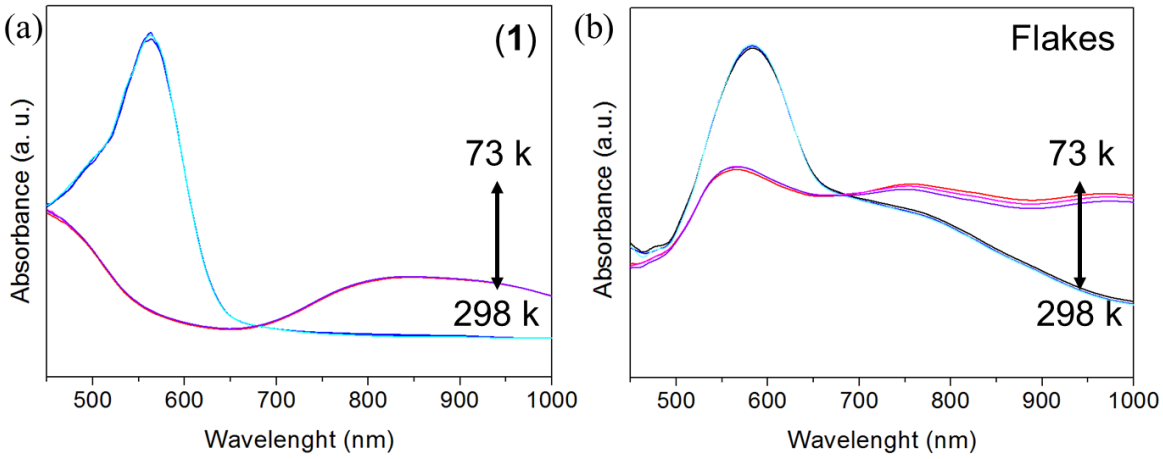

Figure 3.44 Three cycles of cooling-heating. The spectra demonstrate the reversibility of thermochromism associated with spin transition in both (a) bulk material and (b) 2D exfoliated flakes. a.u: Arbitrary units.

Since the study of the 2D flakes was mostly concentrated on the optical properties of the material, additional variable-temperature magnetization studies of the flakes and Raman spectroscopy were carried out with the aim to characterize the SCO in the flakes. Both studies were done in collaboration with the *Switchable Molecular Materials* research group led by Prof. Azzedine Bousseksou. Unfortunately, due to the lack of resolution of these techniques it was not possible to measure the SCO in a single or few layers (as in the case of UV-vis measurements) and large amount of 2D flakes were needed for obtaining an acceptable signal. In the next sections, the results regarding the variable-temperature magnetism and Raman are presented and discussed.

3.2.2.4.2 Magnetization measurements

The complex (**1**) and the 2D flakes were measured by a SQUID for obtaining the $\chi_M T$ vs T characteristic figure. (Figure 3.45).

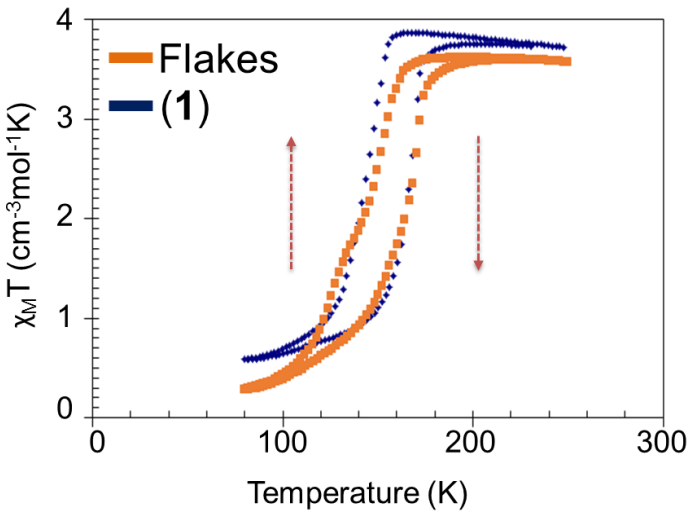

Figure 3.45 Variable-temperature magnetization data of exfoliated flakes (orange) and bulk crystals (blue) that confirmed the presence of the spin transition. The arrows indicate the direction of heating/cooling.

Analysing in detail the results showed in Figure 3.45, for the 2D flakes at room temperature, the $\chi_M T$ value is equal to 3.6 cm^3 mol^{-1} K, in agreement with a virtually full fraction of Fe(II) ions in the HS state. As T was lowered, χMT first decreased somewhat less abruptly and monotonously than in the bulk sample, but around the same temperature Tc↓ = 153 K. When T was increased again, $\chi_M T$ increased around Tc↑ = 168 K denoting a hysteresis loop of 15 K width. The variable-temperature magnetization of the bulk crystals of complex (**1**) has also been included for comparison purposes. At 250 K, the $\chi_M T$ value was equal to 3.7 cm^3 mol^{-1} K, in agreement with a full fraction of Fe(II) ions in the HS state. As T was lowered, χMT first decreased abruptly upon the ST. As the temperature was increased back, χMT followed the same behaviour except for a hysteresis loop (width ~ 20 K) centred at 164 K. The transition temperatures (the temperatures at which 50% of active LS and HS molecules are present) in the cooling and warming modes, respectively, were Tc↓ = 154 K and Tc↑ = 174 K. This hysteresis was retained over successive cooling and heating thermal cycles.

Form the results discussed above; two main conclusions can be extracted:

i. The similarity of the magnetization curves of the powder of flakes and crystals confirmed the chemical stability and the occurrence of the SCO transition upon delamination
ii. Differences between the curves for the crystal and the powder of flakes were less remarkable than those found by optical techniques

The discrepancy between the results obtained for the magnetization data and the optical measurements most likely aroused from the different experimental approach followed in each case. Indeed, in the case of the magnetization data, bulk powder of 2D flakes was used where several interactions between flakes may takes place. On the opposite, optical measurements were obtained over a few layers of flakes deposited on a glass substrate. These results confirm the relevance of the interaction between flakes on the phononic relaxation of the SCO, as otherwise expected.

3.2.2.4.3 Raman spectroscopy measurements

In addition to magnetization measurements, Raman spectroscopy of the 2D flakes was carried out. However, this technique did not have sufficient resolution with the available amount of flakes, in addition to background difficulties, and consequently the results obtained were not reliable enough. For this reason, we needed to increase the number of layers deposited on the substrate (around 40 nm in total thickness) in order to have some signal.

In the Figure 3.46, the Raman spectra of the deposited 2D flakes on silicon substrate recorded at two different temperatures above and below of the ST temperature are shown. The shaded areas highlight the frequencies where the LS state have been split compared with the HS state.

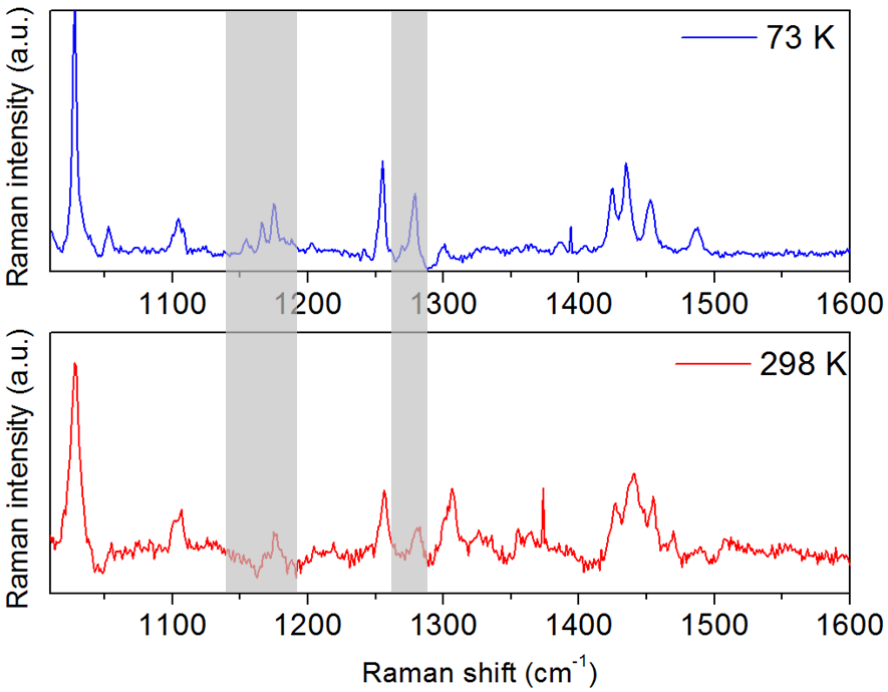

Figure 3.46 Raman spectra for 2D flakes recorded at 73 K (LS, blue) and 298 K (HS, red). The shaded areas highlighted the useful spin-state marker. a.u: Arbitrary units.

The Raman spectroscopy of the layers deposited on silicon substrate showed some differences depending on the temperature. As aforementioned, in the case of the 2D flakes it was not possible to detect Raman signal from the substrate. For this reason, due to the low thickness of some of the layers, it was only possible to detect Raman signal from the layers with thickness around 30-60 nm. However, the received signal from the samples was very low and in some regions was masked by the strong signal corresponding to the silicon substrate. Furthermore, for logical reasons, intensity coming from the material on the substrate was significantly lower if it is compared with the spectra of the pure material. At this point, it was decided to choose a specific area for observation of changes due to the ST within the range of 1000-1600 cm^{-1}. From the results showed in the Figure 3.46 we concluded that:

i. Some changes between the LS and HS spectra were observed.
ii. There is no clearly identifiable change of the spectra of the 2D flakes deposited with the temperature.

The measurements carried out on the 2D flakes were compared with those obtained for the bulk complex (**1**) (Figure 3.47).

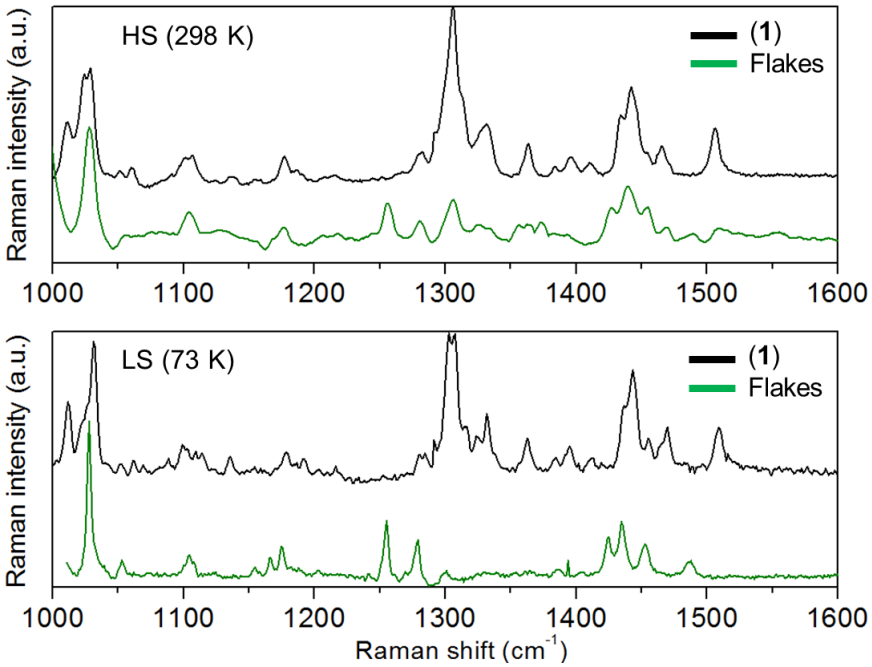

Figure 3.47 Raman spectra of the crystal complex (**1**) (black) and the deposited 2D flakes (green) on silicon substrate recorded at room temperature (top) corresponding to the HS state and at 73 K (bottom) corresponding to the LS state. a.u: Arbitrary units.

From the comparison of the spectra collected at different temperatures for the complex (**1**) and the large amount of flakes deposited on silicon substrates in the energy range of 1000-1600 cm^{-1}, two main aspects can be detected:

i. Firstly, the intensity of the Raman signal of the complex (**1**) was significantly higher than in the case of the substrate with flakes on its surface, which is clearly because the amount of material present in the silicon substrate was much less.

ii. Secondly, it was seen more clearly how some bands have shifted in the spectrum corresponding to the deposited substrate. Moreover, the disappearance of some signals was observed, this may be because the signal strength is not high enough to be visualised.

In this way it is concluded that the fact of depositing material on a substrate after subjecting the material by a process of exfoliation resulted in changes in the signals of the spectra obtained by Raman spectroscopy. The fact that the material was in a thin layer (about 40 nm thick) clearly induces significant changes in the spectrum but can be found certain similarities between them.

Unfortunately, the impossibility of measuring a single layer with these techniques, due to the lack of the resolution, all these changes and differences observed in the results hinder assert that they are intimately due to the SCO phenomenon. Furthermore, interference of many other parameters (layer thickness, substrate, nature of the sample, etc.) that Raman spectroscopy cannot discard, add more

difficulty to interpret the results obtained. The best alternative to properly measure the SCO occurrence in a mono-layer is the use of STM, which allow to accurately measure the small changes appeared in the structure during the ST. This last part will be continued as a future work in order to deeply study the SCO phenomena on the exfoliated layers.

3.2.2.5 Theoretical calculations

Additional ab initio density functional theory (DFT) calculations were done to shed more light on the interpretation of the SCO behaviour. This part was done in collaboration with the *Theory and Simulation* research group led by Prof. Pablo Ordejón (ICN2, Spain).

The theoretical simulation was done considering the experimental bulk structure (Figure 3.48) at two temperatures (110 K and 250 K) as a reference (crystallographic data presented in Table 3.1).

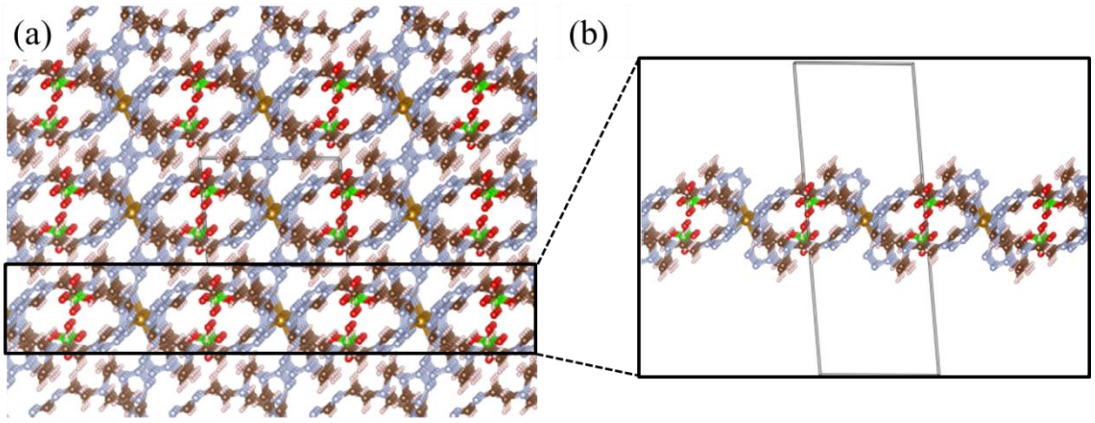

Figure 3.48 Theoretical model. (a) Experimental bulk structure where the unit cell is shown. (b) Structure for the monolayer where the atom positions are fixed to the bulk configuration. The unit cell is shown.

For the low temperature structure (110 K), the LS configuration (S=0) was more stable than the HS one (S=2) by 2.027 eV, whereas for the higher temperature structure (250 K) the HS state was 0.281 eV lower in energy than the LS one. The Projected Densities of States (PDOS) (Figure 3.49) for both configurations showed the expected Fe electronic structure, confirming that the Fe metal ions were isolated, exhibiting only interactions with adjacent N atoms. The additional calculations performed in a single monolayer, fixing the coordinates to the bulk positions, revealed the similarities between bulk crystals and 2D flakes. In the case of a single flake, the low temperature structure (110 K) showed a LS state 2.047 eV lower in energy than the HS configuration. For the high temperature structure (250 K) the HS state was more stable by 0.273 eV. The Fe PDOS in the monolayer (Figure 3.49c,d) was quite similar to the bulk case, showing that the intralayer interaction was hardly affecting the Fe d states, which was less affected by interactions between layers. Both for bulk and monolayer, the electronic structure calculations confirmed the experimentally identified spin state for low (110 K)

and high (250 K) temperature structures and the existence of a ST when decreasing the temperature of the complex.

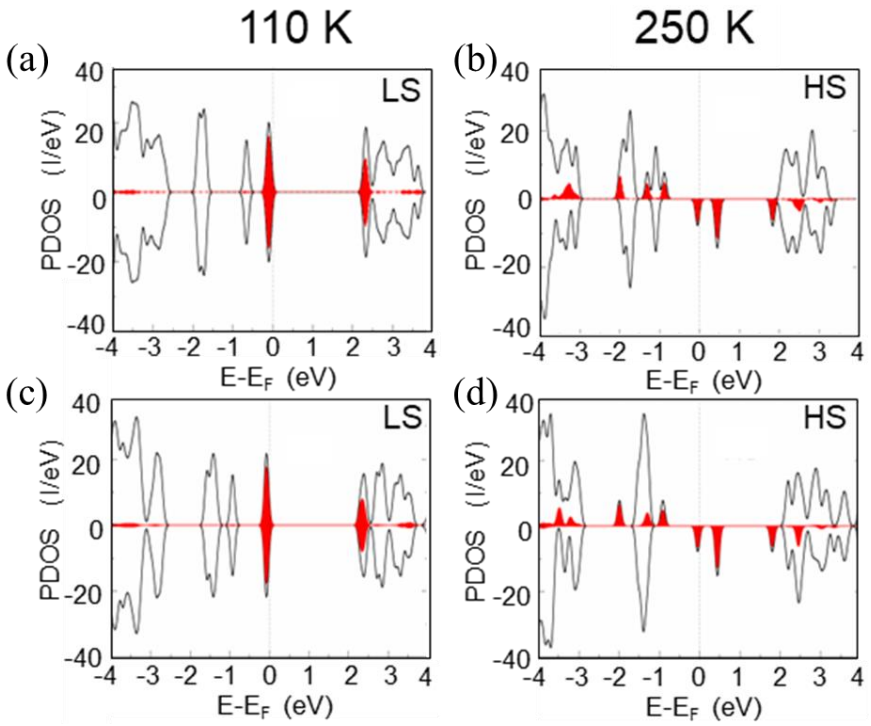

Figure 3.49 Theoretical model. PDOS for the (a,b) bulk complex (**1**) and (c,d) monolayer using the experimental structure obtained at two different temperatures: 110 K (left) and 250 K (right). The red shaded area shows the Fe states.

3.2.3 Application: Low temperature thermochromic films as a proof-of-concept device

As a proof-of-concept device, thermochromic free standing films were obtained by drop casting an aqueous colloidal dispersion of the flakes containing PVA (Figure 3.50). The use of PVA is widely reported on the literature thanks to its intrinsic properties:[49-52]

i. Water-soluble polymer
ii. Excellent film forming features
iii. Adhesive properties
iv. Resistant to oil, grease and solvents
v. High tensile and flexibility properties
vi. Biodegradable

Briefly, the 2D flakes obtained from the LPE of complex (**1**) were added to an aqueous solution containing solubilized PVA. The delaminated flakes were properly dispersed by using ultrasounds for a few seconds. Once a colloidal dispersion was obtained, it was added by drop casting to a plastic

Petri dish (Figure 3.50). After water evaporation at room temperature, the **PVA-2D Flakes** film was easily detached from the container. The film can be handled and cut into the desired morphologies and sizes if needed.

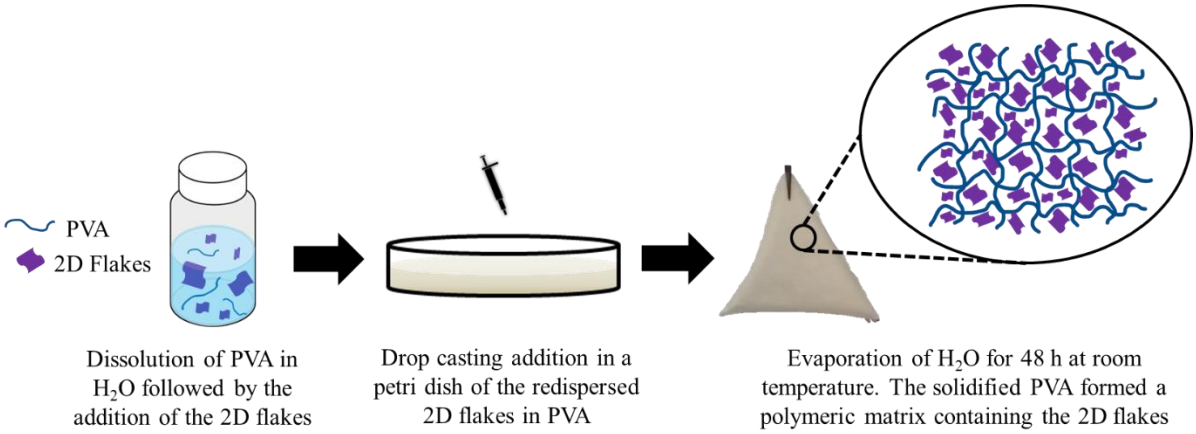

Figure 3.50 Schematic procedure followed for the formation of the **PVA-2D Flakes** hybrid film. The poly(vinyl alcohol) (PVA) was solubilized in water and the flakes added. Once the colloidal dispersion was obtained, the suspension was added by drop casting to a plastic Petri dish. After 48 h, the **PVA-2D Flakes** film had enough consistency for its handling.

As shown in (Figure 3.51), at room temperature the films are translucent (slightly yellowish), characteristic of the HS isomer. Upon cooling down to liquid nitrogen temperature (77 K), the colour of the films changed to an intense pink/purple tonality, characteristic of the LS isomer.

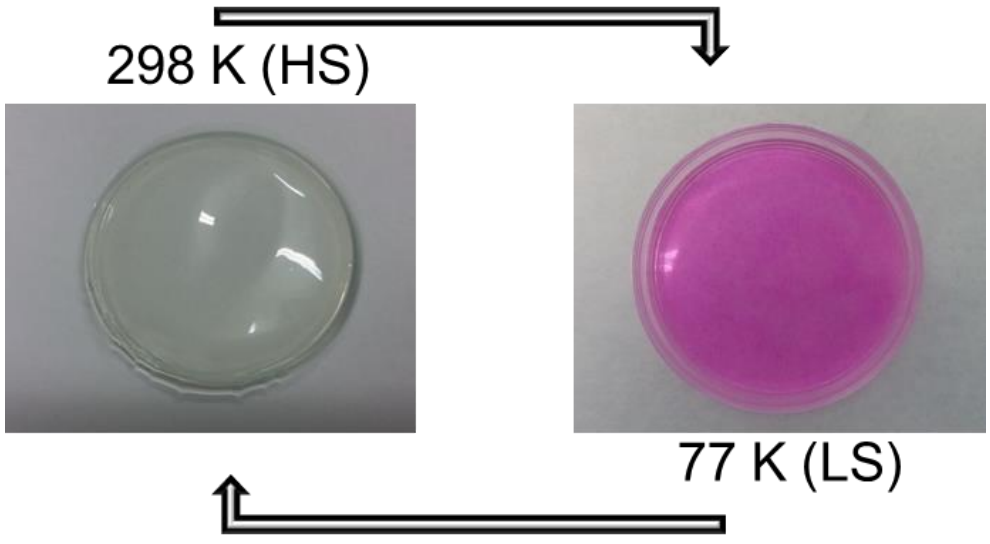

Figure 3.51 2D flakes in a polymeric matrix. The ST was accompanied by a thermochromism of the **PVA-2D Flakes** hybrid film going from room temperature (HS, left) to liquid nitrogen at 77 K (LS, right).

The reproducibility and reversibility of the SCO in films were confirmed by repeated complete cooling and heating cycles. Additionally, several thin films were prepared in order to confirm the viability of the film production method containing 2D flakes. As a representative example, a time-

dependent sequence of photograms obtained after removal of a film from liquid nitrogen and exposition to room temperature is shown in Figure 3.52. As seen, the interconversion was fast, taking place in a few seconds.

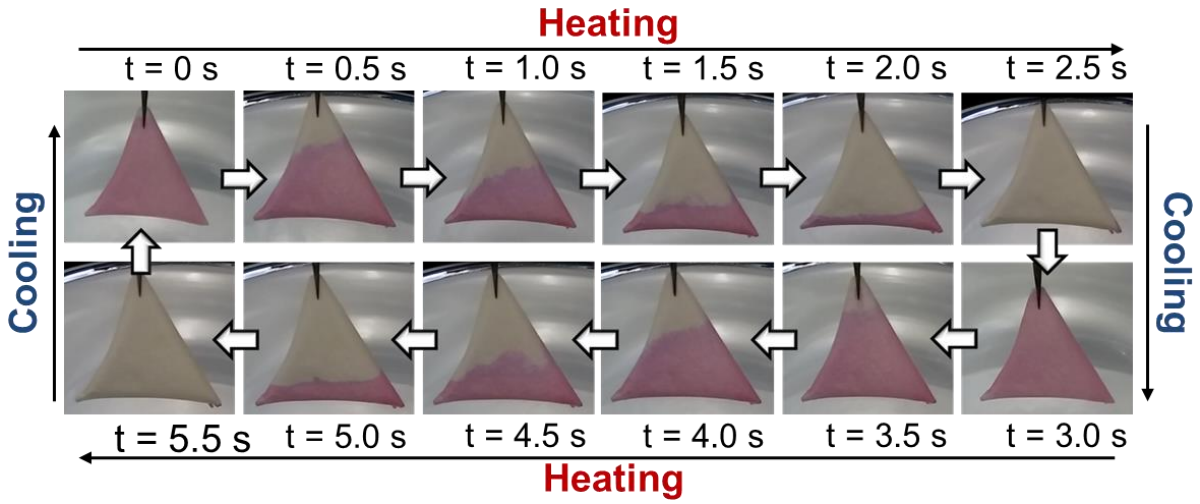

Figure 3.52 Complete cycles of cooling and heating of a **PVA-2D Flakes** hybrid film.

Worth to mention, the chromogenic changes observed were homogenous in the whole film, most likely being an indication of the good dispersion of the flakes within the polymer. Just to confirm this assumption, different sections of the film were analysed by SEM after breaking the material under cryogenic conditions. The result is shown in Figure 3.53. As expected, a good distribution of the films, without relevant phase segregation processes was found.

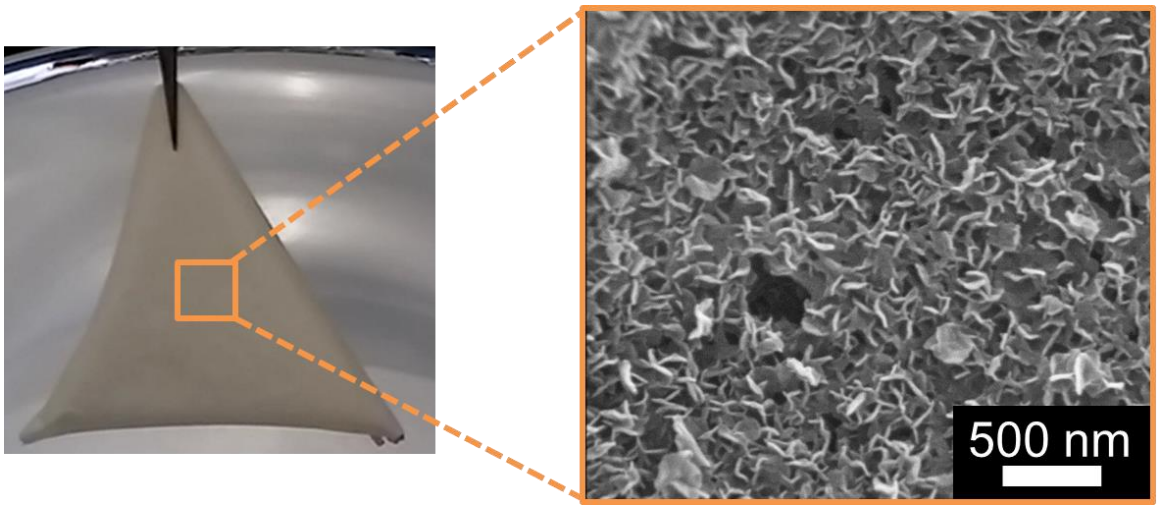

Figure 3.53 SEM image of a film containing the 2D flakes on PVA matrix.

These results demonstrated the retention of the SCO occurrence of the nanoparticles after their embedment in a polymeric matrix. This was mainly explained due to the fact that bistability is an intrinsic property of the flakes.

3.2.4 Summary and conclusions

In summary, we have successfully reported for the first time the obtaining of 2D CP sheet–like SCO, with controlled thicknesses, following the top-down LPE approach. Two main conclusions can be extracted from here:

i. The flakes can be handled as stable colloidal dispersions for many days allowing for their proper transfer to different substrates of relevant interest and technological relevance
ii. We have shown by both experimental and theoretical means that the flakes retain a very similar SCO behaviour compared with the bulk sample

While surprising, as the spin transition is known to be extremely sensitive to even slight changes of intermolecular interactions, these results turn out to be extremely interesting for the development of future SCO hybrid devices. Indeed, previous experiments on crystal grinding has usually a strong impact on the SCO and were shown to lead in many cases to a loss of the hysteresis and a strong increase of residual fractions (i.e. the loss of SCO). At this stage it is still difficult to say what is the behaviour of the flakes in the ensemble measurements (powders and deposited on substrate) while retaining the SCO behaviour. In particular, careful AFM and STM measurements under vacuum will be necessary to properly examine these issues. Nevertheless these results definitely open the door to exciting novel developments, both fundamental and applicative, in the investigation of reduced dimension SCO systems. In this way, we have appropriately dispersed the flakes into PVA, resulting in the formation of free standing low- temperature thin films with thermochromic behaviour. These results demonstrated 2D SCO flakes as robust and reproducible nanoplatforms to translate highly environmentally sensitive SCO systems into future SCO hybrid devices, in a reproducible and controlled manner.

3.2.5 Experimental section

Materials Commercial grade chemicals and solvents were used for synthetic purposes: tris(2-aminoethyl)-amine, triethylorthofromate and sodium azide purchased from Alfa Aesar (Thermo Fisher GmbH, Karlsruhe, Germany), glacial acetic acid and acetonitrile obtained from Scharlab S.L. (Barcelona, Spain), $Fe(ClO_4)_2 \cdot xH_2O$ and ascorbic acid from Sigma-Aldrich (Madrid, Spain). Elemental analyses were performed on Elemental Analyser CHNS Flash 2000 (Thermo Scientific, Madrid, Spain). Caution: Although no problems were faced during the synthesis of the ligand and the coordination polymer (CP), perchlorate salts[53] and tetrazole ligands[54] are potentially explosive and should be handled with extreme care. The synthesis of tris(2–(1H–

tetrazol–1–yl)ethyl)–amine ligand (**L1**) and the coordination polymer {[Fe(**L1**)$_2$](ClO$_4$)$_2$}$_\propto$ (complex (**1**)) were done following the previously reported procedure, which is reproduced in the next section.

Synthesis of Tris(2-(1H-tetrazol-1-yl)ethyl)-amine ligand (L1) The **L1** was synthesized by following the reported procedure with slight modification.[55] A mixture of tris(2-aminoethyl)-amine (5g, 34.19 mmol), sodium azide (7.64g, 117.6 mmol), triethylorthofromate (22.75 g, 153.48 mmol) and glacial acetic acid (100 ml) were refluxed under stirring overnight. Usually tris-tetrazole (t3z) ligands are highly crystalline. Thus, after cooling to room temperature, the white residue was filtered, washed several times with MeOH and recrystallized in acetonitrile. The crystals of **L1** thus obtained were lyophilized. Yield: 1.80 g (Yield: 17 %). Anal. Calcd for $C_9H_{15}N_{13}$ (%): C, 35.41; H, 4.95; N, 59.64. Found: C, 35.89; H, 5.12; N, 59.20. ^{1}H-NMR (400 MHz, DMSO-d6): δ = 3.02 (J(Hz)=2, 6H, t, –CH_2), 4.44 (J(Hz)=2, 6H, t, –CH_2), 9.16 (3H, s, –CH tetrazole) ppm. FT-IR (KBr pellet): 3169 (mb, tetrazole ν$C_{ttz–H}$), 2978w, 2847 (m, aliphatic –CH_2), 1482s, 1453s, 1433m, 1383m, 1351m, 1303m, 1282m, 1253m, 1173m, 1118s, 1099s, 1044m, 995s, 966m, 941m, 871s, 738m, 723m, 677s, 645s, 535s cm^{-1}.

Synthesis of the coordination polymer {[Fe(L1)2](ClO4)2}∝ (1) The complex (**1**) was synthesized by mixing acetonitrile solution (15 ml) of **L1** (40 mg, 0.131mmol) and Fe(ClO4)2·xH2O (16.85 mg, 0.066 mmol) in a vial, a pinch of ascorbic acid was added to this solution and further kept under darkness. After one week, X-ray quality single crystals were obtained via slow evaporation. Yield: 35% (20 mg, 0.023 mmol). Other attempts for the synthesis and crystallization of complex (**1**) from MeOH and EtOH failed resulting in both cases in the exclusive precipitation of the pure ligand **L1**. Anal. Calcd for $C_{18}H_{30}Cl_2N_{26}O_8Fe$ (%): C, 24.98; H, 3.49; N, 42.08. Found: C, 25.13; H, 3.61; N, 42.35. FT-IR (KBr pellet): 3142 (mb, tetrazole ν C_{ttz}–H), 1503m, 1443m, 1362m, 1328m, 1264m, 1175m, 1100s, 1079 (s, ν perchlorate Cl–O) 988s, 952s, 871m, 785m, 757m, 719m, 683s, 664s, 617 (s, δ perchlorate O–Cl–O), 537m, 505m cm^{-1}. The strong broad band around ν = 3139 cm^{-1} identified for the tetrazole Cttz–H group by FT-IR spectroscopy for **L1** is shifted to ν = 3142 cm^{-1} in complex (**1**) due to its coordination to Fe(II). Moreover, the appearance of two strong bands (which is absent in the FT-IR of **L1**) at ν = 1079 and 617 cm^{-1} in (**1**) are attributed to the stretching and bending of Cl–O bond of perchlorate counter anion.

Exfoliation process Coordination polymer (1) was exfoliated in 2D flakes by using the LPE methodology. Different solvents were tested. The process consisted on the addition of 1 mg of the complex (**1**) into eight vials containing the 5 ml of water, methanol (MeOH), ethanol (EtOH), dimethylformamide (DMF), acetone ($(CH_3)_2CO$), chloroform ($CHCl_3$), toluene (Tol) and tetrahydrofuran (THF). The eight vials were placed in an ultrasounds bath (at room

temperature, 60W) for 4, 6 and 12 h. The different samples were characterized by Tyndall DLS measurements and SEM. After 12 h, only the vial containing water and complex (**1**) showed a successful delamination of the layered crystal. After this time, the vial can be placed in an orbital shaker during 24 h for the correct separation and increasing exfoliation yield obtaining the final colloidal suspension (2D flakes). The colloidal suspension remained stable in water at least for a week without any evidence of precipitation and/or colour change. The stability can be improved up to months by the addition of ethanol (water:ethanol 3:1) and storing the suspension avoiding the solvent evaporation. Final step of centrifugation (2000 rpm, 1 min) was added in order to separate the unexfoliated crystals remaining in the pellet and the exfoliated flakes present in the supernatant. For obtaining dried flakes powder, the solvent was evaporated slowly under vacuum conditions. The powder obtained can be easily redispersed in water. These redispersions were done by the addition of 1 mg in 1 mL of H_2O and the corresponding dilutions for the measurements with DLS, FT-IR and AFM. FT-IR (deposited on silicon substrate by drop-casting methodology): 3142 (mb, tetrazole ν Cttz–H), 1500m, 1438m, 1361m, 1327m, 1260m, 1172m, 1199s, 1079 (s, ν perchlorate Cl–O) 988s, 951s, 870m, 785m, 756m, 711m, 681s, 662s, 615 (s, δ perchlorate O–Cl–O), 537m, 505m cm^{-1}.

Transfer of flakes to substrates Two different methodologies were studied for the transfer of colloidal suspensions to substrate: drop casting and spin coating. In both cases clean Si-wafers (0.5 x 0.5 cm^2) were used as a substrate (CNM, Barcelona, Spain). For the drop casting methodology, 15 µl of colloidal suspension after exfoliation process was deposited on the silicon substrate. For the spin coating process, a Speed Mixer DAC 150SD (FlackTek Inc., Landrum, SC, USA) spin coater was used. The substrate was rotated with a drop containing the flakes after the delamination process for 120 s at a speed of 3500 rpm. The substrates containing flakes deposited on the surfaces were dried under argon flow and stored in low humidity conditions under N2 atmosphere.

Preparation of PVA-2D Flakes films Dried 2D flakes (50 mg) were dispersed in a previously prepared poly(vinyl alcohol) (PVA, Sigma-Aldrich) solution (6 mL, 20 wt.%). The dispersion was sonicated during 2 min and slowly transferred to a plastic petri dish (diameter of 5 cm) (Labbox, Barcelona, Spain). The **PVA-2D Flakes** film was obtained after evaporation of the water at room temperature during 24 h. The final film was easily removed from the petri dish once it was dry. The concentration of the flakes was tested from 5-30% in weight.

Powder X-ray diffraction (PXRD) PXRD patterns were recorded on PANalytical X'Pert PRO MRD (Multipurpose Diffractometer) (Malvern PANalytical, Dusseldorf, Germany) equipped with a CuKα radiation source (λ = 1.54184 Å). For the capillary measurements we use a Capillary Spinner which is designed to hold a goniometer (320 mm radius) head into which a

capillary can be placed. The incident optics corresponds to focusing X-ray Mirror, divergent slit 1/2°, mask 10 mm, antiscatter slit 1°, soller slits 0.04 rad and the diffracted optics: X'celerator (detector), antiscatter 7.5 mm, Ni Filter. For the flakes deposited on silicon substrate, the measurements were carried out by using grazing angle mode. (Diffractometer: X'pert Pro MRD (Materials Research Diffractometer) from PANalytical with a goniometer (320 mm radius) in a four-circle geometry. The detector used was a Pixcel 1D which is a fast X-ray detector based on Medipix2 technology. With a wavelength of CuKα anode (lambda=1.540 Å) and incidence angle: 1.55º. The measurement conditions were 2theta range (10-45º); step size= 0.03º; counting time/time per step= 14s).

Single crystal X-ray diffraction (SXRD) One of the block-shaped single crystals was carefully picked up from the mother liquor (CH_3CN), mounted in inert oil, and transferred to the cold gas stream for flash cooling. X-ray single-crystal data of (**1**) were collected at 110, 150 and 250 K on a MAR345 image plate by using MoKα (λ = 0.71073 Å) radiation. Data were integrated by using the Crystalis package (Agilent Technologies (2012). Agilent Technologies UK Ltd., Oxford, UK, Xcalibur/SuperNova CCD system, CrysAlisPro Software system, Version 1.171.34.40.), and the integrate multi-scan absorption method was applied. The structure was solved by direct methods and refined by full-matrix least-squares on |F2| using SHELXL97.5 Non-hydrogen atoms were treated anisotropically. Hydrogen atoms were calculated and refined in riding mode. CCDC 1534951-1534953 contains the supplementary crystallographic data for complex (**1**). These data can be obtained free of charge from The Cambridge Crystallographic Data Centre via *www.ccdc.cam.ac.uk/data_request/cif.*

Scanning Electron Microscopy (SEM) Images obtained from SEM measurements were acquired on a scanning electron microscope (FEI Quanta 650 FEG, Thermo Fisher Scientific, Eindhoven, The Netherlands) in secondary electron mode with a beam voltage between 2 and 20 kV. The samples were prepared by deposition of a drop of the material previously dispersed in water on aluminium stubs followed by evaporation of the solvent under ambient conditions. Before performing the analysis, the samples were metalized by depositing on the surface a thin platinum coating (5 nm) using a high vacuum sputter coater (Leica EM ACE600, Wetzlar, Germany). The images of the films were obtained by using backscattered electrons mode after cutting the film from one side.

Scanning Transmission Electron Microscopy (STEM) Images were obtained using a Magellan 400L from FEI operated at 20 kV and 100 pA. Both Bright Field (BF) and High-Angle Annular Dark Field (HAADF) detectors were used simultaneously. The samples were prepared by drop casting on TEM grids (ultrathin carbon type-A, 400 mesh Cu grids. Ted Pella Inc., Redding,

CA, USA) and dried overnight prior to examination. The digital images were analysed using the ImageJ version 1.2 (NIH, Bethesda, MD, USA) software.

Atomic Force Microscopy (AFM) Surface topography imaging of the different samples was carried out in ambient air in tapping mode using beam shaped silicon cantilevers (Nanosensors, nominal force constant: 5 $N \cdot m^{-1}$, tip radius: ~7 nm) on an Agilent 5500 AFM/SPM microscope (Keysight Technologies, Santa Clara, CA, USA) combined with PicoScan5 version 1.12 (Keysight Technologies) software. An external X-Y positioning system (closed loop, NPXY100E from nPoint, USA) was used. Image processing was done using open source software: WSxM version 3.1 (Nanotec Electronica, Madrid, Spain) and Gwyddion version 2.46 (CMI, Brno, Czech Republic).

UV-visible and Fourier Transform Infrared (FT-IR) Spectroscopy Absorbance spectra of complex (**1**) and 2D flakes were recorded with a Vertex 80 spectrometer (Bruker Optik GmbH, Ettlingen, Germany) in the visible- near-infrared range. Both samples were measured with KBr pellet and additionally, 2D flakes was measured by deposition of the flakes on glass substrate (drop casting method) obtaining the same results. The temperature dependent measurements were done with a cryostat Optistat CFV (Oxford Instruments, Wiesbaden, Germany) cooled with N_2 between 73-298 K. The FT-IR spectra were acquired on an infrared spectrophotometer Tensor 27 (Bruker). The FT-IR spectrum of the flakes deposited on silicon substrate by drop casting was obtained from a Hyperion 2000 FT-IR microscope (Bruker) working in reflexion mode. All the data obtained were processed using the Opus version 7.2.139.1294 (Bruker) software.

Raman Spectroscopy Raman measurements were performed on a XPLORA (Horiba, Kyoto, Japan) Raman microscope system providing a spectral resolution of ca. 3 cm^{-1}. The instrument is equipped with CCD detector (Andor Technology, Oxford Instruments), a x50 objective and a 532 nm Nd:YAG laser which was used at 0.1 mW power in order to avoid excessive laser heating. In order to decrease the slightly fluorescent background of the samples we reduced the spectrometer entrance slit to 50 µm and the confocal hole to 100 µm and acquired spectra after a few min laser exposures.

X-Ray Photoelectron Spectroscopy (XPS) XPS measurements were performed with a Phoibos 150 analyser (SPECS GmbH, Berlin, Germany) in ultra-high vacuum conditions (based pressure 10^{-10} mbar). Monochromatic AlKα was used as X-ray source (1486.6 eV). The electron energy analyser was operated with pass energy of 50 eV. The analyser was located perpendicular to the sample surface. The data was collected every eV with a dwell time of 0.5

sec. Crystals (**1**) and flakes were deposited on silicon substrates and dried under nitrogen. All the data was treated with CasaXPS version 2.3.17PR1.1 (Casa Software LTD, Teignmouth, UK) and OriginPro version 8.0988 (OriginLab Corporation, Northampton, MA, USA) software.

Mössbauer spectroscopy measurements ^{57}Fe Mössbauer spectra were recorded in transmission geometry with a conventional Mössbauer spectrometer equipped with a ^{57}Co(Rh) radioactive source operating at room temperature. The samples were sealed in aluminium foil and mounted on a nitrogen bath cryostat (Oxford Instruments). The spectra were fitted to the sum of Lorentzians by a least-squares refinement using Recoil 1.05 Mössbauer Analysis Software.[6] All isomer shifts refer to α-Fe at room temperature.

Magnetic susceptibilities Magnetic susceptibility data of complex (**1**) was acquired in the temperature range 2-400 K using a Magnetic Property Measurement System (MPMS3) SQUID magnetometer operating at 1000 Oe. Data were corrected for diamagnetic contributions, which were estimated from the Pascal constants.

Calorimetric measurements Differential scanning calorimetry (DSC) measurements were carried out in a $N_{2(g)}$ atmosphere using a DSC (PerkinElmer Inc. DSC Pyris, Waltham, MA, USA) instrument equipped with a cryostat and operating down to 108 K. Temperatures and enthalpies were calibrated over the temperature range 108–300 K using the solid/solid and liquid/solid transitions of pure cyclopentane (99%, Acros).[56] The calibration sample was introduced in an aluminium pan and hermetically sealed using an encapsulating press. The calibration was made at a scan rate of 10 K min^{-1}. The characteristic temperatures, which were assigned to the crystal/crystal transitions of cyclopentane, were obtained by the extrapolation of the maximum peak temperatures.[56] An empty aluminium pan, identical to the one used for the sample, was used as a reference to obtain a reliable baseline. The system produces or uptakes energy in order to keep the temperature of the complex identically to the reference. This energy difference between two resistances (in mW) is transformed by a PYRISTM DSC software version 7.0 (PerkinElmer) in specific heat C_p (J mol^{-1} K^{-1}). The DSC measurement of the sample was carried out at a scan rate of 10 K·min^{-1}, in warming and cooling modes. 20.5 mg sample were encapsulated at room temperature in an aluminium pan and hermetically sealed. The sample was maintained at room temperature for 5 min in order to allow the system to equilibrate, and was further cooled down from 300 to 108 K. The sample was maintained at 108 K for 5–10 min to reach equilibrium, followed by a similar scanning mode as on cooling between 108 K and room temperature for which the data were recorded.

Theoretical model Ab-initio calculations have been performed in the framework of the Density Functional Theory as implemented in the VASP code.[57,58] The Projector Augmented Wave

method has been used to describe the core electrons and the PBE version of the generalized gradient approximation has been used for the exchange and correlation functional.[59] The energy cut-off of the plane wave basis set has been set to 400 eV. All calculations have been done using the Gamma point. Increasing the number of k-points changes the energy less than 1 meV/atom. The experimental structure has been used for all atoms except hydrogen, which positions have been optimized. Additional tests have been done using the DFT+U method[60] with Ueff= 2 eV for *d* Fe electrons. The results remain qualitatively the same, being the main effect a further stabilization of the HS state.

3.2.6 References

1. Zhang, H. *ACS Nano* **2015**, *9*, 9451–9469.
2. Mas-Balleste, R.; Gomez-Navarro, C.; Gomez-Herrero, J.; Zamora, F. *Nanoscale* **2011**, *3*, 20–30.
3. Rao, C. N. R.; Ramakrishna-Matte, H. S. S.; Maitra, U. *Angew. Chem. Int. Ed.* **2013**, *52*, 13162–13185.
4. Colson, J.W.; Dichtel, W. R. *Nat. Chem.* **2013**, *5*, 453–465.
5. Allen, M. J.; Tung, V. C.; Kaner, R. B. *Chem. Rev*. **2010**, *110*, 132–145.
6. Geim, A. K.; Novoselov, K. S. *Nat. Mater.* **2007**, *6*, 183–191.
7. Dreyer, D. R.; Park, S.; Bielawski, C. W.; Ruoff, R. S. *Chem. Soc. Rev*. **2010**, *39*, 228–240.
8. Wang, Q. H.; Kalantar-Zadeh, K.; Kis, A.; Coleman, J. N.; Strano, M. S. *Nat. Nanotech.* **2012**, *7*, 699–712.
9. Chowalla, M.; Shin, H. S.; Eda, G.; Li, L.-J.; Loh, K. P.;Zhang, H. *Nat. Chem.* **2013**, *5*, 263–275.
10. Wang, Q.; O'Hare, D. *Chem. Rev*. **2012** , *112*, 4124–4155.
11. Ma, R.; Sasak, T. *Adv. Funct. Mater*. **2010**, *22*, 5082–5104.
12. Liu, H.; Du, Y.; Deng, Y.; Ye, P. D. *Chem. Soc. Rev*. **2015** , *44*, 2732 – 2743.
13. Lin, Y.; Connell, J. W. *Nanoscale* **2012**, *4*, 6908–6939.
14. Naguib, M.; Mochalin, V. N.; Barsoum, M. W.; Gogotsi, Y. *Adv. Mater*. **2014**, *26*, 992–1005.
15. Ovoselov, K. S.; Geim, A. K.; Morozov, S. V.; Jiang, D.; Zhang, Y.; Dubonos, S. V.; Grigorieva, I. V.; Firsov, A. A. *Science* **2004**, *306*, 666–669.
16. Huang, X.; Zeng, Z.; Zhang, H. *Chem. Soc. Rev*. **2013**, *42*, 1934–1946.
17. C. Tan, H. Zhang, *Chem. Soc. Rev*. **2015**, *44*, 2713–2731.
18. Ma, R.; Sasak, T. *Acc. Chem. Res.* **2015**, *48*, 136–143.
19. Pakdel, A.; Bando, Y.; Golberg, D. *Chem. Soc. Rev*. **2014**, *43*, 934–959.
20. Sakamoto, R.; Takada, K.; Pal, T.; Maeda, H.; Kambe, T.; Nishihara, H. *Chem. Commun.* **2017**, *53*, 5781–5801.

21. Rodenas, T.; Luz, I.; Prieto, G.; Seoane, B.; Miro, H.; Corma, A.; Kapteijn, F.; Llabrés-Xamena, F. X.; Gascon, J. *Nat. Mater*. **2015**, *14*, 48–55.
22. Colson, J. W.; Woll, A. R.; Mukherjee, A.; Levendorf, M. P.; Spitler, E. L.; Shields, V. B.; Spencer, M. G.; Park, J.; Dichtel, W. R. *Science* **2011**, *332*, 228–231.
23. Wang, Y.; Zhao, M.; Ping, J.; Chen, B.; Cao, X.; Huang, Y.; Tan, C.; Ma, Q.; Wu, S.; Yu, Y.; Lu, Q.; Chen, J.; Zhao, W.; Ying, Y.; Zhang, H. *Adv. Funct. Mater.* **2016**, *28*, 4149–4155.
24. Xu, G.; Yamada, T.; Otsubo, K.; Sakaida, S.; Kitagawa, H. *J. Am.Chem. Soc*. **2012**, *134*, 16524–16527.
25. Peng, Y.; Li, Y.; Ban, Y.; Jin, H.; Jiao, W.; Liu, X.; Yang, W. *Science* **2014**, *346*, 1344–1347.
26. Zhang, Y.; Feng, X.; Yuan, S.; Zhou, J.; Wang, B. ***Inorg. Chem. Front.*** **2016**, ***3***, 896–909.
27. Zhan, G.; Zeng, H. C. *Adv. Funct. Mater*. **2016**, *26*, 3268–3281.
28. Dong, R.; Pfeffermann, M.; Liang, H.; Zheng, Z.; Zhu, X.; Zhang, J.; Feng, X. *Angew. Chem., Int. Ed. Engl*., **2015**, *54*, 12058–12063.
29. Hermosa, C.; Horrocks, B. R.; Martínez, J. I.; Liscio, F.; Gómez-Herrero, J.; Zamora, F. *Chem. Sci*. **2015**, *6*, 2553–2558.
30. Araki, T.; Kondo, A.; Maeda, K. *Chem. Commun*. **2013**, *49*, 552–554.
31. Dong, R.; Zhang, T.; Feng, X. *Chem. Rev.* **2018**, *118*, 6189–6235.
32. Chen, Y.; fan, Z.; Zhang, Z.; Niu, W.; Li, C.; Yang, N.; Chen, B.; Zhang, H. *Chem. Rev.* **2018**, *118*, 6409–6455.
33. Amo-Ochoa, P.; Welte, L.; González-Prieto, R.; Sanz-Miguel, P. J.; Gómez-García, C. J.; Mateo-Martí, E.; Delgado, S.; Gómez-Herrero, J.; Zamora, F. *Chem. Commun.* **2010**, *46*, 3262–3264.
34. Noveselov, K. S.; Jiang, D.; Schedin, F.; Booth, T. J.; Khotkevich, V. V.; Mozorov, S. V.; Geim, A. K. *Proc. Natl. Acad. Sci. USA* **2005**, *102*, 10451–10453.
35. Gallego, A.; Hermosa, C.; Castillo, O.; Berlanga, I.; Gómez-García, C. J.; Mateo-Martí, E.; Martínez, J. I.; Flores, F.; Gómez-Navarro, C.; Gómez-Herrero, J.; Delgado, S.; Zamora, F. *Adv. Mater.* **2013**, *25*, 2141–2146.
36. Kondo, A.; Tiew, C. C.; Moriguchi, F.; Maeda, K. *Dalton Trans.* **2013**, *42*, 15267–15270.
37. Nie, W. -X.; Bao, S. -S.; Zeng, D.; Guo, L. -R.; Zheng, L. -M. *Chem. Commun.* **2014**, *50*, 10622–10625.
38. Foster, J. A.; Henke, S.; Schneemann, A.; Fischer, R. A.; Cheetham, A. K. *Chem. Commun.* **2016**, *52*, 10474–10477.
39. Xu, H.; Gao, J.; Qian, X.; Wang, J.; He, H.; Cui, Y.; Yang, Y.; Wang, Z.; Qian, G. *J. Mater. Chem. A* **2016**, *4*, 10900–10905.
40. Liu, H. -L.; Chang, Y. -J.; Fan, T.; Gu, Z. -Y. *Chem. Commun.* **2016**, *52*, 12984–12987.
41. Makiura, R.; Konovalov, O. *Dalton trans.* **2013**, *42*, 15931-15936.

42. Dong, R.; Pfeffermann, M.; Liang, H.; Zheng, Z.; Zhu, X.; Zhang, J.; Feng, X. *Adv. Mater.* **2015**, *27*, 7372–7378.
43. Adarsh, N. N., Dîrtu, M. M., Rotaru, A., Garcia, Y. *Hyperfine Interact.* **2017**, *238*, 60.
44. Bronisz, R. PhD thesis **1999**, University of Wroclaw.
45. Phan, H. V.; Chakraborty, P.; Chen, M.; Calm, Y. M.; Kovnir, K.; Keniley Jr., L. K.; Hoyt, J. M.; Knowles, E. S.; Besnard, C.; Meisel, M. W.; Hauser, A.; Achim, C.; Shatruk, M. *Chem. Eur. J.* **2012**, *18*, 15805–15815.
46. Niel, V.; Thompson, A. L.; Goeta, A. E.; Enachescu, C.; Hauser, A.; Galet, A.; Muñoz, M. C.; Real, J. A. *Chem. Eur. J.* **2005**, *11*, 2047–2060.
47. Delgado, T.; Tissot, A.; Besnard, C.; Guénée, L.; Pattison, P.; Hauser, A. *Chem. Eur. J.* **2015**, *21*, 3664–3670.
48. Kryeziu, M. T.-; Weil, M.; Marunaka, T.; Bousseksou, A.; Hasegawa, M.; Jun, A.; Linert, W. *Dalton Trans.* **2013**, *42*, 15796–15804.
49. Halima, N. B. ***RSC Adv.*** **2016**, ***6***, 39823–39832.
50. Kamoun, E. A.; Kenawy, E.-R.; Chen, X. J. *Adv. Res.* **2017**, *8*, 217–233.
51. Paraossi, G.; Cavalieri, F.; Chiessi, E. *J. Mater. Sci.: Mater. Med* **2003**, *14*, 687–691.
52. Baker, M. I.; Walsh, S. P.; Scwartz, Z.; Boyan, B. D. *J. Biomed. Mater. Res. B* **2012**, *100*, 1451–1457.
53. Wolsey, W. C. J. *Chem. Educ*. **1973**, *50*, 335–337.
54. Benson, F. R. *Chem. Rev*. **1947**, *41*, 1–61.
55. Werner, F.; Tokuno, K.; Hasegawa, M.; Linert, W.; Mereiter, K. *Acta Cryst*. **2010**, *66*, 399–400.
56. Rotaru, A.; Dîrtu, M. M.; Enachescu, C.; Tanasa, R.; Linares, J.; Stancu, A.; Garcia, Y. *Polyhedron* **2009**, *28*, 2531–2536.
57. Kresse, G.; Joubert, D. *Phys. Rev. B* **1999**, *59*, 1758–1775.
58. Kresse, G.; Furthmüller, J. *Phys. Rev. B* **1996**, *54*, 11169–11186.
59. Perdew, J. P.; Burke, K.; Ernzerhof, M. *Phys. Rev. Lett*. **1996**, *77*, 3865–3868.
60. Dudarev, S. L.; Botton, G. A.; Savrasov, S. Y.; Humphreys, C. J.; Sutton, A. P. *Phys. Rev. B* **1998**, *57*, 1505–1509.

Chapter 3.3

Microfluidic Controlled Synthesis of a Spin Crossover Coordination Polymer Through a Pathway Selection Mechanism

In this Chapter, the synthesis by means of a microfluidic methodology of a coordination polymer with well-known spin crossover (SCO) property will be described. The microfluidic approach allowed the synthesis in a controlled interplay manner through the mass transport (diffusion of reagents). The system obtained in form of nanoparticles was compared with its bulk counterpart in order to compare its properties. This system will be used to discuss the role of microfluidics for the synthesis of coordination polymers (CPs) and the retention of the properties. As proof-of-concept, the obtained nanoparticles were embedded in a polymer with the objective of obtaining a composite film for potential applications in the field of sensors.

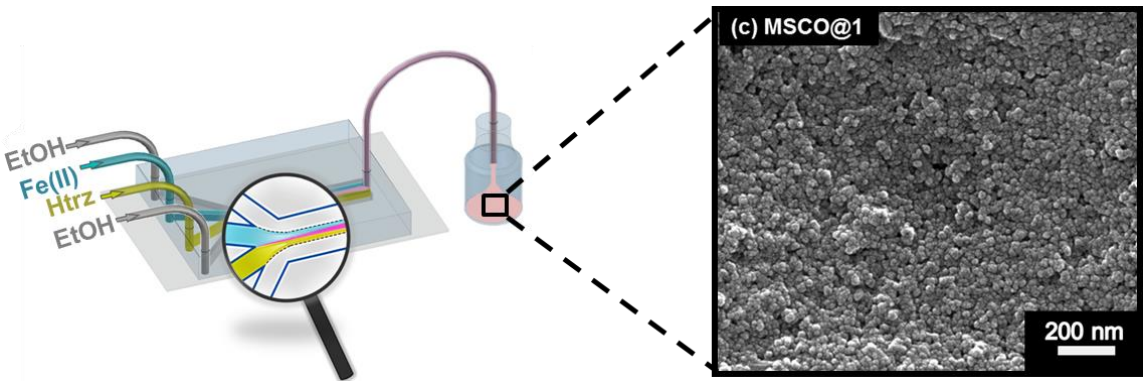

3.3.1 Introduction

As addressed in Chapter 3.2, there are emerging new strategies for the synthesis of CPs. One of these strategies, described in this Chapter, is focused on the use of microfluidic environment for the synthesis of CPs under the control of specific parameters. The work presented in this section was performed in collaboration with the research group of Dr Josep Puigmartí-Luis from the *Department of Chemistry and Applied Biosciences* at *Eidgenössische Technische Hochschule Zürich* (ETH Zürich, Switzerland). The group of Dr Josep Puigmartí-Luis has a wide experience in the use of the microfluidic approach for the synthesis of novel functional materials with different morphologies, sizes and chemical functionalities. In this work, we studied the role of reaction-diffusion (RD) conditions for the selection of specific pathways during the synthesis of a functional CP. Specifically; the microfluidic synthesis of the material was performed by the research group led by Dr Josep Puigmartí-Luis.

3.3.1.1 Microfluidic systems

The main interest of chemists is to have control over the synthesis and properties of the final product. In some way, coordination chemistry allows for control by selecting specific units (metal ions and organic ligands) that form the constituents of the material, which have a specific recognition and interaction. However, having control of the self-assembly of such constituent units into supramolecular architectures with well-defined morphologies and tuneable properties, is one of the challenges that must still be faced.

In this sense, the Nature is mainly based on self-assembly processes where the isolated components organize autonomously and spontaneously into ordered and/or functional structures (e.g. DNA). Its dynamic adaptability makes living systems the most efficient processes ever known. Natural structures are able to change their organization due to external stimuli by controlling the chemical species diffusion and rational supply of external energy inputs.[1] For this reason, a lot of efforts have been focused on the design and study of a bioinspired methodology applicable to the chemistry laboratory for the build of advanced materials. In this scenario, microfluidics takes a relevant role.[2] This methodology is classified as a bottom-up strategy for the synthesis of micro and nanostructures with specific properties and functionalities. Through the control of RD, it is possible to prepare structures with defined shapes, sizes and functions mimicking the processes occurred in the Nature. The use of microfluidics as bioinspired approach for the synthesis of novel functional materials is based on the self-assembly of the former constituents in a controlled environment, where the diffusion, concentration and interface interaction become relevant. For instance, in 2017, Lovrak *et al*. showed how RD control over two or more reactants can be tuned locally for the formation and

self-assembly of free-standing materials within a hydrogel matrix acting as a reaction substrate.[3] The mechanism involved in these technologies consists on the spatio-temporal control of reactant mixing during the self-assembly process. Such control allows even for the isolation and entrapment of intermediate structures that otherwise could not be retained in conventional synthesis processes. One of the main parameters than can be adjusted in a microfluidic device is the flow rate ratio (FRR). The FRR is defined as the ratio between the total flow rate of the sheath flows and the flow rate of the reagent flows, and determines the degree of hydrodynamic focusing.[4] Through the modification of FRR it is possible to achieve unprecedented structures with new and interesting functionalities not reachable in any other way than by means of the exquisite control of the diffusion process (Figure 3.54).

Currently, many efforts are being made in the scientific community to fully harness the aggregation pathway (pathway complexity) in non-covalent synthesis with the ultimate goal of featuring non-equilibrium states (e.g. kinetically trapped or metastable species). Out-of-equilibrium species are of particular interest for their fundamental and technological relevance. These resulting species are key players to gain new insights into nucleation and self-assembly processes as well as to unveil novel structure-property correlations that can give access to more sophisticated functions in man-engineered materials. However, the controlled synthesis of non-equilibrium states still remains a challenge and yet requires traditional approaches, including again the design of complex chemical structures.

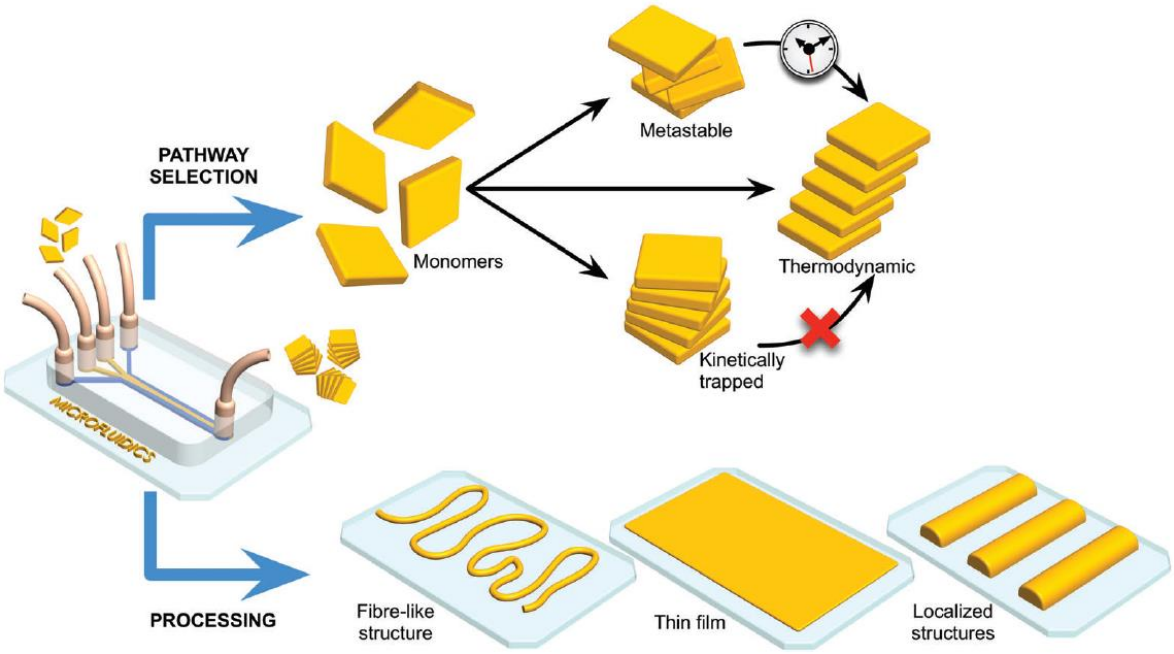

Figure 3.54 Microfluidic methodology lets selection between different pathways in self-assembly processes. The structures obtained from them, correspond to different assemblies and/or thermodynamic states in both thermodynamic equilibrium on non-equilibrium states. Furthermore, through microfluidic reaction, it is possible to have control over the processing of the self-assembled products on different substrates. Reproduced from ref. 2.

Several materials have been synthesized under microfluidic conditions. In the case of organic and inorganic systems, different attempts can be find in the literature. For example, Amstad *et al*. reported the production of amorphous nanoparticles by a microfluidic nebulator.[5] They were able to produce nanoparticles of inorganic and organic materials that usually have high tendency to crystallize (e.g. $CaCO_3$, NaCl or organic drugs). Through a supersonic flow, it was possible to produce droplets of ~100 nm, which its fast drying (faster than crystal nuclei formation), enables the formation of kinetically trapped amorphous states. The microfluidic approach has been used to isolate non-equilibrium states of CPs and shed light on their mechanisms of self-assembly. In 2016, Puigmartí-Luis and co-workers reported the synthesis of isolated kinetically trapped crystal states from a reaction mixing 4,4'-bypiridine and $Cu(NO_3)_2 \cdot 6H_2O$.[6] The authors showed how by controlling the RD conditions in a continuous-flow device, the isolation and study of out-of-equilibrium crystal structures are possible (Figure 3.55).

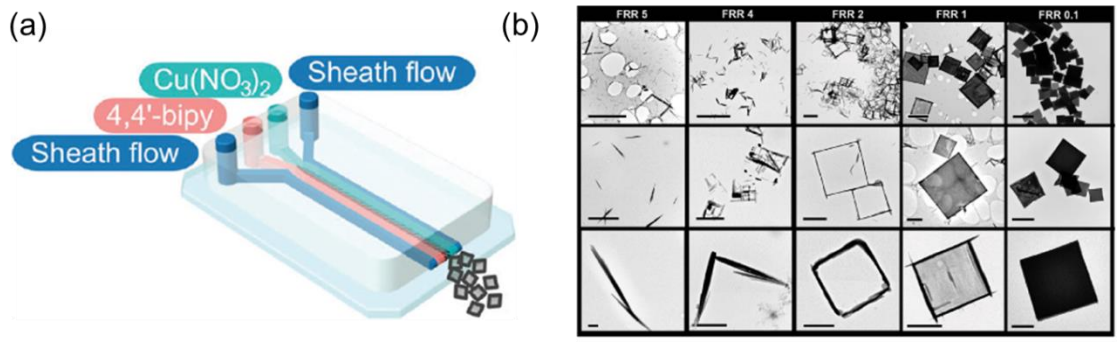

Figure 3.55 (a) Scheme of the microfluidic device used for the isolation of kinetically trapped crystals states. (b) TEM images of the CP synthesized with continuous-flow in a microfluidic device at different flow rate ratios (FRRs), respectively. Reproduced and adapted from ref. 2 and 6.

In the case of MOFs, liquid-liquid interfacial reactions have been used to control the self-assembly. In this sense, Ameloot *et al.* reported the synthesis of MOF layers by using a biphasic synthesis mixture comprising two immiscible solvents containing the precursors (Cu(II) ions and 1,3,5-benzenetricarboxylate ligands).[7] The crystallization took place at the liquid-liquid interface enabling the direct formation of the layers by a self-completing growth (Figure 3.56a). Other well-known MOFs such as HKUST-1, MOF-5, IRMOF-3 and UiO-66, have been synthesized by using microfluidic approach toward confined droplets.[8] This methodology let the formation of the porous structures in an ultrafast way by increasing the reaction kinetics due to the synthesis confinement. While conventional synthesis of the aforementioned MOF structures requires hours or days, with the microfluidic approach the same crystalline structures are obtained within a few minutes (Figure 3.56b).

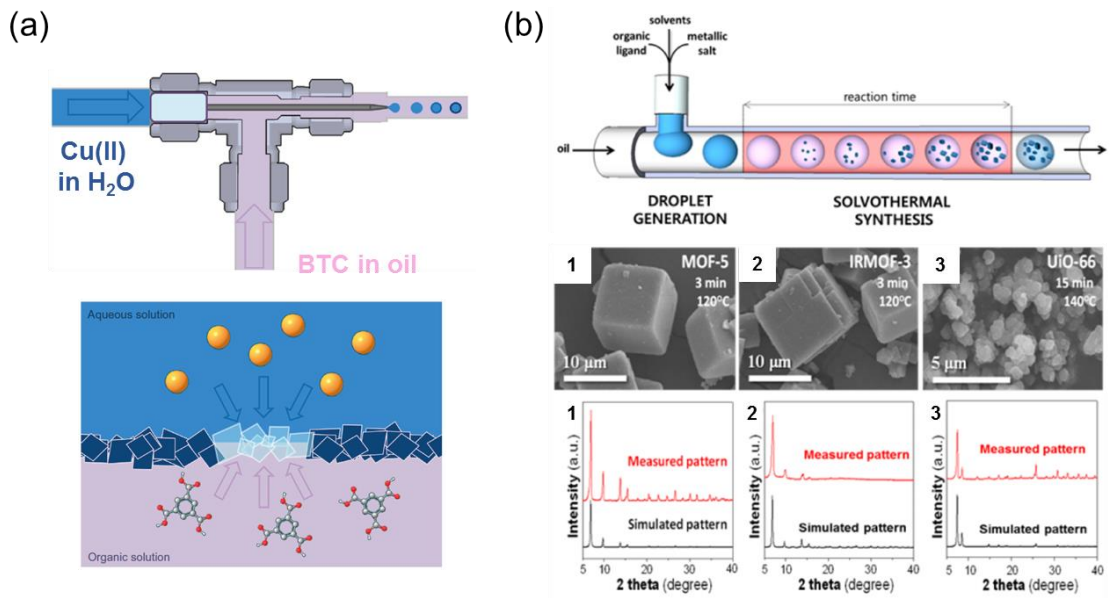

Figure 3.56 (a) TOP: Biphasic set up for the microfluidic approach. The oil phase contains the BTC ligand and the water phase contains Cu(II) ions. BOTTOM: The use of a biphasic synthesis mixture let the formation of the crystals on the defects remaining in the layer, resulting in a self-completing growth. (b) Microfluidic set up for the synthesis of (1) MOF-5, (2) IRMOF-3 and (3) UiO-66. Reproduced and adapted from ref. 7 and 8, respectively.

3.3.1.2 Present challenges

The main challenges in the field of SCO are focused on the obtaining of nanostructures that retain the ST even if it is disturbed after the process. As previously discussed, the micro and nanostructuration of materials with intrinsic SCO have been a focus of interest since many years ago. For this reason our main challenge consists on:

i. Formation of water-stable colloidal suspensions of nanoparticles with SCO behaviour through a new approach under out-of-equilibrium conditions.

For achieve our main goal, the microfluidic methodology was selected. The success of microfluidics is clearly demonstrated through recent studies. This kind of technology is able to rationally design, study and reveal different pathway mechanisms. The use of this approach has associated some difficulties and parameters that should be considered:

i. Monitor supramolecular interactions in real time
ii. Collection and isolation of the structures generated
iii. Properly characterization of the out coming material from the microfluidic device
iv. Precise control of different parameters (temperature, FRR, etc.)
v. Enhance the ability to adjust physical and chemical properties

3.3.1.3 Our choice

In this work, we studied a specific CP complex with well-known SCO based on Fe-tetrazole complex: $[Fe(Htrz)_2(trz)]_n(BF_4)_n$ (**2**), where Htrz stands for 1,2,4−triazole (**H-L2**) and trz for 1,2,4−triazolato (**L2**) (Figure 3.57). This CP has been studied as bulk SCO crystalline material for decades due to the robustness of its magnetic properties.[9,10] The chemical structure of complex (**2**) is shown in Figure 3.57. The reason to choose complex (**2**) for this investigation is twofold. One the one hand, the switchable electronic behaviour of SCO complexes exposed to different external stimuli is highly sensitive to structural modifications of the crystalline network,[11,12] which represents an excellent scenario to benchmark the impact of out-of-equilibrium species in their properties. On the other hand, as aforementioned, complex (**2**) is one of the most studied SCO complexes and an excellent candidate for functional devices derived from it.[13-16] The selection of this widely studied CP, will facilitate the comparison with the materials resulting from the microfluidic approach.

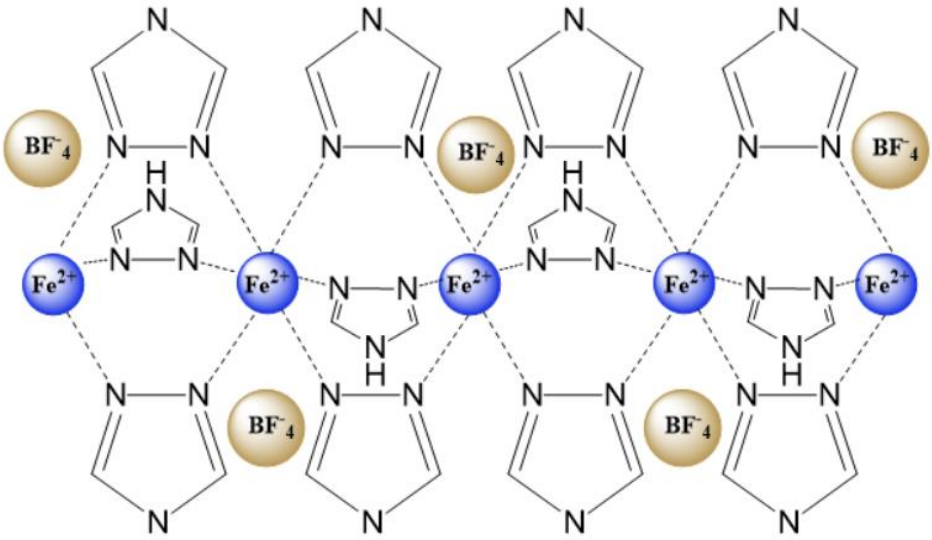

Figure 3.57 Chemical structure of complex (**2**).

There are some examples in the literature regarding the synthesis of nanoparticles of the complex (**2**). However, the methodologies used up to now are related with reverse micelle and surfactants-based approaches.[17,18] The use of stabilizers in these methodologies may affect to the SCO properties of the final product synthesized. For this reason, we hypothesize that the use of microfluidics could allow the controlled synthesis of nanoparticles of complex (**2**).

As previously reported, complex (**2**) has a ST upon heating. This ST was centred around 360 K going from LS to HS during the heating process, which is reversible after cooling to room temperature. All the previous studies already published will be our reference for the characterization of the microfluidic product.

3.3.1.4 Objectives

With the aim to overcome the challenges described in the previous section, different objectives were proposed derived from a main goal:

- Use of a microfluidic device for the synthesis of novel structure derived from $[Fe(Htrz)_2(trz)]_n(BF_4)_n$ (**2**) CP in liquid-liquid interface conditions for the study of the SCO property. The nanoparticles synthesized must show water-stable colloidal stability in water.

The steps followed for the achievement of the main goal were the following:

i. Synthesis of complex (**2**) using a liquid-liquid interphase microfluidic device
ii. Study of the role of the FRR
iii. Complete physicochemical characterization of the resulting materials
iv. Comparison of the SCO property with its bulk counterpart
v. Study of the addition of defects by the BF_4^- counter anion

In this work, we show that while bulk synthesis of complex (**2**) constantly yields a crystalline thermodynamic product that exhibits a single abrupt ST, its microfluidic synthesis leads to a non-equilibrium state that displays a radically different transition from the LS to the HS state.

3.3.2 Results and discussion

3.3.2.1 Synthesis of microfluidic Fe-triazole based CP

The synthesis of complex (**2**) was carried out by the research group of Dr Josep Puigmartí-Luis. The resulting microfluidic product (thereof **MSCO** complexes) with the SCO as functional property, was synthesized as schematized in Figure 3.58. The device consisted on a four-inlet system. In the two middle channels, two ethanol solutions of $Fe(BF_4)_2 \cdot 6H_2O$ (1 M) and Htrz (3 M), respectively, were injected. The flow rate used for their injection was set at 50 µL/min. Additionally, pure EtOH solutions were injected in the two side channels at variable FRR. Specifically, two limit FRR were selected: the lowest one corresponded to a FRR of 2 and with flow rates of 100 µL/min (sample **MSCO@1**) and the highest one corresponding to a FRR of 8 and a flow rates of 400 µL/min (sample **MSCO@2**). The set up selected induced the reaction of the metal ions with the ligand in the liquid-liquid interface where the gradient and concentration is optimum. This occurs in the RD area, where if the parameters are properly controlled, the expected functional materials should be obtained (Figure 3.58b).

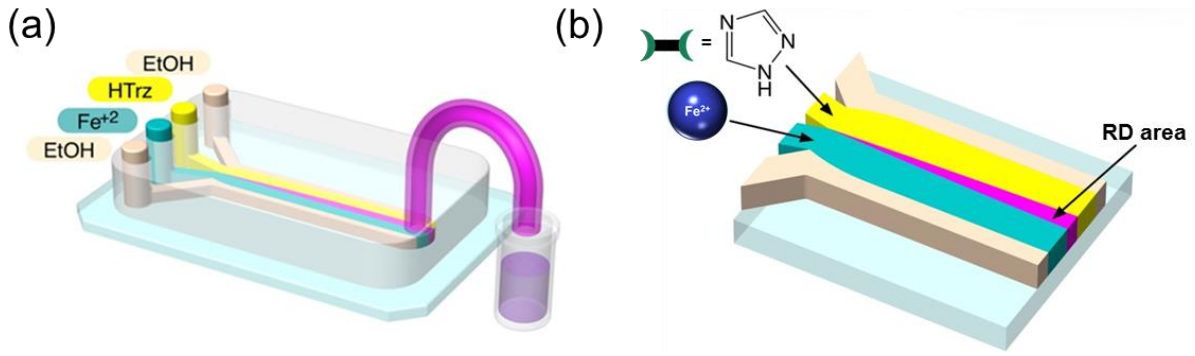

Figure 3.58 (a) Scheme of the microfluidic device used for the synthesis of **MSCO** samples. The two channels in the middle were used for the addition of two ethanolic solutions containing the iron salt (Fe(II)) and the triazole ligand (**H-L2**, HTrz). The other two channels located on both sides of the device were used for the addition of pure ethanol solutions. After the reaction between the components was done, the resulting material was collected from the outlet located at the end of the device. (b) Formation of the reaction-diffusion (RD) area where the components react with each other forming the final product.

This type of configuration induces the slow mixing of the components, which only can interact between them through molecular diffusion. Under this condition, it is possible to establish controlled RD diffusion areas where the constituents are confined in specific conditions avoiding chaotic advection by controlling the spatio-temporal environment (Figure 3.59). The controlled RD inside the microfluidic channel allow specific concentration gradients which stablish an effective RD area mimicking the ones present in Nature.[19]

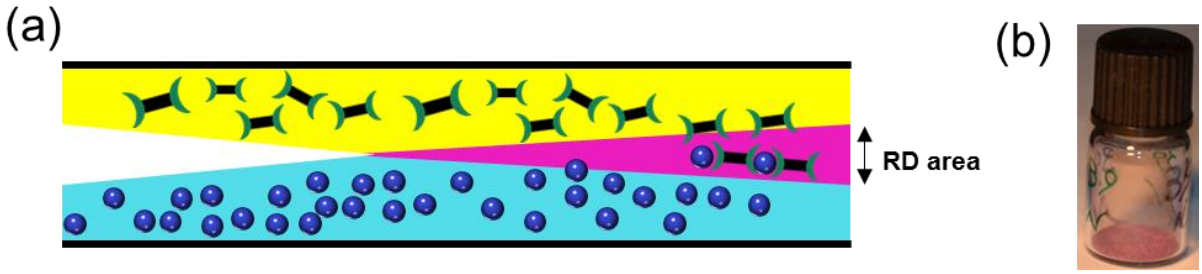

Figure 3.59 (a) Scheme of the continuous flow created in the microfluidic device used for the synthesis of **MSCO** samples. The yellow and blue colours indicate the ethanolic solutions of Fe(II) ions and tetrazole ligands, respectively. The white color belongs to pure solvent area and the RD area is represented in purple. (b) Purple powder obtained after the microfluidic reaction.

Once the microfluidic reaction was finished, the **MSCO@1** and **MSCO@2** samples were diluted in pure EtOH and subsequently centrifuged yielding milligrams of a purple powder (Figure 3.59b). This process was done in order to avoid undesired post-synthetic reactions upon elution from the chip. It is worth to mention that the time used for the reaction in the microfluidic device, from the injection of the reagents until the obtaining of the final product, was of 25.0 and 8.33 ms for the **MSCO@1** and **MSCO@2** samples, respectively. These results indicated the fast synthetic route through microfluidic approach.

3.3.2.2 Characterization

3.3.2.2.1 Morphology and size

Once the samples were completely dried, they were redispersed in EtOH and drop-casted for its imaging by TEM and SEM. As shown in Figure 3.60, the microfluidic synthesis of complex (**2**) yielded nanoparticles with similar sizes for both **MSCO@1** and **MSCO@2** with diameters of 26 ± 9 and 19 ± 7 nm respectively. These synthesized nanoparticles had spherical shape with good homogenous morphology and monodispersity (Figure 3.60). The analysis of the images by using the Image J software, allowed obtaining a distribution of sizes of the nanoparticles. The size dispersion was centred around 20-30 nm without the presence of destructured or unreacted material or larger particles. This indicated in a preliminary way, that the microfluidic system used allows the formation of nanoparticles of complex (**2**) in a homogeneous and reproducible strategy.

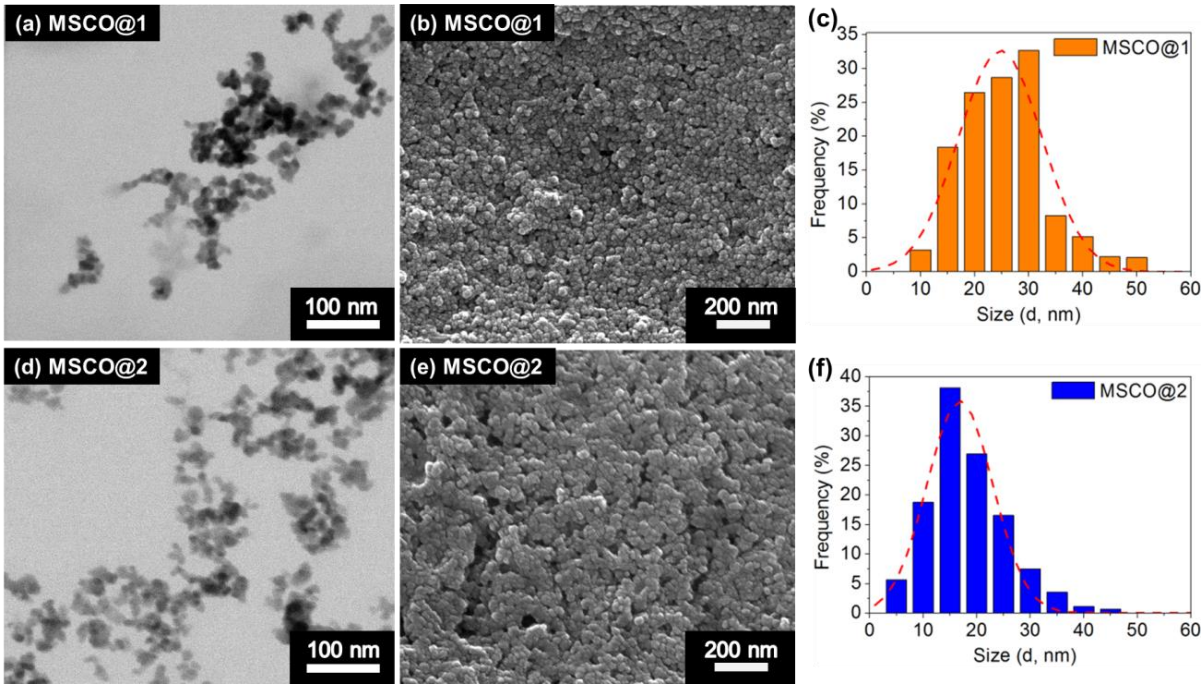

Figure 3.60 Morphological characterization of **MSCO** samples. TEM images of (a) **MSCO@1** and (d) **MSCO@2**; SEM images of (b) **MSCO@1** and (e) **MSCO@2**. The size histogram for each sample is shown in (c) **MSCO@1** and (f) **MSCO@2**.

To determine the stability, size distribution and surface charge (ζ-potential) in solution, the **MSCO@1** and **MSCO@2** systems were redispersed in EtOH and water for a DLS analysis (Figure 3.61). The hydrodynamic diameter obtained was 28.4 ± 3.2 and 22.3 ± 2.2 for **MSCO@1** and **MSCO@2** respectively. Furthermore, the colloidal stability of the dispersions was supported by the high positive surface charge (~ 30 mV) avoiding agglomeration and precipitation of the nanoparticles.

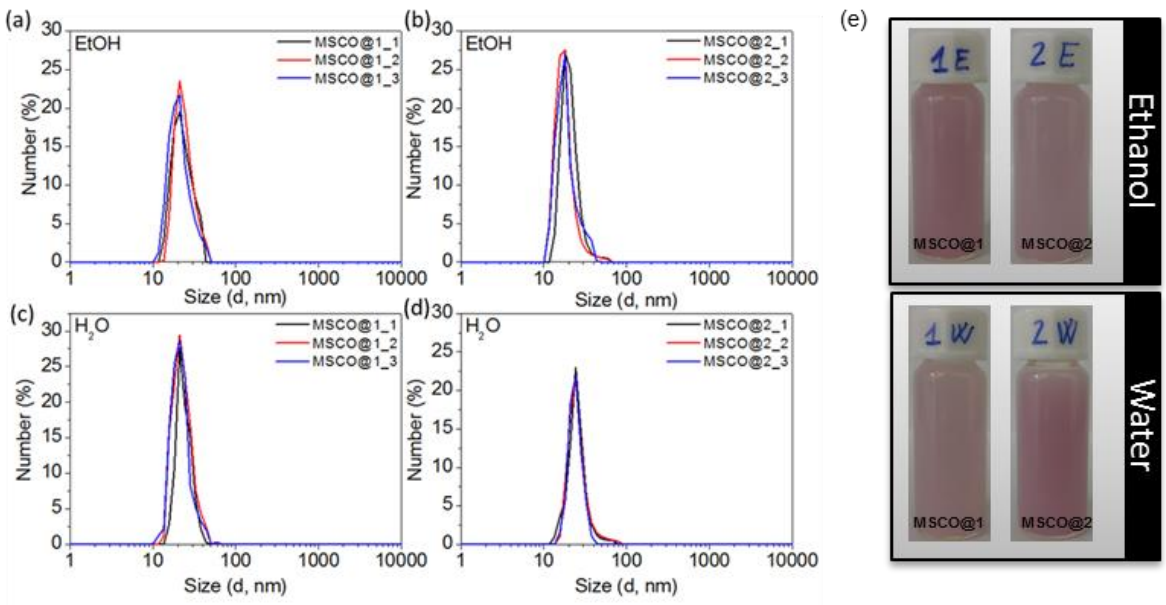

Figure 3.61 Size distributions for **MSCO@1** and **MSCO@2** in solution. The samples were redispersed in EtOH (a) **MSCO@1** and (b) **MSCO@2** and in H_2O (c) **MSCO@1** and (d) **MSCO@2**. (e) Colloidal dispersions of **MSCO** samples. All the measurements were done by triplicate.

The colloidal measurements revealed good polydispersity index (PDI) (PDI < 0.22) and dimensions comparable with those obtained by SEM and TEM measurements (Table 3.2).

Table 3.2 Comparison of size distribution (including standard deviation values) and ξ-potential for **MSCO@1** and **MSCO@2** in different medium.

SCO system	SEM/TEM (nm)	EtOH		H_2O	
		DLS (nm)	ξ-Pot. (mV)	DLS (nm)	ξ-Pot. (mV)
MSCO@1	26 ± 9	28.4 ± 3.2 PDI: 0.19	32.9 ± 1.9	30.2 ± 3.6 PDI: 0.21	33.2 ± 2.4
MSCO@2	19 ± 7	22.3 ± 2.2 PDI: 0.16	30.9 ± 2.1	29.4 ± 4.1 PDI: 0.17	31.7 ± 1.5

These results demonstrated the nano-sized and colloidal stability of the nanoparticles in water without the formation of precipitate, being stable for several weeks. These results suggested the potential use of this system as thermochromic probes. In following sections, they embedment of the microfluidic nanoparticles in PVA as a water-soluble polymer will be described.

3.3.2.2.2 Chemical characterization

Once the morphology and the size of the nanoparticles were determined, the microfluidic samples were chemically characterized by different means. Since the material has a temperature-dependent ST, some of the analyses were done at different temperature range to study the differences between the HS and LS states.

The FT-IR recorded spectra of **MSCO@1** and **MSCO@2** samples clearly indicated that both samples correspond to $[Fe(Htrz)_2(trz)]_n(BF_4)_n$, with representative stretching vibrational bands of protonated (**H-L2**) and deprotonated triazole (**L2**) ligands located at 1536 cm^{-1} and 1497 cm^{-1}, respectively (Figure 3.62 dashed lines). FT-IR spectra were also recorded at three different temperatures (300, 370 and 440 K) in order to corroborate the chemical stability of **MSCO@1** and **MSCO@2** along the heating and cooling processes. The results underscore the persistence of the main peaks although some small shifts and intensity variations were detected. The band corresponding to the stretching of the triazole ring (trz) is located at 1453 cm^{-1} in the LS state (298 K), and it was displaced to 1449 cm^{-1} in the HS state at 440 K.

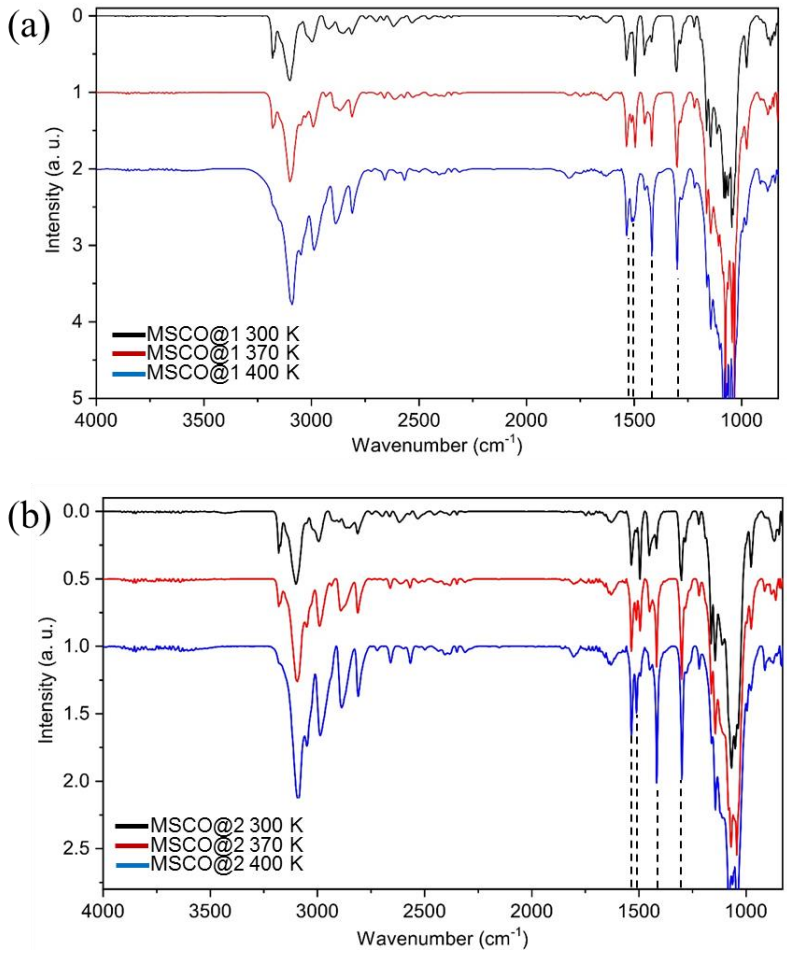

Figure 3.62 Chemical stability for **MSCO@1** and **MSCO@2.** Variable-temperature FT-IR spectra for (a**) MSCO@1** and (b) **MSCO@2** over the heating-cooling cycle (298-440 K). a.u.: Arbitrary units.

Furthermore, once the system was sufficiently cooled to reach the LS state, the spectra recorded were the same compared with the initial ones. This variation resulted in a hysteresis that was observed in different spectroscopies used for the characterization and is characteristic of the SCO materials. Once the spectra of both samples were compared, some differences in terms of relative intensity could be observed. These differences can be attributed to small changes in the composition of the samples synthesized at different FRR, *vide infra*. The influence of the FRR in the self-assembly process will be discussed in the following sections were the role of the counter anion seems to be an important key player for the final properties. Moreover, the absence of a broad band at 3600 cm^{-1} indicated that water was not present in **MSCO@1** nor **MSCO@2**, which was in agreement with previously reported crystallographic data of complex (**2**).[20] The lack of water within the structure was additionally confirmed by thermogravimetric analysis (TGA) (Figure 3.63). The results showed no significant weight loss upon heating until decomposition occurred at T > 450K.

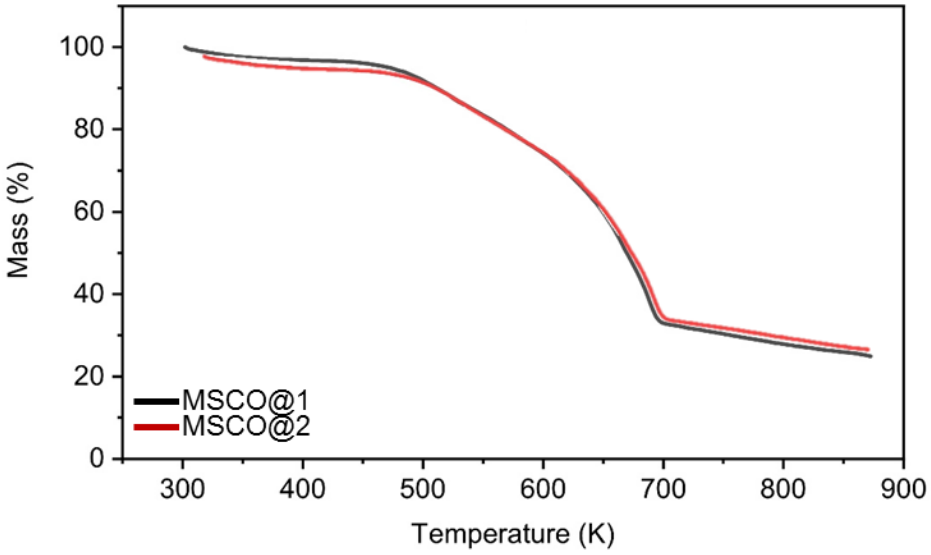

Figure 3.63 Thermogravimetric analysis (TGA) for microfluidic samples **MSCO@1** (black) and **MSCO@2** (red).

In order to determine the chemical environment of the synthesized materials, XPS was used to confirm the chemical bonding of both **MSCO@1** and **MSCO@2** samples. As expected, both spectra were in agreement with the C1s and N1s peaks appearing in very close positions (Figure 3.64).

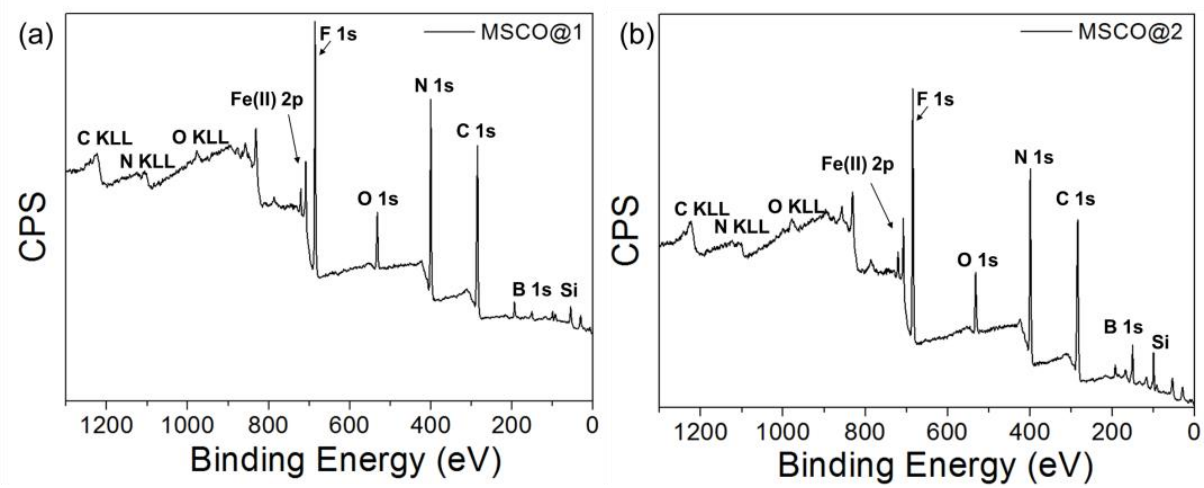

Figure 3.64 Full of X-ray photoelectron spectroscopy (XPS) spectra recorded at room temperature (298 K) of (a) **MSCO@1** and (b) **MSCO@2**. The peaks corresponding to Si 2p and O1s are due to the silicon substrates used for the deposition of the samples. CPS: Counts per second.

Furthermore, the presence of BF_4^- counter anion was confirmed by the appearance of the corresponding peaks for B and F at 195.2 eV and 686.0 eV, respectively. To study in detail the bonding environment of Fe(II) within the complexes deposited on SiO_2, high-resolution XPS curve-fitting was performed. Four different peaks for the C1s spectra of both **MSCO@1** and **MSCO@2** have been properly fitted, corresponding to their four different chemical environments within the Fe(II) complexes (Figure 3.65a,d). These peaks consisted on the presence of aliphatic C and C–H which appeared at 282.9 and 284.7 eV, respectively. Additionally, the contribution of the aromatic C–N and C=N was confirmed by the properly curve-peak fitting at 284.71 and 286.29 eV, respectively. Regarding the N1s spectra (Figure 3.65b,e), two peaks were fitted corresponding to the single (397.8 eV) and double (399.7 eV) bond between N and C and one additional for the FeN_6 chromophore. Finally, XPS measurements confirmed that the Fe(II) nodes retained their oxidation state after the microfluidic synthesis process (Figure 3.65c,f). As shown in Figure 3.65c,f, the peaks corresponding to $Fe2p_{3/2}$ and $Fe2p_{1/2}$ along with their characteristic satellites were present in both **MSCO@1** and **MSCO@2**, which is a typical fingerprint of Fe-triazole complexes with an octahedral coordination and spin switching behaviour.[21]

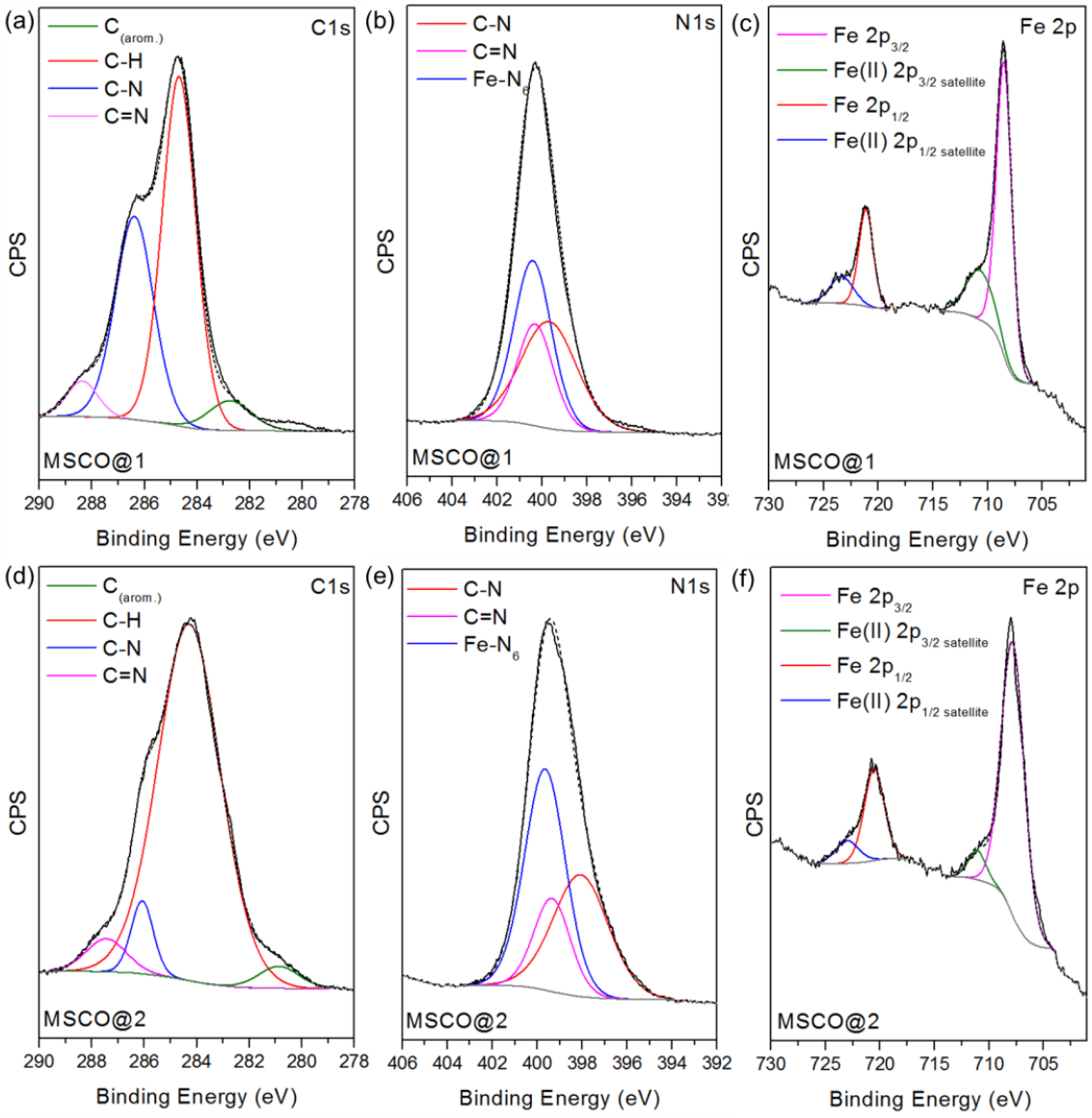

Figure 3.65 Curve-fitting results for C1s, N1s and Fe 2p high-resolution XPS spectra for **MSCO@1** (top) and **MSCO@2** (bottom) and the corresponding deconvolution. CPS: Counts per second.

Additional Elemental energy dispersive X-ray (EDX) measurements confirmed the presence of counter anions due to the appearance of a peak corresponding to the F (Kα = 0.68 keV). Additionally, the presence of C (Kα = 0.28 keV), N (Kα = 0.39 keV) and Fe (Kα = 6.39 keV) were detected, thus confirming the formation of the SCO complex (Figure 3.66).

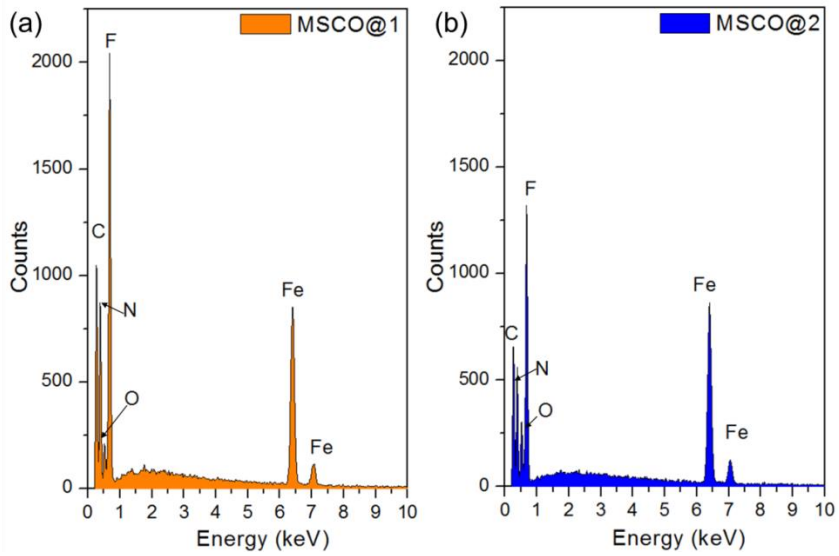

Figure 3.66 Elemental energy dispersive X-ray **(**EDX) composition for (a) **MSCO@1** and (b) **MSCO@2**.

In order to study in deep the composition of the microfluidic samples, the chemical compositional formula of **MSCO@1** and **MSCO@2** was experimentally determined by combination of Inductively-coupled plasma-mass spectroscopy (ICP-MS) and elemental analysis. In Table 3.3, the results obtained for the analysis of %CNH and %Fe together with the adjustment compared with the expected theoretical values, are shown. Additionally, the results are compared with the bulk crystal of complex (**2**) synthesized through conventional approach for comparison purposes (see Experimental section 3.3.5).

Table 3.3 Experimental values for elemental analysis taking into account the ICP-MS measurements.

System	Elemental Analysis (calculated*)				Error
	%C	%H	%N	%metal**	
(**2**)	20.80 (20.66)	2.38 (2.31)	36.03 (36.14)	16.00 (16.01)	0.19%
MSCO@1	19.06 (19.87)	2.56 (2.27)	35.21 (34.76)	15.67 (15.40)	0.97%
MSCO@2	19.70 (19.11)	2.24 (2.22)	33.07 (33.43)	15.24 (14.81)	0.69%

*The percentages in parenthesis are calculated values following the theoretical percentages and considering two constraints: complete coordination sphere and neutral charge; **the values where quantified from ICP-MS.

The results showed the high content of nitrogen due to the presence of the ligand in its unfolded and deprotonated form. Although the results appeared similar, certain differences can be observed

between the microfluidic samples and the bulk material. While the bulk material fits perfectly to its theoretical values, the **MSCO@1** and **MSCO@2** samples differ by a certain percentage. The values were properly adjusted to a chemical formula for each sample presented in Table 3.4.

Table 3.4 Chemical compositional formulas for each complex taking into account the values shown in Table 3.3.

System	Chemical Formula	Percentage
MSCO@1	Fe_1 **H-L2**$_{2.2}$**L2**$_{0.8}$ $(BF_4^-)_{1.2}$	41% H-**L2**, 15% **L2**, 15% Fe
MSCO@2	Fe_1 **H-L2**$_{2.3}$**L2**$_{0.7}$ $(BF_4^-)_{1.3}$	43% **H-L2**, 12% **L2**, 15% Fe
(2)	Fe_1 **H-L2**$_2$**L2**$_1$ $(BF_4^-)_1$	40% **H-L2**, 20% **L2**, 16% Fe

The data obtained for complex (**2**) confirmed, within the experimental error, the formation of the well-known polymeric complex with formula $[Fe(Htrz)_2(trz)]_n(BF4)_n$ (Figure 3.56), i.e. corresponding to the expected stoichiometry triazole/triazolato 2:1 (found: $[Fe(Htrz)_{2.002}(trz)_{0.998}](BF_4)_{1.002}$). On the other hand, and in sharp contrast, the data for both microfluidic **MSCO@1** and **MSCO@2** samples, clearly indicated the formation of a non-stoichiometric form of the Fe-triazole complex with a calculated ratio triazole/triazolato 2.2:0.8 (Table 3.4). These differences could be explained by the presence of an excess of neutral (non-deprotonated) triazole ligands (**H-L2**) which was compensated by extra BF_4^- counter anions, on average one out of every five iron centres along the polymeric chain. We point out that a SCO complex with formula $[Fe(Htrz)_3](BF_4)_2$, i.e. containing only neutral triazole ligands, has been previously prepared from the same precursors ($Fe(BF_4)_2 \cdot 6H_2O$ and Htrz) by using different bulk reaction conditions (e.g. modulating solvent composition and reactants concentrations).[9,22] Note that in our case, microfluidic samples (**MSCO**) and complex (**2**) were prepared under the same reaction conditions. The main difference was that in the former a control mass transport during the coordination reaction was established.[2] To the best of our knowledge, non-stoichiometric Fe-triazole complexes comprising protonation defects are not reported in the literature. This is because, with common bulk synthetic approaches, it is a challenge to harness the ratio of triazole/triazolato species incorporated in the structure.[23] In fact, under thermodynamic control only the favoured stoichiometry triazole/triazolato 2:1 is obtained,[24] and the engineering of protonation defects cannot thus be achieved. This will directly affect to the magnetic properties of the **MSCO** samples. As will be discussed in the next section, these defects have a relevant role in the ST of the resulting materials.

3.3.2.2.3 Study of the spin transition occurrence

3.3.2.2.3.1 UV-vis spectroscopy

The variable temperature behaviour of the fully characterized nanoparticles was investigated in form of pellets of **MSCO@1** and **MSCO@2** samples for UV-Vis for variable-temperature magnetic susceptibility. The ST between the LS and HS states was accompanied with a drastic and reversible thermochromism change going from purple at the LS to yellowish at the HS state (Figure 3.67). For this reason, it was possible to follow the ST of the SCO materials through absorption spectroscopy.

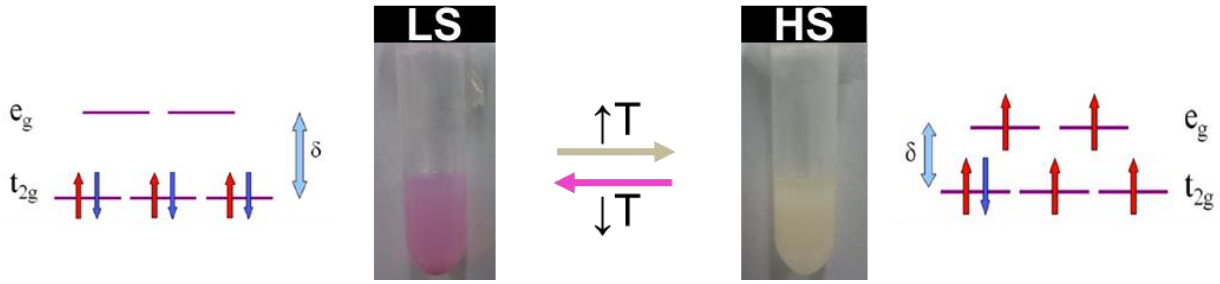

Figure 3.67 MSCO@1 nanoparticles redispersed in water at 298 K (LS, left) and 360 K (HS, right).

The UV-vis spectra of the samples were studied under a full thermal cycle heating from 298 to 440 K and then subsequently cooling back to 298 K. For **MSCO@1**, a band centred at λ = 587 nm was observed at 298 K giving the purple colour to the samples (Figure 3.68).

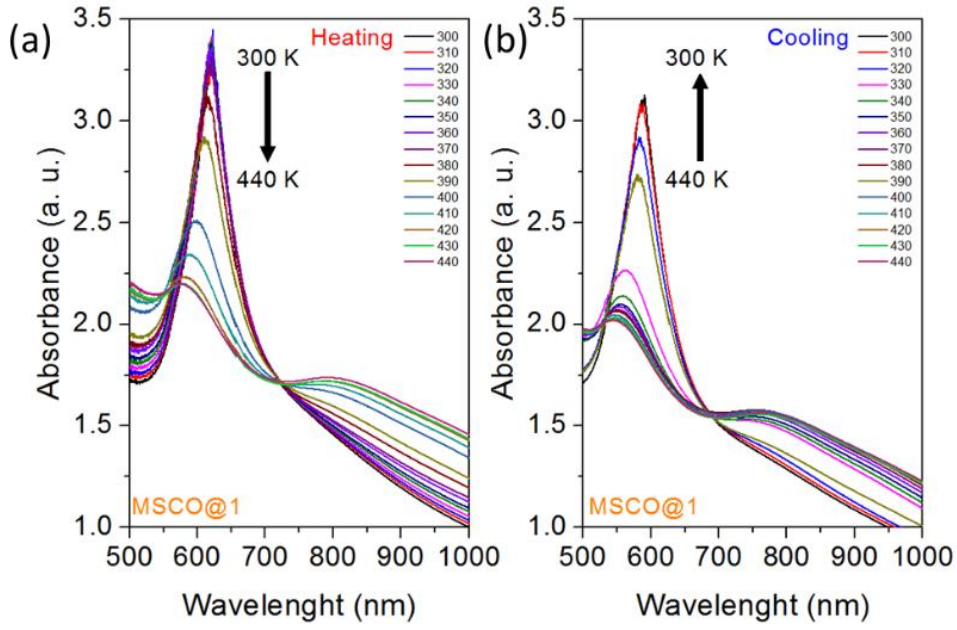

Figure 3.68 Optical properties for **MSCO@1**. Variable-temperature absorption spectra for (a) heating and (b) cooling cycles. Temperatures, in K, are indicated in the graphic. a.u.: Arbitrary units.

Upon increasing the temperature, the maximum in absorbance decreased and a progressive blue shift was observed, presumably due to enhanced light scattering. Additionally, an abrupt decrease of the absorbance was observed between 390-400K. This absorption band, characteristic of LS Fe(II), was attributed to the $^1A_1 \rightarrow {}^1T_1$ ligand field transition. A sufficient increase of temperature induced a decrease of this LS absorption band, while a HS band appeared concomitantly, increasing in intensity in the near-infrared region. The latter one can be attributed to the $^5T_2 \rightarrow {}^5E$ transition. Once the 400 K was reached, the sample was cooled down to room temperature. In this case, the increase of the band associated to the ligand field transition increased less gradually with an abrupt increase between 340-330 K. Although similar behaviour was found for **MSCO@2**, the main bands appeared shifted compared with the **MSCO@1** sample (Figure 3.69).

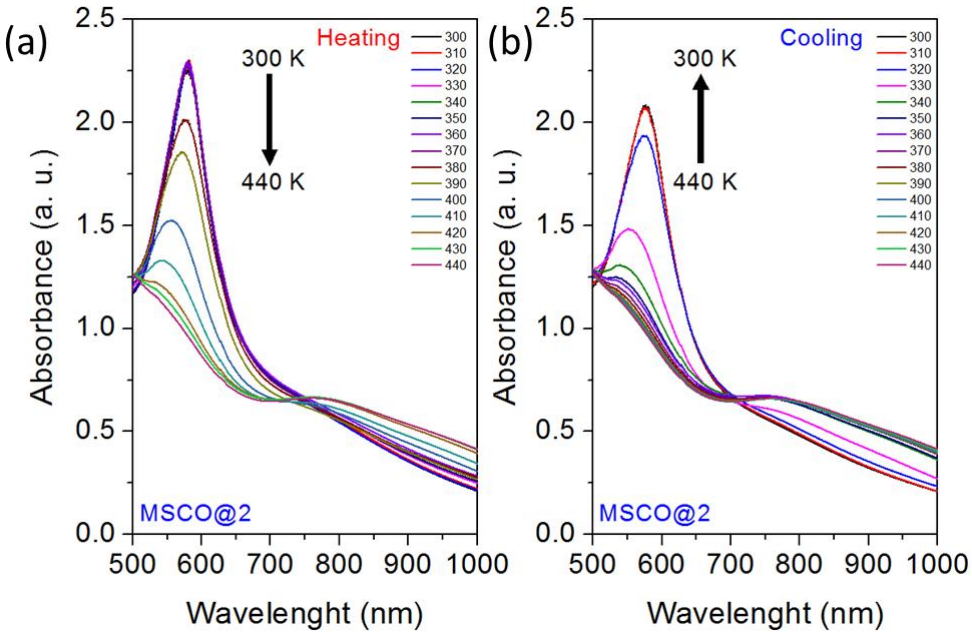

Figure 3.69 Optical properties for **MSCO@2**. Variable-temperature absorption spectra for (a) heating and (b) cooling cycles. Temperatures, in K, are indicated in the graphic. a.u.: Arbitrary units.

In the case of the band associated to the ligand-field transition, it appeared at 593 nm. The heating of the sample produce a gradual decrease of the band with an abrupt change in absorbance between 390-400K, and the cooling was less gradually with an abrupt increase of the absorbance between 330-320 K. These small differences between both samples may be attributed to the different composition especially due to the different content of counter anions that could affect to the ST of the materials. These results were in agreement with previous reported Fe-based tris/tetrazole CPs as we have seen in Chapter 3.2.

3.3.2.2.3.2 Magnetic measurements

In order to perform a deep study on the ST, variable-temperature magnetic susceptibility data for both samples (**MSCO@1** and **MSCO@2**) and bulk crystal of complex (**2**) were obtained and compared. These measurements were performed in collaboration with the *Magnetism and Functional Molecules* (GMMF) research group led by Dr. Guillem Aromí at *Univeristat de Barcelona* (UB, Barcelona, Spain).

The results revealed radically different ST behaviour. Figure 3.70 shows the $\chi_M T$ vs temperature curves (where χ_M is the molar magnetic susceptibility per Fe(II) centre) of the two complexes synthesized by the microfluidic approach and the bulk complex (**2**). The bulk crystals of complex (**2**) were prepared as previously reported and examined.[9] The bulk sample exhibited a strongly cooperative ST at 384 K (Tc↑, Tc is the SCO temperature where the slope changes) from the LS to the HS state, with a large hysteresis upon cooling (Tc↓ = 344 K, ΔT = 40 K) accordingly with that reported in literature.[25-27]

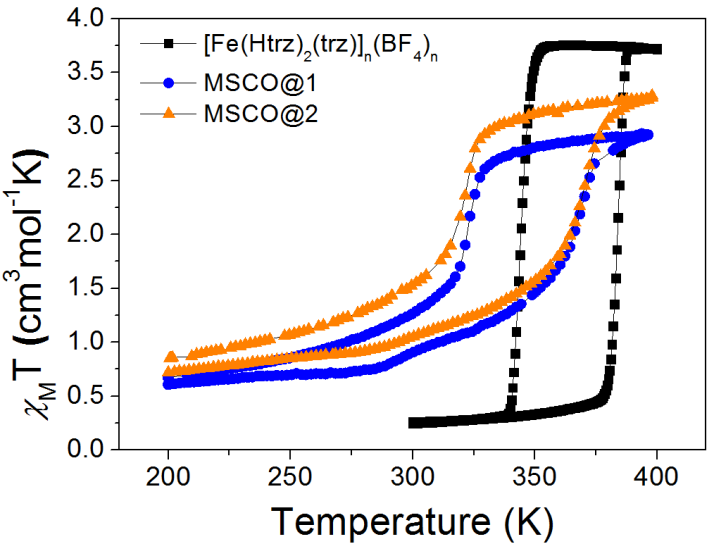

Figure 3.70 Thermal behaviour of the magnetic susceptibility recorded on bulk, **MSCO@1** and **MSCO@2** samples.

On the contrary, samples **MSCO@1** and **MSCO@2** exhibited a very different behaviour showing much less cooperative LS→HS transition. The SCO occurrence featured a more gradual change of $\chi_M T$ vs T at lower temperature and an abrupt change only around 369 K. In addition, and unexpectedly, the hysteresis width observed in the first thermal cycle (ΔT = 46 K) was dramatically reduced in the second (ΔT = 25 K) and third thermal cycles (ΔT = 18 K) for both **MSCO@1** and **MSCO@2**, while it remained practically unaltered for complex (**2**). For microfluidic samples, in both cases, spin transitions were observed and consistent with the absorption spectroscopy measurements where their LS phases retain approximately 20% of the Fe(II) ions in the HS state. Thus, the $\chi_M T$

product at 200 K was 0.61 and 0.71 cm^3 K mol^{-1} for **MSCO@1** and **MSCO@2**, respectively. This percentage of HS centres at low temperature is very common for the previously reported various forms of complex (**2**), especially as NPs, and is attributed to larger surface effect contributions, which presumably favour the HS state of the Fe(II) atoms.[27]

Contrary to what has been previously observed for any of the bulk synthesis of complex (**2**), the polymers obtained by microfluidic synthesis experienced a more gradual SCO at lower temperatures that only becomes abrupt well above room temperature (with identifiable Tc↑ values of ≈ 368 and 371 K, for **MSCO@1** and **MSCO@2**, respectively) (Figure 3.70). The part of the transition which was due to cooperative effects similarly exhibited a wide hysteresis with ΔT of 45 and 50 K and Tc↓ of 323 and 321 K, for **MSCO@1** and **MSCO@2**, respectively. These two distinctly disparate regimes observed in the magnetic curves of **MSCO@1** and **MSCO@2** samples underscore the non-homogeneous nature of the structure generated under RD conditions (kinetic control). Interestingly, both **MSCO@1** and **MSCO@2** behave very similarly but with some differences influenced by the different counter anion doping of the samples.

The **MSCO** samples were measured for more cycles (Figure 3.71). A distinct and unprecedented feature of the hysteresis shown by **MSCO@1** and **MSCO@2** was that a second and third thermal cycle leaded to a dramatic reduction of the hysteresis width: ΔT = 23 and 19 K on the second cycle and ΔT = 17 and 13 K on the third cycle, for **MSCO@1** and **MSCO@2**, respectively. This narrowing was mainly caused by reductions of the SCO temperature of the warming branch (from Tc↑ of 368 K to 339 K for **MSCO@1** and from Tc↑ of 371 K to 319 K for **MSCO@2**).

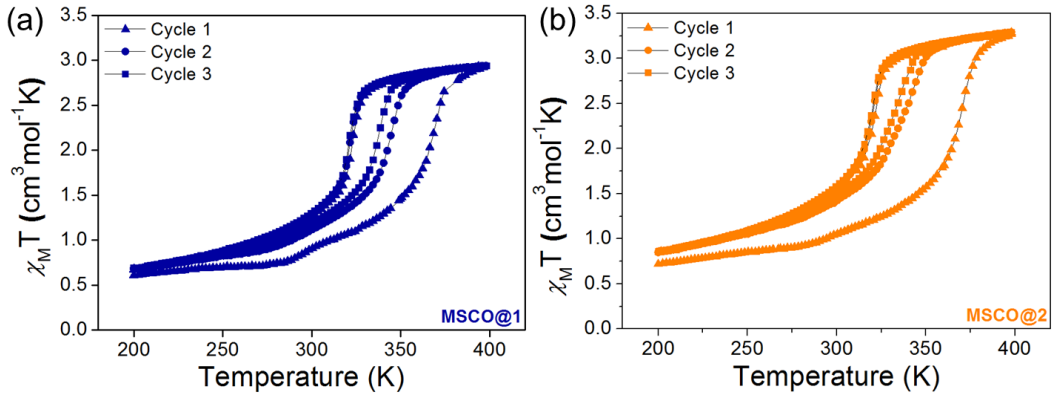

Figure 3.71 Magnetic data recorded over several cycles on (a) **MSCO@1**and (b) **MSCO@2**.

The change of regime observed after the first thermal cycle cannot be attributed to any solvent desorption caused by a temperature increase, since all the experimental evidence, especially those corresponding to FT-IR and TGA (Figures 3.61 and 3.62, respectively) for both microfluidic samples,

indicated that both **MSCO@1** and **MSCO@2** were solvent free. Table 3.5 summarizes the transition temperatures for **MSCO@1**, **MSCO@2** and complex (**2**).

Table 3.5 Transition temperatures of SCO complexes obtained from magnetic measurements for consecutive cycles.

	Magnetic Measurements			
	Cycle	**$T_c\uparrow$ (K)**	**$T_c\downarrow$ (K)**	**ΔT (K)**
(**2**)	1	384	344	40
MSCO@1	1	369	323	46
	2	345	320	25
	3	338	320	18
MSCO@2	1	370	323	47
	2	343	320	23
	3	343	320	16

The differences in the magnetic susceptibility versus temperature curves observed between the microfluidic samples and the complex (**2**) cannot be merely ascribed to the different size/morphology of the respective crystals, which is in agreement with the scarce effect of downsizing complex (**2**) crystals on its magnetic properties extensively reported in the literature.[28] As we have seen with the previous results from chemical analysis, IR and TGA indicated that the narrowing of the hysteresis loop for the obtained microfluidic nanoparticles with successive thermal cycles can be attributed neither to desolvation[Error! Bookmark not defined.] nor to chemical decomposition. Instead, it has to be ascribed to an annealing process of the supramolecular structure of **MSCO@1** and **MSCO@2**. In other words, the synthesis under controlled RD conditions (microfluidic pathway) yields to a metastable non-equilibrium state of a non-stoichiometric complex (**2**) (as previously observed form elemental analysis) characterised by a less abrupt ST. Upon thermal annealing the metastable state of **MSCO@1** and **MSCO@2** equilibrated to a thermodynamic one that featured a much narrower hysteresis and a significantly lower Tc↑. These differences observed on the magnetic properties after comparison of bulk complex (**2**) and microfluidic samples (**MSCO**) can be explained by the different stoichiometric obtained for each samples. As we have seen before, the compositional formulas of **MSCO@1** and **MSCO@2** were different especially for the **H-L2** and **L2** ratio. Therefore, we believe that the presence of such protonation defects is at the basis of the different magnetic properties displayed by **MSCO@1** and **MSCO@2** when compared to complex (**2**). In fact, the SCO phenomenon and degree of cooperativity of the ST is strongly dependent on the crystalline structure and intermolecular non-covalent interaction between the 1D coordination chains, which in turn are bound to be strongly affected by the presence of additional BF_4^- counter anions between them. This could be related to the inclusion of counter anions in the synthesized system by microfluidics, opening the door to defect engineering for the inclusion of modifications in a controlled manner.

3.3.2.2.3.3 Crystallographic measurements and characterization

To get more insights into this annealing process, the crystallinity character of the microfluidic samples was studied by small-angle X-ray scattering (SAXS) and wide-angle X-ray scattering (WAXS). These measurements were done in collaboration with Dr Ramon Pons from the *Institut de Química Avançada de Catalunya* (IQAC-CSIC).

The experiments were performed only for the **MSCO@1** sample. In Figure 3.72a, the SAXS profiles at room temperature of the as prepared microfluidic system, i.e. the metastable state of **MSCO@1** before the annealing and the one corresponding to the annealed product obtained after two heating/cooling cycles (i.e. LS →HS →LS loops) are shown. A significant decrease of the absolute scattering intensity and change of the SAXS profile at low values of the scattering vector ($q < 1$) were observed upon annealing. The SAXS data could be fitted to a polydisperse (Schultz-distribution)[29] compact sphere model giving an average diameter of 23.4 ± 2 nm (with PDI = 0.44) for the metastable state of **MSCO@1**, and of 66 ± 5 nm (with PDI = 0.2) for the annealed one, indicating that the annealing promoted a growth/coalescence of **MSCO@1** nanoparticles (Figure 3.73). Both the increase in size and global intensity reduction in the SAXS profiles were in agreement with the reduction of particle surface.

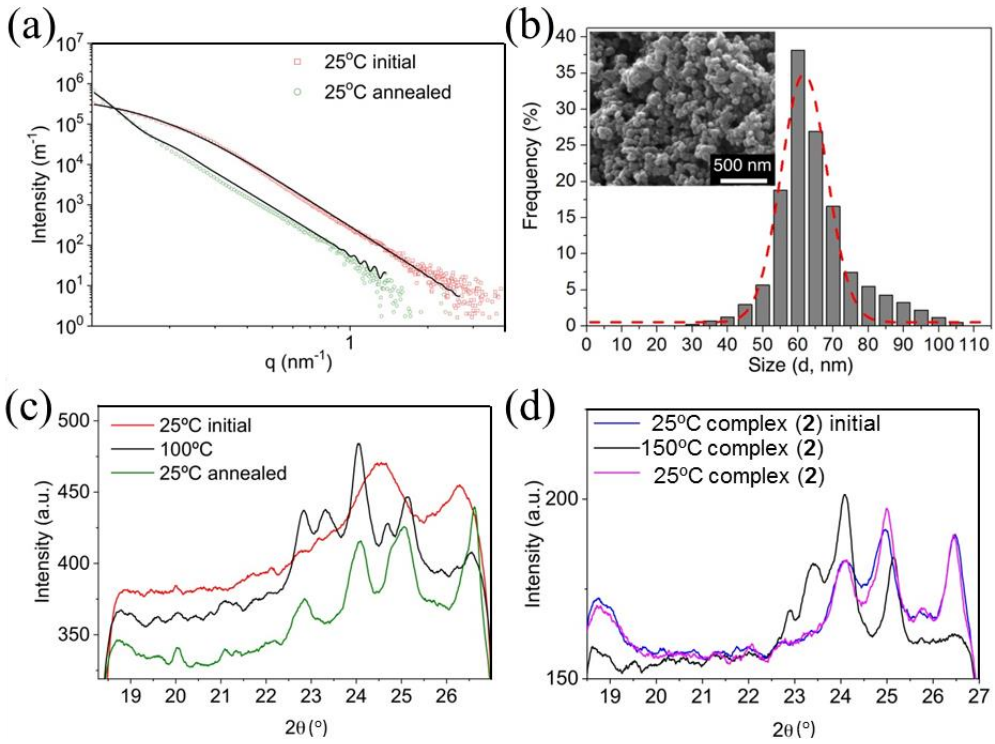

Figure 3.72 (a) SAXS profiles at room temperature (LS state) for the as prepared (metastable, red) and annealed (after two thermal cycles, green) **MSCO@1**. The solid line represents the fit to a polydisperse rigid sphere model. (b) Size distribution histogram of **MSCO@1** after annealing. Inset is showing the SEM image of annealed **MSCO@1**. (c) WAXS profiles of the metastable and annealed forms of **MSCO@1** in the LS state (red and green, respectively) and of **MSCO@1** in the HS state (black). (d) WAXS profiles of initial and cooled complex (**2**) in the LS state (blue and magenta, respectively) and of complex (**2**) in the HS state (black).

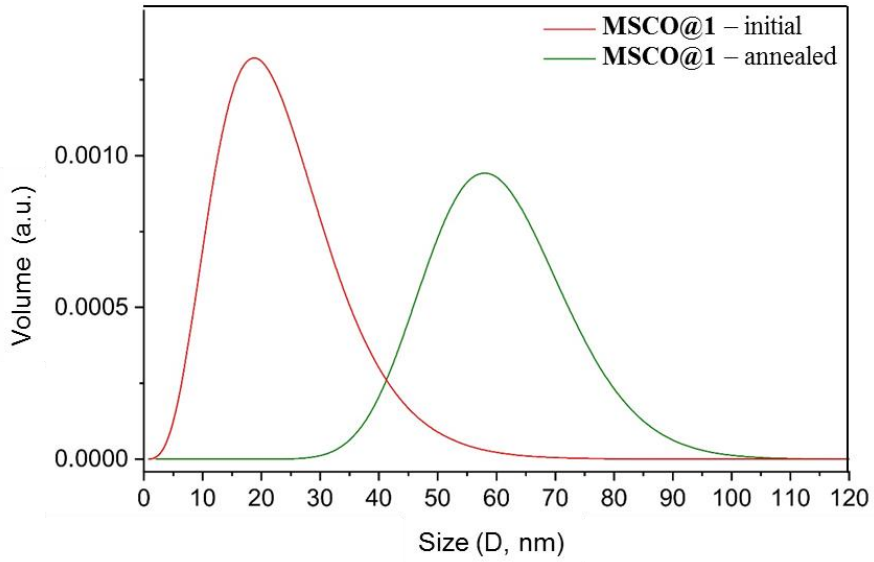

Figure 3.73 Graph showing the average diameter of **MSCO@1** before and after two annealing cycles (red and green curves, respectively). The compact sphere model used to fit the SAXS profiles indicated that the metastable state of **MSCO@1** was composed of particles with an average diameter of 23.4 ± 2 nm (PDI = 0.44), whereas the thermodynamic **MSCO@1** (after annealing) comprised particles with an average diameter of 66 ± 5 nm (with PDI = 0.2). In the former, the value corresponds to the half-maximum width from 10 to 30 nm weighing in mass, and in the latter, to the half-maximum width from 45 to 75 nm weighing in mass).

Moreover, the sizes measured by SEM for the metastable state of **MSCO@1** (Figure 3.60b) and the thermodynamic **MSCO@1** complex (after annealing) (Figure 3.72b) were consistent with the obtained SAXS data. While we cannot exclude, a priori, a small influence of the increase of particle size to the change of the magnetic behaviour upon annealing, we believe that this was not the main contribution.

The WAXS spectrum at room temperature (i.e. in the LS state) of the as prepared **MSCO@1** powder displayed weak and broad scattering peaks at 24.5° an 26.2° as expected for a crystalline material with nanometre-sized domains (Figure 3.72c).[30] When the **MSCO@1** powder was heated up to the HS state, a significant change of the WAXS profile was observed with the appearance of sharper and well-defined new peaks in the region between 22° and 25° and substantial disappearance of the broad feature at 24.5°. More importantly, after annealing (two LS → HS → LS loops), the WAXS spectrum in the LS state of the thermodynamic **MSCO@1** complex was strikingly different from that of the metastable form, displaying sharp features at 22.9°, 24°, 25°and 26.6°. This behaviour clearly indicated that **MSCO@1** undergone a structural rearrangement upon annealing. In marked contrast, the WAXS spectrum in the LS state of as prepared complex (**2**) was perfectly overlapped to that recorded at room temperature after performing LS → HS → LS thermal cycles (Figure 3.72d), thus indicating that the structural changes upon ST were completely reversible in the case of complex (**2**). We believe that the differences in the crystalline structure observed for the metastable and thermodynamic forms of **MSCO@1** aroused from the non-stoichiometric nature of this complex and

likely implied a rearrangement-redistribution of the charge defect along the polymeric chain associated with a rearrangement of the BF_4^- counter anions. The latter resulting in the modification of the hysteresis loop observed upon annealing.

Finally, the DSC measurements on complex (**2**) (Figure 3.74), **MSCO@1** and **MSCO@2** (Figure 3.75) showed an endothermic peak upon heating and an exothermic one upon cooling corresponding to the LS →HS and HS →LS spin transitions respectively. The transition temperatures extracted from DSC peaks were in good agreement with the magnetic measurements, with only small deviations due to the different temperature scanning rates used in both techniques (Table 3.6). Interestingly, the calorimetric peaks for microfluidic samples were broader than those for complex (**2**), which was in line with the less cooperative nature of its spin transitions. Finally, Table 3.6 summarizes the enthalpy and entropy variation (ΔH and ΔS) estimated from the DSC curves in the different heating cooling cycles. Overall, the enthalpy variations associated with all spin transitions were lower for microfluidic samples (**MSCO**) than for complex (**2**). In addition, the data showed that the ΔH associated to the first heating run of both **MSCO@1** and **MSCO@2** was bigger than that for the second one .This suggested that the first heating run did not only involve the LS → HS ST but possibly included also changes undergoing in the supramolecular structure of the complex, which was consistent with both the WAXS and magnetic data. In sharp contrast, the enthalpy and entropy differences between different heating runs for the bulk sample were negligible (Table 3.6).

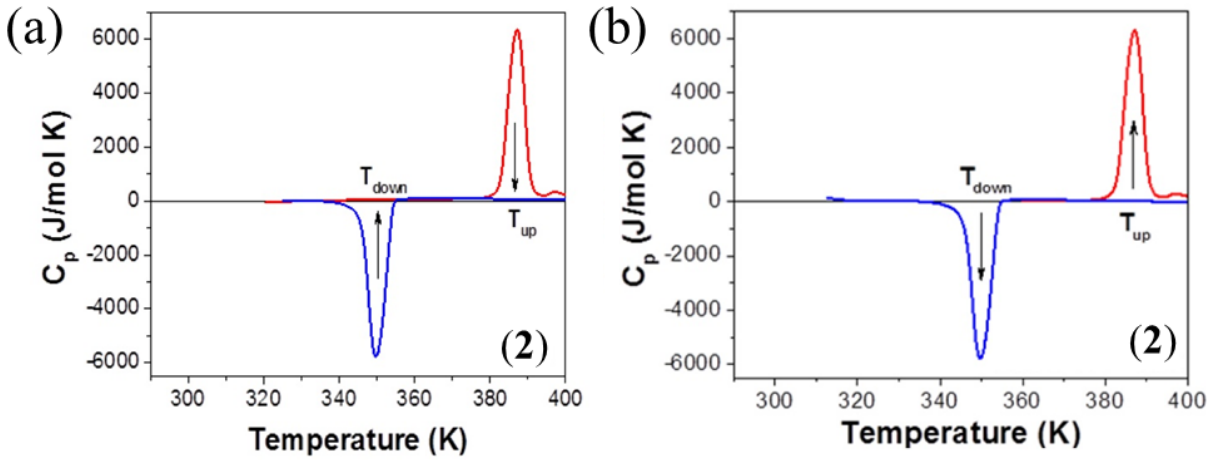

Figure 3.74 Thermal dependence of the heat capacity (C_p) recorded during the first (a) and second (b) thermal cycles for complex (**2**).

Table 3.6 Thermodynamic parameters extracted from the DSC data recorded on first and third thermal cycle respectively.

	$T_c\downarrow$ (K)	$T_c\uparrow$ (K)	$\Delta H\downarrow$ (J/mol)	$\Delta H\uparrow$ (J/mol)	$\Delta S\downarrow$ (J/mol K)	$\Delta S\uparrow$ (J/mol K)
1st Run						
(**2**)	350	387	31307	33508	89.4(4)	86.5(8)
MSCO@1	317	358	8816	14623	27.8(1)	40.8(5)
MSCO@2	322	361	6390	12650	19.8(4)	35.0(4)
2nd Run (After annealing)						
	$T_c\downarrow$ (K)	$T_c\uparrow$ (K)	$\Delta H\downarrow$ (J/mol)	$\Delta H\uparrow$ (J/mol)	$\Delta S\downarrow$ (J/mol K)	$\Delta S\uparrow$ (J/mol K)
(**2**)	350	387	31316	32897	89.4(7)	85.0(1)
MSCO@1	315	320	9615	11845	30.5(2)	37.0(2)
MSCO@2	320	324	4741	4077	14.8(1)	12.5(8)

T↓: switching temperature from HS to LS state; T↑: switching temperature from LS to HS state; ΔH↓: the enthalpy variation from HS to LS state; ΔH↑: the enthalpy variation from LS to HS state; ΔS↓: the entropy variation from HS to LS state; ΔS↑: the entropy variation from LS to HS state.

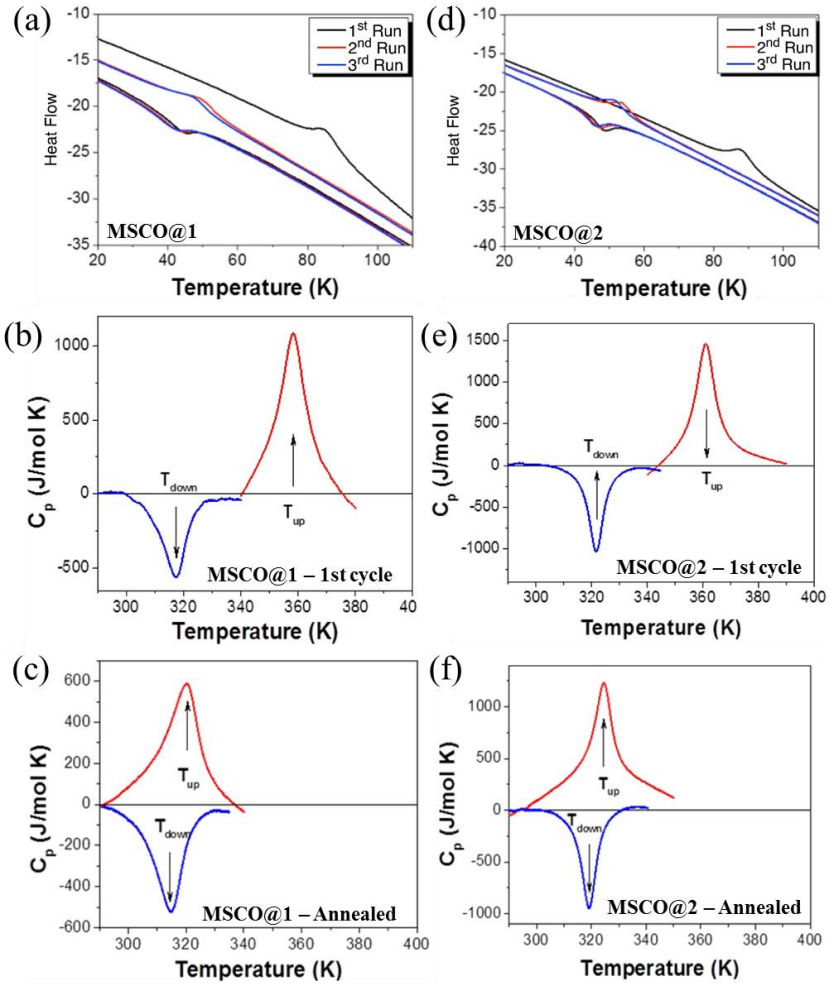

Figure 3.75 DSC curves recorded for (a) **MSCO@1** and (d) **MSCO@2** during consecutive thermal (heating-cooling) cycles. Thermal dependence of the heat capacity recorded during the first cycle for (b) **MSCO@1** and (e) **MSCO@2** and the second thermal cycle after annealing for (c) **MSCO@1** and (f) **MSCO@2**.

3.3.3 Application: Thermochromic films as a proof-of-concept device

Following the same strategy of previous Chapter 3.2.the MSCO nanoparticles were implemented in a polymeric matrix for the formation of a functional composite. The **MSCO** nanoparticles were integrated in a PVA network forming a free-standing hybrid film. The PVA polymer is widely used in industry for different applications such as paper adhesive, coatings, packaging and hydrogel membranes, among others.[31-34] The selection of this polymer was mainly based on its inherent characteristics such as:

i. Water-soluble polymer
ii. Excellent film forming features
iii. Adhesive properties
iv. Resistant to oil, grease and solvents
v. High tensile and flexibility properties
vi. Biodegradable

Briefly, the nanoparticles obtained from the synthesis by using the microfluidic system (**MSCO@1** and **MSCO@2**) were added to an aqueous solution containing solubilized PVA. The nanoparticles were properly dispersed by using ultrasounds for a few seconds. Once a colloidal dispersion was obtained, it was added by drop casting to a plastic Petri dish (Figure 3.76). After water evaporation at room temperature, the **PVA-MSCO** film was easily detached from the container. The film can be handled and cut into the desired morphologies and sizes if needed.

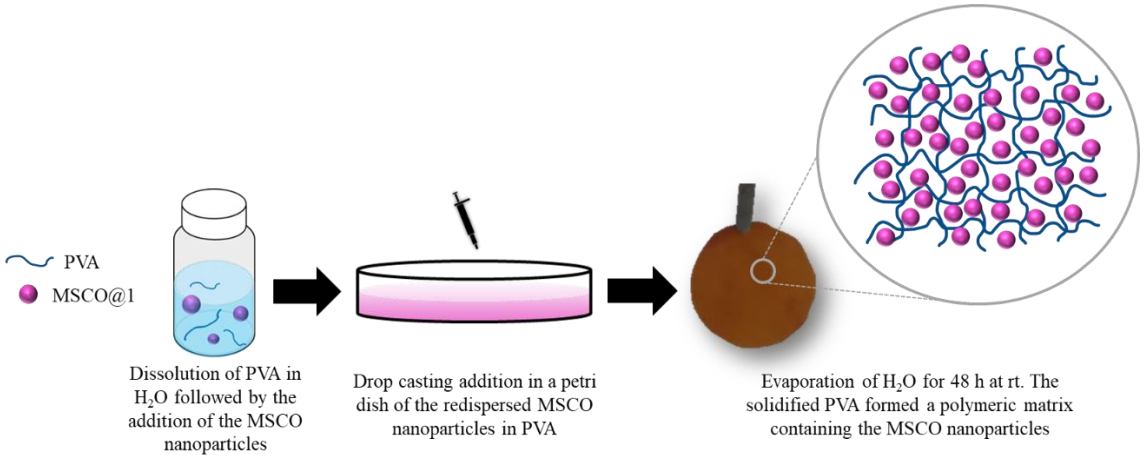

Figure 3.76 Schematic procedure followed for the formation of the **PVA-MSCO** hybrid film. The PVA was solubilized in water and the **MSCO** nanoparticles added. Once the colloidal dispersion was obtained, the suspension was added by drop casting to a plastic Petri dish. After 48 h, the **PVA-MSCO** film had enough consistency for its handling.

Once the film was removed, it was cut in small pieces for its observation by SEM (Figure 3.76 and 3.77). The formed **PVA-MSCO** film had an average thickness of 20-25 µm with homogeneous surface distribution of the material.

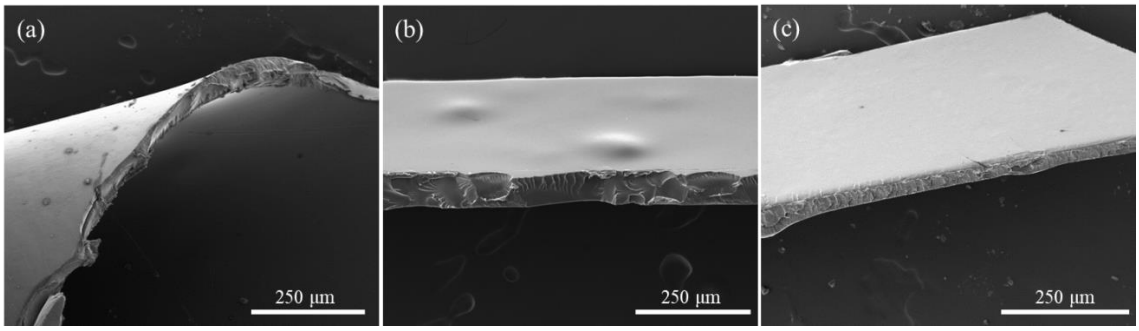

Figure 3.77 SEM images of the **PVA-MSCO** film. The thickness and surface were homogenous along the whole film.

Additionally, the cross-section SEM images, showed the successful integration of the **MSCO** nanoparticles through the network formed by the PVA polymer matrix (Figure 3.78). The **MSCO** nanoparticles retained its size and morphology after the **PVA-MSCO** film formation.

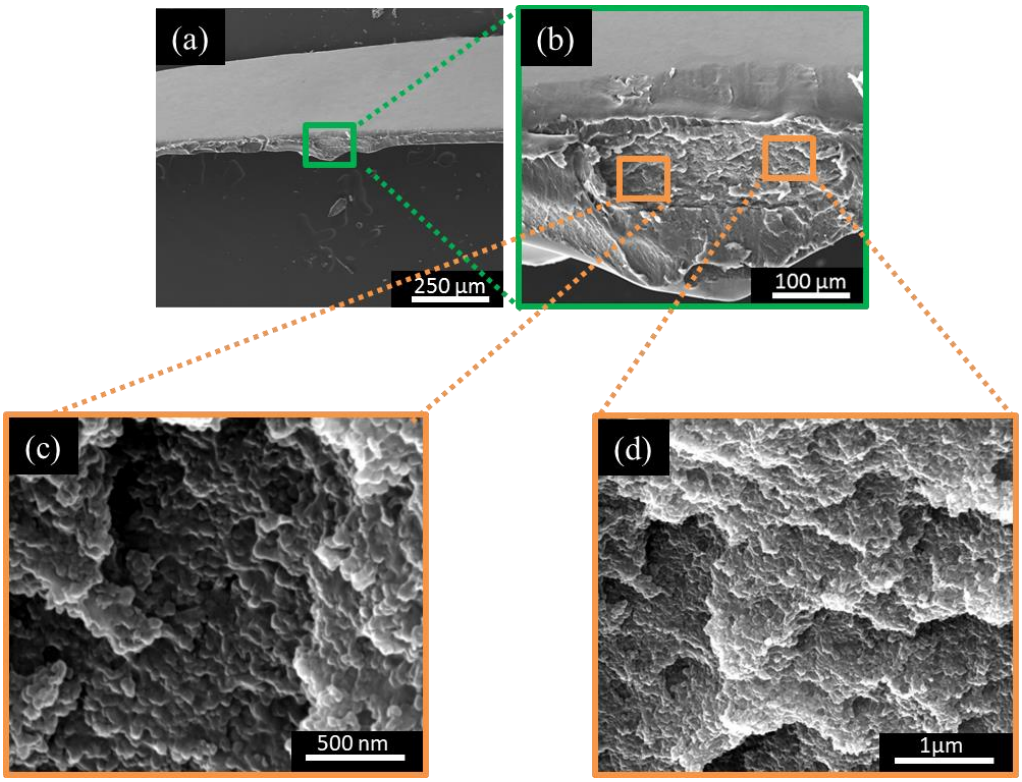

Figure 3.78 SEM images of the cross-section of the **PVA-MSCO** film. (a) Cross-section analysed for the particle size measurement. (b) Amplification of the area marked in panel a. (c d) The nanoparticles can be observed integrated in the PVA polymeric matrix by scanning the zones marked in the panel (b).

Finally, in order to check the chemical stability of the **MSCO** nanoparticles embedded in the PVA polymeric matrix, the ST occurrence was measured by UV-vis spectroscopy (Figure 3.79). The film was cut in small round pieces for its adjustment in the measuring holder.

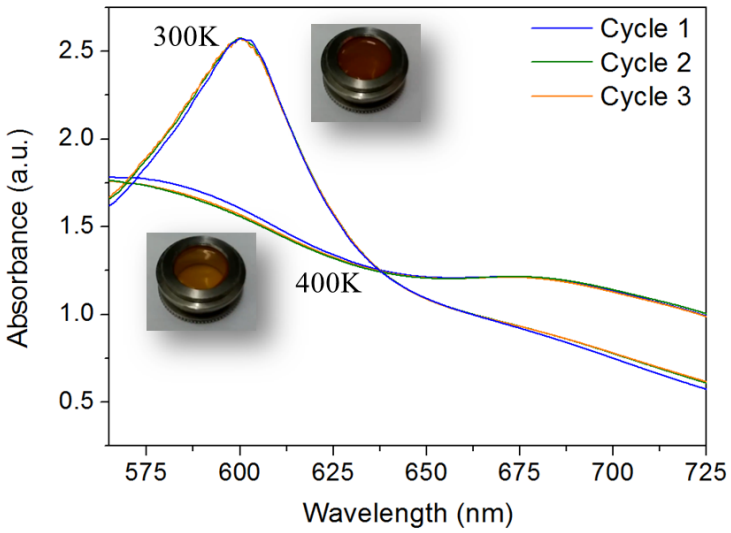

Figure 3.79 Optical properties for **PVA-MSCO** film. Variable-temperature absorption spectra for three complete heating-cooling cycles. The insets images showed the aspect of the film at 300 K (LS state) and 400 K (HS state) showing thermochromic behaviour.

The UV-vis spectra were recorded several times in a complete heating-cooling cycles within the range of 300-400 K. The results showed that the SCO occurrence was retained in the **MSCO** nanoparticles after their integration in the polymeric matrix. The ST was similar to the **MSCO** nanoparticles without the PVA support. The different cycles performed demonstrated the reversibility and robustness of the films (Figure 3.80). Once the film was completely heated up to 400 K, the **PVA-MSCO** thin films became translucid which recovered its initial aspect through the cooling of the film.

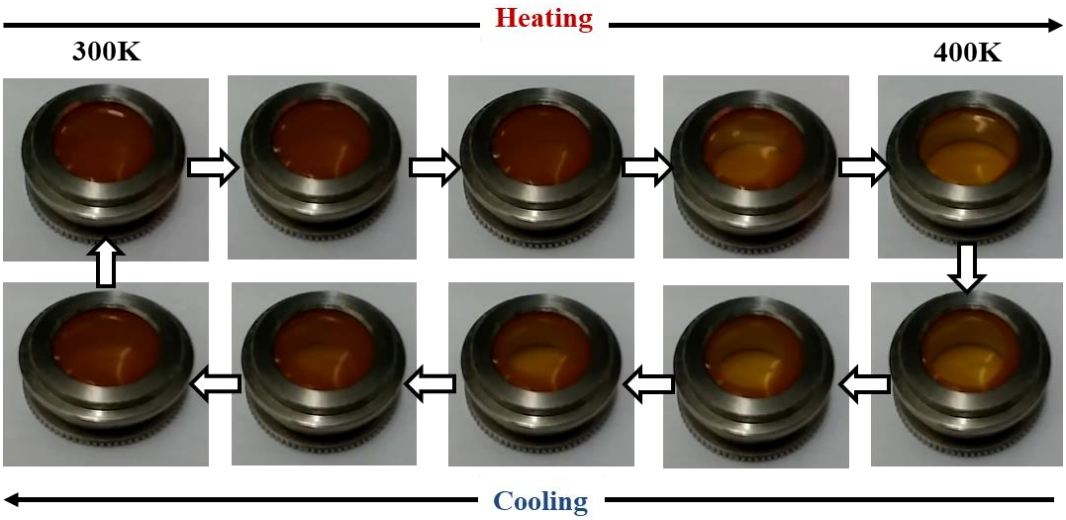

Figure 3.79 Complete heating-cooling cycle of the **PVA-MSCO** film. At 300 K, the film presented its purplish characteristic colour which was more translucid after the heating of the film. Once the temperature was decreased in the cooling step, the **PVA-MSCO** film recovered its original aspect

3.3.4 Summary and conclusions

In this Chapter, the synthesis of $[Fe(Htrz)_2(trz)]_n(BF_4)_n$ (**2**) nanoparticles has been achieved by using a microfluidic device. To the best of our knowledge nanoparticles of complex (**2**) have only been reported by employing batch processes such as the reverse-micelle method with reaction times of up to several hours. There is a unique example of the use of a microfluidic system for the synthesis of complex (**2**),[35] Nevertheless, the authors were not able to obtain the complex (**2**) in the form of spherical nanoparticles. The control of the RD conditions during the synthesis of the nanoparticles allowed three main achievements:

i. Isolation of a kinetic product
ii. Control the defect engineering
iii. Formation of water-stable colloidal nanoparticles with SCO behaviour

The nanoparticles obtained immediately after the reaction (**MSCO@1** and **MSCO@2**) of the starting materials, were associated to a kinetic product which was inaccessible by the classical synthesis of (**2**). The magnetic properties of such product were different form its bulk counterpart but still retaining the ST around room temperature and the thermal hysteresis. Furthermore, the annealing of the microfluidic nanoparticles (**MSCO**) let to achieve the thermodynamic product which had some differences of the as synthesized **MSCO** samples. These results demonstrated how through the control of the mass transport was possible to develop novel and interesting nanostructured materials with properties never seen before. Additionally, the fine tune synthesis of complex (**2**) in the microfluidic device resulted in the formation of nanoparticles with different chemical composition from their crystal bulk. The **MSCO@1** and **MSCO@2** incorporated an increased amount of counter anions in order to compensate the different stoichiometry of the protonated and non-protonated triazole-based ligand. These differences in the counter anion doping could be the main reason for the differences observed in the SCO behaviour.

Finally, as a proof-of-concept, the nanoparticles obtained from the microfluidic device, were redispersed in a polymeric matrix of PVA. The formation of free-standing films containing the nanoparticles showed the retention of the SCO occurrence. This material integration demonstrated the feasibility of these nanoparticles for their use in composites and functional switchable devices.

In conclusion, the data obtained clearly showed that controlled defect engineering and RD microfluidic environments may be the only effective way of tuning structure-properties correlations in a systematic manner. Considering the growing interest in tuning and understanding the SCO phenomenon, and in general the physicochemical properties of porous and non-porous CPs, we believe that the presented approach will open new avenues towards unprecedented and unique functional materials and devices.

3.3.5 Experimental section

Materials The reagents iron(II) tetrafluoroborate hexahydrate ($Fe(BF_4)_2 \cdot 6H_2O$) and 1,2,4-Triazole ($C_2H_3N_3$) were purchased from Sigma-Aldrich GmbH (Germany) and used without further purification. HPLC grade EtOH was obtained from Fluka Chemie AG (Switzerland).

Microfluidic Device Fabrication (*Done by Dr. Puigmartí-Luis research group*) The silicon master mould used for fabrication of the microfluidic device employed in this work was fabricated through standard photolithography processes extensively described elsewhere.[36] The microfluidic device was fabricated by replica moulding of PDMS (SYLGARD 184 Silicone Elastomer Kit) against the previously fabricated master mould. In brief, a mixture of PDMS elastomer and curing agent (10:0.9 ratio by weight, respectively) was casted against the master mould, cured and cut to the target size. The inlets and outlet holes were punched using Biopsy punchers. Before bonding the device to a glass coverslip (Menzel-Glaser, Germany), a thin layer PDMS was spin-coated onto the glass coverslip. Using a corona discharge (Electro-Technic Products, USA) the PDMS slab (incorporating the microfluidic channels and inlet and outlet holes) was bonded to the PDMS coated glass coverslip, yielding the final device. Eventually, the fabricated microfluidic device comprised four inlet channels converging into a single one 1 cm long. The cross-sectional dimensions of inlet channels are 50 μm × 50 μm and 250 μm × 50 μm for the 1 cm long microchannel (i.e. the microchannel where the reaction is conducted).

Synthesis of MSCO@1 and MSCO@2 (*Done by Dr. Puigmartí-Luis research group*) The reagent flows were injected into the inlets of the microfluidic device using a syringe pump system (neMESYS module, Cetoni GmbH, Germany). EtOH solutions of $Fe(BF_4)_2 \cdot 6H_2O$ (1 M) and 1,2,4-triazole (**H-L2**) (3 M) were injected into two middle inlets at the flow rate of 50 μL/min, while pure EtOH flows were injected into the two middle inlets at the flow rate of 100 or 400 μL/min for **MSCO@1** and **MSCO@2**, respectively. The reaction mixture coming out from the outlet was collected in a falcon tube containing 100 mL pure ethanol during 10 min in order to quench by dilution the reaction after microfluidic synthesis. The reagent flows reacted under controlled diffusion conditions in the main channel resulting in the formation of nanoparticles suspended in flow eluting from the outlet tubing.

IR (KBr): ν = 3178 (m; νs(Ctrz−H)), 3102 (s), 2994 (w), 2655 (w), 1796 (w), 1536 (m; νsHtrz), 1497 (m, νstrz), 1453 (m; νs(triazole ring)), 1418 (s), 1300 (s), 1148 (m), 1061 (s), 978 (m), 861 cm^{-1} (m); Anal. Calcd (%) for **MSCO@1**: C 19.87, H 2.27, N 34.76; found: C 19.06, H 2.56, N 35.21. ICP-MS Calcd (%) for **MSCO@1**: Fe 15.40; found: 15.67. Compositional formula for **MSCO@1**: $[Fe(Htrz)_{2.2}(trz)_{0.8}](BF_4)_{1.2}$. Anal. Calcd (%) for MSCO@2: C 19.11, H

2.22, N 33.43; found: C 19.70, H 2.24, N 33.07. ICP-MS Calcd (%) for **MSCO@2**: Fe 14.81; found: 15.24. Compositional formula for **MSCO@2**: $[Fe(Htrz)_{2.3}(trz)_{0.7}](BF_4)_{1.3}$

Isolation of RD-SCO-1 Powder The suspension collected in the falcon tube was centrifuged at 3000 rpm for 5 min in three consecutive steps. After each step, the supernatant was discarded from top and the remaining powder was re-suspended again in fresh ethanol. After three washing steps the suspension was poured onto a glass petri-dish and dried under vacuum yielding **MSCO@1** and **MSCO@2** as a pink powder

Bulk synthesis of complex (2) Complex (**2**) was synthesized following the procedure reported in the literature.[9] A solution of 1,2,4-triazole (**H-L2**, 1.040 g, 1.5 × 10-2 mol) in EtOH (5 mL) was added to a solution of $Fe(BF_4)_2 \cdot 6H_2O$ (1.687 g, 5 × 10-3 mol) in ethanol (10 mL). The purple suspension obtained was left undisturbed for 24 h and filtered. The resulting purple powder (complex (**2**)) was washed with ethanol and dried in air overnight.

Thermogravimetric analysis (TGA) TGA of samples were run on a Netzsch TG 209 F1 thermal gravimetric analyser with samples held in aluminium crucibles at the heating rate of 5 °C/min from 25 to 600 °C.

Scanning Electron Microscopy (SEM) Images obtained from SEM measurements were acquired on a FEI Quanta 650 FEG in secondary electron mode with a beam voltage between 2 and 20 kV. The samples were prepared by deposition of a drop of the material previously dispersed in EtOH or water on aluminium stubs followed by evaporation of the solvent under ambient conditions. Before performing the analysis, the samples were metalized by depositing on the surface a thin platinum coating (5 nm) using a sputter coater (Leica EM ACE600). Before performing the analysis, the samples were metallised with a 5 nm Pt coating.

Transmission Electron Microscopy (TEM) TEM images were obtained with a FEI Tecnai G2 F20 at a voltage of 200 kV. The samples were prepared by drop casting on TEM grids (ultrathin carbon type-A, 400 mesh Cu grids. Ted Pella Inc., Redding, CA, USA) and dried overnight prior to examination. The digital images were analysed using the ImageJ version 1.2 (NIH, Bethesda, MD, USA) software. The EDX measurements were done by using a detector for the quantification of the energies coming from the elements composing the samples.

Dynamic light scattering spectroscopy (DLS) Size distribution in water and EtOH and Zeta-potential measurements were performed in a Zetasizer Nano ZS (Malvern Instruments). The data was collected by Zetasizer 7.02 software. 1 mL of sample was introduced in a disposable capillary cell.

UV-visible and FT-IR spectroscopy Absorbance spectra for **MSCO@1** and **MSCO@2** samples were recorded with a Vertex 80 spectrometer (Bruker Optik GmbH, Ettlingen, Germany) in the visible- near-infrared range. The FT-IR spectra were acquired by changing the corresponding lamp in order to measure in the infrared region. The temperature dependent measurements were done with a cryostat Optistat CFV (Oxford Instruments, Wiesbaden, Germany) in the range 298-440 K. All the data obtained were processed using the Opus version 7.2.139.1294 (Bruker) software.

X-ray photoelectron spectroscopy (XPS) Measurements were performed with a Phoibos 150 analyser (SPECS EAS10P GmbH, Berlin, Germany) in ultra-high vacuum conditions (based pressure 10^{-10} mbar, residual pressure around 10^{-7} mbar). Monochromatic AlKα line was used as X-ray source (1486.6 eV and 300 W). The electron energy analyser was operated with pass energy of 50 eV. The hemispherical analyser was located perpendicular to the sample surface. The data was collected every eV with a dwell time of 0.5 s. A flood gun of electrons, with energy lower than 20 eV, was used to compensate the charge. The **MSCO@1** and **MSCO@2** were deposited on silicon substrates. All the data was treated with CasaXPS version 2.3.17PR1.1 (Casa Software LTD, Teignmouth, UK) and OriginPro version 8.0988 (OriginLab Corporation, Northampton, MA, USA) software.

Inductively coupled plasma mass spectrometry (ICP-MS) ICP-MS was used for the determination of the iron percentage in the **MSCO@1** and **MSCO@2** samples. For the quantification of metal, a dilution 1:100 was necessary for detecting the correct signals. For ICP-MS analysis, atomic spectroscopic analytical standards were purchased from PerkinElmer Pure Plus. The isotope ^{57}Fe was selected as tracer. The iron concentration of each sample was measured using a calibration curve obtained in the range of 0.01−250 ppb of metal. Standard reference material (PerkinElmer) with known values of iron and rare earth elements was analysed with each batch of samples. All the samples were measured per quadruplicate.

Powder X-ray diffraction (PXRD) PXRD patterns were recorded on PANalytical X'Pert PRO MPD (Multipurpose Diffractometer) (Malvern PANalytical, Dusseldorf, Germany) equipped with a CuKα radiation source (λ = 1.54184 Å). For the capillary measurements we use a Capillary Spinner which is designed to hold a goniometer (320 mm radius) head into which a capillary can be placed. The incident optics corresponds to focusing XrayMirror, divergent slit 1/2°, mask 10 mm, antiscatter slit 1°, seller slits 0.04 rad and the diffracted optics: X'celerator (detector), antiscatter 7.5 mm, Ni Filter. For the samples deposited on silicon substrate, the measurements were carried out by using grazing angle mode. The detector used was a Pixcel 1D which is a fast X-ray detector based on Medipix2 technology.

Magnetic susceptibilities (SQUID) Magnetic susceptibility measurements were performed on polycrystalline samples of **MSCO@1** and **MSCO@2** with a Quantum Design SQUID MPMS-5 magnetometer at the *Unitat de Mesures Magnètiques* of the *Universitat de Barcelona* (UB, Barcelona, Spain). Data were corrected for diamagnetic contributions, which were estimated from the Pascal constants

Differential scanning calorimetry (DSC) DSC measurements were carried out in a He atmosphere using a Perkin-Elmer DSC 8500 device equipped with a cryostat. The heating and cooling rates were fixed at 10 K min^{-1}. Temperatures and enthalpies were calibrated over the temperature range of interest (260–420 K) using the solid–liquid transitions of pure indium (99.99%).

Small angle and Wide angle X-Ray Scattering measurements (SAXS/WAXS) Transmission SAXS and WAXS were measured in a S3-MICRO (Hecus X-ray systems GMBH Graz, Austria) incorporating a X-ray source GENIX-Fox 3D X-ray source (Xenocs, Grenoble), which provides a detector focused beam with $\lambda = 0.1542$ nm Cu Kα-line (with more than 97% purity and less than 0.3% Kβ). Both detectors are PSD 50 Hecus. Temperature was controlled by means of a Peltier TCCS-3 Hecus or a resistance TCCS-300. The samples were inserted into glass capillaries with diameters of 1 mm or 0.2 mm and 10 μm wall thicknesses. The thinner capillaries providing improved signal in the WAXS region due to smaller absorption. The SAXS scattering curves are shown as a function of the scattering vector modulus:

$$q = (4\pi/\lambda)\cdot\sin(\theta) \qquad \text{(Equation 1)}$$

Where, 2θ is the scattering angle. The q values with this setup ranged from 0.08 nm^{-1} to 6.0 nm^{-1} in the SAXS regime ($0.1º < 2\theta < 8.5º$). WAXS curves are shown as a function of 2θ with a range from 18.5º to 27º (13.1 to 19 nm^{-1} in q scale). The silver behenate and para-bromobenzoic acid were used to calibrate SAXS and WAXS measurements, respectively. To avoid the detector-width smearing effect, a 1 mm slit was used for the SAXS measurements. To improve the contact of the capillary with the Peltier Block, 1 mm capillaries were inserted in a brass tube with a notch to let X-ray pass. Instead, 0.2 mm capillaries were measured close to the tip of the brass tube also to ensure the good temperature transmission. Spectra were acquired in 20 minutes frames to complete three hours, then the temperature was raised to the high temperature and let to stabilize for 20 min prior to the acquisition. Then, the samples were cooled down to the low temperature. Each annealing cycle was conducted during three hours. Additionally, SAXS data was fitted to a polydisperse sphere model using a Schultz distribution.

3.3.6 References

1. Fialkowski, M.; Bishop, K. J. M.; Klajn, R.; Smoukov, S. K.; Campbell, C. J.; Grzybowski, B. A. *J. Phys. Chem. B* **2006**, *110*, 2482–2496.
2. S. Sevim, S.; Sorrenti, A.; Franco, C.; Furukawa, S.; Pané, S.; deMello, A. J.; Puigmartí-Luis, J. *Chem. Soc. Rev*. **2018**, *47*, 3788–3803.
3. Lovrak, M.; Hendriksen, W. E.; Maity, C.; Mytnyk, S.; van Steijn, V.; Eelkema, R.; van Esch, J. H. *Nat. Commun.* **2017**, *8*, 15317.
4. Knight, J. B.; Vishwanath, A.; Brody, J. P.; Austin, R. H. *Phys. Rev. Lett.* **1998**, *80*, 3863–3866.
5. Amstad, E.; Gopinadhan, M.; Holtze, C.; Osuji, C. O.; Brenner, M. P.; Spaepen, F.; Weitz, D. A. *Science* **2015**, *349*, 956–960.
6. Rubio-Martinez, M.; Imaz, I.; Domingo, N.; Abrishamkar, A.; Mayor, T. S.; Rossi, R. M.; Carbonell, C.; deMello, A. J.; Amabilino, D. B.; Maspoch, D.; Puigmartí-Luis, J. *Adv. Mater*. **2016**, *28*, 8150–8155.
7. Ameloot, R.; Vermoortele, F.;.Vanhove, W.; Roeffaers, M. B.; Sels, B. F.; De Vos, D. E. *Nat. Chem*. **2011**, *3*, 382–387.
8. Faustini, M.; Kim, J.; Jeong, G. –Y.; Kim, J. Y.; Moon, H. R.; Ahn, W. –S.; Kim, D. –P. *J. Am. Chem. Soc*. **2013**, *135*, 14619–14626.
9. Kröber, J.; Audière, J.-P.; Claude, R.; Codjovi, E.; Kahn, O.; Haasnoot, J. G.; Grolière, F.; Jay, C.; Bousseksou, A.; Linarés, J.: Varret, F.; Gonthier-Vassal, A. *Chem. Mater*. **1994**, *6*, 1404–1412.
10. Michalowicz, A.; Moscovici, J.; Ducourant, B.; Cracco, D.; Kahn, O. *Chem. Mater*. **1995**, *7*, 1833–1842.
11. Real, J. A.; Gaspara, A. B.; Muñoz, M. C. *Dalton Trans*. **2005**, 2062–2079.
12. Prins, F; Monrabal-Capilla, M.; Osorio, E. A.; Coronado, E.; van der Zant, H. S. J. *Adv. Mater*. **2011**, *23*, 1545–1549.
13. Rotaru, A.; Gural'skiy, I.y.A.; Molnar, G.; Salmon, L.; Demont, P.; Bousseksou, A. *Chem. Comm*. **2012**, *48*, 4163–4165.
14. Rotaru, A.; Dugay, J.; Tan, R.P.; Gural'skiy, I.A.; Salmon, L.; Demont, P.; Carrey, J.; Molnar, G.; Respaud, M.; Bousseksou, A. *Adv. Mater.* **2013**, *25*, 1745–1749.
15. Lefter, C.; Tan, R.; Dugay, J.; Tricard, S.; Molnar, G.; Salmon, L.; Carrey, J.; Rotaru, A.; Bousseksou, A. *Phys. Chem. Chem. Phys*. **2015**, *17*, 5151–5154.
16. Diaconu, A.; Lupu, S.-L.; Rusu, I.; Risca, I.-M.; Salmon, L.; Molnár, G.; Bousseksou, A.; Demont, P.; Rotaru, A. *J. Phys. Chem. Lett.* **2017**, *8*, 3147–3151.
17. Etrillard, C.; Faramarzi, V.; Dayen, J. –F.; Létard, J. –F.; Doudin, B. *Chem. Comun.* **2011**, *34*, 9663–9665.

18. Ganguli, A. K.; Ganguly, A.; Vaidya, S. *Chem. Soc. Rev*. **2010**, *39*, 474−485.
19. Gonidec, M.; Puigmartí-Luis, J. *Crystals* **2019**, *9*, 12.
20. Grosejan, A.; Négrier, P.; Bordet, P.; Etrillard, C.; Mondieig, D.; Pechev, S.; Lebruad, E.; Létard, J.-F.; Guionneau, P. *Eur. J. Inorg. Chem*. **2013**, 796–802.
21. Coronado, E.; Giménez-Marqués, M.; Martí-Gastaldo, C.; Espallargas, G. M.; Navarro-Moratalla, E.; Waerenborgh, J. C. *Inorg. Chem.* **2013**, *52*, 8451–8460.
22. Zhao, T.; Cuignet, L.; Dîrtu, M. M.; Wolff, M.; Spasojevic, V.; Boldog, I.; Rotaru, A.; Garcia, Y.; Janiak, C.. *J. Mater. Chem. C* **2015**, *3*, 7802–7812.
23. Tailleur, E.; Marchivie, M.; Daro, N.; Chastanet, G.; Guionneau, P. *Chem. Commun.* **2017**, *53*, 4763–4766.
24. Galán-Mascarós, J. R.; Coronado, E.; Forment-Aliaga, A.; Monrabal-Capilla, M.; Pinilla-Cienfuegos, E.; Ceolin, M. *Inorg. Chem.* **2010**, *49*, 5706–5714.
25. Roubeau, O. *Chem. Eur. J*. **2012**, *18*, 15230–15244
26. Coronado, E.; Espallargas, G. M. *Chem. Soc. Rev*. **2013**, *42*, 1525–1539
27. Coronado, E; Galán-Mascarós, J. R.; Monrabal-Capilla, M.; García-Martínez, J.; Pardo-Ibáñez, P. *Adv. Mater*. **2007**, *19*, 1359–1361.
28. Senthil-Kumar, K.; Ruben, M.. *Coord. Chem. Rev*. **2017**, *346*, 176–205
29. Kotlarchyk, M.; Stephens, R. B.; Huang, J. S. *J. Phys. Chem.* **1988**, *92*, 1533–1538.
30. Patterson, A. L. *Phys. Rev.* **1939**, *56*, 978–982.
31. Halima, N. B. ***RSC Adv.*** **2016**, ***6***, 39823–39832.
32. Kamoun, E. A.; Kenawy, E.-R.; Chen, X. J. *Adv. Res.* **2017**, *8*, 217–233.
33. Paraossi, G.; Cavalieri, F.; Chiessi, E. *J. Mater. Sci.: Mater. Med* **2003**, *14*, 687–691.
34. Baker, M. I.; Walsh, S. P.; Scwartz, Z.; Boyan, B. D. *J. Biomed. Mater. Res. B* **2012**, *100*, 1451–1457.
35. Robertson, K.; Flandrin, P. –B.; Shepherd, H. J.; Wilson, C. C. *Chim. Oggi – Chem. Today* **2017**, *35*, 19–22.
36. Abrishamkar, A.; Paradinas, M.; Bailo, E.; Rodriguez-Trujillo, R.; Pfattner, R.; Rossi, R. M.; Ocal, C.; deMello, A. J.; Amabilino, D. B.; Puigmartí-Luis, J. *JoVE (Journal of Visualized Experiments)* **2016**, No. 113, e54193.

Chapter 4

Design of Novel Nanostructured Coordination Polymers for its use in Bioimaging

Chapter 4.1

Introduction

In this part we present the state-of-the-art and some previous examples developed in our research group as an overview of the use of NCPs in the field of theranostics (therapy + diagnosis). Additionally, this Chapter is divided in two sub chapters where a robust, reproducible and scalable methodology for obtaining CPs in the form of nanoparticles is presented. The set of novel synthesized polymers can be applied for potential therapeutic or diagnostic use, but in our case, we focused on the NCPs specifically as nano-probes for bioimaging. Thus, in Chapter 4.2, the synthesis, characterization and use of new iron-based NCPs as contrast agents (CAs) for MRI is described. And, in Chapter 4.3, the synthesis, characterization and use of radioisotopes (^{111}In and ^{64}Cu) for the formation of NCPs as agents for their application in PET / SPECT radioimaging was explored.

4.1 Introduction

4.1.1 Nanotechnology and theranostics

The application of nanobiotechnology in medicine is termed nanomedicine and it has emerged as a promising area of research. The main challenges that nanomedicine will be must overcome are to obtain systems with highly specificity for medical intervention at the molecular scale for therapeutic purposes, involving curing disease or repairing damaged tissues, and for the development of diagnostics in rapid monitoring, targeted cancer therapies, localized drug delivery, improved cell material interactions, scaffolds for tissue engineering and gene delivery systems.

In order to achieve successful research and development in nanomedicine, the interaction of a multitude of disciplines including material science and engineering, cellular biology and clinical translational research, is required. Over the next decades, nanotechnology may fundamentally transform science, technology and society, offering a significant opportunity to enhance human health by novel approaches, especially by enabling early disease detection and diagnosis, as well as precise and effective therapy tailored specifically to the patient (theranostic).

For the advancement of nanomedicine, development of smart materials systems, which are capable of performing multitasking, is needed. Theranostics is a novel concept which involves the integration of diagnosis and therapy in a single platform using nanomaterials. The theranostic nanomedicine thrives on nanoplatforms (nanoparticles, nanotubes, liposomes, quantum dots, etc.) with a set of functionalities that make them attractive to be used in a wide variety of biomedical applications. By using innumerable biomarkers, imaging agents, chemotherapeutic agents, and specific targeting ligands, these multidisciplinary theranostic systems will make a radical change in the field of personalized medicine that is one of the main goals of nanomedicine. This combinated therapy can provide optimized treatment for individuals and early detection of various diseases. Enhanced drug efficiency, better disease management, and improved healthcare are the different impacts experienced by the various *in vitro* and *in vivo* evaluations of nanotheranostic agents.

4.1.2 Nanoscale coordination polymers as potential imaging and theranostic agents

Nanomaterials have an important role in the development of biomedical imaging. In this scenario, NCPs provide an added value thanks to their pre-designed nature, increasing the interest for their application in several imaging techniques, including magnetic resonance imaging (MRI), optical imaging (OI) and radioimaging, among others.[1] More specifically, NCPs have reported diverse properties and advantages over other nanomaterials allowing to overcome some of the challenges in the diagnosis of diseases. The study and development of novel imaging probes based on NCPs has

promoted an exponential growth in the field thanks to their versatility, structural and chemical diversity and tailoring capacity.[2-4] Moreover, incorporating simultaneously diagnostic and therapeutic functionalities in NCPs provides entities that can be used to deliver diagnostic imaging agents and therapeutic drugs at the same time, the so called theranostic nanomedicines. Theranostic, as a combination of therapy and diagnosis agents in a single entity, is one of the cornerstones in cancer research. In fact, theranostic probes aim to monitor the release of the drugs in targeted cancer cells and the drug efficacy in real-time, and to increase the safety of the treatment. Over the past few years there have been an increasing number of theranostics applications. In this section, an overview of some of these strategies developed in our group is presented.

a) *Previous developments in our group: design of advanced functional NCPs*

Our group has demonstrated a wide experience in the synthesis and design of novel and functional NCPs for different applications, especially in nanomedicine field,[4] but also with others interesting applicability such as: separation of oils from water,[5] hybrid nanoparticle-based devices[6] and thermochromic nanostructures,[7,8] among others. These examples demonstrated the enormous versatility of NCPs through its rational design.

Nevertheless, in spite such a broad range of applications, medicine field still represents the technological area in which NCPs have mainly exhibit a broad impact. In this area, the NCPs must fulfil several strict requisites for its potential clinical translation in order to benefit the society from their advantages. This has been our main goal for the development of novel advanced functional NCPs from the design to its performance demonstration in relevant environment. Most of the materials developed by our group are based on mixture of metal ions and organic ligands in presence of poor solvent that induces fast precipitation. This one-pot methodology usually let the formation of nanoparticles with spherical shape due to the tendency to minimize the interfacial free energy between the surface of the precipitated NCPs and the solvent. However, other pioneer approaches has demonstrated its interesting success for the obtaining of NCPs, as for example, the use of DPN nanolithography and their synthesis in ultra-small droplets previously discussed in Chapter 1.[9-11] Although different organic ligands can be used for the synthesis of NCPs, our group have been focused on the use of catechol-[12] and imidazole-based[13] ligands for their mixing with several metal ions arousing a wide range of functionalities and properties. The reason to use this type of ligands lies in their versatility to coordinate different metal ions and the possibility to modulate that coordination depending on the metal ion used or the environmental conditions (pH, temperature, light, magnetic fields, etc.).

The NCPs, in a same way of nanoparticles based on organic polymers, has demonstrated its ability for the encapsulation of therapeutic-active molecules. Different approaches can be followed for the successful encapsulation of drugs within the NCPs structure. In this sense, Amorín-Ferré *et al.* has evaluated the differences between two different methodologies of encapsulation: i) binding of the drug to the polymer framework as a NCP building block and ii) mechanical entrapment of the therapeutic agent within the metal–organic matrix.[14] The NCPs reported were based on the coordination between Co(II) ions with 1,4-bis(imidazol-1-ylmethyl)benzene (Bix) and 3,5-di-tert-butylcatechol as organic ligands. Their formation was done in presence of low amounts of two variations of a fluorescent guest compound, either containing a free chelating catechol moiety or a protected one (Figure 4.1a-c). Accordingly, drug release can take place though different mechanisms. Thus, cargo loaded via direct attachment to the NCPs framework was slowly released upon particle degradation through surface erosion, whereas the encapsulated one was easily released through a diffusion mechanism (Figure 4.1d). As a result, complex drug-delivery profiles are often encountered in NCPs that preclude unambiguous elucidation of the relationship between encapsulation and release mechanisms.

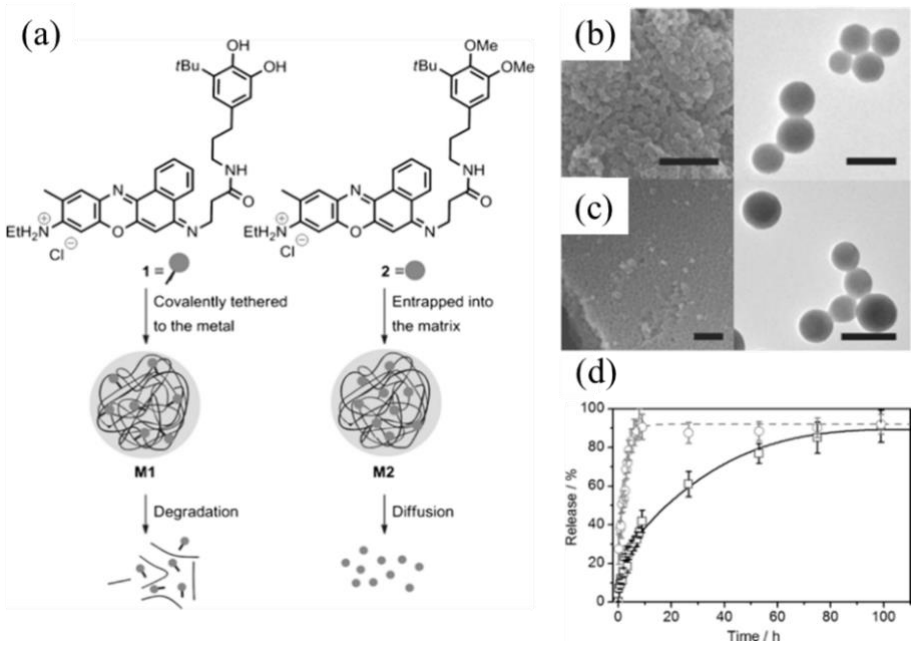

Figure 4.1 (a) Chemical structures of fluorescent guest compounds 1 and 2 used in the formation of structurally-analogous M1 and M2 particles. The degradation and diffusion-controlled release mechanisms in NCPs was studied. (b and c) SEM (left) and TEM (right) images of M1 (b) and M2 (c) particles. Scale bars for SEM are 1 μm and 200 nm for TEM. (d) Release profiles of fluorescent guest molecules from M1 (□) and M2 (○) at 37 °C, averaged over four independent experiments. Reproduced from ref. 14.

Similarly, Novio *et al*. reported the formation of catechol-iron based NCPs containing carboxylic groups as platforms for further functionalization via condensation reactions.[15] As a proof-of-concept, the particles were covalently labelled with bioactive functional moieties as a fluorescent dye or PEG. Moreover, the particles showed efficient cellular uptake and no significant cytotoxicity. Their use as

drug delivery platforms was then modelled encapsulating the anticancer drug camptothecin (CPT), showing an improvement in IC_{50} values as compared with the free drug (6.5-fold increase in efficacy with respect to the free CPT). In the same way, the encapsulation of doxorubicin in NCPs and its subsequent delivery at cellular level was demonstrated Ruiz-Molina and co-workers. The doxorubicin drug was physically encapsulated (21% in weight) with NCPs obtained by coordination of Zn^{2+} with Bix.[16] The release profile indicated a fast release of 80% at 8 hours, followed by an additional release of 15% over the next 2 days. The relatively high load capacity of drugs, their low cytotoxicity, the possibility to image the cell internalization by functionalization with fluorescent groups, and the control of colloidal stability in aqueous dispersions, make the NCPs very promising and under-developed nanoplatforms for applications in drug delivery.

Other widely studied drugs for the cancer treatment consisted on the cisplatin molecules. Cisplatin is used as a chemotherapeutic drug for the treatment of several tumours but its use involves serious side effects such as non-selective toxicity, myelosuppression or development of cisplatin resistance.[17] In order to overcome these major drawbacks, a lot of efforts has been focused over the last decades in the use of Pt(IV) prodrugs, as they can be modified with a range of ligands for the purpose of targeting cancer cells, alteration of metabolic pathways, combination with other therapeutic warheads, and conjugation with nano-drug delivery systems. Early studies of dual-action Pt(IV) prodrugs showed improved cytotoxicity, especially in cisplatin-resistant cells, and the conjugated bioactive ligands exerted the expected mode of action inside cells.[18] In this sense, Ruiz-Molina and co-workers developed a novel nanoparticle platform based on NCPs from the coordination of Zn metal ions, Pt(IV) prodrug and Bix (Figure 4.2).[19]

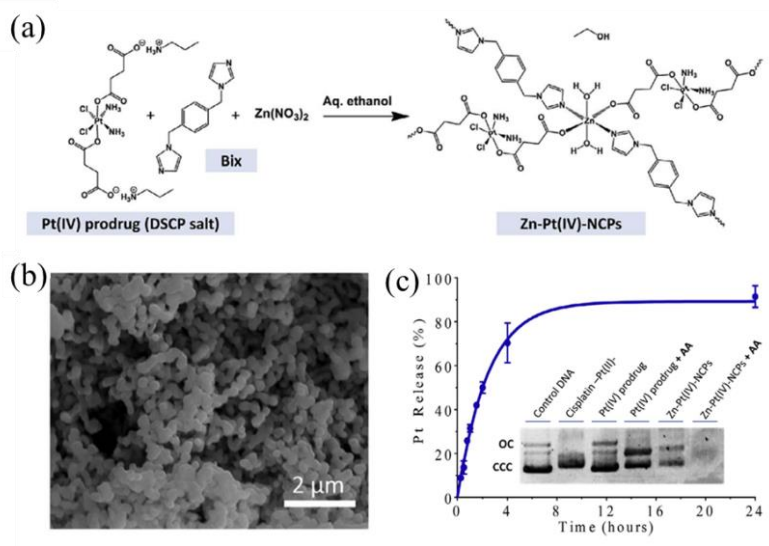

Figure 4.2 (a) Synthesis of Zn-Pt(IV)-NCPs. (b) Scanning electron microscopy (SEM) image of Zn-Pt(IV)-NCPs. c) *In vitro* release kinetics of Pt from Zn-Pt(IV)-NCPs. The inset shows the arose gel electrophoresis of a pBluescript II plasmid DNA treated with the Pt(IV) prodrug or Zn-Pt(IV)-NCPs. Reproduced from ref. 19.

The resulting nanoparticles displayed an average size close to 200 nm, a good stability in physiologic environments, and a controlled drug release of Pt. The in vitro studies demonstrated that Pt(IV)-based NCPs showed an enhanced cytotoxic effect against cell culture of cervical cancer, neuroblastoma and human adenocarcinoma cells in comparison with free Pt(IV) prodrug. This study suggested that the nanostructuration of the prodrug facilitate its activation and induce a change in the mechanism of action related to an increased interaction with the DNA as corroborated by the studies of direct interaction of the Pt(IV) prodrug with DNA.

Most recently, a part of cancer-target therapies, our group has proposed the use of NCPs for the treatment of infection diseases such as AIDS/HIV.[20] In this work, Solórzano *et al.* reported the functionalization of the anti-HIV drug azidothymidine (AZT) with a chelating catechol group through a spacer sensitive to enzymatic hydrolysis (Figure 4.3a). The NCPs were formed by its polymerisation with the bridging Bix ligand and using iron ions as metal nodes. The resulting nanoparticles, with an average size of 147 ± 33 nm, exhibited a high loading content of the antiretroviral drug (25 wt%), an esterase-triggered release and comparable anti-HIV activity to free AZT. Apart from successfully reproduced the effective antiretroviral activity of free AZT prodrug, nanostructuring allows the stabilization of the drug in physiological conditions, the control over the release properties of the drug by pH and the presence of enzymes. The nanoparticles retained inherent multifunctionality due to the presence of iron ions with MRI responses, significant reduction in AZT toxicity and enhancement of the cellular uptake (up to 50-fold increase).

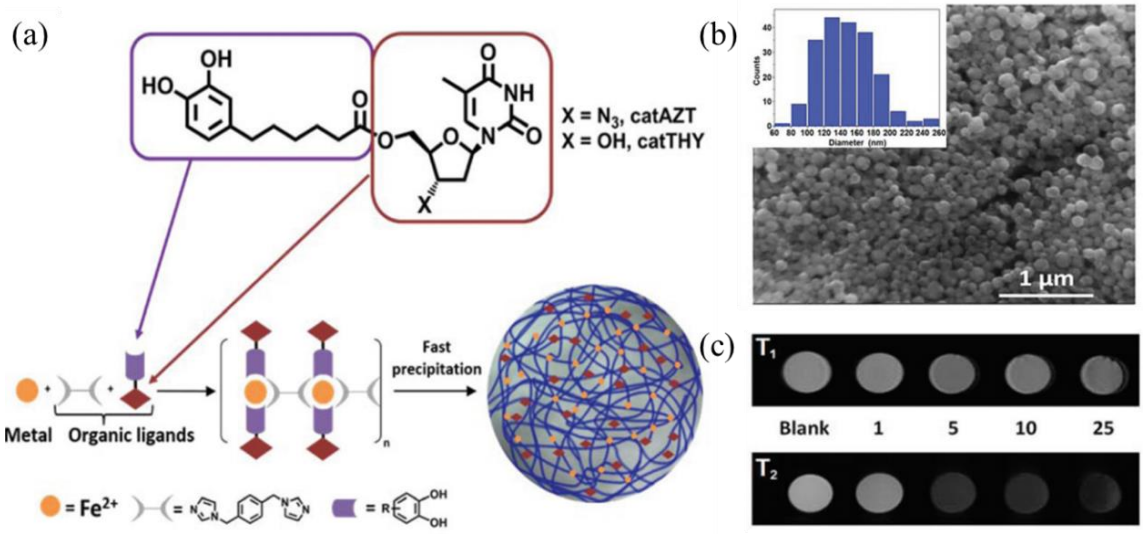

Figure 4.3 (a) Schematic representation of a catechol ligand linked to the antiviral drug AZT by an enzymatically cleavable bond via the carboxylic group. Posterior incorporation of catAZT or catTHY into a mixture containing iron and a bridging bis-imidazol ligand results in nanoparticle formation induced by rapid precipitation of the formed coordination polymer. (b) Representative SEM image of catAZT-NCPs. Inset: Histogram of particle sizes extracted from SEM micrographs (200 particles, mean size 147 ± 33 nm).(c) ^{1}H-MRI T_1 and T_2 phantom maps of catAZT-NCPs in a PBS/agarose 1% solution at pH 7.4 at different concentrations (0, 1, 5, 10, and 25 mM, referred to the Fe concentration). Reproduced from ref. 20.

As we have seen in the last examples, the therapeutic agents can be successfully integrated on the NCPs synthesized showing advantages compared with the administration of the free drug. Other capabilities of NCPs are related to the modulation of drug release processes. As an example, Nador *et al*. developed a pH-responsive bis(catechol)-based cobalt NCPs.[21] In this case, by using an appropriate multitopic bridging organic ligand could be possible to structure well-known functional building blocks in the form of spherical particles with pH-responses while retaining the metal–ligand bond. The bridging ligand, apart from induce polymerization, assures strong coordination capabilities at different pHs Then a pH-triggered response was therefore ensured by introducing a sensitive imine bridge; in this way, it turns out that the NCPs dissociate after a few hours at pH = 5 while remained stable at pH = 7 for long time. These results opened the door for the use of NCPs with improved performances in well-developed fields such as sensing, drug delivery and molecular electronics, among many others.

Although most of the research developments have been focused on the encapsulation and drug release studies, very recently there has been a notable increase of attention towards the development of diagnosis tools based on NCPs, especially concerning bioimaging. As aforementioned, the early diagnosis of a certain disease in a patient sometimes is subjected to an accurate use of bioimaging techniques. For this reason, the development of contrast agents (CAs) for the improvement of different clinical imaging techniques is a pressing concern. In this sense, Nador *et al*. reported dual-fluorescent NCPs for their use in multichannel imaging.[22] The authors reported the synthesis of dual-fluorescent NCPs via a mixed-ligand synthetic strategy incorporating two different fluorescent ligands (Figure 4.4).

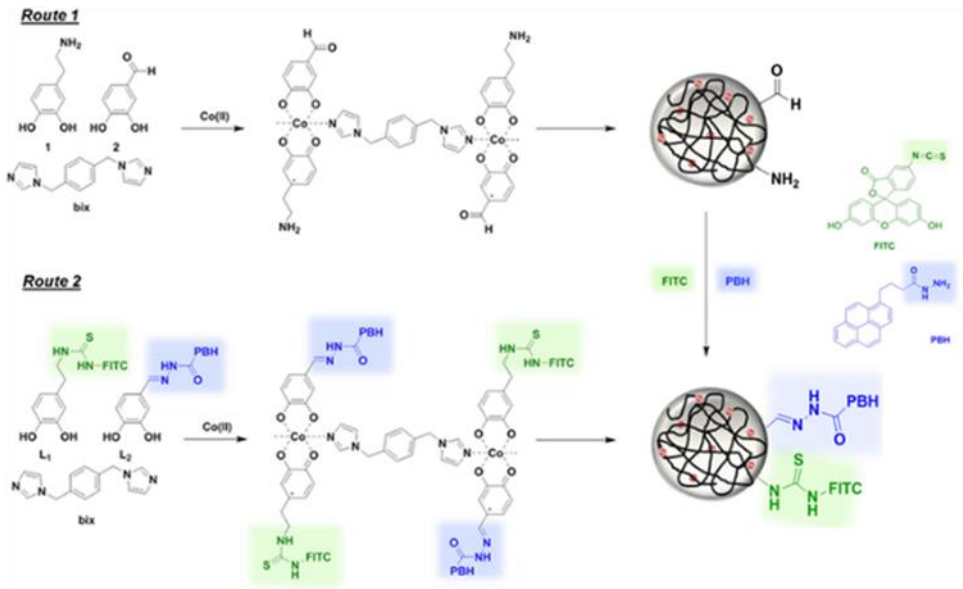

Figure 4.4 (a) Schematic illustration describing two different routes to obtain dual-fluorescent NCPs. Reproduced from ref. 22.

The resulting nanoparticles showed a defined control over their emission properties and morphology, low toxicity and high cellular uptake. This proposed methodology allows functionalize NCPs with a wide variety of fluorescent dyes. The combination of dyes and such dual-wavelength emission properties, could also serve as the basis for ratio-metric sensing of the local chemical environment of the cells when sensitive dyes are used, recognizing the biological targets or monitoring the transformation of the tumours by simultaneously non-invasive fluorescence imaging.

Additionally, the use of NCPs as CAs for MRI has been explored by our group. The first antecedent was explored by Borges *et al.* which reported a novel hybrid dual-mode contrast agent through the hybrid encapsulation of Superparamagnetic Iron Oxide Nanoparticles (SPIONs) into an Fe-based NCP system.[23] The use of a catechol-based Fe(III) NCPs resulted on the formation of a nanostructured matrix able to encapsulate SPIONs in their core. As mentioned, the use of the Fe-based NCPs as contrast agent for MRI was also explored in the aforementioned NCPs for HIV/AIDS treatment that showed MRI activity allowing their use in theranostic applications (Figure 4.3c).[20]

b) Molecular imaging

Molecular imaging (MI) is an emerging field that aims to integrate patient-specific and disease-specific molecular information derived from diagnostic imaging studies. The ultimate goal of MI is the diagnosis of diseases and organism malfunctions through the application of non-invasive techniques (Table 4.1). MI englobes the visualization, characterization and measurement of biological processes at the molecular and cellular levels in humans and other living organisms.[24-26]

Table 4.1 Non-invasive *in vivo* molecular imaging modalities.

Imaging modality	Form of energy used	Spatial resolution (mm)		Acquisition time/frame (s)	Probe mass required (ng)	Sensitivity of detection (Mol/L)	Depth of penetration (mm)
		Clinical	Animal				
MRI	Radiofrequency waves	0.2-0.1	0.025-0.1	50-3000	10^{3}-106	10^{-3}-10^{-6}	>300
CT	X-rays	0.5-1	0.03-0.4	1-300	-	-	>300
PET	Annihilation photons	3-8	1-3	1-300	1-100	10^{-11}-10^{-12}	>300
SPECT	ɣ-photons	5-12	1-4	60-2000	1-1000	10^{-10}-10^{-11}	>300
Ultrasound	High frequency sound waves	0.1-1	0.05-0.1	0.1-100	10^{3}-10^{6}	-	1-200
BLI	Visible to infrared light	-	3-10	10-300	10^{3}-10^{6}	10^{-13}-10^{-16}	1-10
FLI	Visible to infrared light	-	2-10	10-2000	10^{3}-10^{6}	10^{-9}-10^{-11}	1-20

MRI = Magnetic resonance imaging, CT = Computed tomography, PET = positron emission tomography, SPECT = Single-photon emission computed tomography, BLI = Bioluminescence and FLI = fluorescence imaging. Adapted from ref. 1.

The main non-invasive techniques with applicability on MI are summarized and compared in Table 4.1. The different techniques are based on different phenomena which arouses in specific characteristics and advantages in each case. One of the most used imaging techniques in MI is MRI. This technique is mainly based on the application of a magnetic field for the visualization of soft tissue by exploiting the proton density, perfusion, diffusion and biochemical contrasts.[27] Two are the most important advantages offered by MRI: i) high especial resolution (<1mm) and ii) anatomic, physiologic and metabolic information in a single image scan. Furthermore, MRI offers good depth penetration similar to PET and CT modalities. In the case of nuclear imaging approaches (PET and SPECT), the advantages are mainly related with high intrinsic sensitivity and unlimited depth penetration. Specifically, PET has the additional advantage of being fully quantitative. There are several studies in the literature demonstrating the applicability of MI probes for nuclear medicine. In this case, due to the high sensitivity of PET/SPECT modalities, the mass of the MI radiotracers needed is low (ng or μg). Both MRI and PET/SPECT techniques were the focus of interest for the developing of this Thesis and it will be treated in deep in the following chapters.

Another group of MI techniques widely studied are the optical-based imaging tools. Its basis relies on the detection of light photons after their interaction with the tissue. Two main optical imaging (OI) methods can be found in this group of techniques: i) bioluminescence imaging (BLI) and ii) fluorescence imaging (FLI). In the case of BLI, the cellular expression of an enzyme known as luciferase is required. The detection of emitted bioluminescence can be used to monitor the cellular and genetic activity of every cell that expressed the luciferase enzyme. However, due to the low depth of penetration, *in vivo* BLI applications are mainly focused on small mouse models of disease since most of the organs of interest are found no more than 1-2 cm deep within the tissue. On the other hand, FLI let the imaging of surface distribution of fluorescent signals. One approach to obtain fluorescent image can be the genetically-modification of molecules by incorporating the gene for a fluorescence protein. Although the penetration of light through the tissue is a limitation for all OI methods, attenuation and autofluorescence, are minimized in the near-infrared window (NIR 700-900 nm), allowing deep tissue imaging up to 10 cm. The advantages of FI methods include improved relative sensitivity and high resolution (which may be in the sub-millimetre range when imaged endoscopically).

Finally, ultrasound imaging (UI) is based on the formation of high frequency acoustic signals providing high spatial resolution (<1 mm) and excellent anatomical information. Nevertheless, its potential application is limited duet to relatively large size of the imaging probes needed.[28,29]

In this scenario the best features in terms of spatial resolution, sensitivity and depth of penetration correspond to the techniques MRI, CT, and PET/SPECT. Thus, the possibility of integrating into a single nanoprobe a combination of different agents suitable to be used in various modalities of clinical

imaging, make nanotechnology a powerful research field to generate very specific and efficient CAs for bioimaging. The combination of different imaging techniques could facilitate the early detection and better diagnosis of a certain disease.

c) NCPs as imaging probes

The correct application of the non-invasive bioimaging techniques needs the use of specific probes in order to visualize, characterize, and measure biological processes in living systems. These molecular imaging agents can be both endogenous molecules and exogenous probes. Among others, the designed systems with potential applicability for MI must accomplish:[30]

i) **High contrast effect**. The conclusions derived from low quality images can be sometimes misleading. High contrast images with high target-to-background or signal-to-noise ratio ensure appropriate interpretation of physiological and pathological conditions of the diseases. A molecular imaging probe with high uptake and slow wash-out in target tissue, and low uptake and fast clearance from normal organs can provide the improved imaging quality.

ii) **High stability *in vivo***. Although only trace amount of imaging probe is normally given to the living subjects, maintenance of the intact structure of an imaging probe is a big challenge because numerous enzymes or proteases present in serum or targeted tissue may degrade the imaging probe. The image information given from the metabolites of the imaging probe undoubtedly make more difficult the imaging readout and usually makes the understanding of disease highly vague. The quality of the image as well as the validity of the quantitative analysis of the images heavily depends on the in vivo stability of the imaging probe.

iii) **Production and economic feasibility**. The low cost and excellent availability of molecular imaging probes are advantageous for their wide distribution and clinical routine use. High cost and difficult production dramatically hinder the application of an imaging probe albeit it may fulfil all other characteristics.

With the aim of giving solutions to the current drawbacks that hindrance the fully development of the different bioimaging techniques, we have focused our research on design, synthesize and explore the viability of a new set of NCPs for being applied as probes for imaging techniques such as MRI and PET/SPECT.

4.1.3 Scope of the Chapter 4

Research based on nanomedical applications is being focused on the development of multifunctional platforms capable of multitasking once they are introduced into the organism to meet a specific target (cells, tissues or organs). In the literature there are many examples of nanosystems that show high capacities for its transfer to the clinic. Nevertheless, there are today a series of challenges that must be addressed. This Chapter 4 aims to provide knowledge to help answer important still open questions such as:

i. Is there a molecular target relevant to the disease of interest?
ii. Once a target is selected, is there a high affinity ligand that will bind to the target?
iii. What is the appropriate MI system to provide the required spatial resolution, sensitivity and depth penetration for the disease?
iv. For a given clinical imaging technique, can a specific agent be synthesized to detect and give a detailed imaging of the desired molecular target?

In this scenario, NCPs have emerged as a versatile tool capable of offering in the same pre-designed system, a series of unique advantages that can overcome some of the biggest challenges discussed above. In this way, the work presented in this part has been focused on the design of a novel set of NCPs systems based on imidazole- and catechol-based ligands coordinated with different metal ions for their use as molecular imaging probes. In Chapter 4.2, we present four novel NCPs based on Fe(III), Gd(III) and Mn(II) ions which showed MRI-activity for glioblastoma imaging. Specifically, the system based on Fe(III) demonstrated its ability to be a dual-mode contrast agent thus overcoming most of the present challenges in this field. Additionally, in Chapter 4.3, the same approach was used for the design and synthesis of two novel NCPs based on In(III) and Cu(II) and their respective radiometal derivatives showing good activity for PET/SPECT-based imaging. In this case, the NCPs were coated with a catechol-based polymer which allowed to creating a multiplatform anchoring system for subsequent surface functionalization. The nanoparticles were specifically targeted for lung diseases.

4.1.4 References

1. Lim, E.-K.; Kim, T.; Paik, S.; Haam, S.; Huh, Y.-M.; Lee K. *Chemical Reviews* **2015**, *115*, 327–394.
2. Lin, W.; Rieter, W. J.; Taylor, K. M. L. *Angew. Chem. Int. Ed.***2009**, *48*, 650–658.
3. Rieter, W. J.; Pott, K. M.; Taylor, K. M. L.; Lin, W. *J. Am. Chem. Soc.***2008**, *130*, 11584–11585.

4. Novio, F.; Simmchen, J.; Vázquez-Mera, N.; Amorín-Ferré, L.; Ruiz-Molina, D. *Coord. Chem. Rev.* **2013**, *257*, 2839–2847.
5. Novio, F.; Ruiz-Molina, D. Hydrophobic. *RSC Adv.* **2014**, *4* (29), 15293–15296.
6. González-Monje, P.; Novio, F.; Ruiz-Molina, D. *Chem. Eur. J.* **2015**, *21* (28), 10094–10099.
7. Guardingo, M.; Busqué, F.; Novio, F.; Ruiz-Molina, D. *Inorg. Chem.* **2015**, *54* (14), 6776–6781.
8. Imaz, I.; Maspoch, D.; Rodríguez-Blanco, C.; Pérez-Falcón, J. M.; Campo, J.; Ruiz-Molina, D. *Angew. Chem. Int. Ed.* **2008**, *47*, 1857–1860.
9. Guardingo, M.; González-Monje, P.; Novio, F.; Bellido, E.; Busqué, F.; Molnár, G.; Bousseksou, A.; Ruiz-Molina. *ACS Nano* **2016**, *10*, 3206–3213.
10. Bellido, E.; González-Monje, P.; Guardingo, M.; Novio, F.; Sánchez, A.; Montero, M.; Molnar, G.; Bousseksou, A.; Ruiz-Molina, D. *RSC Adv.* **2016**, *6*, 76666–76672.
11. Guardingo, M.; Busqué, F.; Ruiz-Molina, D. *Chem. Commun.* **2016**, *52*, 11617–11626.
12. Faure, E.; Falentin-Daudré, C.; Jérôme, C.; Lyskawa, J.; Fournier, D.; Woisel, P.; Cetrembleur, C. *Prog. Polym. Sci.* **2013**, *38*, 236–270.
13. Adarsh, N. N.; Novio, F.; Ruiz-Molina, D.. *Dalt. Trans.* **2016**, *45*, 11233–11255.
14. Amorín-Ferré, L.; Busqué, F.; Bourdelande, J. L.; Ruiz-Molina, D.; Hernando, J.; Novio, F. *Chem. Eur. J.* **2013**, *19*, 17508–17516.
15. Novio, F.; Lorenzo, J.; Nador, F.; Wnuk, K.; Ruiz-Molina, D. *Chem. Eur. J.* **2014**, *20*, 15443–15450.
16. Imaz, I.; Rubio-Martínez, M.; García-Fernández, L.; García, F.; Ruiz-Molina, D.; Hernando, J.; Puntes, V.; Maspoch, D. *Chem. Commun.* **2010**, *46*, 4737–4739.
17. Avan, A.; Postma, T. J.; Ceresa, C.; Avan, A.; Cavaletti, G.; Giovannetti, E.; Godefridus J. Peters. *Oncologist* **2015**, *20*, 411–432.
18. Wang, Z.; Deng, Z.; Zhu, G. Dalton Trans., 2019, 48, 2536–2544.
19. Adarsh, N. N.; Frias, C.; Ponnoth Lohidakshan, T. M.; Lorenzo, J.; Novio, F.; Garcia-Pardo, J.; Ruiz-Molina, D. *Chem. Eng. J.* **2018**, *340*, 94–102.
20. Solórzano, R.; Tort, O.; García-Pardo, J.; Escribà, T.; Lorenzo, J.; Arnedo, M.; Ruiz-Molina, D.; Alibés, R.; Busqué, F.; Novio, F. *Biomater. Sci.* **2019**, *7*, 178–186.
21. Nador, F.; Novio, F.; Ruiz-Molina, D. *Chem. Commun.* **2014**, *50*, 14570–14572.
22. Nador, F.; Wnuk, K.; García-Pardo, J.; Lorenzo, J.; Solorzano, R.; Ruiz-Molina, D.; Novio, F. *ChemNanoMat* **2018**, *4*, 183–193.
23. Borges, M.; Yu, S.; Laromaine, A.; Roig, A.; Suárez-García, S.; Lorenzo, J.; Ruiz-Molina, D.; Novio, F. *RSC Adv.* **2015**, *5*, 86779–86783.
24. Jaffer, F.A.; Weissleder, R. *JAMA* **2005**, *293*, 855–862.
25. Weissleder, R. Mahmood, U. *Radiology* **2001**, *219*, 316–333.
26. Massoud, T. F., Gambhir, S.S. *Genes Dev*. **2003**, *17*, 545–580.

27. Tempany, C. M.; McNeil, B. J. *JAMA* **2001**, *285*, 562–567.
28. Lanza G. M.; Wickline, S. A. *Curr. Probl. Cardiol.* **2003**, *28*, 625–653.
29. Lindner, J. R. *Nat. Rev. Drug. Discov.* **2004**, *3*, 527–532.
30. Chen, K.; Chen, X. *Curr. Top. Med. Chem.* **2010**, *10*, 1227–1236.

Chapter 4.2

Dual T_1/T_2 Nanoscale Coordination Polymers as Novel Contrast Agents for MRI: A Preclinical Study for Brain Tumour

In the last years, extensive attention has been paid on designing and developing functional imaging contrast agents (CAs) for providing accurate non-invasive evaluation of pathology *in vivo*. However, the issue of false-positives or ambiguous imaging and the lack of a robust strategy for simultaneous dual-mode imaging remain to be fully addressed. One effective strategy for improving it is to rationally design magnetic resonance imaging (MRI) CAs with intrinsic T_1-T_2 dual-mode imaging features. In this work, the development and characterization of one-pot synthesized nanostructured coordination polymers (NCPs) which exhibit dual mode T_1-T_2 MRI contrast behaviour is described. The dual-mode CA (DMCA) capability was evaluated by different means: *in vitro* phantoms, *ex vivo* and *in vivo* MRI, using a preclinical model of murine glioblastoma. The principal advantages of the proposed DMCA in comparison with the commercial CAs lies in the possibility of the simultaneous recording of positive and negative contrast images in a very short period, showing a low toxicity, tumour targeting and biodegradability. These nanosystems are proposed as promising candidates for the development of dual-mode MRI CAs with clear advantages.

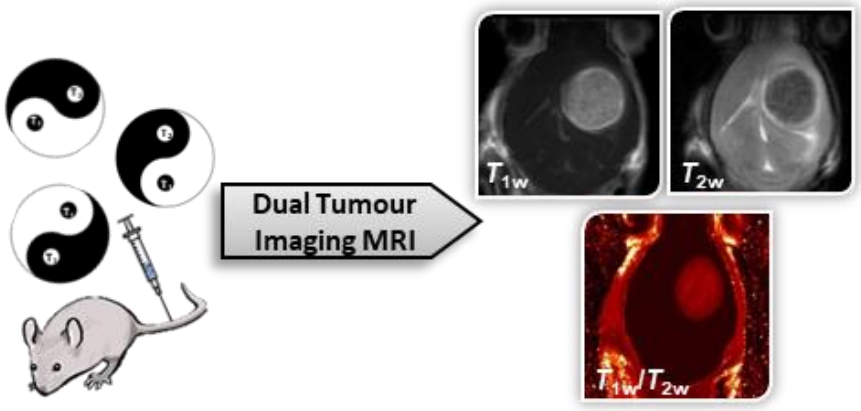

4.2.1 Introduction

There is a plethora of interesting examples of contrast agents (CAs) for clinical imaging technique in the literature, especially for MRI. However, most of them will never reach the market or even clinical trials due to regulatory issues or the difficulty to implement them in the clinical practice. In this section, we will discuss the properties that must to fulfil the MRI CAs for their potential application, the state-of-the-art and the use of coordination chemistry approach for the synthesis of a novel family of CAs for MRI. In this Chapter 4.2, a methodology for the synthesis and complete characterization of novel CAs based on CPs for brain imaging is described. The *ex vivo* and pre-clinical *in vivo* studies were done in collaboration with the *Biomedical Applications of Magnetic Resonance* research group (GABRMN) led by Prof. Carles Arús at the *Universitat Autònoma de Barcelona* (UAB, Cerdanyola del Vallès, Spain) under the supervision of Dr. Ana Paula Candiota and with the contribution of Dr. Nuria Arias-Ramos. The developed systems try to overcome the major drawbacks currently present in the development of CAs and improve the MRI diagnostic tools.

4.2.1.1 The basis of magnetic resonance imaging (MRI)

MRI is a powerful technique for gathering tomographic images of biological soft tissues in a non-invasive manner with a high spatial resolution and depth penetration. This radiation-free technique enables the coding of nuclear magnetization into 2D/3D images, being the most used tool in clinical diagnosis. Though many nuclei can give an MR signal (^{1}H, ^{13}C, ^{23}Na, ^{31}P etc.), only hydrogen nuclei (^{1}H) found in water (in its liquid form) provide sufficient signal for the practical use of MRI.[1] When ^{1}H rich samples are placed in a static magnetic field (Figure 4.5a), $\mathbf{B_0}$, they become polarized, resulting in a net magnetisation aligned (i.e. longitudinal) with the magnetic field.

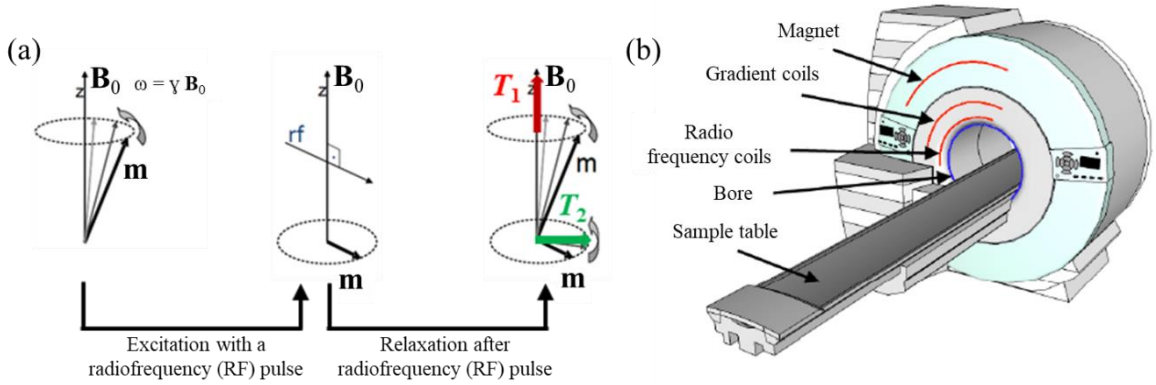

Figure 4.5 (a) Basics of the magnetic resonance phenomenon. After the application of radiofrequency (RF) pulses through a transversal magnetic field ($\mathbf{B_0}$), the relaxation to the equilibrium of the magnetic spins takes place in two different ways: longitudinal (T_1) and transversal(T_2). (b) Schematic set up of clinical magnetic resonance imaging (MRI) equipment. Reproduced from ref. 1.

By using a radiofrequency (RF) coil (Figure 4.5b) tuned to resonate at the Larmor frequency, short pulses of RF radiation excite the nuclear spins, tipping the net magnetization into the plane transverse to $\mathbf{B_0}$. The precession of this transverse magnetization then induces an alternating current in the RF coil, giving the magnetic resonance signal. Further, using magnetic field gradient coils to linearly vary the magnetic field across the sample, causes precession to occur at slightly different frequencies at different locations across the sample; this label the spatial position of the nuclei and is the basis of MRI. One important type of image in MRI is relaxation weighting (w), where the net magnetization returns to equilibrium following an RF pulse. This is described by the return of longitudinal magnetisation (T_1 longitudinal relaxation) and the loss of transverse magnetisation (T_2 transverse relaxation).

The signal intensity of proton-based MRI (^{1}H-MRI) depends on a combination of factors: proton density, T_1 and T_2 relaxivity times and the cell microenvironment.[2,3] However, the contrast observed in MRI as a result of the differences in the intrinsic signal intensity between tissues is not enough for obtaining accurate and sensitive diagnosis. The quality of the images provided after an MRI acquisition usually do not allow differentiating properly the different pathological situations (e.g. tumours). For these reasons, the use of exogenous CAs in MRI diagnosis is needed in order to improve image resolution by enhancing the natural contrast due to their selective accumulation in the region of interest (ROI). CAs can shorten longitudinal and transverse relaxation of protons respectively causing a positive enhancement (i.e., brighter image) in T_1-weighted (T_{1w}) MRI and negative enhancement (i.e. darker image) in T_2-weighted (T_{2w}) MRI in comparison with pre-contrast images.[4-6]

4.2.1.2 State-of-the-art of contrast agents (CAs): The use of NCPs for MRI

The first MRI CA (gadopentetate dimeglumine or Magnevist® as commercial product) was made clinically available in 1988 for imaging blood-brain barrier (BBB) abnormalities. Since then, an exponential increase of investigations has been done to find new agents for MRI diagnosis. There is a big family of gadolinium-based CAs (GBCAs) which are the most used in clinical examinations. However, as natural expansion of the research, other metals have been studied for their use as CAs in order to overcome some drawbacks of GBCAs. In this section, some of the latest examples will be briefly discussed.

Up today, a dozen MRI CAs have been approved by the FDA agency. Of these twelve, only 8 are still commercially available in the United States.[7] All of the 8 commercial MRI CAs are based on small molecules of Gd(III) complexes. Seven of the commercially available agents received their primary indication for imaging lesions of the central nervous system (CNS), but one agent (Gd-EOB-DTPA) received the approval for liver imaging. There are four MR CAs that have FDA approval but

are no longer currently marketed. The Gd(III)-based complex MS-325 was approved for angiographic (blood vessel) imaging. Furthermore, a Mn(II)-based complex (Mn-DPDP) and a SPIONs system (ferumoxide) were approved for liver imaging. Unfortunately, most of the T_1 and T_2 CAs clinically approved for MRI diagnosis have associated several disadvantages. Most of T_1 CAs are based on paramagnetic GBCAs complexes.[8] The presence of Gd(III) has been related with some technical issues and health risks such as headache, nausea, dizziness and severe nephrogenic system fibrosis (NSF).[9-13] Furthermore, long-term deposition of Gd in the human brain due to their incomplete clearance from the organism, has been recently reported.[14,15] Apart from Gd, paramagnetic Mn(II) has been presented as alternative CAs for T_{1w} images. However, the accumulative toxicity arising from Mn(II) which induces neurological degeneration or oxidative stress in cells, might limit its clinical application. On the other hand, typical CA in T_{2w} images are generally based on SPIONs or ferrites.[16,17] Nevertheless, the analysis process of resulting T_{2w} images are laborious due to the low signal body regions that can be confused with haemorrhages, calcifications, fat, blood clots and other possible artefacts in damaged tissue.[18] Nowadays, no T_2 CA is used in the clinics in the Europe. There are only two cases that were approved: Sinerem ® withdrawn since 2007 and Endorem ® which its production has been stopped since 2008. For this reason, the study and development of new and improved T_2 CAs is necessary in order to exploit their properties and benefit society from the use of safe, effective and biodegradable probes as CAs for MRI application.

Recently, NCPs has been proposed as good candidates for their potential use as CAs. Thanks to the rational design that coordination chemistry offers, it is possible to synthesize different complexes by the combination of organic ligands and MRI-active metals, structured or integrate them into a nanoplatform and obtain effective systems as CAs for MRI. The potential multifunctionality of these nanosystems implies longer blood circulation times as compared to common chelates, less metal leaching, and grater area between magnetically centres and the tissue due to the increased surface-to-volume ratio.

4.2.1.3 Dual-mode MRI and dual-mode contrast agents (DMCAs)

At this point, and despite extensive research has been carried out to obtain novel MRI CAs, the single mode CAs are far from being optimum. Current CAs exhibit major limitations in terms of MRI artefacts, imaging ambiguities and health risks. In order to overcome these limitations, a great effort has been done in the combination of techniques in order to stablish dual-imaging procedures (e.g. PET/MRI). This strategy tries to take advantages of the synergistic combination between them (Figure 4.6).

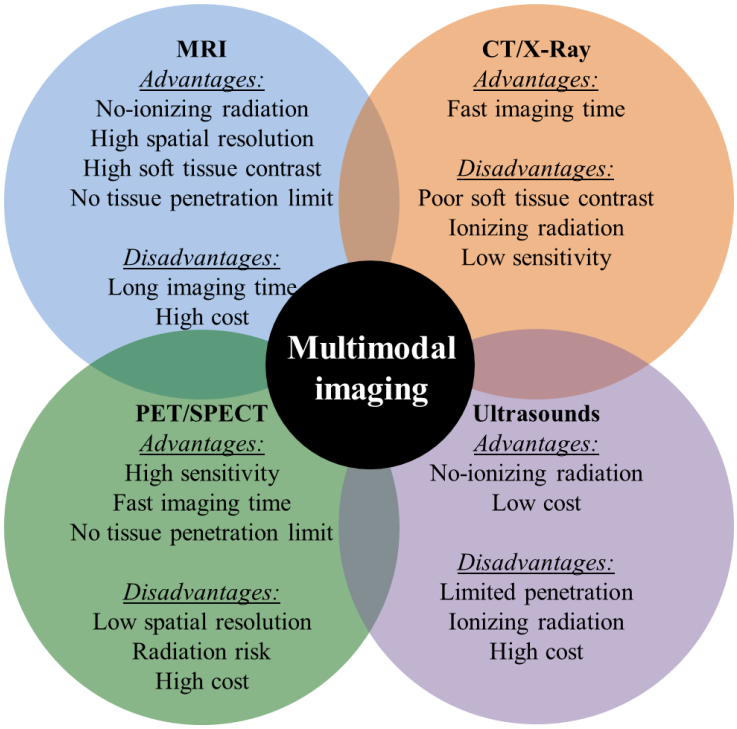

Figure 4.6 Features of the main imaging modalities.

In the literature there are different examples of systems with the ability to be active in more than one MI technique.[19,20] For example, Jin *et al.* reported the combination of MRI/PET in a single platform.[21] In their work, the synthesis of ultra-small iron-gallic acid NCPs (Fe-Ga NCPs) for the incorporation of Cu-64 as radiotracer was shown. Nevertheless, the quantitative determination of relaxivity parameters highlighted that these NCPs can act as moderate T_1 CA due to their low longitudinal relaxivity (r_1 = 3.5 mM^{-1} s^{-1}). This fact was compensated with a low transversal relaxivity value (r_2 = 0.97 mM^{-1} s^{-1}) that decreased the r_2/r_1 ratio, conferring a T_{1W}-dominated CA. Most recently, Chen and co-workers reported the formation of polyphenol-based nanoplatforms for MRI/PET dual-modality imaging.[22] The authors described the strategy for the formation of polymeric structures through the coordination of metals (Fe(III), Mn(II) and Zr-89) with polyphenol-based ligands yielding nanostructures which efficiently accumulated in the tumour. These two examples highlighted the increasing interest for the development of multimodal imaging platforms. Although from a scientific point of view the multimodal imaging platforms present interesting aspects, from the point of view of practicality and translation to the clinic they find several obstacles still very difficult to overcome. Currently there are no clinical available hybrid systems that combine different techniques in a single equipment, thus hindering the patient examination. For this reason, dual-modal MRI has demonstrated enough merits and good perspectives in practical diagnosis to avoid such limitations by simply adjusting the acquisition sequences.[23] Furthermore, T_1/T_2 dual-mode MRI is performed by single scanner, ensuring a perfect match of spatial and temporal imaging parameters being more beneficial compared to other bimodal imaging techniques.[24,25]

In this scenario, the development of novel T_1/T_2 dual-mode contrast agents (DMCAs) with clinical proof of their in vivo performance is a pressing concern. DMCAs can be selectively tuned to visualize by bright or dark T_{1w} and T_{2w} images in order to obtain complementary and more precise information by cross-validation of the possible false-positives.[26]

The synthesis of T_1/T_2 DMCAs in a single platform is currently a challenge. In this sense, different strategies based on nanoscale engineering have been developed during the last years. These strategies consisted mainly in i) direct conjugation of T_1 compounds (e.g., Gd or Mn-containing systems) and T_2 compounds (e.g., SPIONs).[20,27-29] (ii) T_2 materials doped with T_1 contrast materials;[19,30-32] (iii) magnetic nanoparticles with rational modulation of size and magnetization;[5,33] and (iv) integration of T_1 contrast materials with non-magnetic porous materials.[34-37] However, these strategies are often involved in laborious procedures with multi-step synthesis. Furthermore, the possibility of quenching effect between T_1 and T_2 due to the interaction between both relaxation times, requires a delicate control limiting their production and clinical applications.[22]

Based on this rationale some NCPs have been reported recently as DMCAs. Different approaches for synthesizing DMCAs are: Eu co-doping of a Gd NCP complex,[38] the use of porphyrin ligands for the chelation of Fe,[39] or polydopamine-based coordination complex and its affinity for Fe ions.[32]

4.2.1.3.1 Previous developments in our group: The case of hybrid SPION@NCPs

Encouragingly, previous studies showed that biodegradable NCPs could provide T_{1w} properties and be combined with T_{2w} CAs to obtain nanosystems with dual-mode MRI properties.[40] Our group reported in the past a hybrid T_1/T_2 system by the encapsulation of SPIONs (acting as T_2 CA) into an iron-based CP (acting as T_1 CA) (Figure 4.7).

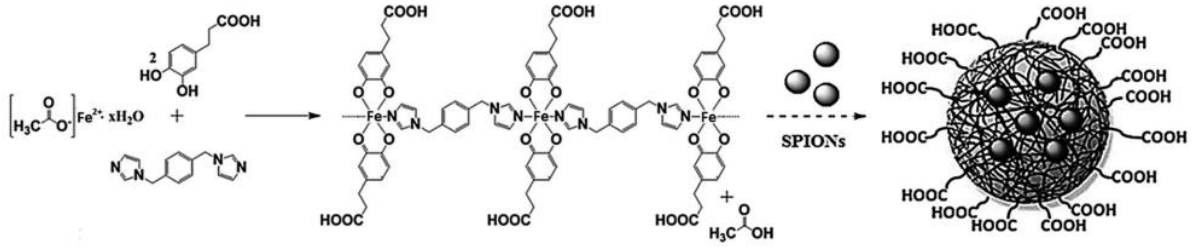

Figure 4.7 Synthesis of Fe-based CP and in situ encapsulation of SPIONs to generate the hybrid nanomaterial SPION@CPP-Fe. Reproduced from ref. 40.

The results demonstrated the excellent performance of the Fe-based CP as a dual T_1/T_2 CA for MRI with values similar to the commercial CAs or related Fe(III) complexes. Additionally, the developed nanosystem showed notable robustness in a wide range of pH and no toxicity. Following this strategy, we developed a set of NCPs as CAs with potential dual-mode behaviour *in vitro* and *in vivo*, which are presented in this Chapter.

4.2.1.4 Nanoparticles as brain tumour CAs: The case of glioblastoma

In this work, we present the synthesis of NCPs complexes for its potential use as CA of a glioblastoma. The glioblastoma is one of the most common and lethal tumours of the central nervous system.[41] It belongs to malignant gliomas which are a group of heterogeneous and invasive brain tumours derived from glial cells. As reported, the 5-year survival rate for glioblastoma is limited to 5%.[42] Despite of remarkable advances in basic and clinical research, the clinicians are yet unable to provide realistic therapy for this kind of tumours. For this reason, providing to the community with novel systems which enhances its early diagnosis could help to the increase of the effectiveness of therapies. Nanoparticles have being used in clinical studies and pre-clinical models for different applications in brain tumours for its improvement from a diagnosis and therapy point of view.[43-45] The main challenge of a nanosystem to reach the brain is to cross the BBB and the most used strategy is the attachment of peptides on the nanoparticle surface that act as BBB shuttle.[46] Nevertheless, some brain diseases in advanced stage have the BBB compromised as in the case of glioblastoma. In this specific pathology, the BBB becomes permeable to different molecules and the microenvironment involved changes, creating a disorganization of vessel structures resulting in an uncontrolled cell migration and in abnormal vascular architecture.[47] In this scenario, nanoparticles can play an important role especially in the area of CAs by crossing the BBB and enhancing the tumour imaging. Currently, most of the examples of nanoplatforms able to cross the BBB for the treatment and diagnosis of tumour brains are related with gold- and iron-based nanoparticles.[47,48] Gold nanoparticles has demonstrated their successful accumulation in tumours for hours allowing the imaging of the affected area by MRI. Nevertheless, there is still no evidence of their use in clinical trials mainly due to their unclear interaction with the metabolism and their potential toxic effects on humans. Regarding iron-based nanoparticles, although the SPIONs systems have emerged as a good candidate for brain imaging, their potential us is still limited due to the need of detailed understanding of their *in vivo* effects.

As we have seen, toxicity issues related with solid metal nanoparticles force to researchers to develop more efficient, safer alternatives with greater tuneability options. Based on this, we proposed in this work for the first time the use of NCPs as potential candidates for the imaging of glioblastoma tumours. Furthermore, we used MRI as the gold standard equipment for the diagnosis and pre-surgical planning of brain imaging.

4.2.1.5 Present challenges

Despite the progress of DMCAs, some questions remain to be addressed before the clinical application of DMCAs becomes a reality:

i. Facile and cheap synthesis procedures with possibilities for scale up
ii. Chemical stability in biological environment by non- toxicity and non-accumulation in the organism (e. g. avoiding the use of Gd and Mn ions)
iii. High efficiency in different tissues by good biodistribution
iv. *In vitro* and *in vivo* proof of their performance

These key parameters must be considered during the rational design of novel DMCAs overcoming the main drawbacks of current clinical approved CAs. Therefore, there is still need to overcome the disadvantages of single modality CAs by the preparation of robust DMCAs which are supposed to minimize the risks of ambiguity and improve the diagnostic sensitivity. Furthermore, in case of brain tumours, the information provided by a T_2 and especially by a DMCA in its diagnosis or monitoring, is not fully evaluated yet.

4.2.1.6 Our choice

The knowledge of our group in the development of NCPs was the starting point in this work for the successful synthesis of NCPs-based MRI CAs. In this Chapter, the synthetic protocol included the polymerization process of different coordination complexes obtained by the combination of ligands such as 1,4-Bis(imidazol-1-ylmethyl)benzene (**L3**, Bix), 3,4-dihydroxycinnamic acid (**L4**, dhc) and diethylenetriaminepentaacetic acid (**L5**, DTPA) with a variety of metal salts (Fe(II), Mn(II) and Gd(III)) for the synthesis of a set of MRI-active NCPs (Figure 4.8). Through this rationale design, four NCPs complexes were obtained: **Fe-NCP**, **Gd-NCP**, **Mn-NCP** and **GdDTPA-NCP**. All the systems were fully characterized by different physicochemical techniques and its behaviour in physiological medium *in vitro* and *in vivo* was tested.

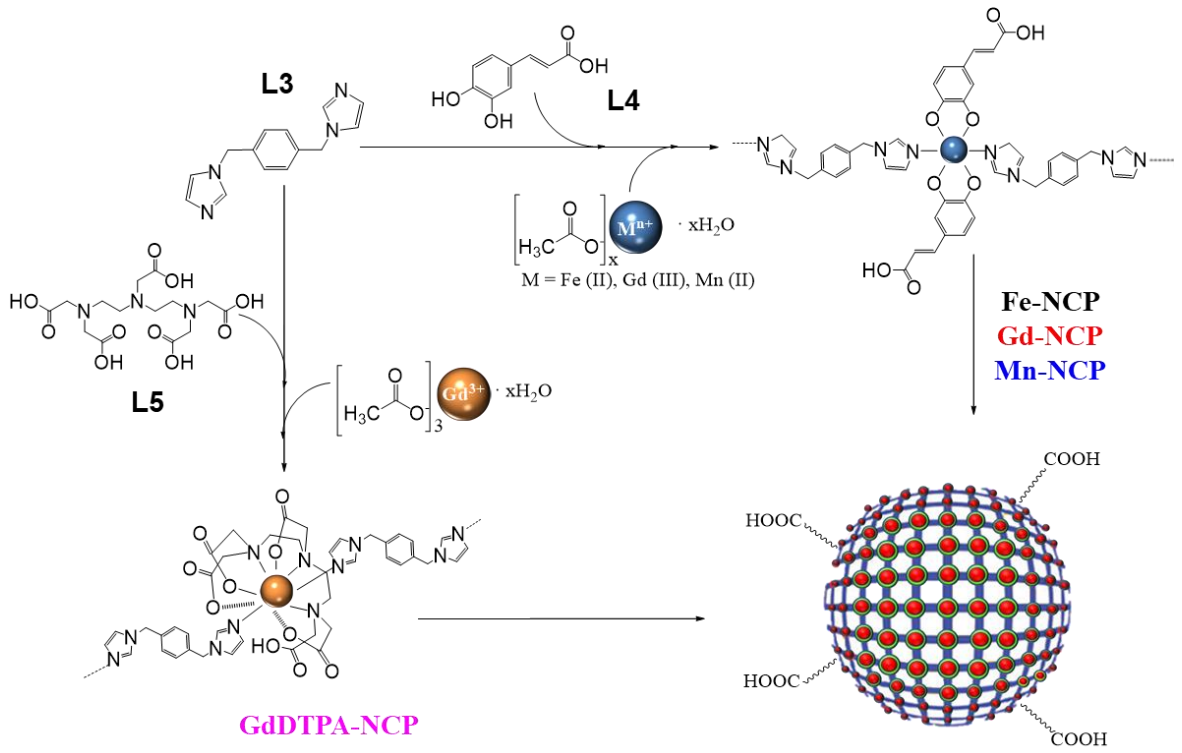

Figure 4.8 Scheme for the synthesis of the different NCPs complexes developed in this work. From the **L3** together with **L4** and combining them with Fe(II), Gd(III) and Mn(II) metal salts, three NCPs complexes were synthesized: **Fe-NCP**, **Gd-NCP** and **Mn-NCP**. Following similar strategy, **L3** was combined with **L5** and Gd(III) metal salt for the synthesis of **GdDTPA-NCP**.

Most of the clinically approved CAs are not able to cross the intact BBB but can reach a lesion if at some point the BBB is disrupted as in the case of glioblastoma tumours.[49] For this reason, the model selected for the *in vivo* studies was the GL261 murine model. The immunocompetent GL261 mouse glioma line is one of the most widely used to study the glioblastoma disease and is usually inoculated into C57BL/6 strain, resulting in invasive and infiltrative tumours, characteristics which can be similarly found in human patients with glioblastoma.[50]

4.2.1.7 Objectives

With the aim to overcome the challenges aforementioned, different objectives were proposed derived from the following two main goals:

- Design, synthesis and characterization of novel NCPs based on active MRI ions (Fe(III), Gd(III) and Mn(II)) for their use as DMCAs for glioblastoma imaging
- The systems must accomplish i) moderate chemical stability, ii) water-colloidal stability, iii) low toxicity and biocompatibility, iv) intrinsic T_1 and T_2 imaging activity *in vitro* and *in vivo* and v) good biodistribution with low up-take by liver and kidneys.

The steps followed for the achievement of the main goals were the following:

i. Synthesis of complexes **Fe-NCP**, **Gd-NCP**, **Mn-NCP** and **GdDTPA-NCP**
ii. Complete physicochemical and biological characterization *in vitro*
iii. Pre-clinical *in vivo* studies with a glioblastoma mice model
iv. Comparison with commercial CAs

In this work we show how the coordination chemistry allows the successfully design of novel NCPs that incorporate MRI-active metals polymerised with organic ligands. Furthermore, the dual activity of one of the systems will allow its transfer to pre-clinical studies to evaluate its performance in an *in vivo* environment.

4.2.2 Results and discussion

4.2.2.1 Synthesis of the NCPs complexes

The synthesis of NCPs containing three different paramagnetic ions widely used as CAs for MRI (Fe(III), Gd(III) and Mn(II)) was achieved. The NCPs where synthesized using a previously published methodology[51] through the reaction of $Fe(CH_3COO)_2$, $Gd(CH_3COO)_3 \cdot 6H_2O$ or $Mn(CH_3COO)_3$ metal salts with **L3**and **L4** as a co-ligand in a 1:1:2 molar ratio and using EtOH as solvent. These reactions afforded the formation of the nanoparticles named **Fe-NCP**, **Gd-NCP** and **Mn-NCP**, respectively (Figure 4.9).

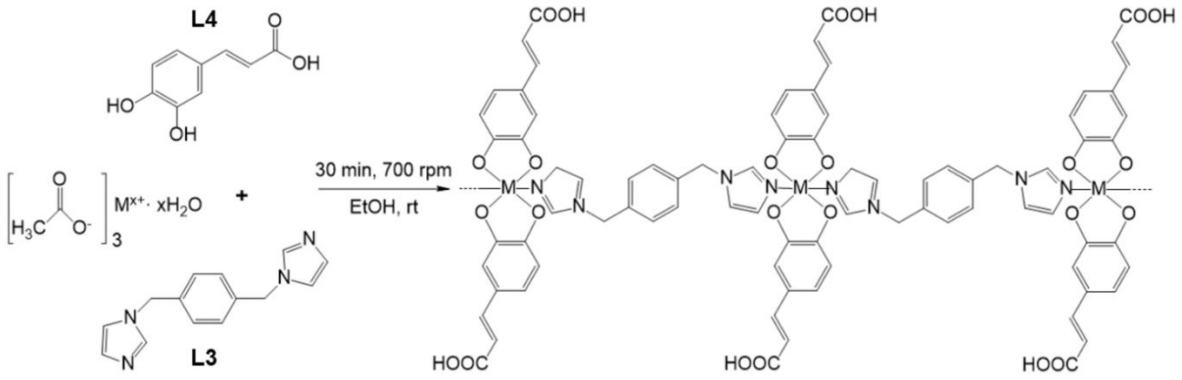

Figure 4.9 Synthesis of the NCPs complexes. The metallic salts M stands for Fe(II), Gd(III) and Mn(II) for **Fe-NCP**, **Gd-NCP** and **Mn-NCP**, respectively.

Alternatively, the polymerisation of the well-known commercial CA for MRI Gadopentetate dimeglumine (GdDTPA, **Gd-L5**) was tested. Different approaches were followed until the successful polymerisation of the GdDTPA unit (Figure 4.10). The first approach consisted on the polymerisation of the commercial GdDTPA-chelate with **L3**. Nevertheless, all the parameters tested in the reactions

did not allow the properly polymerisation of the chelate (Figure 4.10a). The only possible strategy for the polymerisation of the complex was to add the reactants separately before the formation of the chelation complex between the Gd(III) ions and the **L5** and generate *in situ* the GdDTPA complex. In this approach, the polymerisation reaction took place by the direct mixing of an aqueous solution containing $Gd(CH_3COO)_3 \cdot 6H_2O$ with the **L3** and **L5** as a co-ligand in EtOH allowed the polymerisation and consequent precipitation of the NCPs (Figure 4.10b).

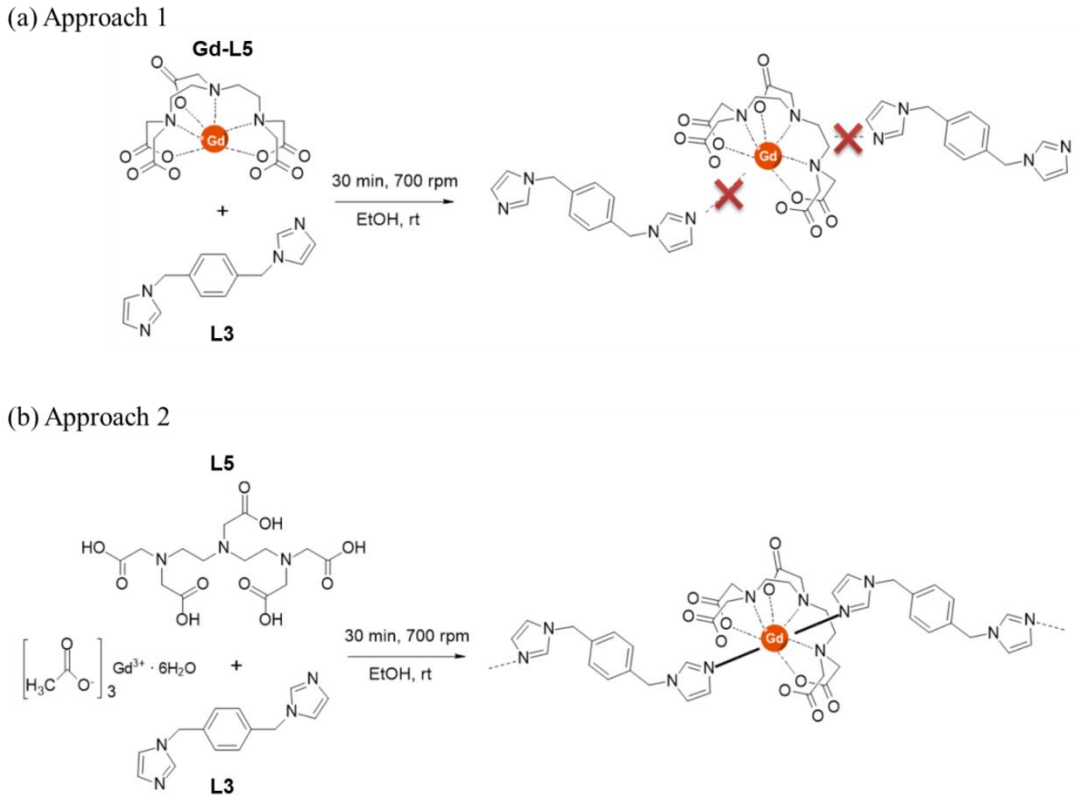

Figure 4.10 Synthesis approaches for the GdDTPA-NCP complex. (a) The approach 1 which consisted on the reaction of the GdDTPA complex with the ligand **L3**, which did not form the expected polymerisation. (b) The separately mixture of the ligands **L3** and **L5** without its chelation with Gd, allowed the polymerisation of the **GdDTPA-NCP** complex.

Similar situation was found for the polymerisation of the Manganese-based commercial CA (Mangafodipir trisodium, MnDPDP, **Mn-L6**) (Figure 4.11). The first approach consisted on the polymerisation of the commercial MnDPDP-chelate with **L3**. However, all the attempts were unsuccessful and the coordination of the MnDPDP-chelate was not achieved (Figure 4.11a). At this point, we thought that due to steric hindrance the **L3** ligand was not able to coordinate with the metal centre. For this reason, we decide to change the ligand for a similar one but with less rigidity (Figure 4.11b). This ligand consisted of 1,6-Bis(imidazol-1-yl)hexane (**L7**) with longer aliphatic chain compared with **L3** allowing the coordination with the MnDPDP-chelate. This longer chain of C_6 conferred to the ligand enough flexibility for the formation of a coordination bond with the manganese-metal centre of the MnDPDP-chelate. Nevertheless, the resulting polymer showed very

low reproducibility and not enough chemical stability in aqueous solution and, for this reason, the system was discarded for further studies.

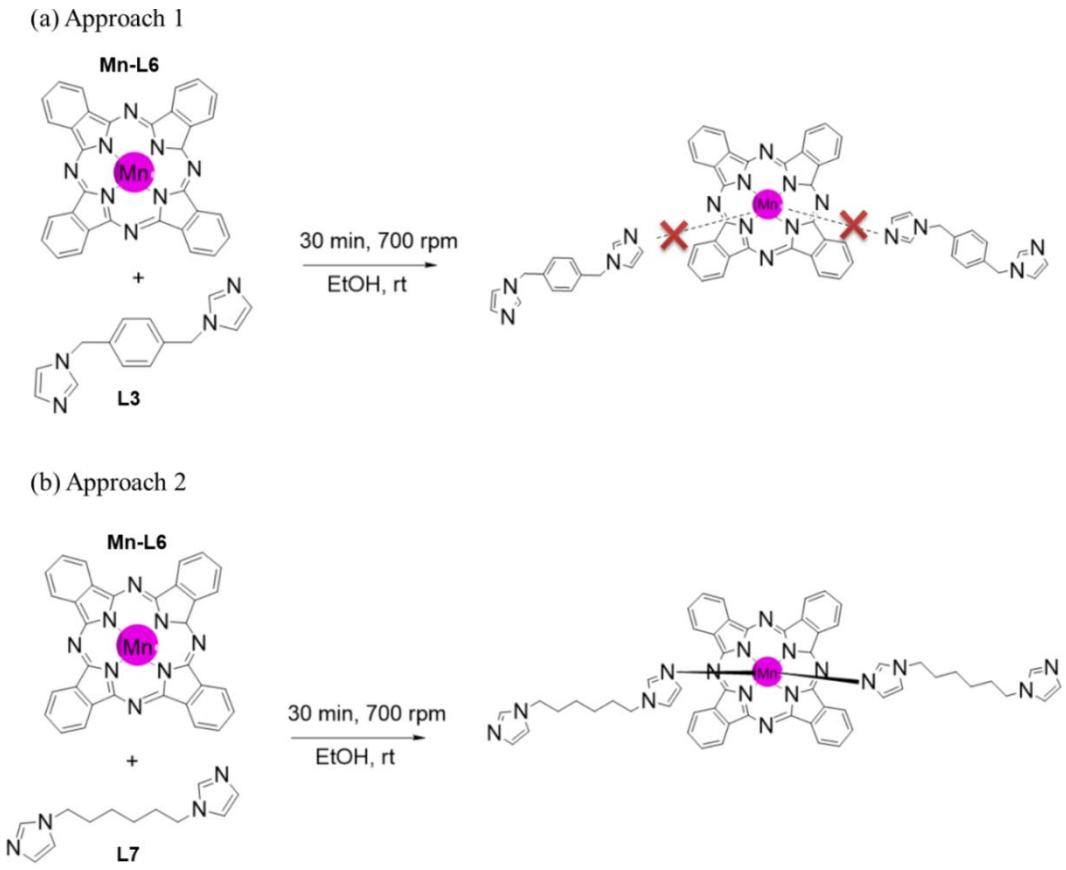

Figure 4.11 Synthesis approaches for the **MnDPDP-NCP** complex. (a) The approach 1 which consisted on the reaction of the MnDPDP complex with the ligand **L3** did not form the expected polymerization. (b) The use of a more flexible ligand (**L7**) allowed the polymerization of the **MnDPDP-NCP** complex.

Finally, the methodology of the synthesis for all the NCPs complexes was optimized and set up as represented in Figure 4.12:

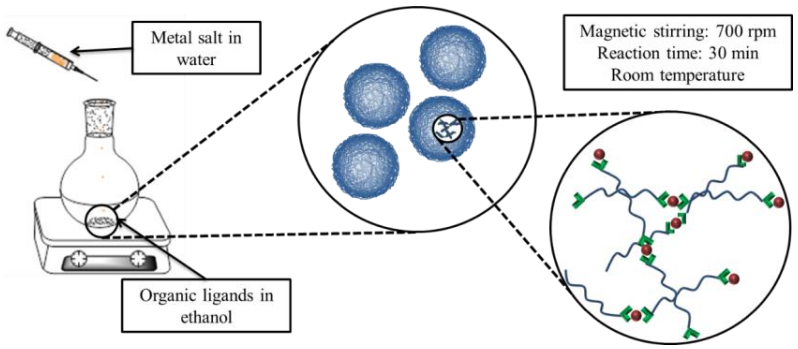

Figure 4.12 Solvent-induced precipitation method for the synthesis of **Fe-NCP**, **Gd-NCP**, **Mn-NCP** and **GdTPA-NCP**.

4.2.2.2 Characterization

4.2.2.2.1 Morphology and size

The morphology and size of the NCPs in solid state were characterized by SEM (Figure 4.13). The results showed the formation of homogenous spherical nanoparticles with diameter of: 45 ± 5 nm (**Fe-NCP**), 70 ± 3 nm (**Gd-NCP**), 130 ± 7 nm (**Mn-NCP**) and 75 ± 8 nm (**GdDTPA-NCP**).

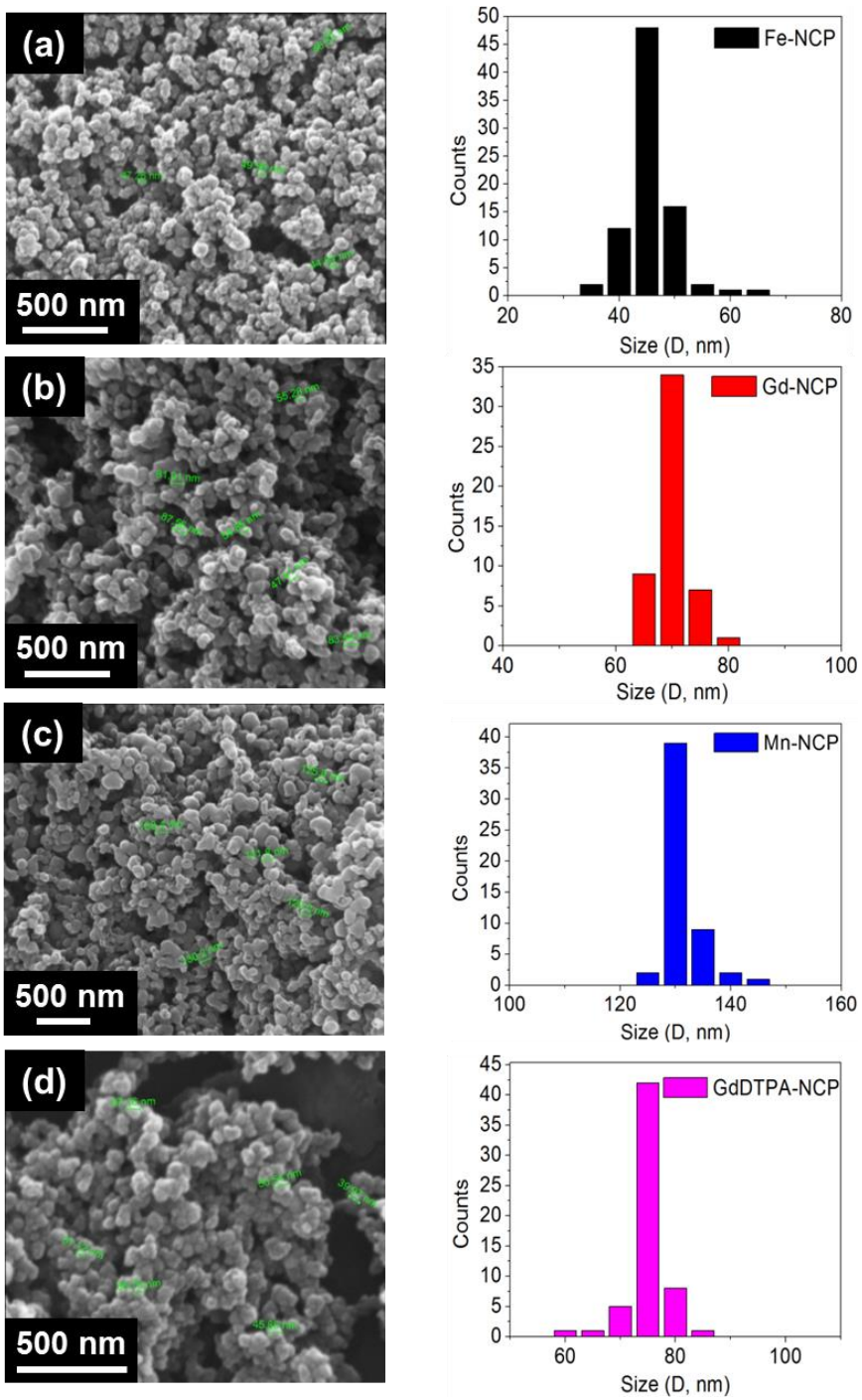

Figure 4.13 SEM images for (a) **Fe-NCP**, (b) **Gd-NCP**, (c) **Mn-NCP** and (d) **GdDTPA-NCP**. Next to each SEM image, the corresponding size histogram for each NCP complex is shown.

Additionally, the stability of the NCPs in simulated physiological medium was evaluated. The NCPs were redispersed in phosphate buffer saline (PBS) and the hydrodynamic size was measured by DLS. The measurements showed higher hydrodynamic diameters in comparison with SEM measurements, since the diameter that is obtained by this technique is the diameter of a sphere that depend not only on the size of the particle core, but also on any surface structure, as well as the concentration and type of ions in the medium. In general, good monodispersion values (PDI < 0.20) and colloidal stability were found for all samples, except for the Mn-based NCP (**Mn-NCP**), which start to aggregate in a relatively short time (sedimentation observed after 1 h). This aggregation process can be related to the surface charge or the low chemical stability of the nanoparticles in water. Indeed, the ξ-potential measurements of the NCPs showed strong negative values for Fe and Gd-based NCPs (-31.2 and -27.2 mV, respectively). Otherwise, Mn-NCP shows weaker ξ-potential values (-15.4 mV) inducing low electrical repulsion between the nanoparticles (Table 4.2).

Table 4.2 Comparison of size distribution (including standard deviation values) and ξ-potential for NCPs in different media.

NCP system	SEM (nm)	PBS		PBS-BSA	
		DLS (nm)	ξ-Pot. (mV)	DLS (nm)	ξ-Pot. (mV)
Fe-NCP	45 ± 5	97 ± 32	-31.2	56 ± 21	-19.1
Gd-NCP	70 ± 3	121 ± 23	-27.2	73 ± 18	-14.7
Mn-NCP	130 ± 7	189 ± 21	-15.4	151 ± 23	-2.20
GdDTPA-NCP	75 ± 8	143 ± 17	-23.9	80 ± 15	-11.9

With the aim to mimic the physiological environment and improve the colloidal stability of the NCPs, the nanoparticles were dispersed in a solution containing PBS and BSA (0.5 mM) at physiological conditions.[52,53] The results obtained demonstrated an improvement on the dispersions and colloidal stability of the NCPs in aqueous media, reducing the visible aggregation and showing hydrodynamic diameters close to the mean size values obtained by SEM (Table 4.2 and Figure 4.14).

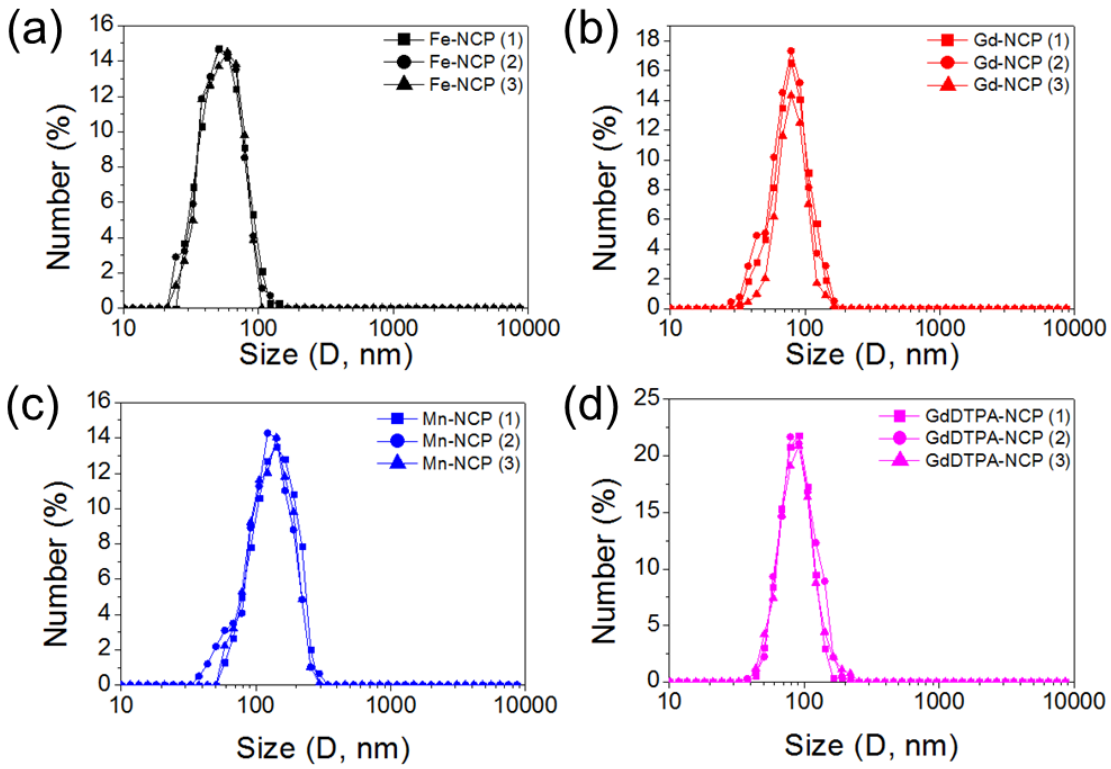

Figure 4.14 Dynamic light scattering (DLS) measurements for (a) **Fe-NCP**, (b) **Gd-NCP**, (c) **Mn-NCP** and (d) **GdDTPA-NCP** systems redispersed in PBS-BSA. The average distribution size is shown with its corresponding deviation. D: hydrodynamic diameter.

All the measurements were done by triplicate and along the time, showing the high colloidal stability of the NCPs-BSA complex in PBS. The nanoparticles stabilized with PBS-BSA showed higher hydrodynamic diameter being the **Mn-NCP** the biggest system (Figure 4.15).

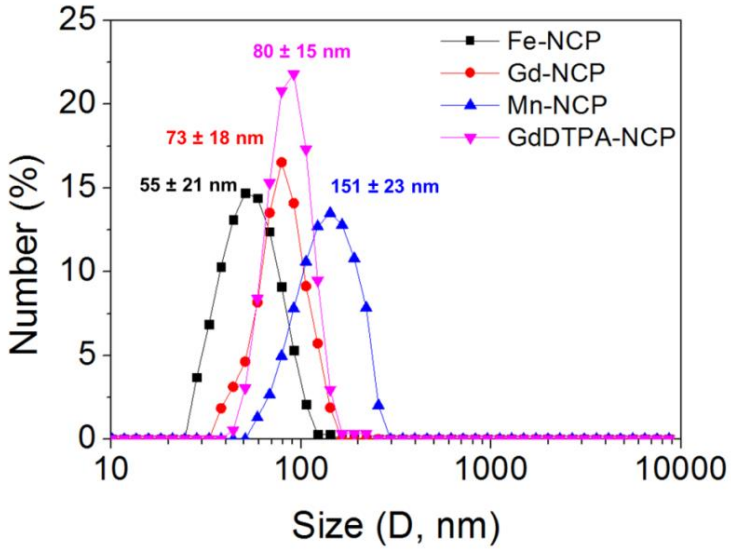

Figure 4.15. Size comparison between the NCPs system synthesized and redispersed in PBS-BSA. The average distribution size is shown with its corresponding deviation. D: hydrodynamic diameter.

4.2.2.2.2 Chemical characterization

The amorphous nature of the NCPs synthesized, as confirmed by powder XRD (Figure 4.16), made it necessary the use of several characterization techniques in order to study and confirm the chemical composition and coordination structure. For this reason, the chemical characterization of the resulting nanoparticles was performed by different complementary techniques. The coordination of the metals with the organic ligands was confirmed by FT-IR spectroscopy. The spectra obtained for **Fe**/**Gd**/**Mn-NCPs** showed the almost disappearance of the bands corresponding to the catechol –OH groups of **L4** in the range of ν = 3000-3500 cm^{-1}, denoting their deprotonation for the coordination with the corresponding metal (Figure 4.17).

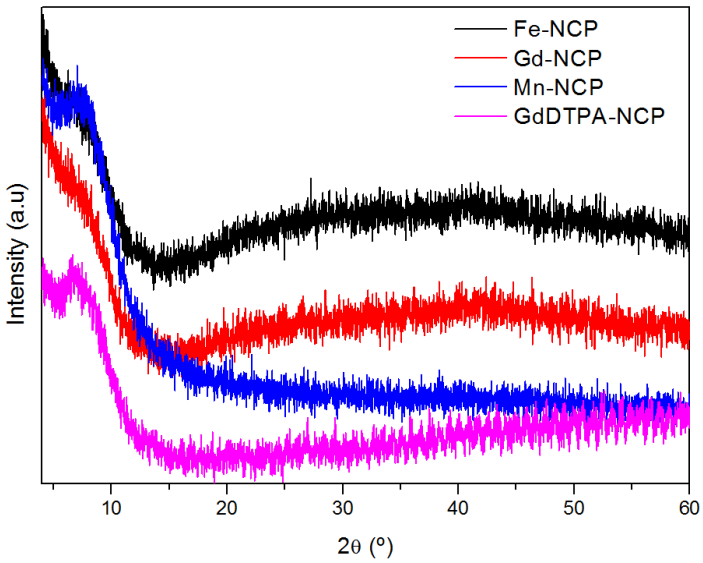

Figure 4.16 PXRD spectra of the different samples. a.u: Arbitrary units.

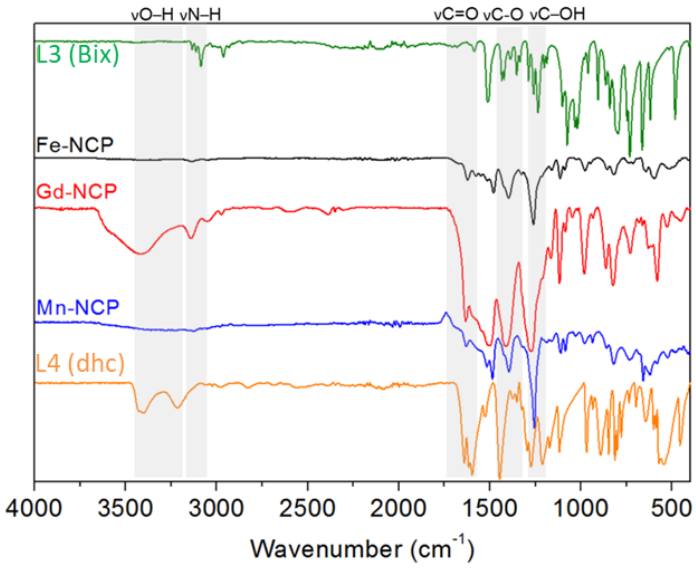

Figure 4.17 FT-IR spectrum for the **Fe-NCP**, **Gd-NCP** and **Mn-NCP** complexes. For comparison, the spectra of **L3** and **L4** are showed.

Moreover, the vibration band assigned to a C–O stretch for the catechol coordinated to the metal appeared in the range 1400-1420 cm^{-1}. The prevalence of carboxylic acid groups was confirmed by the presence of the characteristic vibrational bands of C=O and C–OH in the range ν = 1650-1580 cm^{-1} and 1250-1200 cm^{-1}, respectively. Additionally, typical vibrational bands of **L3** (ν = 1520, 1232, 1105 cm^{-1}) were observed in the IR spectra. In the specific case of **GdDTPA-NCP**, the coordination of the carboxylic groups to Gd(III) ions, was confirmed by the presence of the characteristic vibrational bands of the COO^- carboxylate group at ν = 1590 cm^{-1} and ν = 1380 cm^{-1} (Figure 4.18).

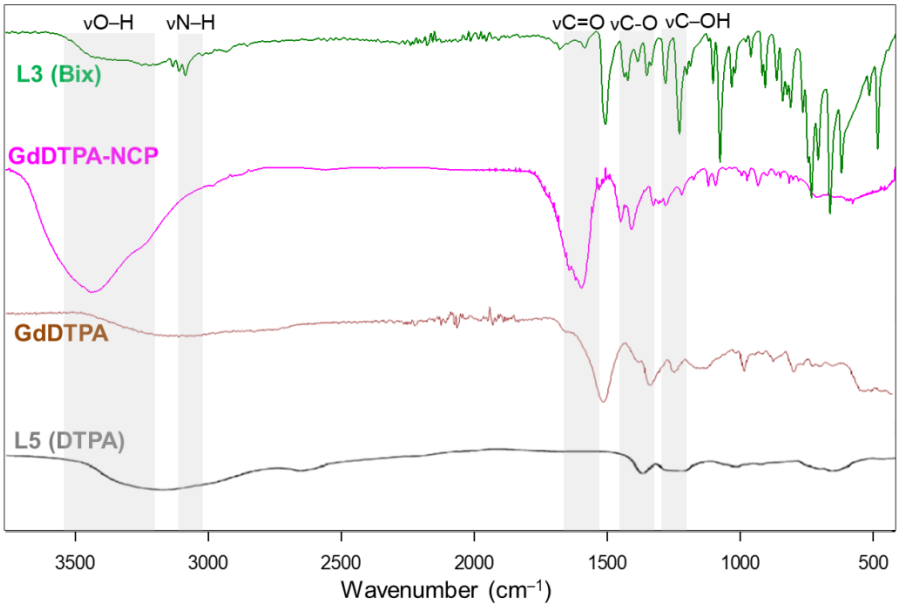

Figure 4.18 FT-IR spectrum for the **GdDTPA-NCP** complex. For comparison, the spectra of **L3** and **L5** are showed.

The comparison between **GdDTPA-NCP** complex and the Gd commercial CA (GdDTPA) FT-IR spectra, reflected a good agreement on GdDTPA related signals and the presence of the additional peaks corresponding to the Bix (**L3**) ligand used as linker between metal centres (Figure 4.18). The FT-IR spectroscopy allowed to elucidate the infrared patterning of the NCPs synthesized. However, more information on the chemical composition was needed in order to assure the formation of the expected systems and stablish a chemical formula for the resulting material.

In order to shed more light in this issue, the XPS measurements were performed for the analysis of atomic chemical bonding of the NCPs complexes deposited on silicon substrates by drop casting method. In all the cases, the C1s, N1s and O1s peaks yielded a very similar spectrum as expected and appeared in closely position for each specific system confirming a similar coordinative environment (Figure 4.19).

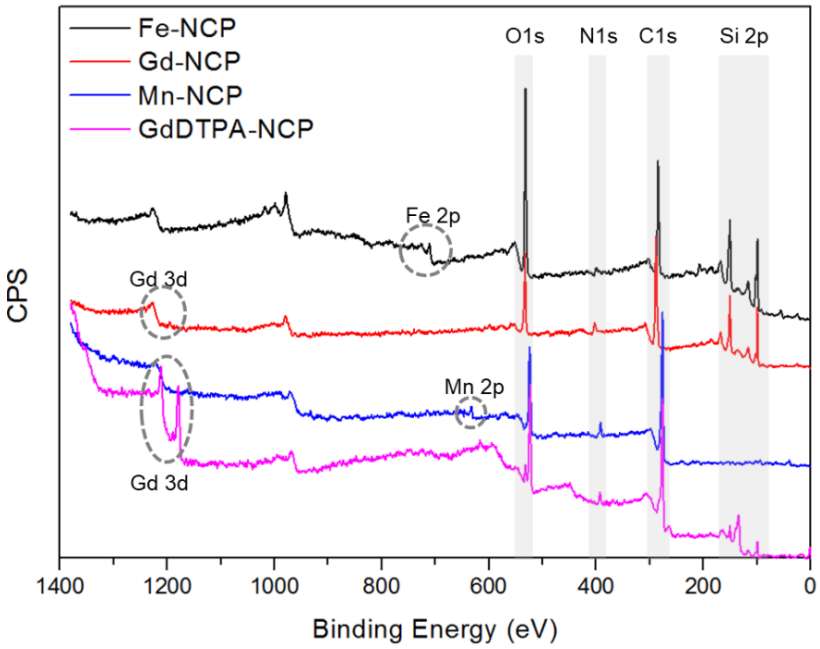

Figure 4.19 X-ray photoelectron spectroscopy (XPS) spectra of the NCPs systems deposited on silicon substrate. CPS: Counts per second.

To study in detail the bonding environment of the different NCPs, high-resolution XPS curve-fitting was performed. Figure 4.20 and 4.21 shows the XPS spectra with the fitting results for each peak of the four NCPs complexes. In the case of **Fe-NCP** and **Mn-NCP** for the C1s band, three peaks were properly fitted, which would correspond to three chemical environments. The peaks confirmed the presence of C–O and the C–N aromatic contribution from the **L3** ligand. Additionally, in the Gd-based NCPs a fifth peak appeared which was attributed to the C=O double bond, confirming the presence of the carboxylic groups exposed on the surface of the nanoparticles (Figure 4.20). The N1s spectra of all the complexes confirmed the presence of C–N and C=N assigned to the aromatic rings of the **L3** ligand. For the O1s spectra, the presence of the C–O and C=O was confirmed thus indicating the retention of free carboxylic groups on the NCPs synthesized. Interestingly, the O1s spectra demonstrated the coordination of the Gd(III) ions through the O by the presence of the Gd-O peak (Figure 4.21).

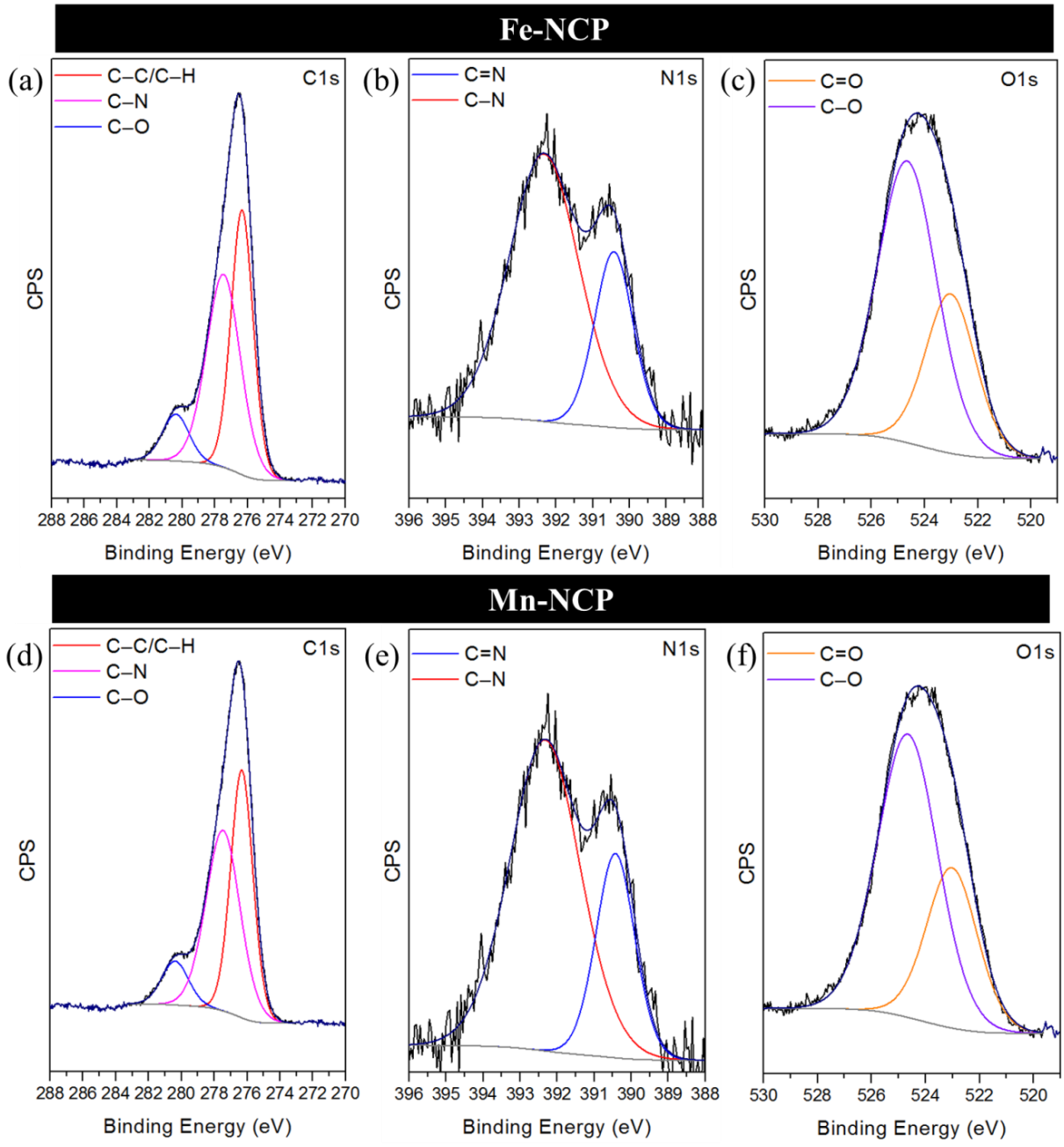

Figure 4.20 Curve-fitting results for C1s, N1s and O1s high resolution spectra corresponding to the (a,b,c) **Fe-NCP** and (d,e,f) **Mn-NCP** complexes. CPS: Counts per second.

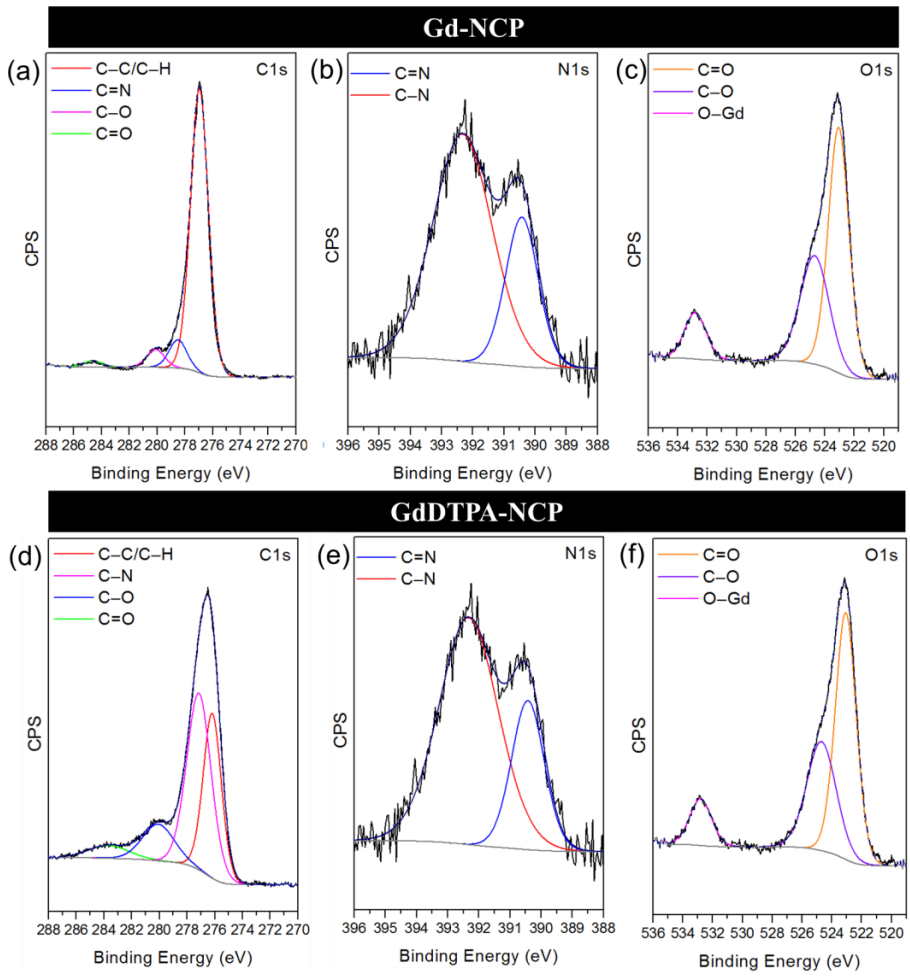

Figure 4.21 Curve-fitting results for C1s, N1s and O1s high resolution spectra corresponding to the (a,b,c) **Gd-NCP** and (d,e,f) GdDTPA-NCP complexes. CPS: Counts per second.

Finally, XPS measurements confirmed the presence and the oxidation state of the metals being Fe(III), Gd(III) and Mn(II) in each case (Figure 4.22).

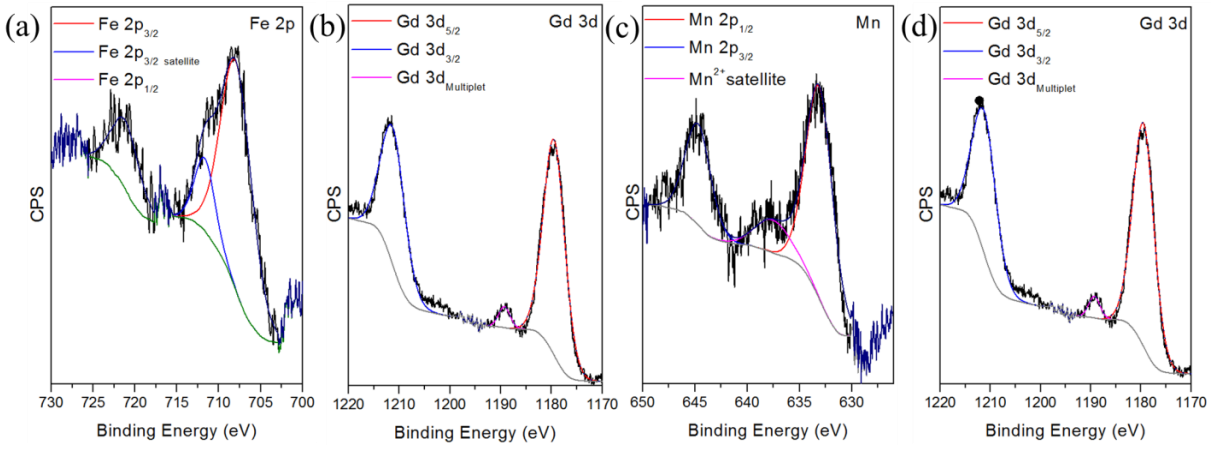

Figure 4.22 Gd 3d Metal-high resolution spectra corresponding to the Fe 2p, Gd 3d and Mn 2p present in the corresponding NCPs.

Additionally, Mössbauer spectroscopy confirms that Fe-NCP show a high-spin Fe(III) oxidation state (Figure 4.23), thus confirming the oxidation process from Fe(II) to Fe(III) during the synthesis of the **Fe-NCP**. This electronic modification results from a redox interplay during the synthesis reaction between the metal ion and the electroactive catechol ligands in presence of oxygen as previously reported.[54]

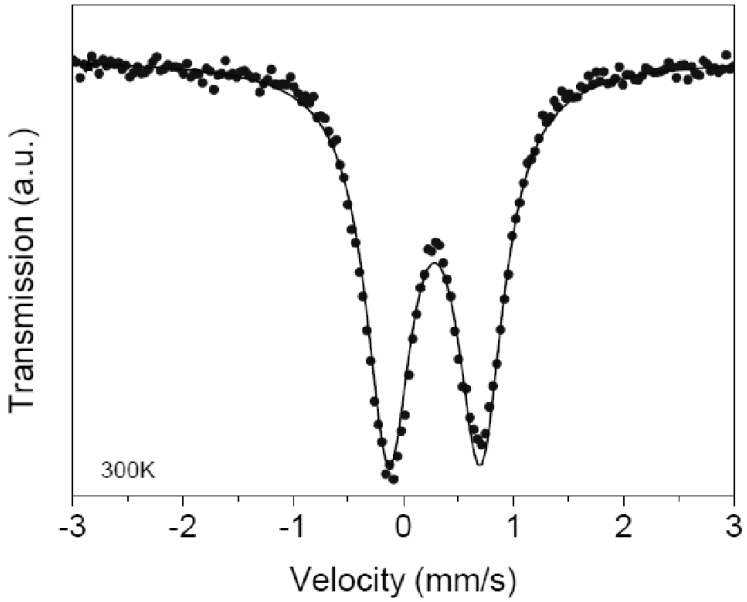

Figure 4.23 Mössbauer spectra for Fe-NCP at 300 K. Experimental data (dots), and computer fitted spectrum (line). The fitting was centred at an isomeric shift $\delta = 0.39 \pm 0.01$ mm/s attributed to high-spin Fe(III) ions.

Finally, the average chemical compositional formula of different complexes was experimentally calculated by combination of ^{1}H-NMR, ICP-MS and elemental analysis. The ligand ratio of NCPs was obtained from ^{1}H-NMR and the metal percentage from ICP-MS (Table 4.3).

Table 4.3 Experimental values for elemental analysis considering the ICP-MS and ^{1}H-NMR measurements.

NCPs	**Elemental Analysis (theoretical*)**				**^{1}H-NMR**	**Error**
	%C	%H	%N	%metal**	**L3** : **L4** or **L5****	
Fe-NCP	47.00 (47.03)	3.82 (4.58)	5.92 (5.86)	11.85 (12.05)	1:2.7	0.21%
Gd-NCP	38.00 (38.79)	3.20 (4.06)	6.08 (5.89)	29.90 (29.50)	1:1.8	0.49%
Mn-NCP	52.40 (53.07)	4.10 (5.19)	8.26 (8.44)	7.67 (7.74)	1:1.7	0.65%
GdDTPA-NCP	46.89 (46.75)	4.70 (4.87)	14.45 (13.92)	20.50 (20.07)	2:1	0.58%

*The theoretical values were obtained taking into account the 1H-NMR ligand ratios; **the values where calculated from ICP-MS; *** **L3** = Bix, **L4** = dhc, **L5** = DTPA.

These results together with the elemental analysis of C, N and H, help to elucidate an average compositional formula (Table 4.4). As the NCPs are obtained out of equilibrium, it is worth mentioning that elemental analysis of different nanoparticles batches slightly differed from the expected values for a 1(metal ion):1**L3**:2**L4** (or **L5**) ratio. These differences have been tentatively attributed to the plausible encapsulation of free ligand or solvent molecules within the particles and the formation of secondary structures such as oligomers.[55,56] In order to get consistent results, the different analyses were done for three different batches, obtaining a robust and reproducible results.

Table 4.4 Chemical compositional formula for each NCP complex taking into account the values shown in Table 4.3.

NCPs	Chemical Formula	Percentage
Fe-NCP	Fe_1 **L3**$_{0.49}$ **L4**$_{1.30}$ $(AcO^-)_{0.25}(H_2O)_{3.82}$	25% **L3**, 49% **L4**, 12% Fe
Gd-NCP	Gd_1 **L3**$_{0.57}$ **L4**$_{1.03}$ $(AcO^-)_{0.30}(H_2O)_{3.11}$	26% **L3**, 34% **L4**, 30% Gd
Mn-NCP	Mn_1 **L3**$_{1.07}$ **L4**$_{1.82}$ $(AcO^-)_{0.28}(H_2O)_{3.09}$	35% **L3**, 46% **L4**, 8% Mn
GdDTPA-NCP	Gd_1 **L3**$_{1.39}$ **L5**$_{0.70}$ $(H_2O)_{1.2}$	46% **L3**, 33% **L5**, 21% Gd

L3 = Bix, **L4** = dhc, **L5** = DTPA

4.2.2.2.3 Biodegradability of the NCPs (Chemical stability in solution)

Once the nanoparticles were completely characterised, the biodegradability in solution of the NCPs synthesised was evaluated in order to study its behaviour in physiological conditions. First of all, the size and the surface ξ-potential modification of the NCPs were studied at different pH in aqueous saline media (PBS buffer). The pH of the dispersions containing the NCPs was modified in the range of pH 4-9 (Figure 4.24).

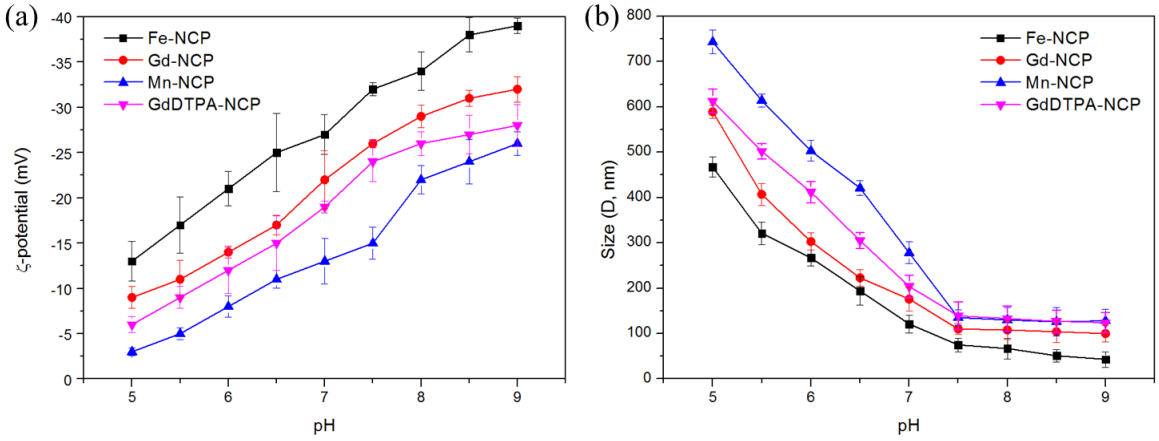

Figure 4.24 (a) ζ -potential in function of pH. (b) Particle size in function of pH, Data is shown as mean ± standard deviation

When the suspensions were acidified (pH = 4), the protonation of the carboxylic acid, and the consequent reduction of ξ-potential, induced the aggregation and precipitation of the nanoparticles. This aggregation was observed by the drastically increase of the hydrodynamic size (Figure 4.24b) reaching values of few hundreds nm depending on the NCP system. On the other hand, the lowest particle size value was obtained at pH = 9 in which a high percent of carboxylic groups were deprotonated and the surface charge is highly negative resulting in less aggregation due to electrostatic repulsion between nanoparticles (Figure 4.24). For values below pH 4 or above pH 9, the decomposition of the polymeric material becomes evident due to the complete and irreversible dissolution of the nanoparticles within a few seconds. In general, for all the complexes, the results showed that in the range of pH 4-9 the aggregation-dispersion process was reversible.

In order to evaluate the colloidal and chemical stability of the nanoparticles in physiological conditions, dispersions of specific concentrations of the different NCPs were followed for 24 h and 48 h. In a typical experiment, the nanoparticles were placed inside a dialysis bag immersed in a PBS buffer solution at pH = 7.4 and 37 ^{o}C. The chemical stability of the NCPs was studied by FT-IR spectroscopy (Figure 4.25). Form the spectra obtained, **Fe-NCP** remained invariant after 48 h thus demonstrating he high stability of the coordination structure. In the case of **Gd-NCP** and **GdDTPA-NCP** nanoparticles (Figure 4.25b and 4.25d, respectively), they were stable during 12 h and the spectra remained without detectable changes.

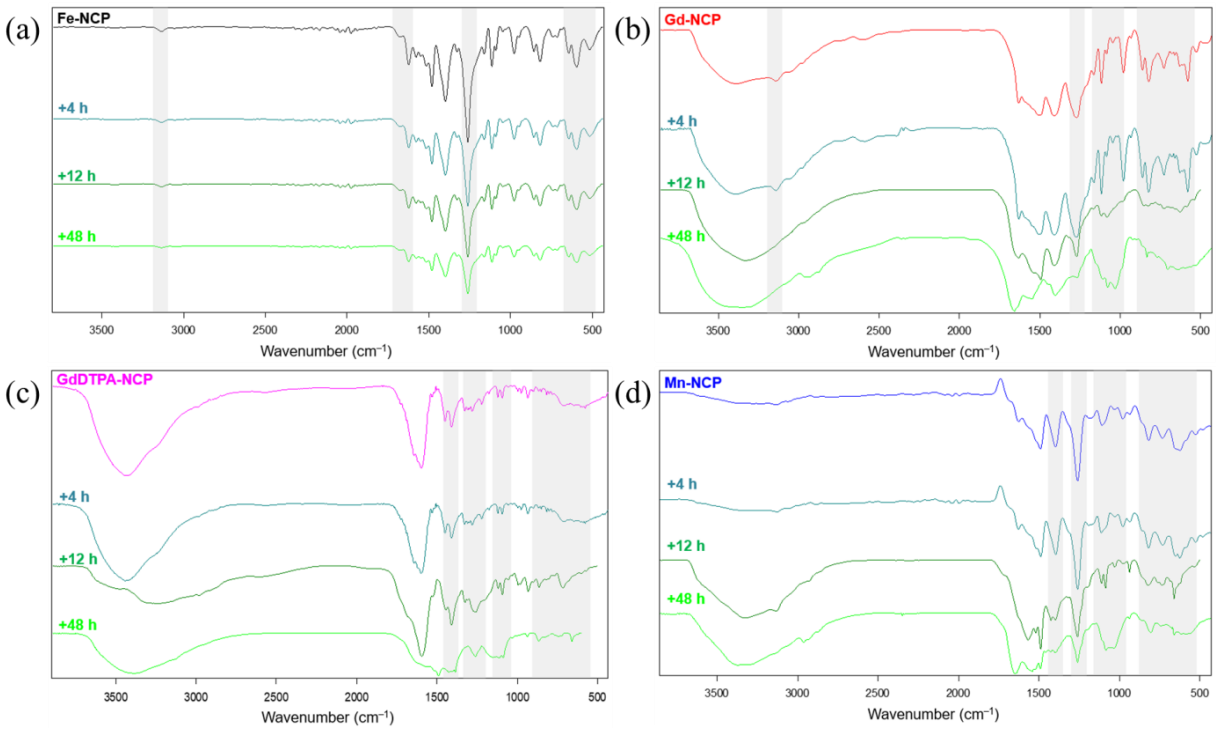

Figure 4.25 FT-IR spectra at different times for (a) **Fe-NCP**, (b) **Gd-NCP**, (c) **GDTPA-NCP** and (d) **Mn-NCP**.

However, for long periods, the FT-IR spectra denoted significant changes in chemical composition. Finally, **Mn-NCP** nanoparticles (Figure 4.25) showed less stability in aqueous media since significant variations were detected at 12 h.

Complementary, the liberation of metal, most likely arising from degradation of NCPs, was quantified from outside the dialysis bag using ICP-MS spectrometry taking several aliquots at different time points (Figure 4.26 and Table 4.5). In this case, an analogous experiment was performed at pH = 5 (acidified PBS). The results indicated a gradual biodegradation for **Fe-NCP** which reached the 50% metal leaching after 8 h at pH 7.4. The **Gd-NCP**, and specially **Mn-NCP**, were less stable taking into account their decomposition rates showing significant leaching (50% at 5 h and 2 h for **Gd-NCP** and **Mn-NCP**, respectively). In general, the NCPs were less stable at acid pH realising the half of the metal at shorter times compared with the same experiment at physiological pH. In the case of **GdDTPA-NCP**, although the chemical stability was maintained up to 6 h, the degradation turned evident for longer times. This was confirmed by the successive disappearance of vibrational bands due to the chemical decomposition (Figure 4.25d). The 50% of the metal outside the dialysis bag was measured after 2 h and 1.5 h at pH = 7.4 and 5, respectively. These results clearly demonstrated the low chemical stability of the **GdDTPA-NCPs** compared with the analogous systems.

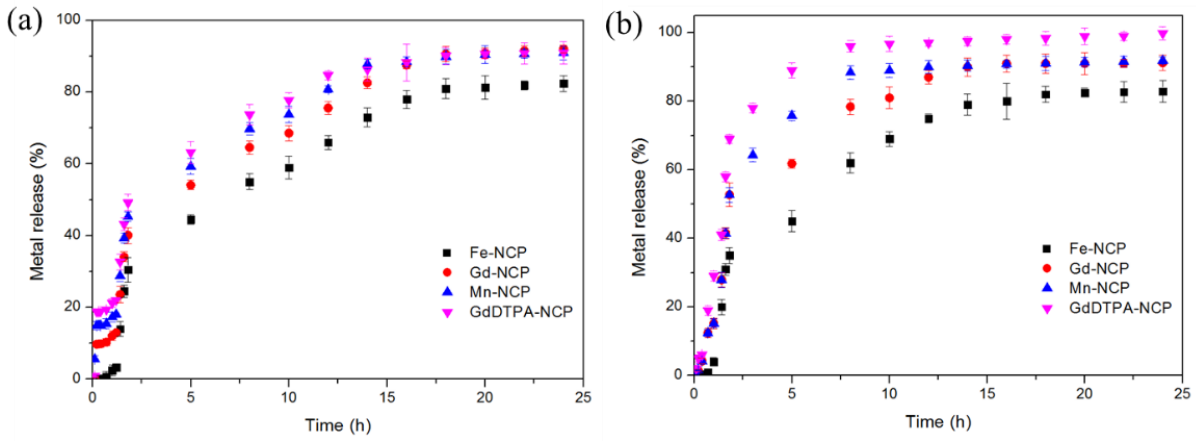

Figure 4.26 Stability of the NCPs systems at (a) pH = 7.4 and (b) pH = 5 in PBS-BSA. Data is shown as mean ± standard deviation.

Table 4.5 Time needed for the release of the 50% of Fe(III), Gd(III) and Mn(II) for each NCP at two different pH.

	pH = 7.4	**pH = 4.5**
Fe-NCP	8 h	5.5 h
Gd-NCP	5 h	2 h
Mn-NCP	2 h	1.5 h
GdDTPA-NCP	2 h	1.5 h

In the same way, the chemical degradation was observed when UV-vis spectra were recorded at different times for the different systems in solution (PBS, pH 7.4). The degradation of the nanoparticles and metal release were associated with the significant appearance of absorption bands in the wavelength range 400-600 nm, which corresponded to the absorption of soluble metal complexes in solution (Fe(III) at 590 nm after 24 h, Gd(III) at 450 nm after 12 h, Gd(III)DTPA at 550 nm after 12 h and Mn(III) at 450 nm after 4 h) (Figure 4.27). If each case is separately analysed, the stability of **Fe-NCP** nanoparticles (Figure 4.27a) remained practically intact after 12 h.

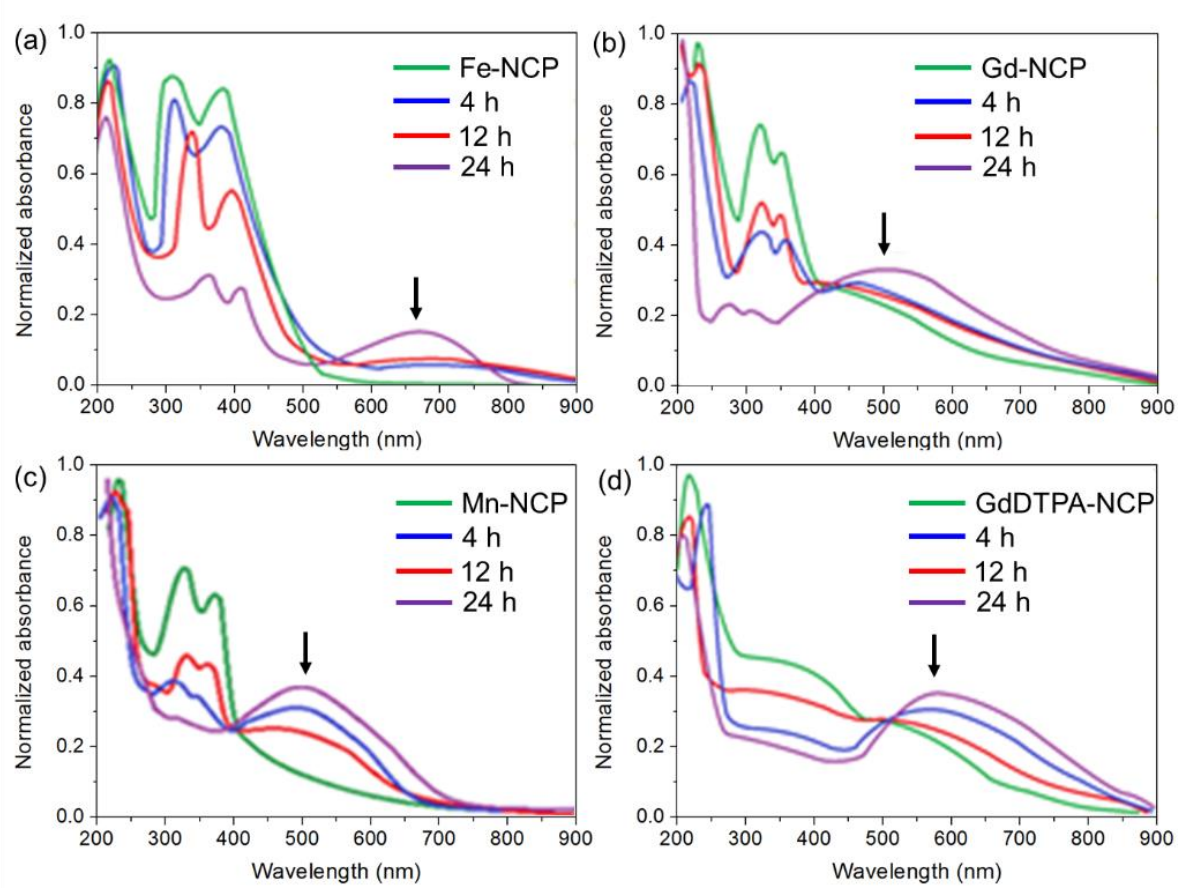

Figure 4.27 UV-vis spectra at different times for (a) **Fe-NCP**, (b) **Gd-NCP**, (c) **Mn-NCP** and (d) **GdDTPA-NCP**. a.u: Arbitrary units.

From 24 h, it was possible to observe an increase in the corresponding metal band (indicated by an arrow). The increase of this band was attributed to the low release of Fe ions to the environment and thus the nanoparticles were beginning to degrade slowly. In the case of **Gd-NCP** complex (Figure 4.27b), a remarkable increase in the metal band (indicated by an arrow) at 12 h was detected. The **Mn-NCP** nanoparticles were less stable than the others. As observed in the graph (Figure 4.27c), the manganese metal band started to increase after 4 h.

Moreover, after 24 h, other characteristics bands of **Mn-NCP** (observable in the green spectrum) disappeared. All these changes indicated the low stability of the system and, thus, rapid degradation in comparison with other systems. For the nanoparticles with gadolinium chelate (**GdDTPA-NCP**), a significant increase in the metal band after 12 h was detected (Figure 4.27d).

Considering the overall results concerning colloidal and chemical stability, a notably better performance of **Fe-NCP** in comparison to the other nanoparticles was corroborated. This stability was enough for the *in vitro* and *in vivo* MRI acquisition and allowed to propose this nanosystem for further pre-clinical experiments due to its stability and long-term biodegradability that suggest no bioaccumulation within the organism avoiding undesirable side effects.

4.2.2.2.4 Biocompatibility: cytotoxicity assays and reactive oxygen species (ROS) generation

The biocompatibility of NCPs using *in vitro* viability assays on HeLa (human cervix carcinoma) cells was evaluated after 24 and 72 h incubation with different concentrations of NCPs. This study was done in the facilities of the *Institut de Biotecnologia i Biomedicina* (IBB-UAB, Cerdanyola del Vallès, Spain) under the supervision of Dr. Julia Lorenzo. As shown in Figure 4.28a, after 24 h, Fe- and Gd-based NCPs did not show significant toxicity at metal concentrations up to 100 µM, meanwhile manganese-based NCPs showed a notable toxicity just above 10 µM. At highest concentrations (200 µM) and longest incubation times (72 h) only the Fe-based NCPs did not show significant toxicity (Figure 4.28b) in comparison with Gd- and Mn-NCP.

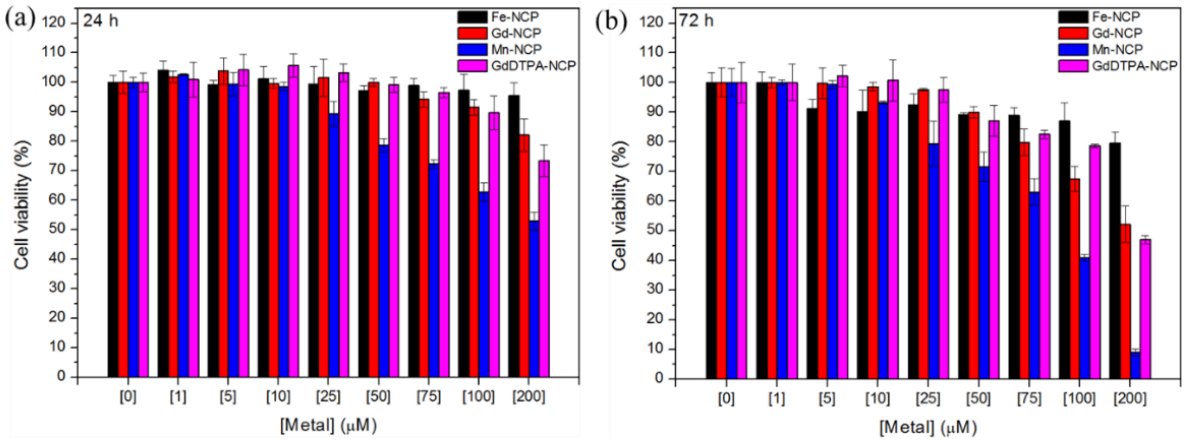

Figure 4.28 The effect of the NCPs on cell viability n in HeLa cells. Concentration-dependent cytotoxicity effects of NCPs were evaluated after (a) 24 h and (b) 72 h of incubation.

Comparatively, the toxic effect of these two last complexes was very similar to the commercial gadolinium (GdDTPA) and manganese (MnDPDP) CAs, respectively (Figure 4.29). The results suggested that Gd-based CAs had lower toxicity at higher concentrations when compared to the commercial chelating agent (GdDTPA). This may indicated that the polymerisation of the discrete GdDTPA molecules gave it greater stability and therefore a slightly lower toxicity. This became more evident for the toxicity assessed after 72 h (Figure 4.29b). However, this did not happen in the case of nanoparticles based on Mn. As shown in the graph (Figure 4.29c,d), both synthesized NCP system and the commercial complex had very similar toxicities without being able to decrease after polymerisation.

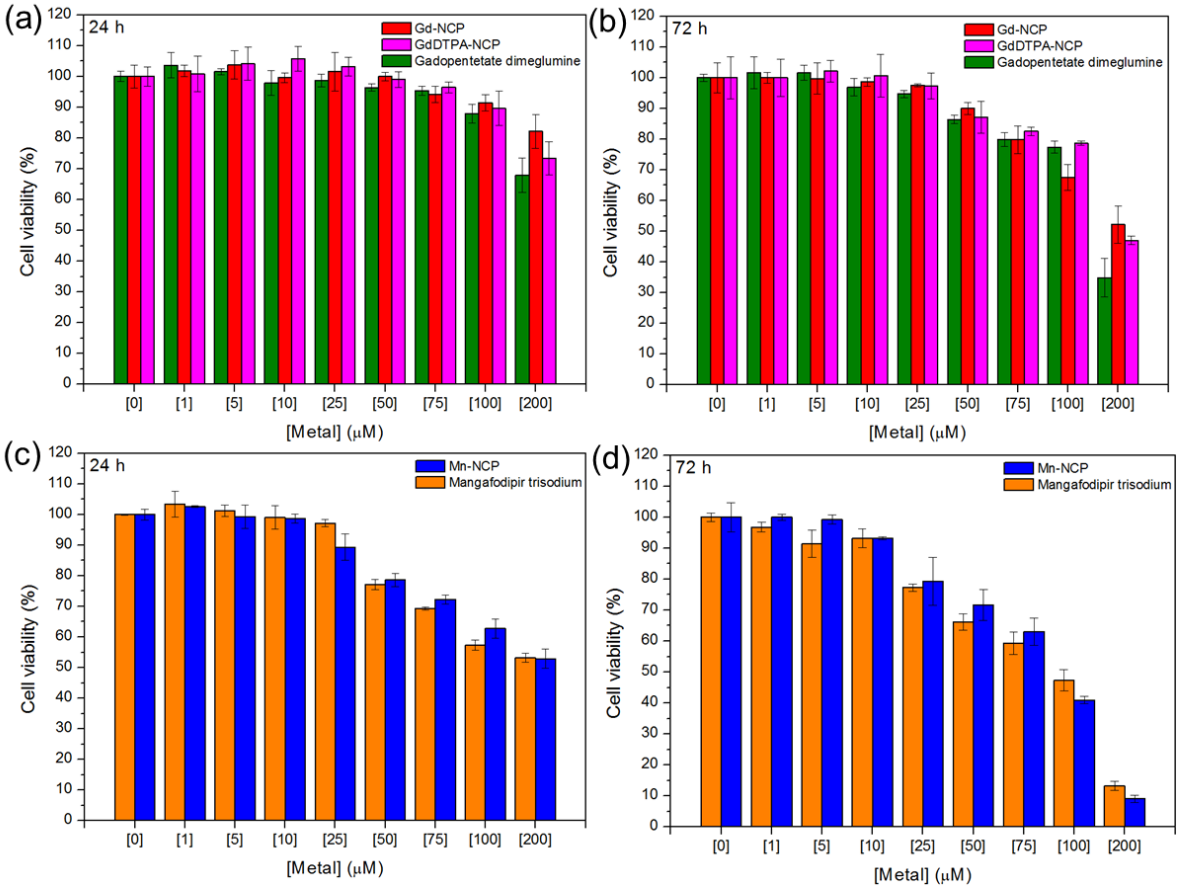

Figure 4.29 *In vitro* cytotoxicity of Gd-based and Mn-based NCPs and comparison with commercial contrast agents (CAs) in human cervix carcinoma Cell line (HeLa): (a) and (b) show the comparison of the systems containing gadolinium and commercial contrast agent (GdDTPA) at 24 h and 72 h respectively; (c) and (d) show the comparison between the systems containing manganese and commercial contrast agent (MnDPDP) at 24 h and 72 h respectively. The results are expressed for the different concentrations of metal in the NCPs complexes. Data is shown as mean ± standard deviation.

One explanation for the toxicity detected can be attributed to the generation of reactive oxygen species (ROS). It is well known that many of the heavy metal ions can induce generation of reactive radicals and cause cellular damage via depletion of enzyme activities through lipid peroxidation and

reaction with nuclear proteins and DNA.[57,58] The production of ROS induced by nanomaterials plays a vital role in genotoxicity and oxidative DNA damage involving mutagenesis, carcinogenesis and aging-related diseases.[59]

Particularly, metal-based nanoparticles can induce toxicity due to the ionic species generated from nanomaterial dissolution in a suspending medium or a biological system. In this sense, different studies were carried out by incubation of HeLa cells for 24 h with different concentrations of nanoparticles from 0 to 200 μM (based on metal concentration) and using 1 mM H_2O_2 as a positive control for the ROS generation (Figure 4.30). All results were compared with the GdDTPA and MnDPDP CAs (Figure 4.30b). If the production of ROS by the different nanoconstructs is compared with their cytotoxic effect, there is a strong correlation between cell viability and ROS production.

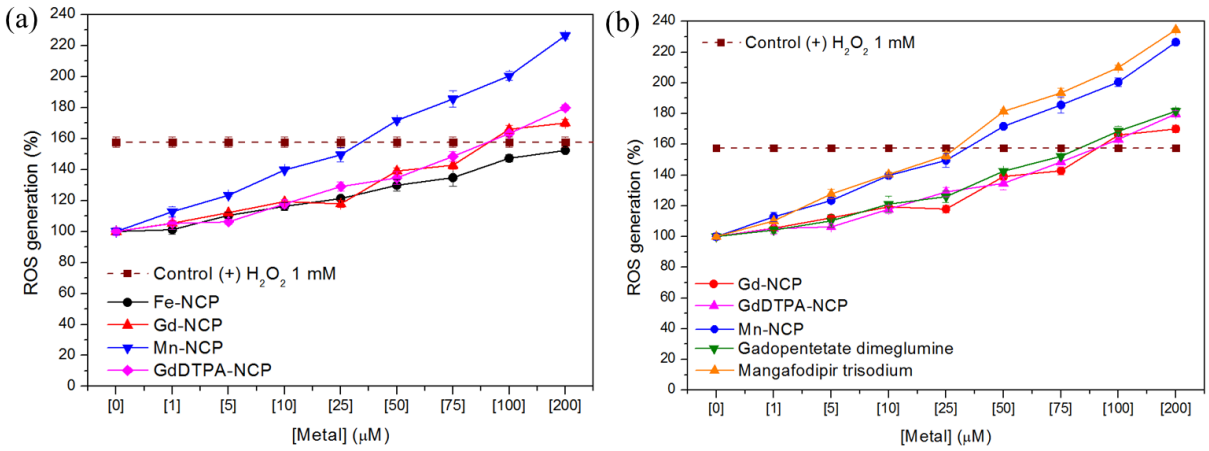

Figure 4.30 The effect of the NCPs on reactive oxygen species (ROS) generation in HeLa cells. The ROS generation was evaluated for 24 h for (c) NCPs and (d) compared with commercial CAs. Data is shown as mean ± standard deviation.

Thus, meanwhile **Fe-NCP** induced a low production of ROS in a dose-dependent manner even for high concentrations, the Gd-based NCPs had an increased ROS generation especially at concentrations higher than 100 μM. The most dramatic response corresponds to the **Mn-NCP** which presented a notable ROS production above 25 μM. Since most of the examples of metal-induced ROS production are related to the presence of redox-active metals in solution, it is interesting to mention that the appearance of a band at 450 nm during the degradation of Mn-NCP indicated the oxidation of Mn(II) to Mn(III).[60] This fact would justify the increased toxicity observed with this system since Mn(III) results in higher oxidative reactivity in comparison with Mn(II) analogous.[61]

As observed in the previous studies, the chemical stability in aqueous solution of the different NCPs can be stated in the following order: **Fe-NCP**>**Gd-NCP**>**GdDTPA-NCP**>**Mn-NCP** that interestingly matches with the increasing order of cytotoxicity effect.

4.2.2.2.5 Relaxivity properties of NCPs: in vitro and ex vivo MRI studies

a) In vitro

To evaluate the feasibility of NCPs synthesised as a platform for MRI, the longitudinal (r_1) and transversal (r_2) relaxivity values were determined by T_{1w} and T_{2w} images acquisition for all the dispersions containing the samples at different metal concentrations. Thus, the NCPs were redispersed in PBS-agarose 1% solution at pH = 7.4 and measured as phantoms in a Biospec MRI equipment of 7T. This representation allowed elucidating the relaxivity parameters for each NCP by isolating the slope of the lineal regression adjustment. The phantoms images are presented in Figure 4.31a-d, and the obtained r_1 and r_2 values are summarized in Table 4.6. The redispersion of the nanoparticles in the solid matrix of PBS-agarose, allowed measuring the phantoms at different concentrations and time points in an environment that somehow simulates the viscosity and consistency of the biological tissues. This agarose-based mimicking tissue method has been widely used in the literature in order to obtain the relaxivity parameters of several CAs.[62] This kind of designed matrix let the mimics of different properties such as morphological, mechanical, electric, and/or electromagnetic intrinsic characteristics of the human organ/tissue by selecting the appropriate materials. Many polymeric gels have been suggested as convenient materials capable of producing phantoms simulating thermal and mechanical behaviour, and also permeability properties of human organs/tissues.

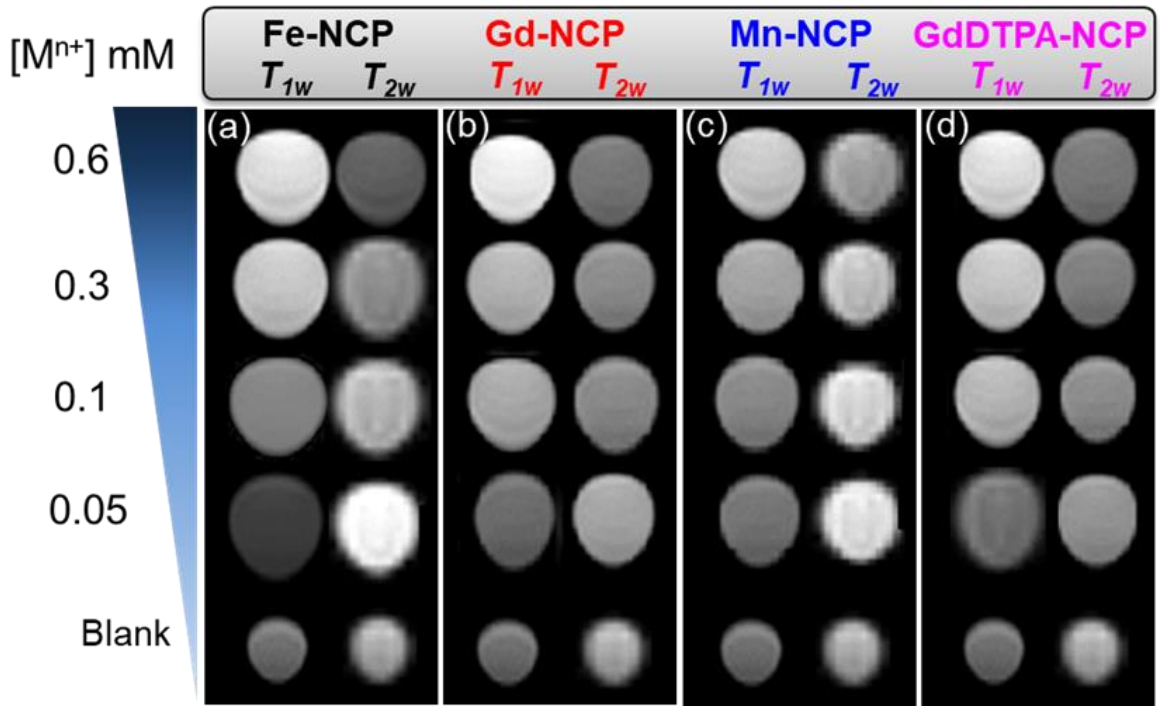

Figure 4.31 *In vitro* contrast effect of NCPs. Different phantoms series for each NCP complex at decreasing metal concentration: (a) **Fe-NCP**, (b) **Gd-NCP**, (c) **Mn-NCP** and (d) **GdDTPA-NCP**. The blank corresponds to the PBS-Agarose (1%) matrix.

Table 4.6 *In vitro* r_1 and r_2 parameters for all NCPs and comparison with the commercial CAs GdDTPA and MnDPDP.

	***In vitro* phantoms**			
	Medium	r_1 **(mMs^{-1})**	r_2 **(mMs^{-1})**	r_2/r_1
Fe-NCP	PBS + Agarose	5.3 ± 0.1	10.9 ± 0.3*¥	2.1
Gd-NCP		4.4 ± 0.2	4.9 ± 0.2	1.1
Mn-NCP		3.7 ± 0.1	2.1 ± 0.1	0.6
GdDTPA-NCP		4.5 ± 0.4	5.1 ± 0.3	1.1
GdDTPA		4.4 ± 0.2	4.6 ± 0.7	1.1
MnDPDP		3.1 ± 0.5	2.3 ± 0.1	0.7
Vehicle		-	-	-

*= p<0.05 in comparison with GdDTPA, MnDPDP, Fe-NCP, Gd-NCP; ¥= p<0.05 in comparison with GdDTPA

The r_1 values were determined to be 5.3 ± 0.1 mM^{-1} s^{-1} for **Fe-NCP**, 4.4 ± 0.2 mM^{-1} s^{-1} for **Gd-NCP**, 4.5 ± 0.4 mM^{-1} s^{-1} for **GdDTPA-NCP**, and 3.7 ± 0.1 mM^{-1} s^{-1} for **Mn-NCP**. The values obtained were comparable with the commercial GdDTPA (4.4 ± 0.7 mM^{-1} s^{-1}) except for the **Fe-NCP** complex which significantly improved the referenced value. Concerning the T_{2w} MR images, clear differences were found. In **Fe-NCP**, the T_{2w} MR image intensity decreased (Figure 4.31a) with a concentration increase of Fe ions. Thus, the r_2 value for **Fe-NCP** was 10.9 ± 0.3 mM^{-1} s^{-1}, which is about twice higher than the corresponding commercial GdDTPA (r_2 = 4.6 ± 0.2 mM^{-1} s^{-1}). This increased value was ascribed to the combined effects of the local inhomogeneous magnetic fields created by the NCPs and the exchange of water between NCPs and the environment.[63]

The MR behaviour of CAs relies on the relaxivity ratio (r_2/r_1). If the material behaves as a T_2 contrast agent, $r_2/r_1 \geq 10$ and as T_1 contrast agent if $r_2/r_1 \leq 2$.[64] Therefore, nanoparticles with an intermediate r_2/r_1 ratio can be excellent candidates as T_1/T_2 DMCAs. In our case, the *in vitro* phantom imaging studies agreed with this assumption for **Fe-NCP**, since the relaxivity ratio r_2/r_1 is 2.1, indicating its potential use as DMCA. The r_1 value of **Fe-NCP** was comparable or even higher than those found for previously reported Fe-based CPs,[65,66] or molecular complexes,[67] which exhibit r_1 values up to 3.0 mM^{-1} s^{-1}. Such good response is directly related to the **Fe-NCP** capacity to modify the relaxation times of the water protons in the surrounding medium when a magnetic field is applied. On the one hand, it has been reported that catechol-based ligands maximize second-sphere interactions with water molecules, and therefore to enhance T_1, through hydrogen bonding with the oxygen atoms of the Fe–O–R linkages.[68] On the other hand, the coordination polymer probably contained water molecules strongly coordinated to the metal sites, as well as free water molecules. These labile water molecules were probably in exchange with bounded water molecules, diffusing through the polymeric matrix.[69] The mobility of the metal coordinated water in the first and second coordination spheres should induce an effect on the relaxation times of the water protons, resulting on the observed ratio r_2/r_1.

In the case of Gd-based nanoparticles (**Gd-NCP** and **GdDTPA-NCP**) although they performed satisfactorily as T_1 CAs, no significant effect as T_2 CA was detected and the r_2 values obtained (4.9 ± 0.2 mM^{-1} s^{-1} and 5.1 ± 0.3 mM^{-1} s^{-1}, respectively) were comparable to the commercial GdDTPA complex (4.6 mM^{-1} s^{-1}) resulting in $r_2/r_1 \sim 1$ ratio. The same trend was observed for **Mn-NCP**, which showed a typical behaviour of a T_1 contrast agent with $r_2/r_1 = 0.6$ ratios exhibiting value comparable to the Mn-based commercial MnDPDP CA ($r_1 = 3.1 \pm 0.5$ mM^{-1} s^{-1}, $r_2 = 2.3 \pm 0.1$ mM^{-1} s^{-1}).

b) Ex vivo

Before performing *in vivo* studies, it was necessary to select the appropriate candidate which produces the best relative performance in a tissue-like environment.[70,71] Although *in vitro* T_1 and T_2 relaxivity times were calculated, the results obtained from them are not usually comparable in real tissue. Most of the *in vitro* strategies used to evaluate the CAs performance, are not able to reproduce the *in vivo* conditions that could modify their ability to generate contrast.[72-74]

For these reasons, *ex vivo* studies were conducted essentially as reported previously.[62] Briefly, each contrast NCPs was added to a PBS-BSA solution vehicle (1.25 μM in terms of metal concentration) and 4 μl of the resulting dispersions were intracranial administered *post mortem* to euthanized mice. The relative contrast enhancement (RCE values) was calculated for each CA. In this case, RCE values give information about the contrast improvement of an administered CA in comparison with the cerebral area without CA injected (For more detail see Experimental section 4.2.4). A solution of commercial GdDTPA CA was used for comparison purposes. For statistical reasons, three ROIs were selected in T_{1w} and T_{2w} images, corresponding to CA administration points (Figure 4.32a,b).

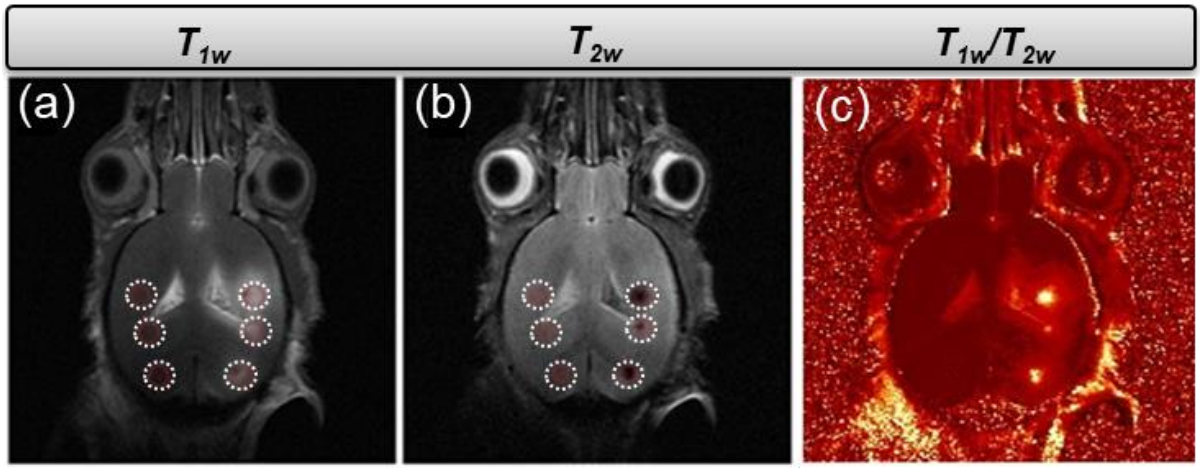

Figure 4.32 *Ex vivo* contrast effect of **Fe-NCP**. The *ex vivo* **Fe-NCP** (a) T_{1w} and (b) T_{2w} MRI images obtained after stereotactic injection of **Fe-NCP,** and (c) post-processing of T_{1w} and T_{2w} images by an algebra algorithm of imaging division (T_{1w}/T_{2w}). The dashed circles show the selection of regions of interest (ROIs) for the relative contrast enhancement (RCE) calculation.

The T_{1w} and T_{2w} RCE calculated for each studied CA and vehicle are shown in Table 4.7. **Fe-NCP** and **Gd-NCP** presented RCE T_1 comparable with the two commercial CAs GdDTPA and MnDPDP (with no significant differences). **Mn-NCP** produced poorer and non-reproducible results presumably due to the low stability of these nanoparticles in solution. Regarding RCE T_2, **Fe-NCP** presented the best T_{1w}/T_{2w} result, although significance was only reached in comparison with commercial MnDPDP, probably due to high value dispersion. The dual potential of this CA was more clearly observed when the calculated ratio of RCE T_1/T_2 was considered. Ideally, a DMCA should present high absolute values for RCE T_1 (signal increase) and low absolute values for RCE T_2 (signal decrease), resulting in a high RCE T_1/T_2 ratio, as observed for **Fe-NCP** (RCE T_1/T_2 = 7.7) (Table 2). In this case, the *ex vivo* studies validated the enhanced performance described *in vitro* for **Fe-NCP**. Additionally, the low toxicity and high chemical stability make this Fe-based complex the best candidate for its pre-clinical study.

Table 4.7 *Ex vivo* relative contrast enhancement (RCE for T_1 and T_2) for all NCPs and comparison with the commercial CAs GdDTPA and MnDPDP.

		Ex vivo		
	Medium	**RCE% (T_1)**	**RCE% (T_2)**	**RCE% (T_1/T_2)**
Fe-NCP		269.0 ± 28.0	44.9 ± 26.0**	7.7 ± 4.5
Gd-NCP		278.6 ± 56.0	70.1 ± 25.4	4.2 ± 1.1
Mn-NCP	PBS	300.9 ± 47.7	97.4 ± 14.5	3.2 ± 1.1
GdDTPA-NCP	+	180.0 ± 64.3	78.6 ± 2.8	2.3 ± 0.8
GdDTPA	BSA	253.1 ± 32.8	74.9 ± 17.6	3.6 ± 1.4
MnDPDP		300.9 ± 47.7	97.4 ± 14.5	3.2 ± 1.1
Vehicle		118.6 ± 8.8	122.9 ± 11.5*¥	0.97 ± 0.07*¥€

*= p<0.05 in comparison with GdDTPA, MnDPDP, **Fe-NCP**, **Gd-NCP**; ¥= p<0.05 in comparison with GdDTPA; €= p<0.05 in comparison with **Mn-NCP**; **= p<0.05 in comparison with MnDPDP CA.

4.2.2.2.6 *In vivo MRI studies: tolerability, MRI imaging and biodistribution*

a) Tolerability

As aforementioned, **Fe-NCP** showed the best results as a potential DMCA for MRI. For this reason, this system was selected for its study in pre-clinical *in vivo* experiments. Before *in vivo* assays, a tolerability study to determine the maximum safe dose for **Fe-NCP** complex was done. The study was carried out following a protocol adapted and previously reported[75,76] In a typical experiment, increasing amounts of **Fe-NCP** (0.03 to 0.4 mmol Fe kg^{-1}) were intravenously (i.v.) administered (via tail vein) to n = 3 mice with a 2-day rest period between injections. An additional group of 3 mice was injected with the vehicle as control (PBS with 0.5 mM Mouse Serum Albumin (MSA)). Mice body weight and other welfare parameters were followed for 30 days after the last administration. In these conditions, a dose of 0.4 mmol $kg^{-1}$of **Fe-NCP** proved safe and no body weight loss or toxicity symptoms observed during injections and for the 30-day period after the last administration (Figure 4.33).

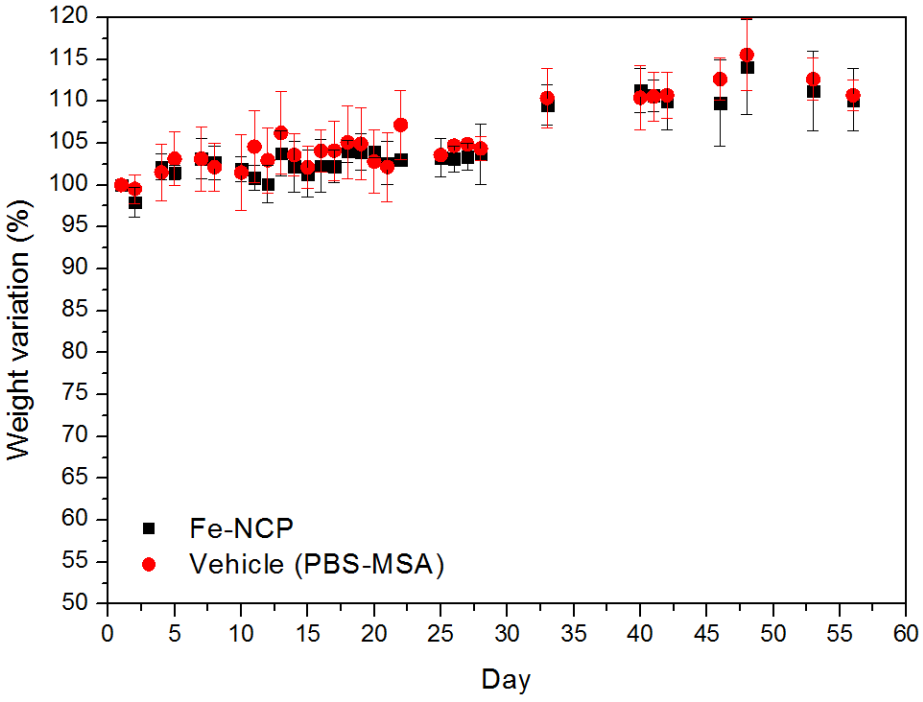

Figure 4.33 Mean weight variation of n = 3 wild type (wt) mice injected with **Fe-NCP** complex (black points) and for n = 3 wt mice injected with the vehicle (PBS-MSA, red points). Data is shown as mean ± standard deviation. Initial mice weight measured the first day of **Fe-NCP** i.v. injection is considered as 100%.

This value perfectly matches safety administration ranges for Fe-based nanoparticles, which can be up to 0.6 mmol kg^{-1}.[77-80] This is a clear added value of **Fe-NCP** in comparison with Gd-based CAs, which are widely used in clinical practice but are not exempt of undesired effects.[81]

b) MRI studies

For the *in vivo* CAs study, GL261 glioblastoma tumour-bearing mice were i.v. injected with 107.1 ± 6.4 µl containing the equivalent dose of 0.4 mmol metal kg^{-1}. The commercial GdDTPA CA was administered first, as reference for direct comparison (the complete description of the procedure and acquisition parameters is detailed in Experimental section 4.2.4). Representative T_{1w} (Figure 4.34a,b) and T_{2w} (Figure 4.34c,d) images were acquired pre- and post- CA injection.

In a second experiment, **Fe-NCP** was administered and T_{1w} and T_{2w} images acquired. Consequently, dual enhancement images were obtained through a post-processing algebra algorithm application (T_{1w}/T_{2w}, Figure 4.34e,f).

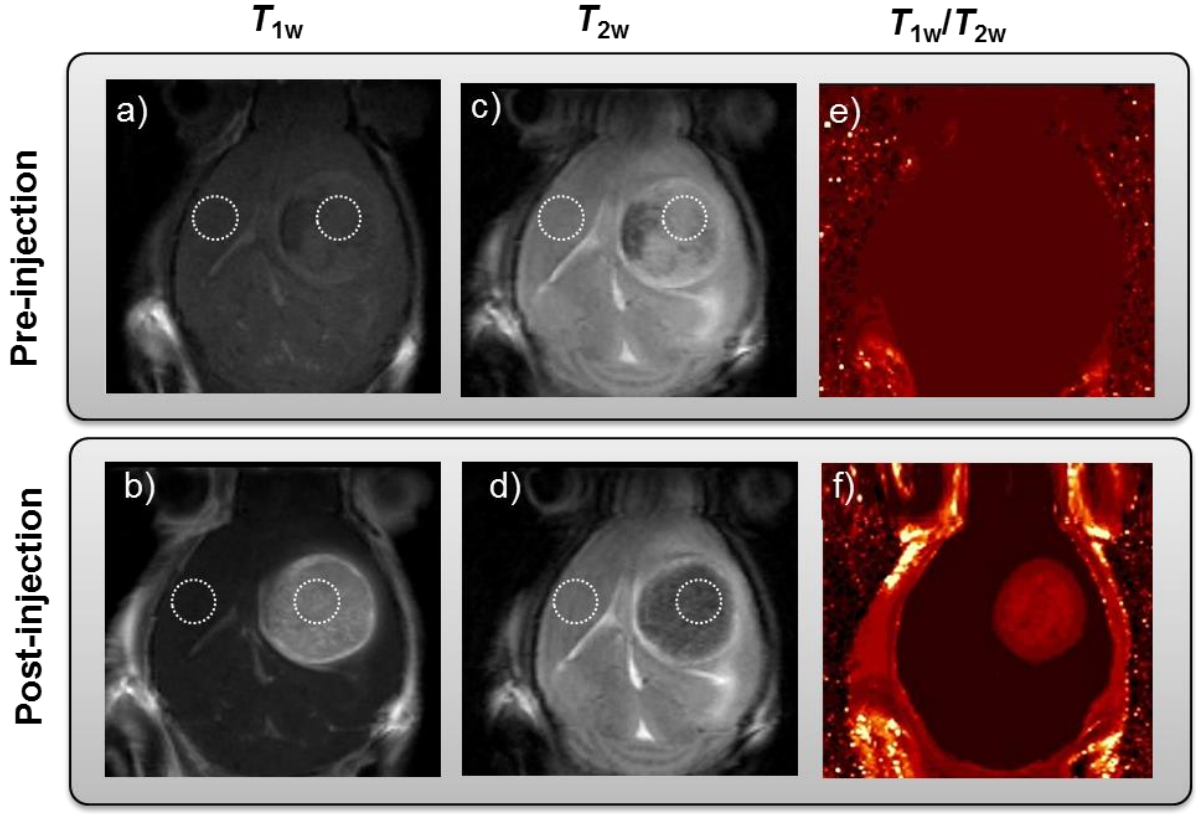

Figure 4.34 Representative example of *in vivo* study of GL261 tumour bearing mice (mouse number C1210) administered with **Fe-NCP** (0.4 mmol Fe Kg^{-1}). In the first row, MR images obtained before injection (pre-injection) are shown: (a) T_{1w} image, (b) T_{2w} image and (c) image obtained from an algebra algorithm of imaging division (T_{1w}/T_{2w}). In the second row, MR images after injection obtained at T_{1max} (post-injection) are shown: (d) T_{1w} image, (e) T_{2w} image and (f) image obtained from an algebra algorithm of imaging division (T_{1w}/T_{2w}). The dashed circles show the selection regions of interest (ROIs) for the relative contrast enhancement (RCE) calculation

The relative contrast enhancement (RCE) values (Table 4.8) were calculated by manual selection of two ROIs in each MRI slice: one corresponding to the tumour region and a second one to the contralateral normal brain tissue (Figure 4.34). In this case, the RCE values give information about the contrast improvement before (normalized as 100%) and after CA injection.

Table 4.8 *In vivo* relative contrast enhancement (RCE) for the **Fe-NCP** complex and the commercial contrast agent GdDTPA.

	In vivo relative contrast enhancement (RCE %)					
	T_{1w} (increase)[a]			**T_{2w} (decrease)[a]**		
	T_{1max}	**2 h**	**24 h**	**T_{2min}**	**2 h**	**24 h**
Fe-NCP	317.4 ± 15.4 *** ¥	123.5 ± 4.6 ***	88.3 ± 6.7 ***	73.7 ± 14.4 £,€	103.1 ± 9.9	79.4 ± 4.2 £
GdDTPA	250.9 ± 3.1 *	111.8 ± 2.7 *	101.0 ± 4.0	106.8 ± 2.9 **	102.1 ± 7.0	102.3 ± 7.3
Vehicle PBS-MSA	101.2 ± 1.8					

[a]The 100% RCE is the normalized reference value corresponding to the pre-injection MRI. *= $p<0.05$ in comparison with GdDTPA RCE T_{1w} pre-injection; **= $p<0.05$ in comparison with GdDTPA RCE T_{2w} pre-injection; ***= $p<0.05$ in comparison with Fe-NCP T_{1w} pre-injection; £= $p<0.05$ in comparison with Fe-NCP T_{2w} pre-injection; ¥= $p<0.05$ in comparison with GdDTPA at T_{1max}; € = $p<0.05$ in comparison with GdDTPA at T_{2min}. If the obtained values ranged >95 to <105% (i.e. less than 5% variation respect to pre-injection), they were considered as "no change" respect to pre-injection.

Maximum T_1 RCE signal increase (T_{1max}), showed remarkable differences between commercial GdDTPA (250.9 ± 3.1% at 6.1 ± 1.1 min) and **Fe-NCP** (317.4 ± 9.4% at 9.4 ± 1.1 min), which was notably superior ($p<0.05$). In T_{2w} images, no minimum signal decrease (and accordingly no T_{2min}) was observed for GdDTPA, which even show a slight signal increase (106.8 ± 2.9% at 2.6 ± 1.1 min). However, **Fe-NCP** showed a notable T_{2w} signal decrease with the minimum mean RCE value observed (73.7 ± 14.4%, with 26% decrease) at 5.3 ± 1.1 min. Significant differences were observed for RCE T_1 curves of GdDTPA, **Fe-NCP** and vehicle (Figure 4.35).

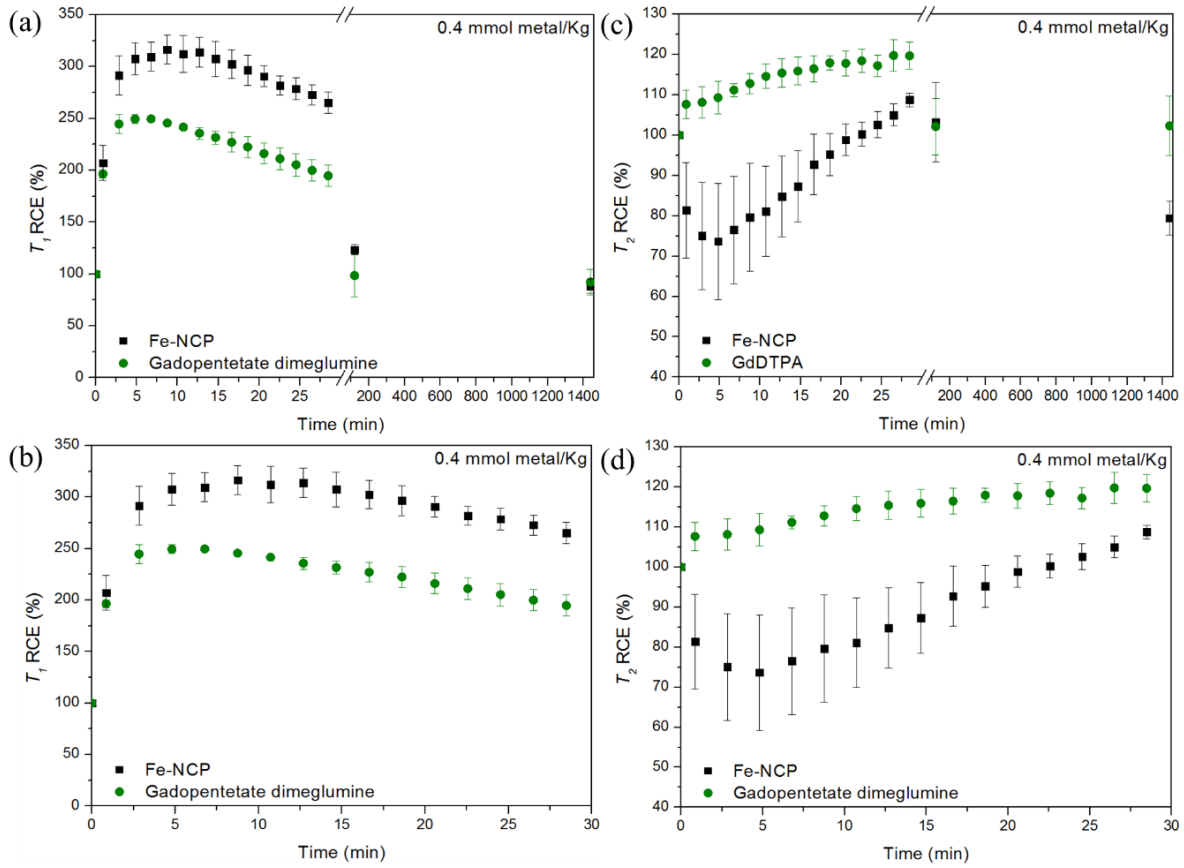

Figure 4.35 T_1 and T_2 relative contrast enhancement (RCE) in GL261 tumour-bearing mica after intravenous injection of a dose of 0.4 mmol kg^{-1} of commercial Gd contrast agent (Gadopentetate dimeglumine, GdDTPA, green points) and **Fe-NCP** complex (black points). For T_1 RCE(%) mean kinetics ± SD of T_1 RCE (%) during (a) 24 h and (b) 30 min of acquisition. For T_2 RCE(%) mean kinetics ± SD of T_2 RCE (%) during (c) 24 h and (d) 30 min of acquisition. Significant differences were found between the evolution of both curves with UNIANOVA test.

Additionally, the basal RCE values for **Fe-NCP** were completely recovered after 24 h and 30 min post-injection for T_1 and T_2, respectively. These values confirmed the rapid biodegradability of **Fe-NCP** and its potential as DMCA for MRI (see Figure 4.35f where RCE T_1/T_2 ratio is shown). It is worth noting that for **Fe-NCP**, the T_{1max} was observed at 9.4 ± 1.1 min, meanwhile for the commercial CA the maximum was achieved at 6.1 ± 1.1 min. This difference may be related to the greater retention and accumulation of the nanostructured material due to the enhanced permeability and retention effect (EPR) of nanoparticles in tumours as described in previous works.[65] In our case, the **Fe-NCP** nanoparticles were able to produce T_1 and T_2 RCE at reasonably short times in the pre-clinical glioblastoma model (between 3.95 and 10.72 min after administration for maximum T_1/T_2 effect). This behaviour would be a clear advantage, allowing the acquisition of both data types (T_{1w} and T_{2w}) in the same exploration, instead of performing two explorations with a large interlude. Thus, these nanoparticles present a clear interest for future studies, bearing a strong translational potential. This is not restricted to contrast enhancement, as they could be also used as nanocarriers for tumour-drug release and therapy in addition to diagnosis.[82,83]

c) *Biodistribution*

To further verify the biocompatibility studies and *ex vivo*/*in vivo* properties as MRI CAs, the biodistribution of **Fe-NCP** nanoparticles was studied. The quantification of Fe(III) levels within the different organs was done by using ICP-MS. In Figure 4.36, the biodistribution of iron from **Fe-NCP** in the main organs, including the tumour, is shown. The results are based on the quantification of µg Fe mg^{-1} protein at 2 min and 24 h after injection of two different **Fe-NCP** doses (0.2 mmol Fe kg^{-1} and 0.4 mmol Fe kg^{-1}).

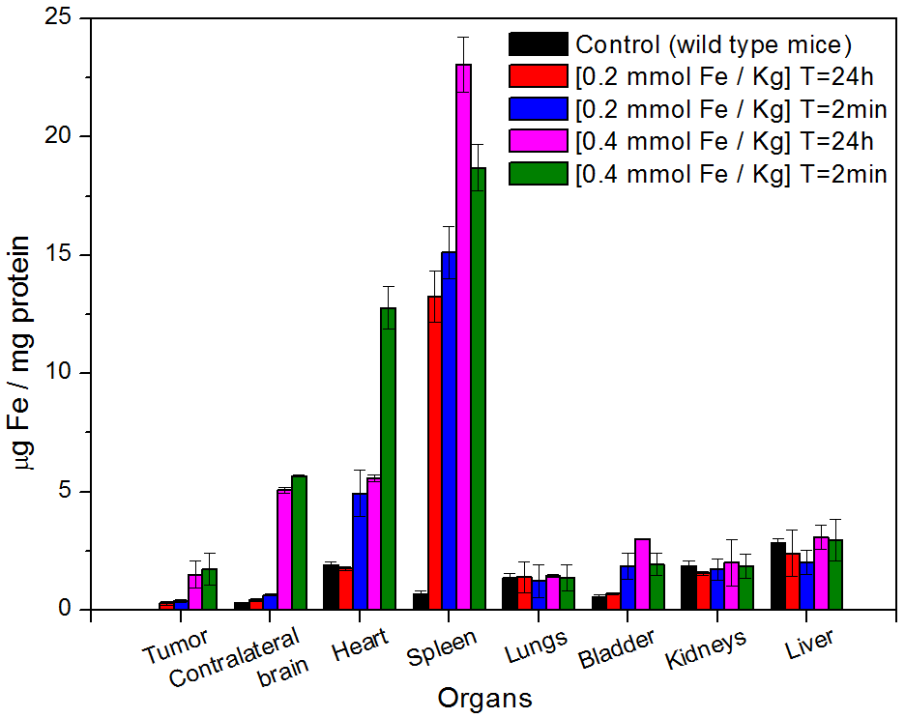

Figure 4.36 Biodistribution of **Fe-NCP** in mouse organs. **Fe-NCP** was injected into mice intravenously with a dosage of 0.2 or 0.4 mmol Fe kg^{-1} body weight. The concentration of Fe in different tissues was detected by ICP–MS at various time points post injection. Data is shown as mean ± standard deviation.

The experimental results indicated a dose-dependent biodistribution. On the one hand, the very short-term biodistribution (2 min) of low doses of **Fe-NCP** showed a low accumulation in heart and bladder, and notable retention in spleen. On the other hand, no increased levels of iron were detected in the tumour and contralateral brain area. However, when increasing the injected dose up to 0.4 mmol Fe kg^{-1}, 2 min of circulation time was enough to observe the presence of **Fe-NCP** in the brain and tumour. After 24 h, for the low dose administration no increase in the concentration of iron was detected in any organ except spleen. Nevertheless, at high doses, notable accumulation was still observed in tumour, brain and bladder. At the same time, the considerable decrease in concentration observed in heart and the increasing concentration in bladder must be attributable to the decrease of nanoparticles in blood circulation and consequent excretion. The accumulation observed in the lungs,

liver and kidneys are negligible and no significant differences were found in comparison with the basal values (control wild type mice). As observed, **Fe-NCP** resulted in a minimal tissue accumulation and gradual degradation/excretion without bioaccumulation. These results confirmed the rapid excretion of the nanoparticles due to the intrinsic biodegradability of the **Fe-NCP** complex. Actually, the gradual increase concentration of iron in bladder was an indicative of a gradual biodegradation of the Fe-NCP since the size needed to pass through the kidneys and reach the bladder should be smaller than 8 nm.[84] The large uptake of the **Fe-NCP** observed in spleen indicated its important role in the nanoparticle pharmacokinetics based on their rapid clearance by the mononuclear phagocytic system (MPS) which is common for unmodified nanoparticles bigger than 40 nm.[85,86] Although the persistence of **Fe-NCP** in the spleen may arise initial concerns, no adverse effects were detected in the 30 day-long tolerability assays described before.

Is worth to mention that considering the clinical translation potential of **Fe-NCP**, the limit Fe-administered doses in humans should be considered. According to literature, the doses cannot be calculated by direct extrapolated from mice to humans for the body weight due to the differences between both species.[87] Alternatively, a factor of 1/12 is commonly applied when calculating doses. In a standard case of a 70 kg human patient, the final Fe-administered dose would be around 130 mg of Fe content in the **Fe-NCP** (equivalent to 1.8 mg Fe/kg). This value is far below the maximum Fe concentration for i.v. in humans which is described to be 15 mg/kg.[88]

4.2.3 Summary and conclusions

Different NCPs based on Fe(III), Gd(III) and Mn(II) paramagnetic ions have been synthesized and tested as novel contrast probes with improved features in comparison to commercial CAs. From the different synthesized NCPs, only **Fe-NCP** shows relevant advantages in terms of:

i. Chemical and colloidal stability, low cytotoxicity, and MRI relaxivity results as DMCA
ii. The *in vivo* MRI shows its T_1 and T_2 contrast potential, allowing almost simultaneous recording of positive and negative contrast images in a very short period (between 3.95 and 10.72 min after administration for maximal contrast effect)
iii. This reduced time is a clear advantage in comparison with other DMCAs previously described, during which the **Fe-NCP** complex shows a high enough contrast activity for diagnosis
iv. The tolerability and biodistribution assays indicate the persistence of the nanoparticles in the tumour and the gradual clearance through the kidneys denoting the biodegradability of the system.

This work will pave the way for development of enabled biodegradable nanoparticles with T_1/T_2 dual-mode MRI contrast enhancement, obtained fast and safely, and which represents a clear advantage in comparison with other DMCAs. To the best of our knowledge, this is the first report on the fabrication of **Fe-NCP** for T_{1w}/T_{2w} contrast enhancement for the diagnosis and visualization of glioblastoma *in vivo* allowing the imaging of cerebral lesions. Our work would help to the development of novel one-pot NCP-based DMCA systems as a valid strategy with potential applications in theranostic and clinical translation to T_1- T_2 dual mode MRI.

4.2.4 Experimental section

Materials Solvents and starting materials were purchased from Sigma–Aldrich (Merck, Madrid, Spain) and used as received, without further purification, unless otherwise stated. 1,4-Bis(imidazol-1-ylmethyl)benzene (**L3**, Bix) was synthesized according to previously reported methodology.[89]

Characterization Scanning electron microscopy (SEM) was performed for platinum-metallized samples on a FEI Quanta 650 FEG (Thermo Fisher Scientific, Eindhoven, The Netherlands) in mode operation of secondary electrons (SE) with a beam voltage between 5 and 20 kV. Fourier-transform infrared spectra (FT-IR) were recorded on a Tensor 27 FT-IR spectrometer (Bruker Optik GmbH, Berlin, Germany) with KBr pellets. Ultraviolet-visible spectroscopy (UV-Vis) was performed using a Cary 4000 UV-vis-NIR spectrometer (Agilent Technologies, Santa Clara, CA, USA) within range wavelengths from 200 to 800 nm and a 1 cm path length quartz cuvette (QS 10 mm). The baseline was corrected using a blank sample of pure solvent. All the measurements were taken under atmospheric conditions. Dynamic light scattering (DLS) measurements for obtaining size distribution and zeta potential (ζ-potential) of the nanostructures were performed using a Zetasizer Nano ZS 3600 (Malvern Instruments, U.K.) All analysed samples were diluted in order to obtain a concentration of nanoparticles suitable for the experimental calculation of size dispersion. The data reported are values coming from the mean of measurements for each sample which were measured per quadruplicate. Inductive coupled plasma-mass spectroscopy measurements (ICP-MS) were obtained using an ICP-MS NexION 300X (Perkin Elmer, San Francisco, CA, USA). All samples were measured in argon atmosphere. X-ray photoelectron spectroscopy (XPS) measurements were performed with a Phoibos 150 analyser (SPECS GmbH, Berlin, Germany) in ultra-high vacuum conditions (based pressure 10^{-10} mbar). Monochromatic AlKα was used as X-ray source (1486.6 eV). The electron energy analyser was operated

with pass energy of 50 eV. The analyzer was located perpendicular to the sample surface. The data was collected every eV with a dwell time of 0.5 s and treated with CasaXPS version 2.317PR1.1 /Casa Software LTD, Teignmouth, UK).

Synthesis of Fe-NCP, Gd-NCP and Mn-NCP 1,4-Bis(imidazole-1-ylmethil)-benzene (**L3**, Bix – 60 mg, 0.25 mmol) and 3,4-dihydroxycinnamic acid (**L4**, dhc – 90 mg, 0.5 mmol) were dissolved in 15 mL of ethanol under vigorous and homogenous magnetic stirring (700 rpm) during 30 minutes at room temperature. Subsequently, the solution was treated with an aqueous solution containing metal salt either $Fe(CH_3COO)_2$ (43.5 mg, 0.25 mmol in 2 mL H_2O; for Fe-NCP), $Gd(CH_3COO)_3 \cdot 6H_2O$ (83 mg, 0.25 mmol in 2 mL H_2O; for Gd-NCP) or $Mn(CH_3COO)_2$ (61 mg, 0.25 mmol in 2 mL H_2O; for Mn-NCP), which turned the solution either black-purple, yellow and dark green, respectively, and led to rapid formation of a precipitate.

Fe-NCP: IR (KBr): 3140 (w, δ (C–H_{ring})), 2974 (w), 1678 (w), 1623 (s, ν(C=N)), 1575 (w), 1519 (s, ν(C–H_{ring})), 1481 (s, ν(C–O)), 1398 (s), 1263 (s, ν(C–O)), 1105 (m), 980 (m), 864 (s, δ(N-H_{ring})), 521 (s, Fe–O) cm^{-1}. Anal. Calcd (%) for **Fe-NCP**: C 47.03, H 4.58, N 5.86; found: C 47.00, H 3.82, N 5.92. ICP-MS Calcd (%) for **Fe-NCP**: Fe 12.05; found: Fe 11.85. Compositional formula: $Fe_1L3_{0.49}L4_{1.30}(AcO^-)_{0.25}(H_2O)_{3.82}$.

Gd-NCP: IR (KBr): 2926 (w, δ (C-H_{ring})), 2853 (w, ν(C–$H_{aliphatic}$)), 1631 (s, ν(C=N)), 1520 (w, νC–H_{ring})), 1416 (s, ν(C-O)), 1271 (s, ν(C–O)), 1121 (m), 978 (m), 864 (s, δ(N-H_{ring})), 542 (s, Gd–O) cm^{-1}. Anal. Calcd (%) for **Gd-NCP**: C 38.79, H 4.06, N 5.89; found: C 38.00, H 3.20, N 6.08. ICP-MS Calcd (%) for **Gd-NCP**: Gd 29.50; found: Gd 29.90. Compositional formula: $Gd_1L3_{0.57}L4_{1.03}(AcO^-)_{0.30}(H_2O)_{3.11}$.

Mn-NCP: IR (KBr): 3128 (w, δ (C–H_{ring})), 2972 (w), 2934 (w, ν(C–$H_{aliphatic}$)), 1629 (s, ν(C=N)), 1520 (w, νC–H_{ring})), 1489 (s, ν(C–O)), 1261 (s, ν(C–O)), 1110 (m), 859 (s, δ(N–H_{ring}), 558 (s, Mn–O) cm^{-1}. Anal. Calcd (%) for **Mn-NCP**: C 53.07, H 5.19, N 8.44; found: C 52.40, H 4.10, N 8.26. ICP-MS Calcd (%) for **Mn-NCP**: Mn 7.74; found: Mn 7.67. Compositional formula: $Mn_1L3_{1.07}L4_{1.82}(AcO^-)_{0.28}(H_2O)_{3.09}$.

Synthesis of GdDTPA-NCP 1,4-Bis(imidazole-1-ylmethil)-benzene (**L3**, Bix – 60 mg, 0.25 mmol) and diethylenetriaminepentaacetic acid (**L5**, DTPA – 84 mg, 0.25 mmol) were dissolved in 15 mL of ethanol under vigorous and homogenous magnetic stirring (700 rpm). Subsequently, the solution was treated with and aqueous solution containing metal salt

$Gd(CH_3COO)_3 \cdot 6H_2O$ (Gadolinium (III) acetate - 83 mg, 0.25 mmol in 2 mL H_2O), which turned the solution deep yellow and led to rapid formation of a precipitate.

GdDTPA-NCP: IR (KBr): 2980 (w, δ ($C–H_{ring}$)), 1678 (w, ν(C=N)), 1598 (w, ν$C–H_{ring}$)), 1411 (s, ν(C–O)), 1266 (s, ν(C–O)), 1118 (m), 931 (m), 866 (s, δ($N–H_{ring}$), 549 (s, Gd–O) cm^{-1}. Anal. Calcd (%) for **GdDTPA-NCP**: C 46.75, H 4.87, N 13.92; found: C 46.89, H 4.70, N 14.45. ICP-MS Calcd (%) for **GdDTPA-NCP**: Gd 20.07; found: Gd 20.50. Compositional formula: $Gd_1L3_{1.39}L5_{0.70}(H_2O)_{1.2}$.

All the synthesis reactions were carried out during 30 minutes under room temperature and atmospheric conditions. The obtained precipitates were centrifuged (7500 rpm, 5 min) and washed with water and ethanol. The precipitates were vacuum dried, and the solvent was removed.

Functionalization of NCPs with BSA All the systems synthesized were functionalized with Bovine or Mouse Serum Albumin (BSA or MSA, respectively) in order to obtain better dispersions reducing the formation of aggregates in solution. All the solutions were prepared in a phosphate buffer (PBS, pH = 7.4) with a physiological concentration of BSA (0.5 mM). The nanoparticles were added to the solution containing BSA and PBS under magnetic stirring at 37 ^oC during 1h.

Quantitative magnetic resonance imaging phantoms (MRI-Phantoms) The samples of nanoparticles were dispersed using agarose (1%) in phosphate buffer solution (PBS) at pH = 7.4. For all families of nanostructures, five samples at decreasing concentrations (0.6, 0.3, 0.1, 0.05 and 0 mM of metal mL^{-1}) were prepared in 1.5 mL Eppendorf tubes. The total volume was adjusted up to 1 mL with agarose in PBS. The dispersions were well dispersed in an ultrasound bath just before the solidification of medium. Acquisition sequences for assessing longitudinal relaxation (T_1) and transversal relaxation (T_1) were carried out with Biospec USR70/30 (Bruker) at 7 Tesla (300 MHz) of magnetic field.

Cell culture Human cervical carcinoma cells (HeLa) were used to test the toxicity of the different nanostructures synthesized and current commercial CAs. Cell line was obtained from the American Type Culture Collection (ATCC; Manassas, VA, USA) and maintained in MEM Alpha medium (Invitrogen) supplemented with 10% (v/v) heat inactivated fetal bovine serum (FBS) and incubating them at 37 ^oC under atmosphere with 95% humidity and 5% CO_2.

Cell viability studies HeLa cells in logarithmic growth phase were seeded by adding 3000 cells/well in 100 μL final volumes in 96-well microplates. After 24 h, cells were treated with increasing doses of the NCPs or commercial CAs based on Gd (Gadopentetate dimeglumine, GdDTPA, Guerbet, Roissy, France) and Mn (Mangafodipir trisodium, MnDPDP, Bayer Healthcare). The effect on cell viability after 24h and 72h was determined using the PrestoBlue reagent assay, which is based on the metabolic reduction of resazurin on resorufin. A Victor3 (Perkin Elmer) fluorimeter plate reader was used to obtain the measurements by fluorescence reading directly from 96-well microplates at an excitation wavelength of 531 nm and emission wavelength of 572 nm. The percentage of cell viability was calculated by dividing the absorbance of each well by the corresponding to the control wells (cells without treatment). The cytotoxicity studies were carried out by triplicate and a minimum of four independent experiments performed on different days. The data was treated with GraphPad Prism software (Version 4.0).

Intracellular reactive oxygen species (ROS) generation studies Measurement of intracellular ROS activity was based on fluorescence emission measurements using CellRox Green Reagent (Molecular Probes). HeLa cells were seeded in 96-well microplates allowed to attach and grow during 24 h. After this time, cells were treated 24 h more with NCPs or commercial CAs. Finally, 20 μL of CellRox reagent was added to each well and incubated for 30 min. Two controls were made: one with cells treated only with cell culture medium as a reference value, and second with H_2O_2 (as an oxidative stress inducer for positive control). The measurements were recorded at an excitation wavelength of 485 nm and emission wavelength of 535 nm using a Victor3 (Perkin Elmer) fluorimeter.

Animal models Animal studies were approved by the local ethics committee, according to the regional and state legislation (protocol DMAH-8333/CEEAH-2785). C57BL/6J female mice of 12 weeks of age, weighting 21.4 ± 1.2 g (n = 12) were purchased from Charles River Laboratories (l'Abresle, France) and housed in the animal facility of the Universitat Autònoma de Barcelona. For *ex vivo* studies, control C57BL/6J mice were used. For *in vivo* studies, GL261 tumour-bearing mice were used, except for tolerability evaluation.

MRI Studies All MRI studies were performed at the joint nuclear magnetic resonance facility of the Universitat Autònoma de Barcelona and Centro de Investigación Biomédica en Red – Bioingeniería, Biomateriales y Nanomedicina (CIBER-BBN) (Cerdanyola del Vallès, Spain), Unit 25 of NANBIOSIS, www.nanbiosis.es. The 7T Bruker BioSpec 70/30 USR spectrometer

(Bruker BioSpin GmbH, Ettlingen, Germany) equipped with a mini-imaging gradient set (400 mT/m) was used for MR acquisitions.

MRI ex vivo studies The CAs were dispersed in 2 ml PBS added with 0.5 mM BSA. The amount finally used for each animal was 5 nmol of metal dissolved in 4 µl PBS - BSA solution. Commercial solutions of CAs based in Gd, (GdDTPA) and Mn (MnDPDP) were used as standards to compare the enhancement obtained with the NCPs synthesized. Three injection points were used in each mouse (n = 2 for each CA). High resolution T_{1w} and T_{2w} MR images (TR/TE =4200/12 ms) were acquired using a rapid acquisition with relaxation enhancement (RARE) sequence for a morphological characterization of the investigated tissue. All the CAs administrations were done *post mortem* using a stereotactic holder.

Tolerability Studies Increasing amounts of Fe-NCP (0.03 to 0.4 mmol Fe Kg^{-1}) were intravenously (i.v.) administered to n = 3 mice with a 2-day rest period between injections. An additional group of n = 3 wild type (wt) mice was injected with the vehicle for *in vivo* studies (PBS) added with 0.5 mM MSA. Mice body weight and other welfare parameters were followed up for detection of any signs of animal suffering during 30 days after the last administration. No higher doses were tested in this assay.

MRI in vivo studies GL261 tumour-bearing mice (n = 3, 12.7 ± 0.6 days after tumour implantation, tumour volume 38.1 ± 27.5 mm^3) were placed in a mouse bed and anesthetized with isoflurane 0.5–1.5% in O_2. Breathing (60-80 breaths/min) and temperature (37-38 °C) were constantly monitored (SA Instruments, Inc., New York, USA). A first experiment with commercial GdDTPA administration was carried out. A second experiment with Fe-NCP was performed with n = 3 mice. The amount of CA injected in tumour-bearing mice was 107.1 ± 6.4 µl (0.4 mmol metal kg^{-1}). In order to assess both T_1 and T_2 RCE, T_{1w} and T_{2w} images (TR/TE = 200/8.5 ms and 4200/12 ms, respectively) were acquired before and immediately after i.v. injection of CA. Three T_{1w} and three T_{2w} images were acquired before the CA injection. Then, alternated T_{1w} – T_{2w} images were acquired continuously during 30 min after CA administration, resulting in a total of 15 frames for T_{1w} and 15 frames for T_{2w} images. In addition, individual T_{1w} and T_{2w} acquisitions were also performed at 2 and 24 h after CA administration. Studies were also conducted (n = 3) with the vehicle of administration (PBS added with 0.5 MSA) with a standard DCE-MRI sequence consisting in T_{1w} MRI acquisitions in a total of 70 frames, with no T_2 alternating sequences.

Processing and post-processing of MR data. For *ex vivo* studies, ROIs were selected in T_{1w} and T_{2w} images, corresponding to the CAs administration points. They were manually defined after visual inspection in the area of maximum enhancement and an equivalent area of contralateral parenchyma. The relative contrast enhancement (RCE) - injection site ROI vs. contralateral parenchyma - obtained in each case was used for calculations (see Equation 1). Only the slice with better defined contrast-enhanced region in the best study was used for measurements. For dual enhancement images, T_{1w} and T_{2w} images were processed with the algebra algorithm (MR signal T_1 /MR signal T_2) provided by Paravision 5.1.

$$\mathrm{RCE}(\%)_{ex\ vivo} = \left(\frac{S_{(i)}}{S_{(c)}}\right) \text{ x } 100 \qquad \text{(Equation 2)}$$

Where S (i) is the absolute signal intensity of the "ipsilateral" region with respect to the contrast administration and that visually shows contrast enhancement, and S (c) is the absolute signal intensity of the equivalent contralateral region.

For *in vivo* studies, two ROIs were manually selected in each slice: one corresponding to the tumour area and the second corresponding to contralateral normal brain tissue. Then, RCE for each slice was calculated as in *ex vivo* studies. Mean RCE of the three images acquired before CA injection was referred as 100%, and then RCE signals of images acquired after CA injection were estimated accordingly.

Statistical analysis Normality of the distribution values was inspected with Kolmogorov-Smirnov test. Variance equality was estimated with Levene's test. Student's t-test was used for RCE bilateral comparisons. The *in vitro*, *ex vivo* and *in vivo* RCE evolution during the first 30 minutes was performed with UNIANOVA. Significance level was set to 0.05.

Biodistribution studies ICP-MS was used for the biodistribution of Fe-NCP. For each experimental group, prior to injection, a nanoparticle aliquot was saved for the determination of iron concentration in the injected material. After the *in vivo* experiments, the mice were euthanized and the organs of interest (brain, tumour, lungs, bladder, kidneys and liver) excised and stored at -80 ºC. Previous to ICP-MS measurements, organ samples were thoroughly washed with PBS and blotted dry to minimize the contribution of any nanoparticles still circulating in the blood. The organs were weighted into vials and digested overnight at 70 ºC with 1 ml of protein extraction reagent (T-PER™, Thermo Fisher Scientific) per 100 mg of tissue and 10 mL of aqua regia (1HNO_3:3HCl, trace metal grade) (v/v). After that, the organs were sonicated with an ultrasounds probe (Branson 550, Emerson, St Louis, MO, USA) for 10 cycles until the complete digestion (300 W, 10 min). For the quantification of metal, a dilution 1:100 was necessary for detecting the correct signals. For ICP-MS analysis, atomic spectroscopic analytical standards were purchased from PerkinElmer Pure Plus. The isotope

^{57}Fe was selected as tracer. The iron concentration of each sample was measured using a calibration curve obtained in the range of 0.01-500 ppb of metal. Standard reference material (PerkinElmer) with known values of Iron was analysed with each batch of samples. All the samples were measured per quadruplicate. For protein quantification a Bradford kit protocol was used (Quick Start Bradford Dye reagent X1, Biorad, Hercules, CA, USA). The biodistribution of iron ions was plotted per µg of protein content in each organ. The results were expressed as mean ± SD. An unpaired Student's t-test was used. Significant level was set to 0.05.

4.2.5 References

1. Haunes, H.; Holmes, W. M. The Emergence of Magnetic Resonance Imaging (MRI) for 3D Analysis of Sediment Beds. Chapter 1, Section 5.4; **2013**.
2. Weissleder, R.; Ross, B. D.; Rehemtulla, A.; Gambhir, S. S. Molecular Imaging: Principles and Practice. Shelton, CT, USA: People's Medical Publishing House; **2010**.
3. Cabrera-García, A.; Checa-Chavarria, E.; Pacheco-Torres, J.; Bernabeu-Sanz, A.; Vidal-Moya, A; Rivero-Buceta, E.; Sastre, G.; Fernández, E.; Botella, P. *Nanoscale* **2018**, *10*, 6349−6360.
4. Li, Z.; Yi, P. W.; Sun, Q.; Lei, H.; Zhao, H. L.; Zhu, Z. H.; Smith, S. C.; Lan, M. B.; Lu, G. Q. *Adv. Funct. Mater*. **2012**, *22*, 2387−2393.
5. Na, H. B.; Song, I. C.; Hyeon, T. *Adv. Mater*. **2009**, *21*. 2133−2148.
6. Jun, Y.-W.; Lee, J.-H.; Cheon, J. *Angew. Chem. Int. Ed.* **2008**, *47*, 5122−5135.
7. Wahsner, J.; Gale, E. M.; Rodríguez-Rodríguez, A.; Caravan, P. *Chem. Rev.* **2019**, *119*, 957−1057
8. Joseph, A.; Villaraza, L.; Bumb, A.; Brechbiel, M. W. *Chem. Rev*. **2010**, *110*, 2921−2959.
9. Rogosnitzky, M.; Branch, S. *Biometals* **2016,** *29*, 365−376.
10. Ramalho, J. ; Semelka, R. C.; Ramalho, M.; Nunes, R. H.; AlObaidy, M.; Castillo, M. *AJNR Am. J Neuroradiol.* **2016**, *37*, 1192−1198.
11. Lee, N.; Hyeon, T. *Chem. Soc. Rev*. **2012**, *41*, 2575−2589.
12. Hasebroock, K. M.; Serkova, N. J. *Expert Opin. Drug Metab. Toxicol.* **2009**, *5*, 403−416.
13. Khawaja, A. Z.; Cassidy, D. B.; Al Shakarchi, J.; McGrogan, D. G.; Inston, N. G.; Jones, R. G. *Insights Imaging* **2015**, *6*, 553−558.
14. Kanal, E.; Tweedle, M. F. *Radiology* **2015**, *275*, 630−634.
15. McDonald, R. J.; McDonald, J. S.; Kallmes, D. F.; Jentoft, M. E.; Murray, D. L.; Thielen, K. R.; Williamson, E. E.; Eckel, L. J. *Radiology* **2015**, *275*, 772−782.
16. Yang, H.; Zhang, C.; Shi, X.; Hu, H.; Du, X.; Fang, Y.; Ma, Y.; Wu, H.; Shi, X. *Biomaterials* **2010**, *31*, 3667−3673.

17. Ho, D.; Sun, X.; Sun, S. *Acc. Chem. Res*. **2011**, *44*, 875–882.
18. Lee, N.; Yoo, D.; Ling, D.; Cho, M. –H.; Hyeon, T.; Cheon, J. *Chem. Rev*. **2015**, *115*, 10637−10689.
19. Lee, D. -L.; Koo, H.; Sun, I. -C.; Ryu, J. H.; Kim, K.; Kwon, I. C. *Chem. Soc. Rev*. **2012**, *41*, 2656–2672.
20. Ni, D.; Ehlerding, E. B.; Cai, W. *Angew. Chem. Int. Ed*. **2019**, *58*, 2570–2579.
21. Jin, Q.; Zhu, W.; Jiang, D.; Zhang, R.; Kutyreff, C. J.; Engle, J. W.; Huang, P.; Cai, W.; Liu, Z.; Cheng, L. *Nanoscale* **2017**, *9* (34), 12609–12617.
22. Wang, J.; Sanwg, W.; Yang, Z.; Shen, Z.; Wang, Z.; Jacobson, O.; Chen, Y.; Wang, Y.; Shao, M.; Niu, G.; Dai, Y.; Chen, X. *J. Mater. Chem. B*, **2019**, Advance Article.
23. Zhou, Z.; Bai, R.; Munasinghe, J.; Shen, Z.; Niea, L.; Chen, X. *ACS Nano* **2017**, *11*, 5227−5232.
24. Zhou, Z.; Huang, D.; Bao, J.; Chen, Q.; Liu, G.; Chen, Z.; Chen, X.; Gao, J. *Adv. Mater*. **2012**, *24*, 6223–6228.
25. Shin, T.-H.; Choi, J.-S.; Yun, S.; Kim, S.; Song, H.-T.; Kim, Y.; In Park, K.; Cheon, J. *ACS Nano* **2014**, *8*, 3393–3401.
26. Zhang, L.; Liang, S.; Liu, R.; Yuan, T.; Zhang, S.; Xu, Z.; Xu, H. *Colloids Surf. B Biointerfaces* **2016**, *144*, 344−354.
27. Choi, J. S.; Lee, J. H.; Shin, T, H.; Song, H. T.; Kim, E. Y.; Cheon, J. *J. Am. Chem. Soc*. **2010**, *132*, 11015−11017.
28. Im, G. H.; Kim, S. M.; Lee, D.-G.; Lee, W. J.; Lee, J. H.; Lee, I. S. *Biomaterials* **2013**, *34*, 2069−2076.
29. Li, F.; Zhi, D.; Luo, Y.; Zhang, J.; Nan, X; Zhang, Y.; Zhou, W.; Qiu, B.; Wen, L.; Liang, G. *Nanoscale* **2016**, *8*, 12826−12833.
30. Huang, G.; Li, H.; Chen, J.; Zhao, Z.;Yang, L.; Chi, X.; Chen, Z.; Wang, X.; Gao, J. *Nanoscale* **2014**, *6*, 10404−10412.
31. Wang, X.; Zhou, Z.; Wang, Z.; Xue, Y.; Zeng, Y.; Gao, J.; Zhu, L.; Zhang, X.; Liu, G.; Chen, X. *Nanoscale* **2013**, *5*, 8098−8104.
32. Yang, L.; Zhou, Z.; Liu, H.; Wu, C.; Zhang, H.; Huang, G.; Ai, H.; Gao, J. *Nanoscale* **2015**, *7*, 6843−6850
33. Li, Z.; Yi, P. W.; Sun, Q.; Lei, H.; Zhao, H. L.; Zhu, Z. H.; Smith, S. C.; Lan, M. B.; Lu, G. Q.; *Adv. Funct. Mater.* **2012**, *22*, 2387−2393.
34. Niu, D.; Luo, X.; Li, Y.; Liu, X.; Wang, X.; Shi, J. *ACS Appl. Mater. Interfaces* **2013**, *5*, 9942−9948.
35. Courant, T.; Roullin, V. G.; Cadiou, C.; Callewaert, M.; Andry, M .C.; Portefaix, C.; Hoeffel, C.; de Goltstein, m. C.; Port, M.; Laurent, S.; Elst, L. V.; Muller, R..; Molinari, M.; Chuburu, F. *Angew. Chem., Int. Ed*. **2012**, *51*, 9119− 9122.

36. Chen, Y.; Ai, K.; Liu, J.; Ren, X.; Jiang, C.; Lu, L. *Biomaterials* **2016**, *77*, 198−206.
37. Wang, L.; Lin, H.; Ma, L.; Jin, J.; Shen, T.; Wei, R.; Wang, X.; Ai, H.; Chen, Z.; Gao, J. *Nanoscale* **2017**, *9*, 4516−4523.
38. Wang, G. D.; Chen, H.; Tang, W.; Lee, D.; Xie, J. *Tomography* **2016**, *2*, 179−187.
39. Zhu, W.; Liu, Y.;Yang, Z.; Zhang, L.; Xiao, L.; Liu, P.; Wang, J.; Yi, C.; Xu, Z.; Ren, J. *J. Mater. Chem. B* **2018**, *6*, 265−276.
40. Borges, M.; Yu, S.; Laromaine, A.; Roig, A.; Suarez-Garcia, S.; Lorenzo, J.; Ruiz-Molina, D.; Novio, F. *RSC Adv*. **2015**, *5*, 86779−86783.
41. Delgado-López, P. D.; Corrales-García, E. M. *Clin. Transl. Oncol*. **2016**, *18*, 1062–1071.
42. Ostrom, Q.T.; Gittleman, H.; Liao, P.; Rouse, C.; Chen, Y.; Dowling, J.; Wolinsky, Y.; Kruchko, C.; Barnholtz-Sloan, J. *Neuro Oncol.* **2014**, *16*, 1–63.
43. Hernández-Pedro, N. Y.; Rangel-López, E.; Magaña-Maldonado, R., Pérez de la Cruz, V.; Santamaría del Ángel, A.; Pineda, B.; Sotelo, J. *Biomed. Res. Int*, **2013**, 351031.
44. Day, E. S.; Zhang, L.; Thompson, P. A.; Zawaski, J. A.; Kaffes, C. C.; Gaber, M. W.; Blaney, S. M.; West, J. L. *Nanomedicine* **2012**, *7*, 1133–1148.
45. Cheng, W.; Ping, Y.; Zhang, Y.; Chuang, K. –H.; Liu, Y. *J. Healthc. Eng.* **2013**, *4*, 26–46.
46. Oller-Salvia, B.; Sánchez-Navarro, M.; Giralt, E.; Teixidó, M. *Chem. Soc. Rev*. **2016**,*45*, 4690–4707.
47. Meola, A.; Rao, J.; Chaudhary, N.; Sharma, M.; Chang, S. D. *Front. Neurol*. **2018**, *9*, 328.
48. Shevtsov, M.; Multhoff, G. *Curr. Drug Metab.* **2016**, *17*, 733–744.
49. Dubois, L. G.; Campanati, L.; Righy, C.; D'Andrea-Meira, I.; Spohr, T. C. L.; Porto-Carreiro, I.; Pereira, C. M.; Balça-Silva, J.; Kahn, S. A.; DosSantos, M. F.; Oliveira, M. A. R.; Ximenes-da-Silva, A.; Lopes, M. C.; Faveret, E.; Gasparetto, E. L.; Moura-Neto, V. *Front. Cell Neurosci.* **2014**, *8*, 418.
50. Szatmári, T.; Lumniczky, K.; Désaknai, S.; Trajcevski, S.; Hídvégi, E. J.; Hamada, H.; Sáfrány, G. *Càncer Sci.* **2006**, *97*, 546–553.
51. Novio, F.; Lorenzo, J.; Nador, F.; Wnuk, K.; Ruiz-Molina, D. *Chem. Eur. J*. **2014**, *20*, 15443−15450
52. Aires, A.; Ocampo, S. M.; Cabrera, D.; de la Cueva, L.; Salas, G.; Teran, F. J.; Cortajarena, A. L. *Mater. Chem. B* **2015**, *3*, 6239−6247.
53. Mariam, J.; Sivakami, S.; Dongre, P. M. *Drug Delivery* **2016**, *23*, 2668−2676.
54. Jo, D. H.; Chiou, Y.-M.; Que, L. Jr. *Inorg. Chem.* **2001**, *40*, 3181−3190.
55. Nador, F.; Novio, F.; Ruiz-Molina, D. *Chem. Commun.* **2014**, *50*, 14570−14572.
56. Amorín-Ferré, L.; Busqué, F.; Bourdelande, J. L.; Ruiz-Molina, D.; Hernando, J.; Novio, F. *Chem. Eur. J*. **2013**, *19*, 17508–17516.
57. Birben, E.; Murat Sahiner, U.; Sackesen, C.; Erzurum, S.; Kalayci, O. *World Allergy Organ J.* **2012**, *5(1)*, 9–19.

58. Stohs, S. J.; Bagchi, D. *Free Radic. Biol Med.* **1995**, *18*, 321–336.
59. Fu, P. P.; Xia, Q.; Hwang, H.-M.; Ray, P. C.; Yu, H. *J. Food Drug Anal.* **2014**, *22*, 64–75.
60. Cotton, F. A.; Wilkinson, G.; Murillo, C. A.; Bochmann, M. in Advanced Inorganic Chemistry. *John-Wiley and Sons, Inc*. New York, 6th edn., **1999**, p. 761.
61. Chen, J. Y.; Tsao, G. C.; Zhao, Q.; Zheng, W. *Toxicol Appl Pharmacol*. **2001**, *175*, 160–168.
62. Sanchez, L. M.; Arciniegas, L.; Alvarez, V. A.; Gonzalez, J. S. in Materials for Biomedical Engineering. *Elsevier Inc.*, Amsterdam, **2019**, Chapter 14, p. 435.
63. Wartenberg, N.; Fries, P.; Raccurt, O.; Guillermo, A.; Imbert, D.; Mazzanti, M. *Chem. Eur. J*. **2013**, *19*, 6980–6983.
64. Srivastava, S.; Awasthi, R.; Tripathi, D.; Rai, M. K.; Agarwal, V.; Agrawal, V.; Gajbhiye, N. S.; Gupta, R. K. *Small* **2012**, *8*, 1099–1109.
65. Guo, J.; Ping, Y.; Ejima, H.; Alt, K.; Meissner, M.; Richardson, J. J.; Yan, Y.; Peter, K.; von Elverfeldt, D.; Hagemeyer, C. E.; Caruso, F. *Angew. Chem. Int. Ed.* **2014**, *53*, 5546–5551.
66. Wang, J.; de Keizer, A.; van Leeuwen, H. P.; Yan, Y.; Vergeldt, F.; van As, H.; Bomans, P. H. H.; Sommerdijk, N. A. J. M.; Stuart, M. A. C.; van der Gucht, J. *Langmuir*, **2011**, *27*, 14776–14782.
67. Rodríguez, E.; Simoes, R. V.; Roig, A.; Molins, E.; Nedelko, N.; Slawska-Waniewska, A.; Aime, S.; Arus, C.; Cabañas, M. E.; Sanfeliu, C.; Cerdán, S.; García-Martín, M. L. *Magn. Reson. Mater. Phys., Biol. Med*. **2007**, *20*, 27–37.
68. Schwert, D. D.; Richardson, N.; Ji, G.; Radüchel, B.; Ebert, W.; Heffner, P. E.; Keck, R.; Davies, J. A. *J. Med. Chem*. **2005**, *48*, 7482–7485
69. Horcajada, P.; Chalati, T.; Serre, C.; Gillet, B.; Sebrie, C.; Baati, T.; Eubank, J. F.; Heurtaux, D.; Clayette, P.; Kreuz, C.; Chang, J.-S.; Hwang, Y. K.; Marsaud, V.; Bories, P.–N.; Cynober, L.; Gil, S.; Férey, G.; Couvreur, P.; Gref, R. *Nat. Mat*. **2010**, 9, 172–178.
70. Bouchard, L.-S.; Anwar, M. S.; Liu, G. L.; Hann, B.; Gray, J. W.; Wang, X.; Pines, A.; Chen, F. F. *Proc Natl Acad Sci* USA **2009**, *106*, 4085–4089.
71. Candiota, A. P.; Acosta, M.; Simoes, R. V.; Delgado-Goni, T.; Lope-Piedrafita, S.; Irure Yoldi, A.; Marradi, M.; Bomatí-Miguel, O.; Miguel-Sancho, N.; Abasolo, I.; Schwartz, Jr. S.; Santamaria, J.; Penadés, S.; Arús, C. *J. Nanobiotechnology* **2014**, *12*, 1–14.
72. Mustafi, D.; Peng, B.; Foxley, S.; Makinen, M. W.; Karcmar, G. S; Zamora, M.; Ejnik, J.; Martin, H. *J. Biol. Inorg. Chem.* **2009**, *14*, 1187–1197.
73. Marradi, M.; Alcántara, D.; de la Fuente, J.; García-Martín, M.; Cerdan, S.; Penadés, S. *Chem Commun.* **2006**, *26*, 3922–3924.
74. Gheorghe, D. E.; Cui, L.; Karmonik, C.; Brazdeikis, A.; Penaloza, J. M.; Young, J. K.; Drezek, R. A.; Bikram, M. *Nanoscale Res Lett*. **2011**, *6*, 1–12.
75. Saldana-Ruiz, S.; Soler-Martin, C.; Llorens, J. *Toxicol Lett*. **2012**, *208*, 125–132.

76. LASA; NC3Rs, Guidance on dose level selection for regulatory general toxicology studies for pharmaceuticals. Laboratory Animal Science Association & National Centre for the Replacement, R. a. R. o. A. i. R., Ed. London, **2009**.
77. Funk, F.; Ryle, P.; Canclini, C.; Neiser, S.; Geisser, P. *Arzneimittel-Forschung* **2010**, *60(6a)*, 345–353.
78. Cheng, W.; Ping, Y.; Zhang, Y.; Chuang, K. H.; Liu, Y. *J. Healthc. Eng.* **2013**, *4(1)*, 23–45.
79. Gu, L.; Fang, R. H.; Sailor M. J.; Park, J. H. *ACS Nano* **2012**, *6(6)*, 4947–4954.
80. Wei, Y.; Zhao, M.; Yang, F.; Mao, Y.; Xie, H.; Zhou, Q. *Sci Rep*. **2016**, *6*, 29110.
81. Ramalho, J.; Ramalho, M.; Jay, M.; Burke, L. M.; Semelka, R. C.. *Magn. Reson. Imaging* **2016**, *34(10)*, 1394–1398.
82. Nador, F.; Wnuk, K.; García-Pardo, J.; Lorenzo, J.; Solorzano, R.; Ruiz-Molina, D. *ChemNanoMat* **2018**, *4*, 183–193
83. Adarsh, N. N.; Frias, C.; Ponnoth Lohidakshan, T.M.; Lorenzo, J.; Novio, F.; Garcia-Pardo, J.; Ruiz-Molina, D. *Chem. Eng. J.* **2018**, *340*, 94–102.
84. Choi, H. S.; Liu, W.; Misra, P.; Tanaka, E.; Zimmer, J. P.; Ipe, B. I.; Bawendi, M. G.; Frangioni, J. V. *Nat Biotechnol.* **2007**, *25*, 1165–1170
85. Crayton, S. H.; Elias, A.; Al-Zaki, A.; Cheng, Z.; Tsourkas, A. *Biomaterials* **2012**, *33*, 1509–1519.
86. Yoo, J. W.; Chambers, E.; Mitragotri, S. *Curr. Pharm. Des.* **2010**, *16*, 2298–2307.
87. Zuñiga, J. M.; Orellana, J. M.; Tur, J. M. In Ciencia y Tecnología Animal de Laboratorio. Universidad de Alcalá de Henares – Sociedad Española para las Ciencias del Animal de Laboratorio (SECAL), Alcalá de Heanres, **2008**.
88. Gozzard, D. *Drug Des. Devel. Ther.* **2011**, *5*, 51−60.
89. Adarsh, N. N.; Novio, F.; Ruiz-Molina, D. *Dalton Trans.* **2016**, *45*, 11233−11255.

Chapter 4.3

Modular Assembly of Radiolabelled Catechol-Based Nanostructured Coordination Polymers for Lung Targeting

In this Chapter, nanoscale coordination polymers (NCPs) based on the coordination between indium (In(III)) and copper (Cu(II)) ions and a mixture of rationally selected organic ligands were synthesized via fast solvent-induced precipitation method and studied as potential agents for radioimaging. The resulting NCPs were coated with a novel catechol-based polymer which included poly(ethylene glycol) (PEG) in its structure to generate highly stable nanoparticles in physiological conditions. Additionally, the incorporation of folic acid (FA) to the PEG chains enhanced their targeting properties for specific tissues such as lung or liver, and tumour accumulation. The NCPs developed, can be used as radiotracers for single-photon emission computed tomography (SPECT) and positron emission tomography (PET). The *in vitro* and *in vivo* studies corroborated their versatility, easy and fast synthesis, and biocompatibility. These NCPs presented high biocompatibility, excellent imaging properties, interesting biodistribution profile and rapid body clearance. The obtained results indicate that the developed nanoplatforms could be very promising systems for further clinical translation concerning imaging-guide cancer therapy, especially for pulmonary drug delivery due to their preferential accumulation in lungs.

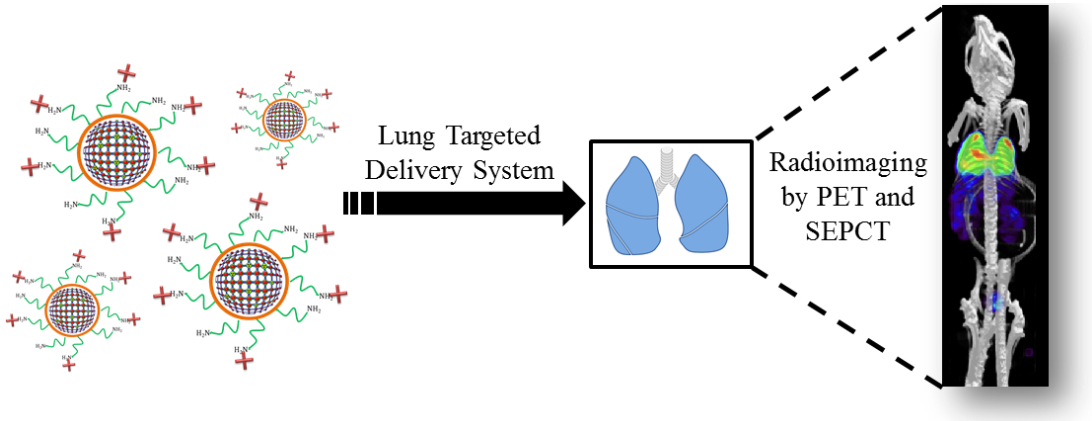

4.3.1 Introduction

The use of radiotracers for diagnostic applications has been studied for decades. Despite numerous efforts to obtain new, more effective and, above all, more secure systems, there are still certain issues that must be addressed. In this Chapter 4.3 we present, in a similar way to the previous Chapter 4.2, a method for the polymerisation of radiotracers forming nanoparticles with special features to be applied in radioimaging. However, in contrast to the previous Chapter, the synthetic nanoparticles have been coated with a new multifunctional coating based on catechols developed to universally coat almost any surface. To prove its effectiveness, nanoparticles are targeted by including a targeting molecule (folic acid) and their biodistribution *in vivo* by means of single-photon emission computed tomography (SPECT) and positron emission tomography (PET) techniques has been performed. This last part has been developed in collaboration with the *Hafeli Lab* research group led by Prof. Urs Hafeli at *University of British Columbia* (UBC, Vancouver, Canada) under the supervision of Dr. Cristina Rodríguez-Rodríguez.

4.3.1.1 The basis of positron emission and single-photon emission computed tomography (PET/SPECT) imaging

Nuclear medicine can be defined as the use of radioactive materials for the diagnosis and treatment of patients and the study of human diseases. The radiation emitted can be classified into electromagnetic high-energy photons (e. g. x-rays, ɣ-rays, annihilation photons) and charged particles (e. g. β^-, β^+, α).

PET and SPECT scans are acquired following administration of a radiotracer. The radiotracer accumulates in the tissue to be studied, and its radionuclide decays by emission of energy. In the case of PET imaging, the radiotracer emits a positron (anti-electron). After travelling at most a few millimetres, a positron will collide with an electron by an annihilation process, simultaneously releasing two gamma photons (ɣ-ray photons) with energy of 511 keV into opposite directions (Figure 4.37a). These two photons are detected by the PET camera and simultaneously localized within a fixed period of time by a series of opposing detectors, which correspond to multiple rings of scintillation crystals. By collecting a statistically significant number of radioactive events, mathematical algorithms reconstruct a three-dimensional image that shows the distribution of the positron-emitting molecules in the whole body. On the other hand, the SPECT imaging is based on the ɣ-ray photons emitted from the internal distributed radiotracer within the body of the patient and are detected by a single or a set of collimated radiation detectors (Figure 4.37b). Most of the detectors used in current SPECT systems are based on a single or multiple scintillation detectors of sodium iodide doped with thallium (NaI(Tl)). In SPECT, projection data are acquired from different views around the patient whole body.

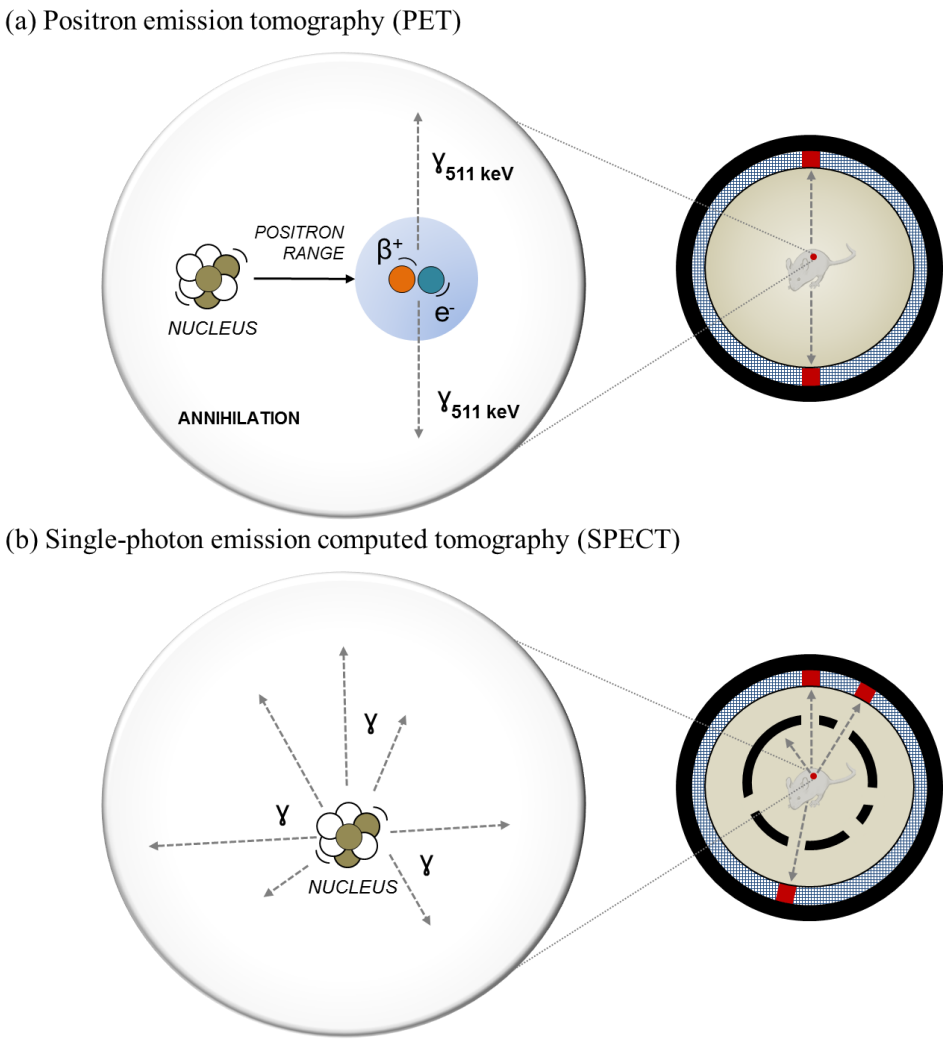

Figure 4.37 PET and SPECT basis. (a) The image from PET scan is obtained due to the detection of two ɣ-ray photons emitted in the same direction but different sense with energy of 511 keV. This emission is originated from the annihilation process between a positron (emitted by the radiotracer) and one electron from the body of the patient. The two ɣ photons are detected simultaneously and converted into electrical signals which subsequently is filtered and reconstructed for the conformation of the image. (b) The image from the SPECT analysis is obtained through the ɣ disintegration of a radionuclide inside the body. The SPECT radiotracers are ɣ-emitting isotopes which directly produce the ɣ-rays emission. The obtained images are bidimensional but can be combined from different positions and reconstructed in a 3D image.

Both PET and SPECT have some advantages and disadvantages summarized in Table 4.9. Basically, SPECT imaging allows the use of a greater number of isotopes that are easier to obtain (at the laboratory scale) and whose life is longer compared to active PET radiotracers. In the latter case, advanced facilities are needed to produce positron emitting radiotracers such as the Cyclotron, which also makes its production more expensive. In terms of sensitivity, the PET imaging allows higher values. Additionally, with PET scan is possible to perform quantitative analysis. Due to the short time of the PET-active radiotracers, the increase in injected doses is usually necessary. However, this can be compensated due to the greater sensitivity of the technique. From a clinical point of view, SPECT is the most used technique and is experiencing a continuous growth. In the case of PET imaging, its high costs make it less common. Nevertheless, it has demonstrated a high potential for the diagnosis

of neural and cardiology diseases. Furthermore, the use of ^{18}F combined with a glucose derivative (2-Fluoro-2-desoxi-D-glucosa, FDG) for the cancer diagnosis, is becoming a routine.

Table 4.9 Advantages, disadvantages and clinical use of SPECT and PET imaging techniques.

Method	Advantages	Disadvantages	Clinical use
SPECT	-Resolution limited by technology only -Low sensitivities -Can differentiate between isotopes with different radiation energies	-2D planar images and reconstructed 3D -Semiquantitative data only	-Readily available and in widespread use -Wide range of clinically tested tracers
PET	-High sensitivity -3D acquisition -Good resolution, but with a physical limit -Quantification possible	-Short-lived isotopes -Isotopes produced in cyclotrons -Expensive tracer production -Expensive equipment -Higher tissue dose, but compensated with higher sensitivity	-^{18}[F]FDG becoming routine in oncology -Special applications un neurology and cardiology

4.3.1.2 State-of-the-art of radiotracers: The use of NCPs for PET/SPECT

One of the most important characteristics of a radiotracer is that it can facilitate the study of the components of a homeostatic system without disturbing their function. Radionuclide imaging has emerged as a sophisticated and powerful technique for the detection, imaging and monitoring of several diseases. PET and SPECT imaging have some advantages compared with other imaging techniques such as FI, MRI, or CT (Figure 4.6):[1]

i. Superior detection sensitivity (down to picomolar range)
ii. Deeper signal penetration (especially when compared with optical imaging)
iii. Better quantitative capacity

The potential safety concerns related with the use of radiotracers is a specific issue of this technique that researchers must face in an effective way. Most nanomaterials, and especially inorganic and non-biodegradable nanoparticles, are trapped in the reticuloendothelial system (RES) organs such as liver and spleen, resulting in poor excretion of nanoparticles from the body and in a potential long-term toxicity.[2] Usually, the radiometals suitable for PET/SPECT (Table 4.10) imaging need a chelator molecule to form stable complexes.[3] Selection of the chelator must be specific for each radiometal based on its physicochemical properties such as oxidation state, coordination number and kinetic inertness, among others.

Table 4.10 Radiotracers for PET and SPECT techniques

Radionuclides for PET			Radionuclides for SPECT		
Nuclide	**$T_{1/2}$ (min)**	**SA (Ci µmol^{-1})**	**Nuclide**	**$T_{1/2}$ (min)**	**SA (Ci µmol^{-1})**
^{82}Rb	1.20	150400	^{99m}Tc	360	522
^{15}O	2.07	917630	^{67}Ga	4320	40
^{122}I	3.62	51912	^{111}In	4020	47
^{62}Cu	9.76	19310	^{123}I	780	237
^{13}N	10.0	18900			
^{11}C	20.4	9220			
^{94m}Tc	52.0	3614			
^{68}Ga	68.3	2766			
^{77}Br	96.0	1960			
^{18}F	110	1708			
^{66}Ga	567	331			
^{64}Cu	768	245			
^{86}Y	884	213			
^{89}Zr	4709	39.9			
^{124}I	6048	31.0			

Different radionuclides used for PET and SPECT imaging techniques. The marked radionuclides were the used in work presented in this Chapter. $T_{1/2}$: half-life time. SA: specific radioactivity.

In this scenario, NCPs may be good candidates for the inclusion of radiometals in a safer strategy, allowing the formation of predesigned systems with good biocompatibility and biodegradability and avoiding the potential risks of using radiometals. In this Chapter 4.3, we present a successful strategy for the nanoscale coordination polymerization of ^{111}In (active in SPECT imaging) and ^{64}Cu (active in PET imaging) (Table 4.10). Previously, the most recent examples in the literature for the use of PET/SPECT-active NCPs are discussed.

There are several approaches for the synthesis of PET- and SPECT-active nanoparticles. The different methods can be mainly classified in three different approaches: i) post-radiolabelling, ii) pre-radiolabelling and iii) direct radiolabelling without chelators.[4] In the first strategy, the nanoparticles are previously formed and subsequently radiolabelled in a post-processing step by attaching a exogenous on the surface and adding the corresponding radiometal chelator (frequently used chelators are DOTA, NOTA, DFO, DTPA or phthalocyanines).[5-9] Nevertheless, this surface functionalization, results in a decreased available surface for the PEGylation or targeting molecules which have a significant effect in the final biodistribution by decreasing the circulation time and offering less affinity.[10-12] Furthermore, the use of chelating agents are often involved in high-temperature incubation processes with radionuclides for their binding that can induce the degradation and the consequent loss of activity of sensitive molecules like antibodies, peptides or other functional proteins. In order to overcome this limitation, the second group of strategies appeared as alternative. In this case, the radionuclide chelation is done in a previous step before its attachment in the surface of the nanoparticles.[13-14] However, it should be noted that the use of specific chelators, which are able

to coordinate with certain radioisotopes, limits the possibilities for the formation of novel platforms. For this reason, nowadays the main strategy is focused on the one hand in the use of chelator-free systems, avoiding the laborious synthesis procedures with extreme conditions and, on the other hand, the reduction of the side effects due to the use of radionuclides.

The first precedent of NCPs containing radiometals was published in 2014 for Oh *et al*.[15] The authors described a synthesis strategy for the formation of CP nanoparticles as radiotracers. In this work, NCPs with a ɣ-emitting radionuclide (^{198}Au) were prepared by the coordination polymerization of Au^{3+} ions and an imidazole-based ligand. This reaction resulted in the formation of radio-active nanoparticles with a diameter of 5-7 nm. The performed physicochemical characterization of such NCPs revealed the successful introduction of the Au radionuclides in the polymeric structure. The use of the same strategy but employing other ligands, corroborated the success of such methodology for the formation of NCPs as potential radiotracers.[16] However, the lack of *in vitro* and *in vivo* studies makes it impossible to know their behaviour in biological systems.

Shen et al. reported a one-step synthesis of renal-clearable ultrasmall NCPs for the chelator-free of ^{64}Cu radionuclides, enabling PET imaging.[17] The NCPs were formed by the coordination between W(IV) ions and gallic acid (GA) as bridging ligand. Then, they were mixed with a solution containing ^{64}Cu which presumably attached to the phenol groups of GA. The resulting nanoparticles were further PEGylated for biocompatibility and together with their ultra-small size (1.61 ± 0.23 nm) helped to the rapid and effective renal clearance as validated by PET imaging. Although the developed nanoparticles did not induced cytotoxicity, the biodistribution results showed the retention in the RES especially with high values in liver. This system demonstrated a feasible strategy for the formation of radioimaging-active NCPs avoiding the long-term side effects. These NCPs greatly enhanced the efficacy of cancer radiotherapy by inhibiting the tumour growth owing to the radio-sensitizing function of tungsten with strong X-ray absorption with no additional side effects.

Most recently, in 2018, Lu et al. reported the ^{64}Cu loading of NCPs for PET imaging.[18] The radiolabelling was performed by encapsulating phthalocyanines in water-dispersible PEG coated nanoparticles using mild conditions. The radiochemistry yield achieved was high, reporting values more than >90% of radionuclide chelation. With this strategy nanoparticles were produced in a wide distribution size range (from 70 to 160 nm) but fitting the common sizes of bio-applied nanoparticles. The development of these nanoplatforms for rapid and facile radionuclide labelling expands the applications of NCP-based radioimaging.

As mentioned above, there are few examples of NCPs and their use as radiotracers. This is because, in general, NCPs are less explored for biological and biomedical imaging in comparison with MOFs and NMOFs, which received much more attention in the past years.[19,20] NCPs have been examined mainly as CAs for MRI, CT, and OI, but few studies were carried out with radiolabelling

CPs. For this reason, there is a need to study and develop this kind of nanosystems to explore their use in radioimaging. Furthermore, efforts for providing more evidence of the effectiveness of these systems in terms of stability, biocompatibility, biodegradability and *in vivo* performance have to be done.

4.3.1.3 Multifunctional catechol-based coating

Polydopamine (PDA) has arisen as a promising approach to obtain bio-coatings due to its simplicity, universality, easy functionalization and favourable interactions with biological materials.[21] The coating process usually takes place in two main steps. First, formation of PDA, through the oxidative polymerization of dopamine, generates a product which adheres to a wide range of materials and presents different functional groups available for subsequent functionalization. Then, the posterior reaction of these functional groups with functional molecules, allows increasing biocompatibility, targeting or signalling properties. Following this approach, PDA and PDA-like coatings has emerged as a pivotal component in the construction of versatile surfaces, including tissue regeneration, antifouling, antibacterial, antioxidant, cell adhesion, and peptide-embedded surfaces.[22] This type of polymers are bioinspired by the Nature where catechols are a key player in several structures (Figure 4.38).[23-25]

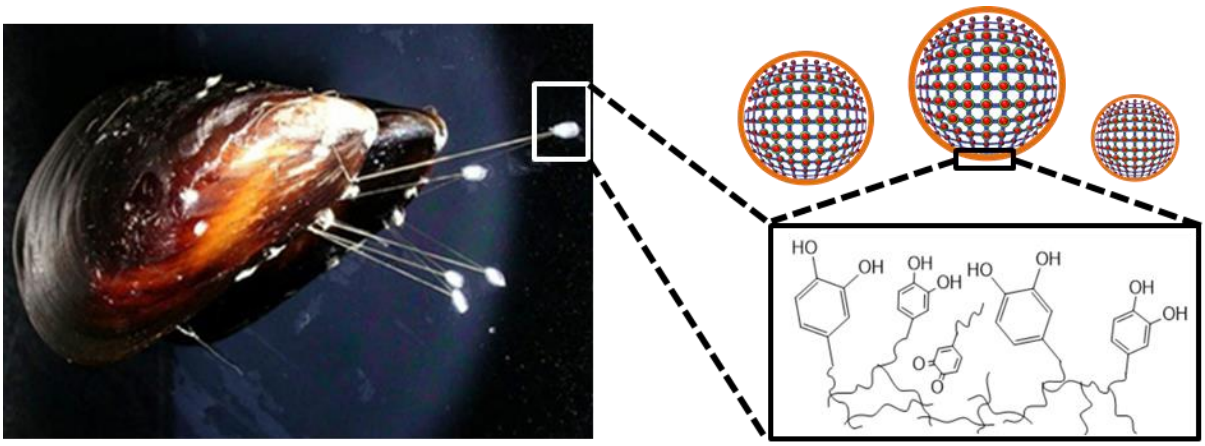

Figure 4.38 Mussel-mimetic polymer as universal coating for different materials.

In this work, we developed a PDA-like coating through the cross-linking in one step reaction between the pyrocatechol (**L8**) and the hexamethylenediamine (**L9**). The developed coating demonstrated its versatility as biofunctional platform enhancing the stability, biodistribution and functionality properties of the nanoparticles coated.[26] Regarding the growth of the coating, the previous results demonstrated that the thickness on flat surfaces follows an almost linear trend with

time under the reaction conditions. The chemical characterization performed suggest that its superficial chemical composition also changes with time, thus opening the possibility of tuning its reactivity in function of this parameter. Furthermore, the versatility of this platform for its functionalization following both nucleophilic and electrophilic attack approaches, was corroborated. For this reason, the specific objective of this coating is to confer more water-stability to the colloidal suspensions of the developed nanoparticles providing protection against aggregation once injected *in vivo*. Additionally, the post-functionalization of the coating will allow for the PEGylation (resulting in increased blood circulation) and targeting (for specific diseases).

4.3.1.4 Target: Lung diseases

In this work, we face the challenge of getting nanocarriers by combining metal-catechol nanoparticles and PDA-like coatings with preferential targeting for lung. The imaging/treatment of lung diseases, including lung cancer and tuberculosis, represents one of the most challenging problems in clinical practice as conventional drugs cannot be effectively delivered and targeted. Indeed, pulmonary drug delivery systems for inhalation administration in aerosol form results in many problems related to the short duration of clinical effects, rapid clearance of nanoparticles by the pulmonary mucus, block of airways from inflammation or mucus plugs, or other undesirable effects due to the rapid absorption of some drugs from the lung epithelium. For this reason, increasing attention has been paid to the intravenous administration. The intravenous route is one of the most commonly method used for the delivery of larger drug doses into the body.[27] This route allows to deliver directly drugs entrapped in vehicles such as microsphere, microcapsules, liposomes or nanoparticles into general circulation thus avoiding the first metabolism barrier.

At present, different lung-targeted drug delivery systems (LTDDS), including nanoparticles, nanocapsules and liposomes are administered intravenously.[28-30] However, the development of proper nanocarriers is on its infancy and further research is fully required. The main objective is the development of LTDDS able to deliver the drug in the lungs in an effective way increasing the drug concentration in lung tissue by reducing drug distribution in other organs and tissues. Some of the targeted-lung diseases are related with asthma, local infections, tumours and pulmonary hypertension, among others. The physical and chemical properties of the nanosystems would determine the lung deposition, mucus penetration, and subsequent biodistribution of administered therapeutic NPs. One of these key parameters is the size of the system to be introduced into the organism. However other combined effects such as hydrophilicity and charge, regulate subsequent transport through the pulmonary cavity and to the rest of the organism. When design a nanoparticle for the lung-target, the following parameters must be addressed:[31]

i. **Size**: The optimal diameter of the nanoparticles must fit some requirements depending on the interests. In this sense, the optimal diameter is: (a) between 500 nm and 5μm to achieve deep lung deposition, (b) < 500 nm or > 6 μm and hydrophilic surface to avoid rapid clearance by alveolar macrophages, and (c) < 200 nm for efficient mucus penetration and intracellular drug delivery.[32-35]
ii. **Target specificity**: The specific binding of molecules with target-recognition to receptors overexpressed in lungs allows the lung-uptake enhancement by reducing the internalisation in other tissues.
iii. **Surface charge**: Coating of NPs with inert polymers such as PEG showed promising results in penetrating into the highly visco-elastic human mucus secretions, minimizing adhesive interactions of NPs with mucus and protecting them against clearance by alveolar macrophages.[29,36]
iv. **Biodegradability**: In order to avoid long-term accumulation and immunotoxicity, the designed nanosystems must be biodegradable. The nanoparticles have to degrade in a rational period of time in small parts that do not promote cytotoxicity or inflammatory effects.

4.3.1.5 Present challenges

PET and SPECT imaging techniques has appeared as strong candidates due to the exponential growth in demand in the use of higher resolution imaging techniques that allow an in-depth and precise diagnosis. Although the enormous potential of these techniques, their use is limited by the cost of the technology, the limited number of radiotracers that are used at clinical level and the toxicity associated to the administration of the commercial radiotracers. For this reason, a strategy to improve these techniques, and the cost associated, consisted on the development of low-cost synthetic procedures and the increase of the effectivity and efficiency of the radiotracers with non-toxic effects. In this way, some of the challenges that must be faced are:

i. Simplification of the synthesis processes
ii. Use of safer formulations for its use in the clinics
iii. Increase the radionuclides payload
iv. Make available surface for its functionalization with (bio)molecules of interest
v. More examples of PET-active radiotracers
vi. Promote the *in vivo* assays to proof the performance of the novel radiotracers

Additionally, catechol-based materials still face challenges to overcome before ensuring the maturity of the area. One of them is the synergistic combination of various phenol-based components within a single nanoconstruct, which is expected to yield unique materials with emergent properties.

4.3.1.6 Our choice

In this Chapter 4.3, a successful strategy for the polymerisation of radionuclides for the formation of NCPs is presented. For the development of these materials, two different radiometals were selected: ^{111}In(III) and ^{64}Cu(II) for SPECT and PET imaging, respectively. Following the same approach presented in Chapter 4.2, the coordination of the metals was achieved by mixing them with the organic ligands **L3** and **L4** (Figure 4.39). Through this rationale design, two NCPs complexes were obtained: **In-NCP** and **Cu-NCP**.

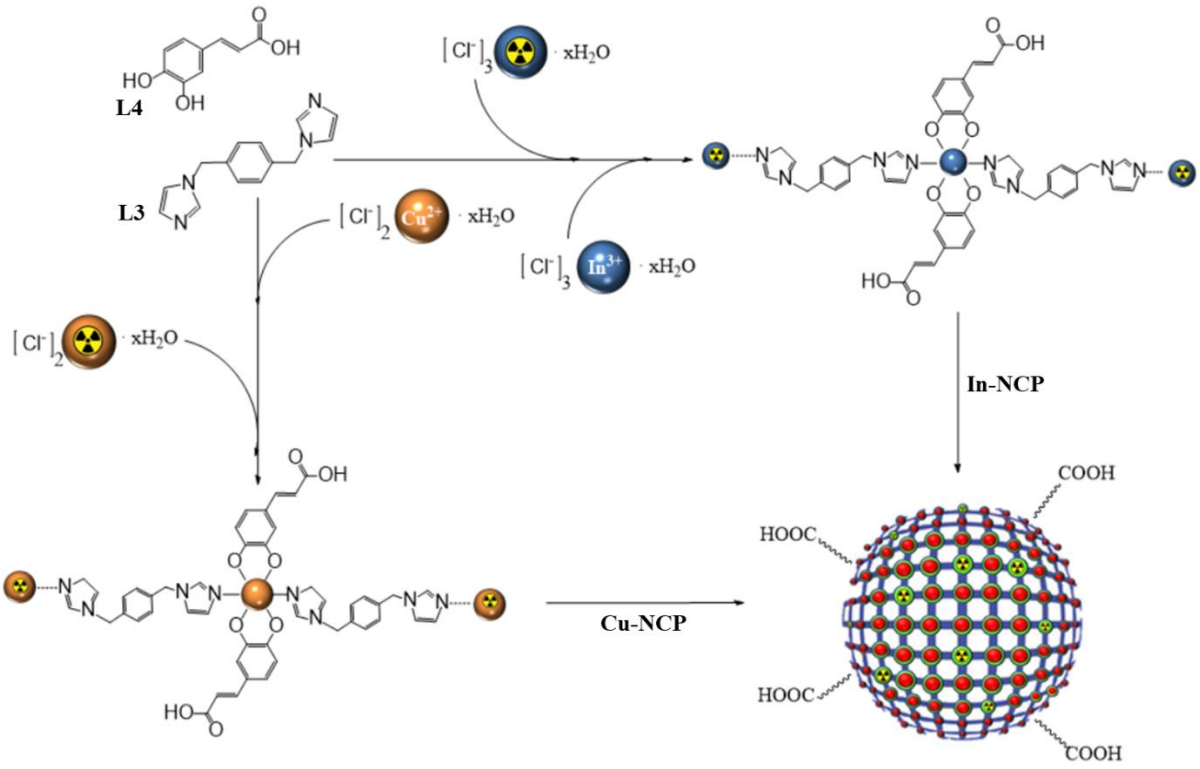

Figure 4.39 Scheme for the synthesis of the different NCPs complexes developed in this work. From the **L3** together with **L4** and combining them with $InCl_3$ and $[^{111}In]Cl_3$ or $CuCl_2$ and $[^{64}Cu]Cl_2$ metal salts, two NCPs complexes were synthesized: **In-NCP** and **Cu-NCP**.

A step forward was carried out in this Chapter 4.3 from the knowledge acquired in the work presented in Chapter 4.2: a novel catechol-based coating was developed for the coating of the NCPs. This multifunctional platform was used for the PEGylation and subsequent functionalization with

folic acid molecules for the study of its tissue and tumour-targeting (Figure 4.40). The tumour model selected (CT26-mouse colon carcinoma), was subcutaneously inoculated in mice.

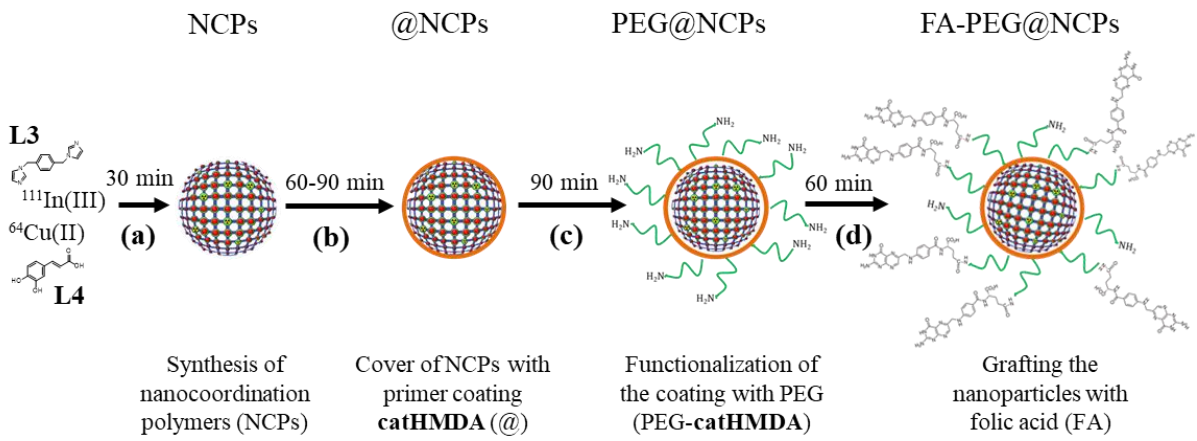

Figure 4.40 Schematic procedure followed for the final synthesis of coated NCPs functionalized with folic acid molecules used for the *in vivo* assays. (a) Polymerization reaction through fast-precipitation method in ethanol. (b) formation of the **catHMDA** coating through the crosslinking between **L8** and **L9**. (c) PEGylation of the nanoparticles with **L10**. (d) Targeting the NCPs by grafting folic acid molecules (**L11**).

4.3.1.7 Objectives

With the aim to overcome the challenges aforementioned, different objectives were proposed derived from the following two main goals:

- Design and synthesis of novel NCPs containing active PET/SPECT radionuclides (^{111}In(III) and ^{64}Cu(II)), for their use as radiotracers in radioimaging with targeting properties.
- Obtaining of nanoconstructs that meet certain requirements, such as: i) chemical stability, ii) water-colloidal stability, iii) low toxicity and biocompatibility, iv) enough payload activity *in vitro* and *in vivo* and v) good biodistribution with low uptake by liver and kidneys.

The steps followed for the achievement of the main goal were the following:

i. Synthesis of complexes **In-NCP** and **Cu-NCP**
ii. Coating of the systems with a catechol-based polymer
iii. PEGylation and functionalization of the NCPs with folic acid
iv. Complete physicochemical and biological characterization *in vitro*
v. Pre-clinical *in vivo* studies with mice model

In this work we show how coordination chemistry allows the successfully design of novel NCPs that incorporate PET/SPECT-active metals polymerised with organic ligands.

4.3.2 Results and discussion

4.3.2.1 Synthesis of the NCPs complexes

The synthesis of NCPs containing two different metal ions widely used as active radiotracers for SPECT (^{111}In) and PET (^{64}Cu) was achieved. Following a previously reported methodology,[37] the reaction of $InCl_3$ and [^{111}In]Cl_3 or $CuCl_2$ and [^{64}Cu]Cl_2 with **L3** (Bix) and **L4** (dhc) as a co-ligand in 1:1:2 molar ratio, yielded the formation of nanoparticles named as **In-NCP** and **Cu-NCP**, respectively (Figure 4.41). The mixture of metals (In^{3+} and Cu^{2+}) and their respective radioisotope (^{111}In(III) and ^{64}Cu(II)) was done in water and subsequently added to an ethanolic solution containing the ligands (**L3** and **L4**). After addition of the metal salts, the fast precipitation of the resulting coordination polymer generated directly the nanostructuration of the material. Using this methodology NCPs of 87 ± 11 nm and 95 ± 5 nm in size were obtained for **In-NCP** and **Cu-NCP**, respectively.

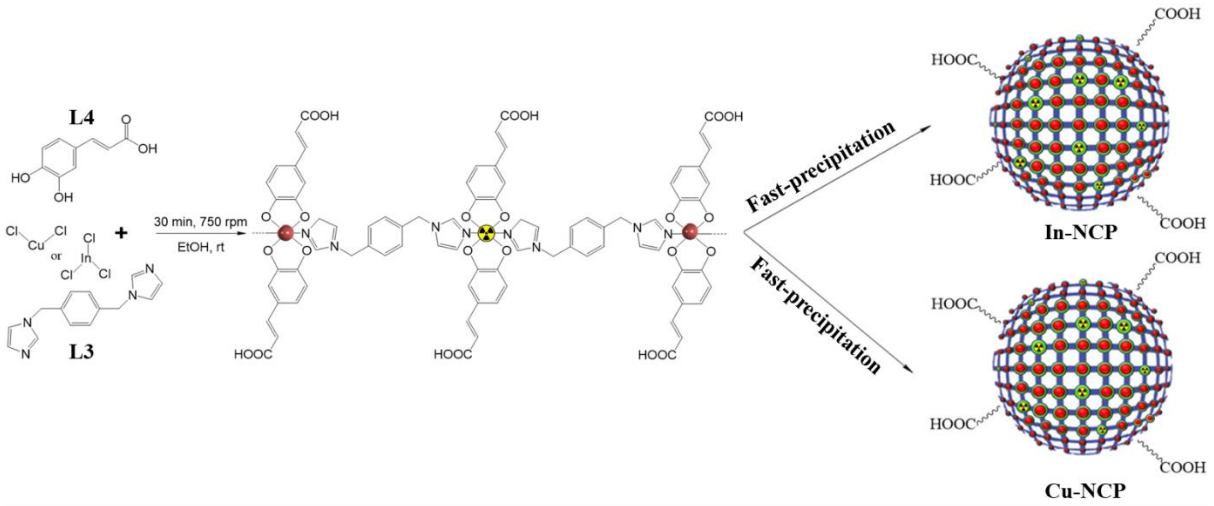

Figure 4.41 Synthesis of the NCPs complexes. The metallic salts were mixed with its respective radiometal $^{111}InCl_3$ and $^{64}CuCl_2$ for **In-NCP** and **Cu-NCP**, respectively.

4.3.2.1.1 Coating of NCPs

The synthesised nanoparticles were coated with a PDA-like coating previously reported.[26] The coating consisted on a catechol-based polymer obtained from the cross-linking between the pyrocatechol (**L8**, cat) and the hexamethylenediamine (**L9**, HMDA) under mild oxidizing conditions (Figure 4.42).

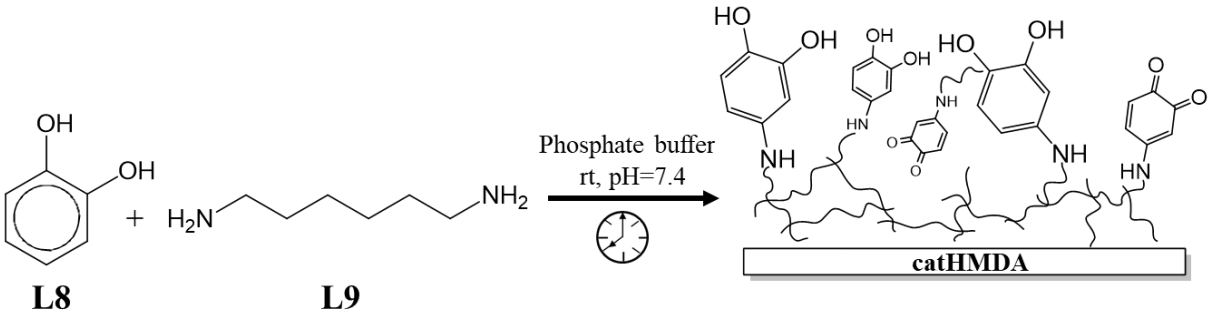

Figure 4.42 Schematic representation of the copolymerization between pyrocatechol (**L8**) and hexamethylenediamine (**L9**) (**catHMDA**).

Through the entrance of oxygen, the copolymerization reaction can be controlled with the reaction time reaching de formation of the catechol-based polymer named as **catHMDA**. The chemical environment of the **catHMDA** coating change with time during its formation. The number of exposed amino groups is increased over time during the polymerization reaction through crosslinking between **L9** and **L10**. The previous study of the **catHMDA** copolymer demonstrated the successful formation of a functionalizable PDA-like coating. Regarding the growth of the coating, the measurements performed showed that the thickness of **catHMDA** on flat surfaces follows an almost linear trend with time under the reaction conditions. The chemical characterisation, suggested that its superficial chemical composition also changes with time, thus opening the possibility of tuning its reactivity in function of this parameter. The versatility of this platform for its functionalisation following both nucleophilic and electrophilic attack approaches was demonstrated.[27] Overall, these results demonstrated the potential of **catHMDA** as a universal coating that can act as a flexible platform for further functionalisation with, for example, (bio)molecules of interest in biomaterials science, amongst others.[26] For the first time, in this Thesis we have demonstrated the potential use of **catHMDA** for the coating and functionalisation of nanoparticles for its use in biomedical applications.

4.3.2.1.2 PEGylation and folic acid grafting

The efficiency of the coating was demonstrate by the successful anchoring of PEG molecules and folic acid (FA, **L11**) moieties for their specific targeting by folate receptors overexpressed in cancer cells.[38-40] Firstly, after the coating with **catHMDA**, the NCPs were PEGylated with PEG molecules containing amino endings groups (**L10**, poly(ethylene glycol) bis(amine), 3000 MW) (Figure 4.43). This step allowed the formation of the PEG-coated NCPs named as **PEG@In-NCP** and **PEG@Cu-NCP**.

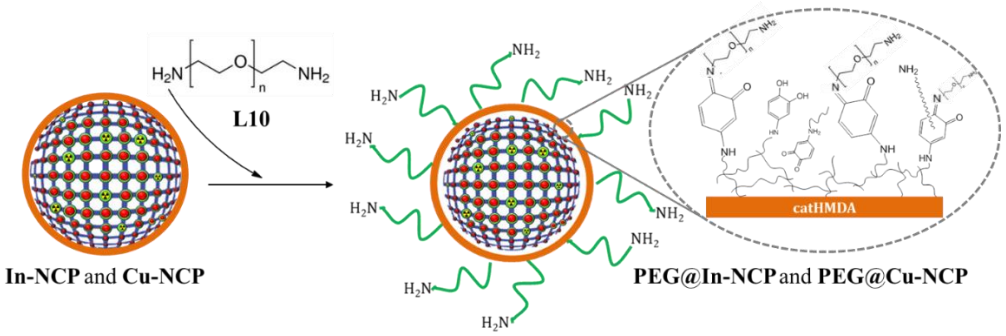

Figure 4.43 Scheme of the PEGylation process of the coated nanoparticles. The proposed mechanism involved the covalent binding of the (bis)amino PEG (**L10**) molecules through nucleophilic attack of amines on the carbonyl groups present in the quinone rings of the c**atHMDA** coating.

The (bis)amino PEG chains formed covalent bonds by nucleophilic attacks of amines on the carbonyl groups of the quinone rings (Figure 4.43), which seem to be present in large amounts for intermediate reaction times.

In a subsequent step, the nanoparticles were functionalized with FA (**L11**) for the study of the role of this molecule present on the NCPs surface for the interaction with the targeted-folate receptors in tumours or tissues. Thus, the unreacted and free ending-amino groups exposed from the coating were used to attach covalently FA molecules through a carbodiimide-assisted amidation reaction (Figure 4.44). This last step let the target-functionalisation of the NCPs named as **FA-PEG@In-NCP** and **FA-PEG@Cu-NCP**.

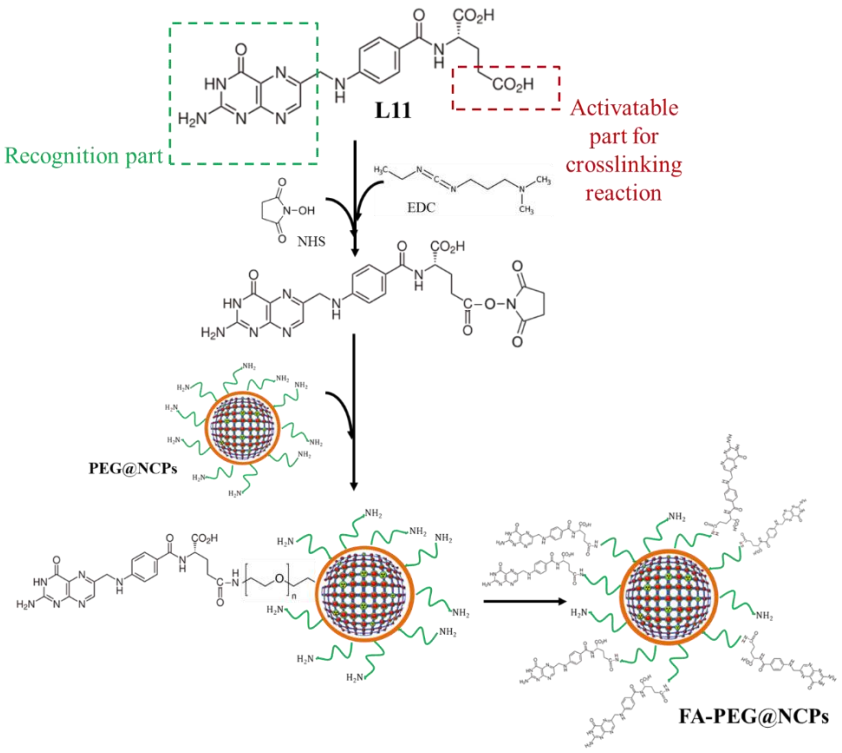

Figure 4.44. Schematic procedure for the grafting of the nanoparticles with folic acid molecules.

The FA molecules were attached on the free amino groups located on the surface of the coating. The resulting nanoparticles were successfully obtained, and their physicochemical characterisation is presented in the following section.

To sum up, the NCPs systems used for the *in vivo* assays were obtained through a three-step methodology (Figure 4.45). First, the synthesis of the nanoparticles containing both the metal and its respective radioisotope were synthesised. After 30 min of reaction, the NCPs product was washed and resuspended in PBS for its coating with **catHMDA** copolymer. After the coating procedure, the nanoparticles were washed and subsequently grafted with FA.

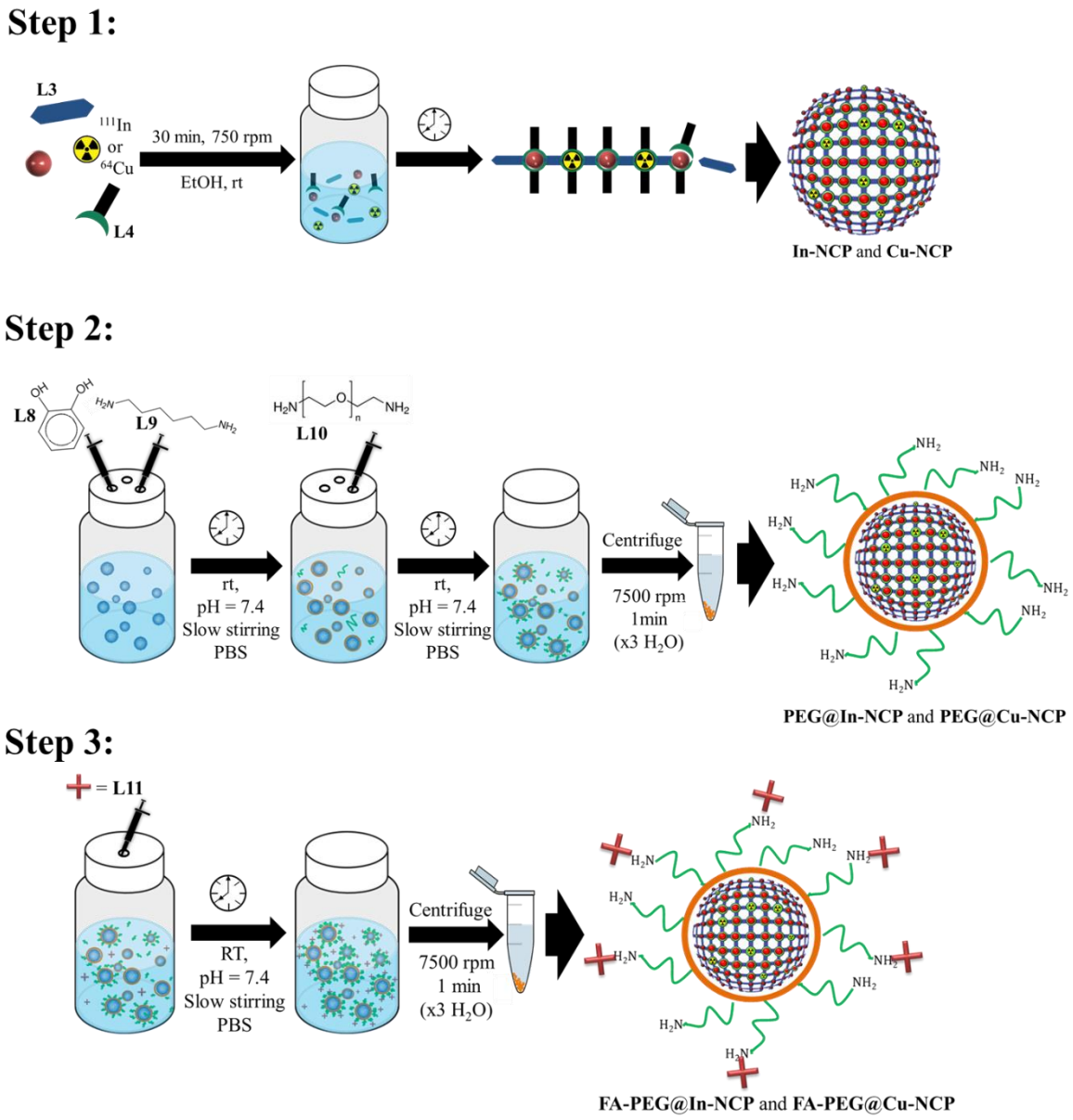

Figure 4.45 Complete schematic procedure for the synthesis, coating and functionalisation of the NCPs. In the first step, the nanoparticles containing either ^{111}In or ^{64}Cu radiometals were synthesised. In a second step, the nanoparticles were resuspended in PBS solution and the reactants (**L8**) and (**L9**) added in order to form the catHMDA coating. The universal platform obtained with the coating was functionalised in the last third step with folic acid molecules (**L11**).

4.3.2.2 Characterization

4.3.2.2.1 Morphology and size

The naked and coated NCPs systems were characterized by SEM and DLS for the determination of the particle size and ζ-potential (Figure 4.46 and Table 4.11). The SEM images of naked NCPs reveal the presence of spherical nanoparticles with average sizes around 74 nm and 86 nm for **In-NCP** and **Cu-NCP**, respectively.

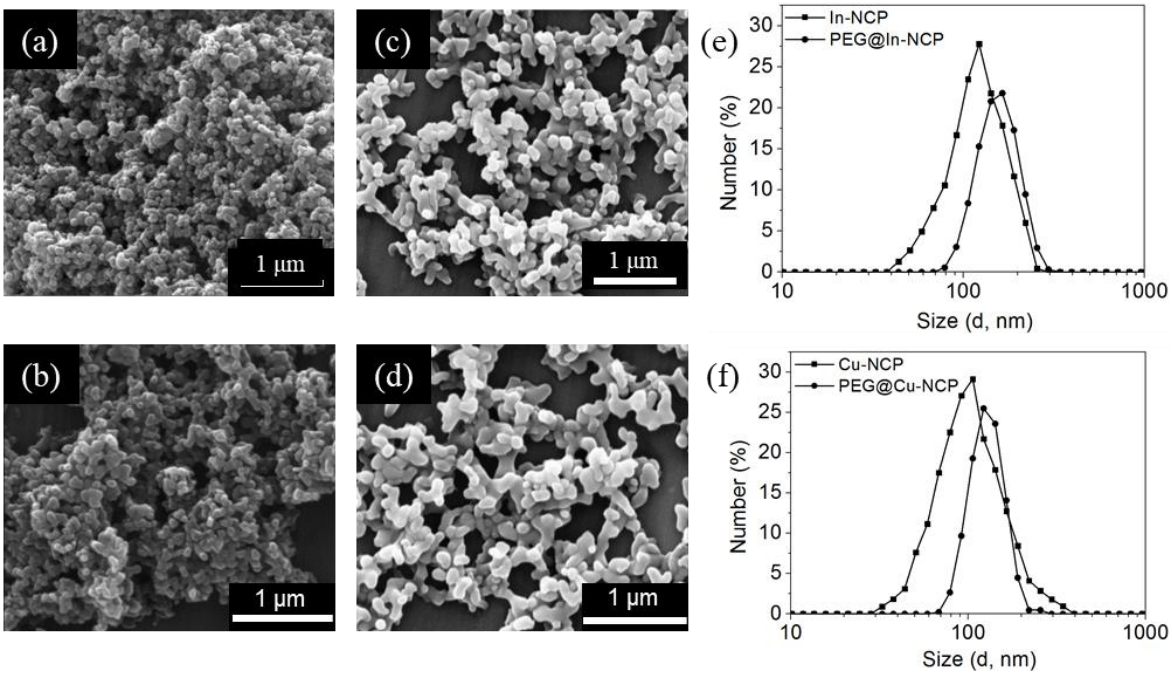

Figure 4.46 Morphology of NCPs complexes. SEM images of (a) **In-NCP**, (b) **Cu-NCP**, (c) **PEG@In-NCP** and (d) **PEG@Cu-NCP**. The nanoparticles were redispersed in PBS (pH = 7.4) before and after coating for (e) **In-NCP** and (d) **Cu-NCP**.

These results were in agreement with DLS measurements in PBS solution, which shows diameters of 87 ± 11 for **In-NCP** and 95 ± 5 nm for **Cu-NCP**. The ζ-potential was measured revealing negative charges (~ -25 mV) for naked nanoparticles resulting from the partial deprotonated carboxylic groups of the **L4** ligand at pH = 7.4.

Table 4.11 Comparison of size distribution and ζ-potential (including standard deviation values) for NCPs before and after coating.

NCP system	PBS (pH = 7.4)			
	Before coating		After coating	
	Size (nm)	ζ-potential (mV)	Size (nm)	ζ-potential (mV)
In-NCP	87 ± 11	-23.9 ± 2.2	123 ± 6	29.6 ± 3.3
Cu-NCP	95 ± 5	-27.2 ± 2.9	127 ± 8	28.1 ± 4.1

Although naked NCPs exhibit good dispersion in PBS they start to aggregate and precipitate after 24 h. After coating and PEGylation of NCPs, the sizes increased up to around 120 nm for both systems (named **PEG@In-NCP** and **PEG@Cu-NCP**) as observed by SEM. In solution, DLS measurements in PBS showed higher hydrodynamic diameters ($D_{In\text{-}NCP}$ = 123 ± 6 nm; $D_{Cu\text{-}NCP}$ = 127 ± 8 nm) with good monodispersion values (PDI < 0.20), obtaining very stable colloidal dispersions for long time. Furthermore, the PEGylation of nanoparticles induced a notably change on the charge surface measured by ζ-potential going from negative values of uncoated nanoparticles to positive values (~ +30 mV) when the nanoparticles are coated and functionalized with the bis-amino PEG chains (Table 4.11). This was probably due to the presence of amines groups of PEG molecules on the surface which were protonated at pH = 7.4. After functionalization with FA no appreciable changes in size, stability or ζ-potential were observed in the resulting nanoparticles named **FA-PEG@In-NCP** and **FA-PEG@Cu-NCP**.

4.3.2.2.2 Chemical characterisation

The chemical structure and formation of NCPs was characterised by different complementary techniques (FT-IR, EDX, XPS, NMR, ICP-MS). The FT-IR spectroscopy of **In-NCP** and **Cu-NCP** corroborated the coordination between the metal and the ligands by the appearance, modification and shift of specific bands (Figure 4.47).

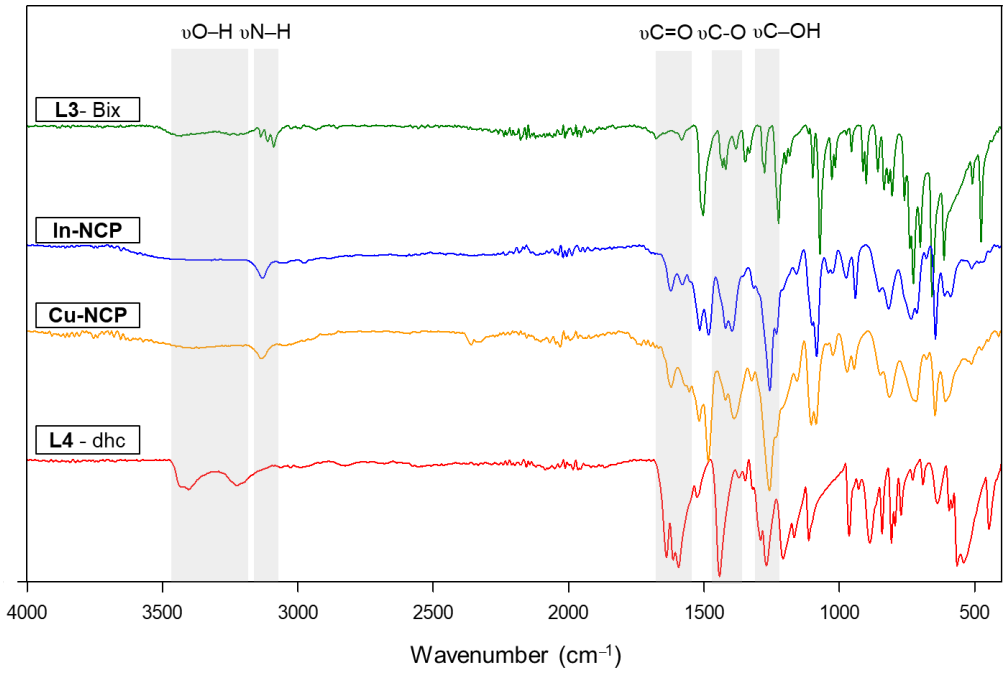

Figure 4.47 FT-IR spectrum for both NCP (**In-NCP** and **Cu-NCP**) complexes and the ligands used (**L3** and **L4**).

The decrease of intensity observed in the frequency bands around ν = 3000-3500 cm^{-1} was attributed to the deprotonation of catechol groups (–OH) present in **L4**. Complementarily, the resulting vibrational band assigned to the C–O stretching corresponding to the catecholate moiety bonded to metal centres appeared in the range of 1400-1420 cm^{-1}. The broad band around 730-740 cm^{-1} can be attributed to the deformation of the imide-five-ring from **L3** ligand due to its coordination to the corresponding metals. Additionally, typical vibrational bands of **L3** (ν = 1520, 1232, 1105 cm^{-1}) were also observed in the IR spectra.

In the same way, the coating and PEGylation of coated NCPs was confirmed by FT-IR. The spectra clearly showed the appearance of intense bands at ~ 2900 cm^{-1} and ~ 1150 cm^{-1} corresponding to the C–H bonds from the alkyl chain and the stretching vibration of C–O–C, respectively (Figure 4.48).

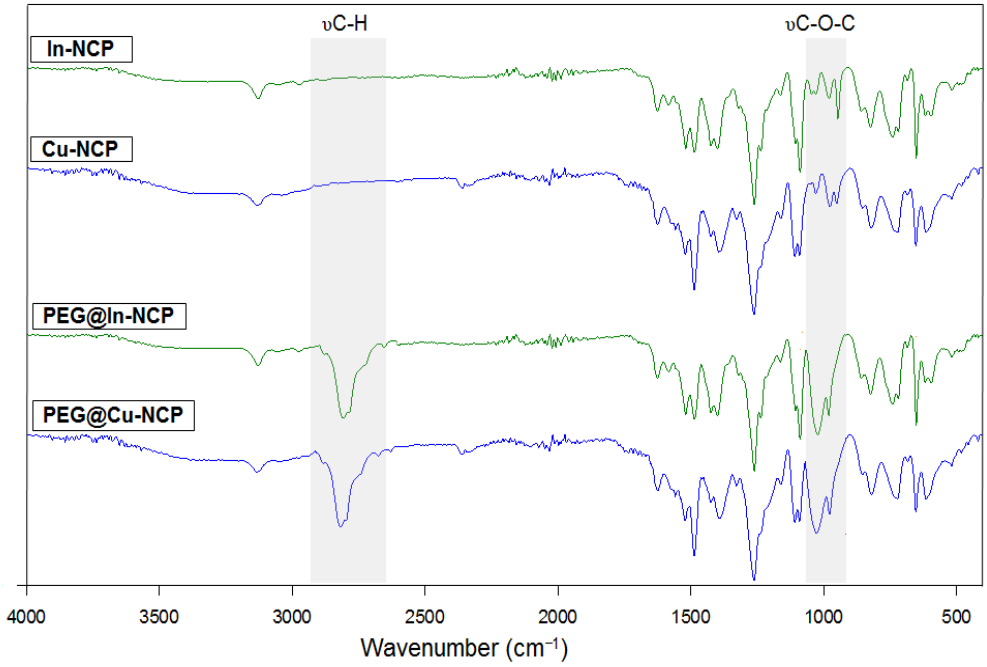

Figure 4.48 FT-IR spectrum for both PEG@NCPs complexes compared with uncoated nanoparticles.

In order to complete the chemical characterization, XPS measurements were done for the study of the atomic chemical bonding of the NCPs synthesized. In both In-NCP and Cu-NCP, the C1s, N1s and O1s peaks yielded similar spectrum as expected (Figure 4.49).

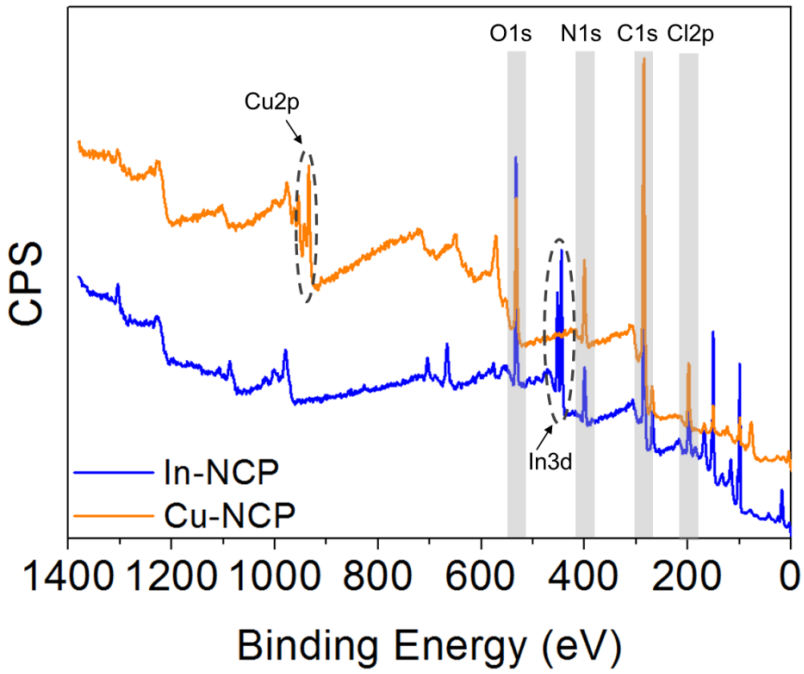

Figure 4.49 X-ray photoelectron spectroscopy (XPS) spectra of the NCPs systems deposited on silicon substrate. CPS: Counts per second.

Additionally, for both NCPs complexes, the presence of Cl^- as counterion was found. The band at 198 eV was attributed to the metallic Cl2p. The integration of Cl^- in the polymeric structure as counterion stabilized the coordination polymer by compensating the charges and completing the coordination sphere. For the detailed study of the bonding environment of the NCPs, high-resolution XPS curve-fitting was carried out. Figure 4.50 shows the deconvolution of the XPS spectra for C1s, N1s and O1s.

In both complexes, the C1s band was fitted in three peaks, which would correspond to three different chemical environments. The peaks confirmed the presence of C–O and the C–N aromatic contribution form the **L3** ligand. The N1s spectra of all the complexes confirmed the presence of C–N and C=N assigned to the aromatic rings of the **L3** ligand. In the case of the O1s peak spectra, the presence of the C–O and C=O bonding was confirmed thus indicating the maintenance of free carboxylic groups on the surface of the NCPs synthesized.

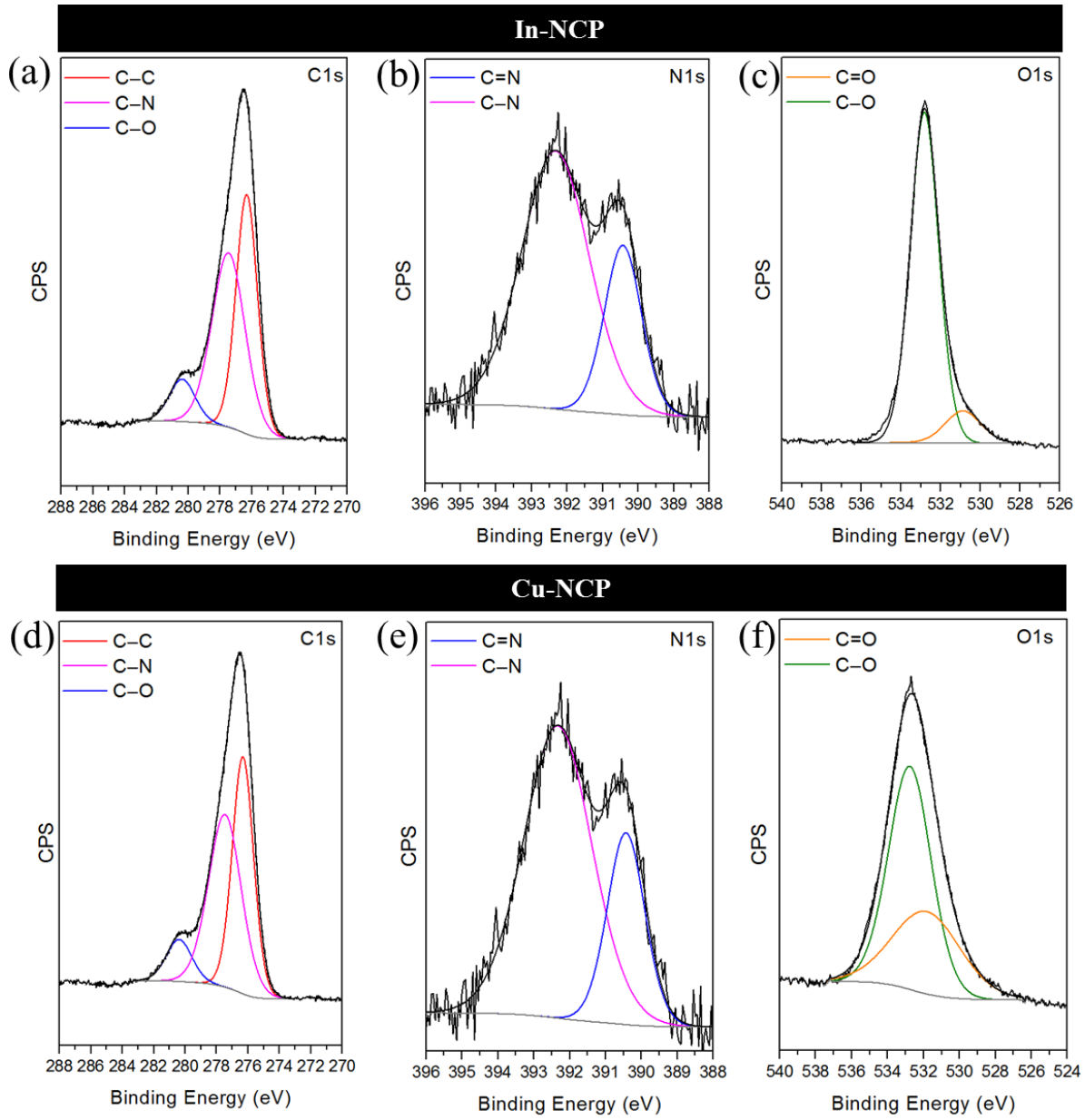

Figure 4.50 Curve-fitting results for C1s, N1s and O1s high resolution spectra corresponding to the (a,b,c) **In-NCP** and (d,e,f) **Cu-NCP** complexes. CPS: Counts per second.

The presence of In and Cu metals and their oxidation state was studied in deep. In the Figure 4.51, the energy bands corresponding to the In3d and Cu2p are showed. For the first case, the In(III) oxidation state was confirmed by the well definition and detection of the $In3d_{5/2}$ and $In3d_{3/2}$ spin-orbit components. In the case of Cu-based NCP, the Cu(II) oxidation state was corroborated by the detection of the Cu2p peak which has significantly split spin-orbit components (Δ=19.75eV) between the $Cu2p_{3/2}$ and $Cu2p_{1/2}$ components. Additionally, Cu(II) has observable and characteristic satellite features which were detected at 943 eV and 965 eV.

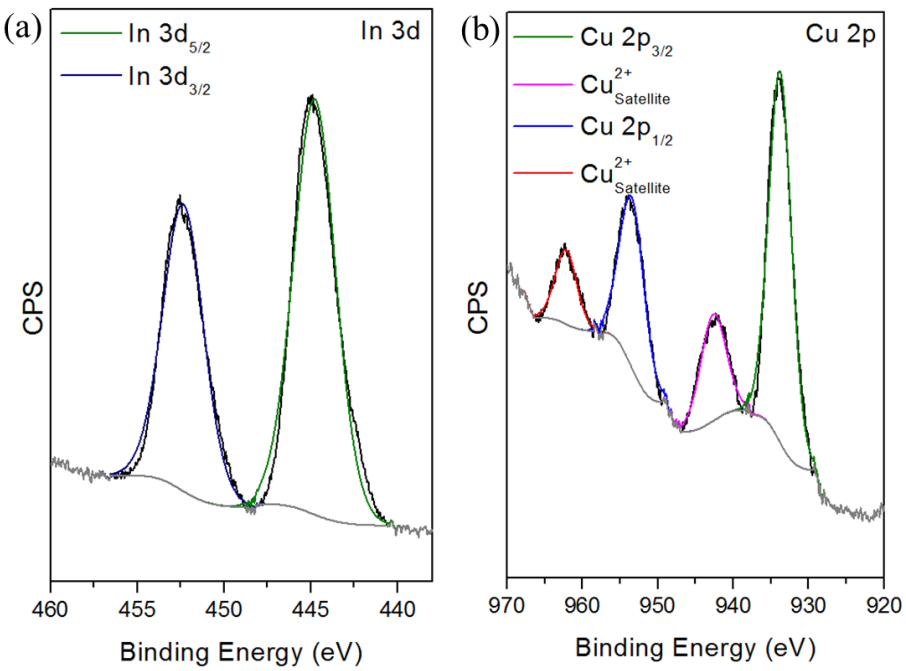

Figure 4.51 Curve-fitting results for (a) In3d and (b) Cu2p high resolution spectra corresponding to **In-NCP** and **Cu-NCP**, respectively. CPS: Counts per second.

Once the NCPs were coated with the **catHMDA** copolymer, the presence of the main elements and the Cl^- counter anion was corroborated by EDX by measuring on different NCPs batches form different synthesis (Figure 4.52).

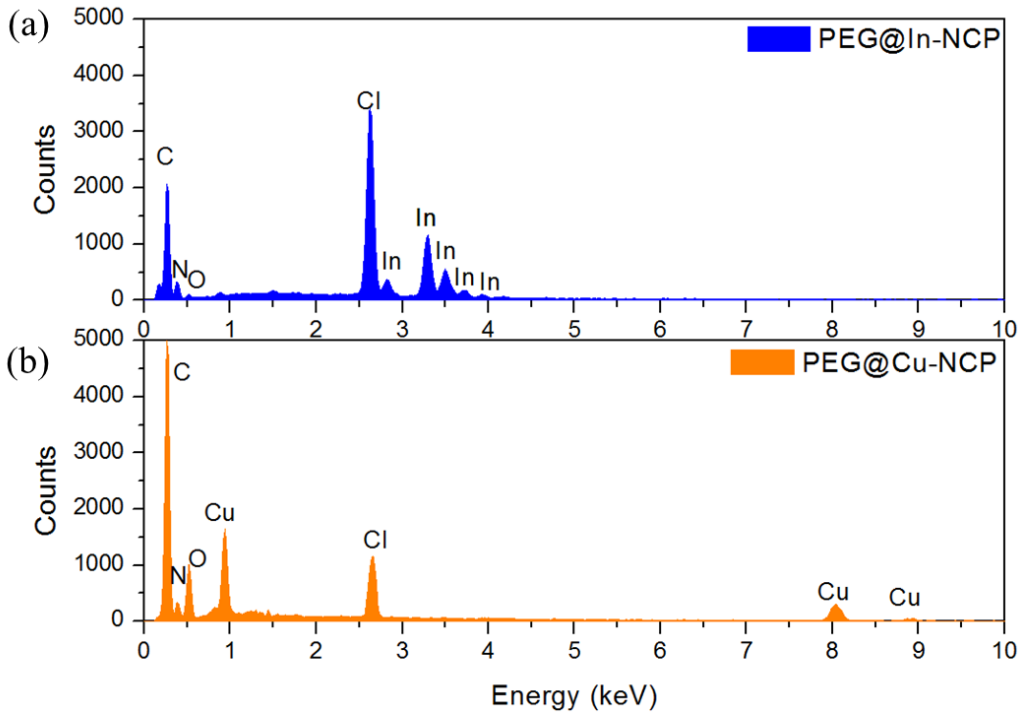

Figure 4.52 EDX spectra for both PEG@NCPs complexes: (a) **PEG@In-NCPs** and (b) **PEG@Cu-NCPs**.

The chemical compositional formula was experimentally determined by combination of ^{1}H-NMR (Figure 4.53) for the calculation of ligands ratio once the nanoparticles were dissolved in acid media, and ICP-MS, for the measurement of metal percentage present in each NCP system (Table 4.12). These results together with the elemental analysis of C, N and H content, resulted on a tentative compositional formula for **In-NCPs**: $In_1\mathbf{L3}_1\mathbf{L4}_{1.43}Cl_2(H_2O)_{0.9}$ and for **Cu-NCPs**: $Cu_1\mathbf{L3}_1\mathbf{L4}_{1.96}Cl_{2.1}(H_2O)_2$ (Table 4.13).

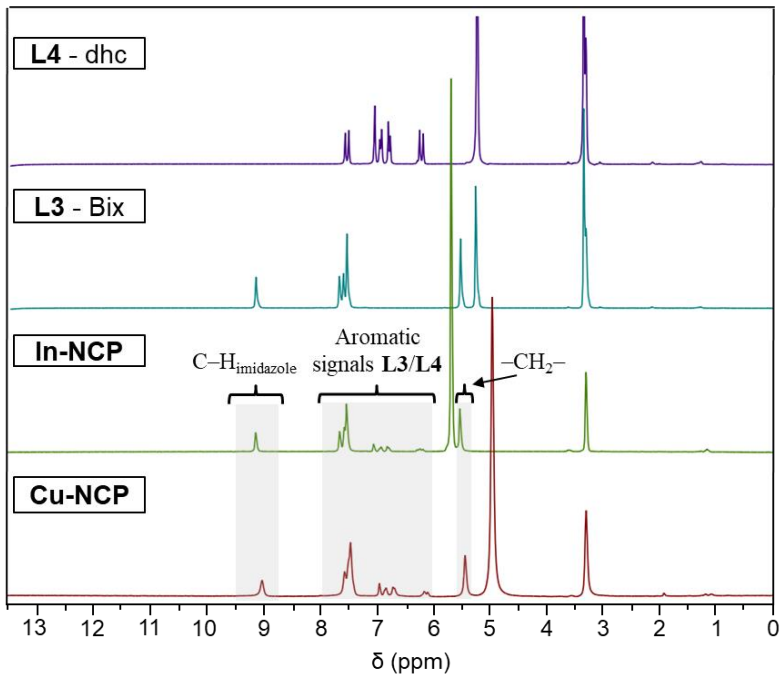

Figure 4.53 ^{1}H-NMR spectra for the **L3**, **L4** ligands and the NCPs synthesized. (Solvent: MeOH-d_4+DCl).

In the Figure 4.53, the spectra of the **In-NCP** and **Cu-NCP** nanoparticles after demetallation and complete dissolution with DCl in MeOH-d_4 are shown. Signals from the **L3** and **L4** ligands can be detected. The signal at δ = 9.1 ppm was attributed to the 2H from the C–H of the imidazole ring and the signal located at δ = 5.5 ppm belong to the methylene groups (–CH_2–) present in **L3**. Additionally, in the range between δ = 8.0 – 6.0 ppm, different peaks can be assigned to the aromatic signals of both **L3** and **L4**.

Table 4.12 Experimental values for elemental analysis considering the ICP-MS and ^{1}H-NMR measurements.

NCP system	Elemental Analysis (theoretical*)				^{1}H-NMR	Error
	%C	%H	%N	%metal**	**L3**:**L4***	
In-NCP	45.36 (46.25)	3.68 (3.93)	8.41 (8.03)	17.21 (16.45)	1:1.43	0.88%
Cu-NCP	49.65 (50.01)	4.29 (4.95)	6.88 (6.93)	8.35 (7.87)	1:1.96	0.96%

*The theoretical values were obtained taking into account the ^{1}H-NMR ligand ratios; **the values where calculated from ICP-MS; *** **L3** = Bix, **L4** = dhc.

Table 4.13 Chemical compositional formula for each NCP complex considering the values shown in Table 4.12.

NCPs	Chemical Formula	Percentage
In-NCP	In_1 **L3**$_1$ **L4**$_{1.43}$ $(Cl^-)_2(H_2O)_{0.9}$	34% **L3**, 37% **L4**, 17% Fe
Cu-NCP	Cu_1 **L3**$_1$ **L4**$_{1.96}$ $(Cl^-)_{2.1}(H_2O)_2$	30% **L3**, 44% **L4**, 8% Cu

L3 = Bix, **L4** = dhc.

As the NCPs were obtained out-of-equilibrium, it is necessary to remark that elemental analysis of different nanoparticles batches slightly differ from the expected values for a 1(metal ion):1**L3**:2**L4** ratio. These differences have been tentatively attributed to the plausible encapsulation of free ligand or solvent molecules within the particles and the formation of secondary structures such as oligomers.[41,42] This fact was already observed during the synthesis of the NCPs systems in Chapter 4.2. Finally, the absence of diffraction peaks observed by PXRD indicates the amorphous nature of all the samples. (Figure 4.54).

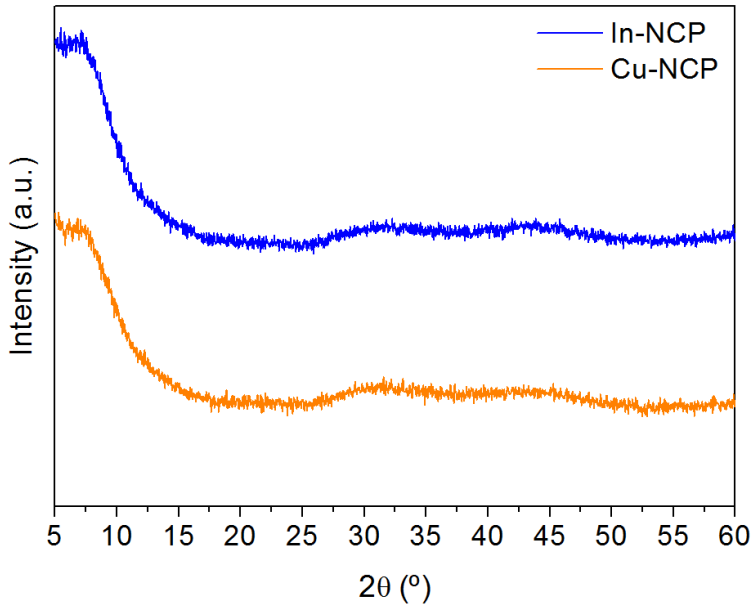

Figure 4.54 PXRD spectra of the different samples. a.u: Arbitrary units.

4.3.2.2.3 Radiolabelled NCPs: Activity and radiochemistry yield (RCY)

As aforementioned, two PET/SPECT-active NCPs systems were properly synthesised. The inclusion of the radiometal in the polymeric structure was achieved through the mixing of an aqueous solution containing $InCl_3$ or $CuCl_2$ salts and a small quantity of the corresponding radiotracer ^{111}In or ^{64}Cu salts (ratio 1:2.1 radiometal:metal) with an ethanolic solution containing both **L3** and **L4** organic

ligands. This one-pot synthesis together with the coordination versatility of the ligands used, allowed the polymerisation and coordination of the radioisotopes in the nanoparticle structure which precipitate directly from the reaction solution in few minutes. After the coating with **catHMDA**, PEGylation and post-functionalisation with FA molecules, the resulting NCPs were washed and isolated. The loading of radiometal was followed during the whole synthesis at different steps by measuring the activity using a ɣ counter (Table 4.14).

Table 4.14 Activity values for **PEG@In-NCP** and **PEG@Cu-NCP** at different steps of the synthesis process. The values are shown in average of several syntheses. Data is shown as mean ± standard deviation. The values are time-decay corrected for each radioisotope.

Process step	Activity (MBq)	
	^{111}In	^{64}Cu
Remain in Eppendorf after radioisotope addition	0.29 ± 0.04	0.21 ± 0.04
Remain in vial after synthesis of NCPs	11.40 ± 0.46	1.52 ± 0.27
NCPs after each wash	0.08/0.07 /0.07	0.04/0.03/0.0.3
Remain in the supernatant (After wash the PEG@NCPs)	0.29 ± 0.14	0.33 ± 0.16

These measurements allowed to calculate the final radiochemistry yield (RCY %) which refers to the amount of radiometal in the polymeric structure. The measured percentage of radioisotope in the resulting material resulted in 71% and 87% for **PEG@In-NCP** and **PEG@Cu-NCP**, respectively (Table 4.15).

Table 4.15 Activity values for **PEG@In-NCP** and **PEG@Cu-NCP** used for the radiochemistry yield (RCY) (%) calculation. The values are shown in average of several syntheses. Data is shown as mean ± standard deviation. The values are time-decay corrected for each radioisotope.

Process step	Activity (MBq)	
	^{111}In	^{64}Cu
Added radiotracer	94.35 ± 36.26	38.11 ± 5.92
Precipitated NCPs after washes	67.34 ± 2.96	33.67 ± 2.59
PEG@NCPs (after washes)	66.97 ± 7.77	32.93 ± 6.29
RCY	71 ± 4 %	87 ± 2 %

These values confirmed the high RCY achieved with this strategy and the notable increasing values in comparison with most of the previous nanosystems reported.[43] Such highly efficient and stable chelator-free labelling of ^{111}In and ^{64}Cu NCPs corroborated their suitability for *in vivo* SPECT/PET imaging.

4.3.2.2.4 Biodegradability of NCPs

Once the nanoparticles were completely characterised, the chemical and colloidal stability in solution of the resulting NCPs at different pH was evaluated. A complete study in the range of pH 5-9 was performed for the naked NCPs (**In-NCP** and **Cu-NCP**) and after their coating with **catHMDA** and its subsequent PEGylation (**PEG@In-NCP** and **PEG@Cu-NCP**). The measurements on size and ζ-potential of the NCPs were measured in water by changing the pH from acidic to basic conditions, allowing the study of the colloidal and chemical stability (Figure 4.55 and Figure 4.56). For the uncoated NCPs, when the pH was acidified, the nanoparticles tend to aggregate due to the reduction of the ζ-potential towards values close to neutral. This loss of negative charge was a consequence of the gradual protonation of the carboxylic acid groups (Figure 4.55).

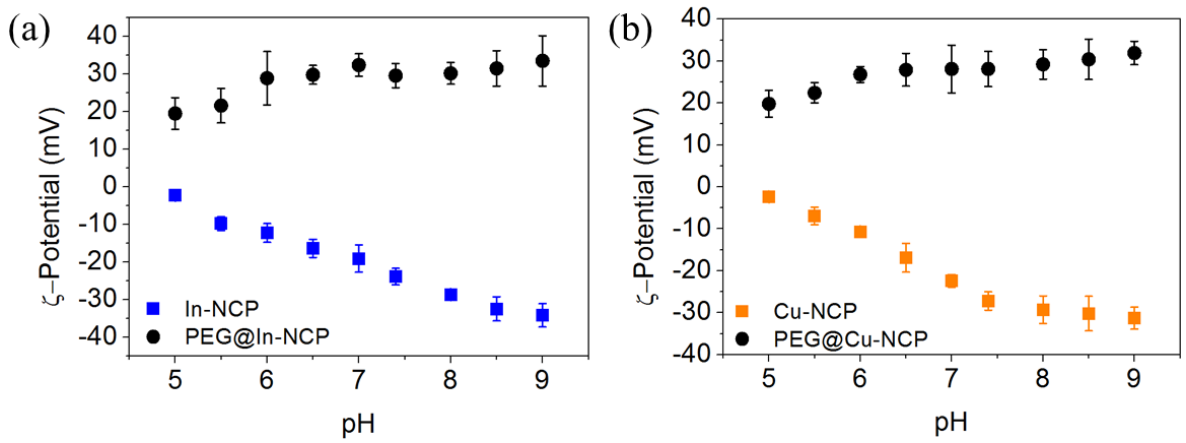

Figure 4.55 ζ -potential values for (a) **In-NCP** and **PEG@In-NCP** and (b) **Cu-NCP and PEG@Cu-NCP** in function of pH. D: Hydrodynamic diameter. Data is shown as mean ± standard deviation.

In the opposite way, when the pH became basic the DLS measurements indicated the presence of a greater number of negative charges on the surface by the decrease of the ζ-potential to high negative values. These changes on the surface charge were directly related with the increase and decrease of the nanoparticles size due to aggregation-redispersion process. When the pH is acidified, the size of the NCPs became higher by the agglomeration of the nanoparticles due to the loss of electrostatic repulsion (Figure 4.56). This electrostatic repulsion was again recovered once the pH was basified due

to the deprotonation of the carboxylic acids which favoured the increase of negative charges. Additionally, the size was maintained almost constant at pH 8-9. For pH more acidic than 4 or more basic than 10 the nanoparticles suffered a fast and irreversible decomposition.

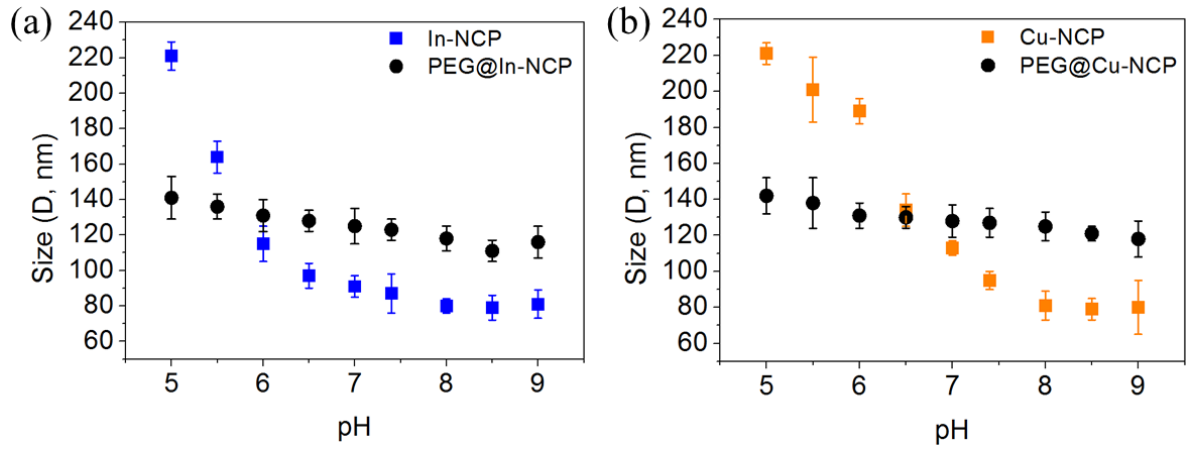

Figure 4.56 Particle size values for (a) **In-NCP** and **PEG@In-NCP** and (b) **Cu-NCP** and **PEG@Cu-NCP** in function of pH. D: Hydrodynamic diameter. Data is shown as mean ± standard deviation.

Interestingly, once the nanoparticles were coated with **PEG-catHMDA**, the stabilisation of the NCPs and its dependence with the variation of the pH was tested (Figure 4.55 and 4.56, black dots). In the case of the ζ-potential, the values were positive and maintained in a range of ~20-30 mV between pH 5-9, which was translated in a high colloidal stability of the nanoparticles in the pH range tested. Furthermore, the chemical and colloidal stability of the NCPs before and after the coating and PEGylation was studied by dialysis in physiological conditions (incubation with PBS + mouse plasma at 37°C) for long time (7 days) and at two different pH = 7.4 and 5.2 (Figure 4.57).

As metal release came mainly from the gradual degradation of the NCPs, the quantification of metal in solution was detected and quantified by ICP-MS and related to the chemical stability of the NCPs. Thus, the results indicated that, for naked NCPs, the release of 50% of the metal contained took 7.5 h in the case of **In-NCP** and 6.0 h in the case of **Cu-NCPs** at physiological pH, being notably faster when the pH decreased (Table 4.16, Figure 4.57a-b). The faster degradation in acidic pH was related to the induced ligand protonation and demetallation process. When the same analysis was performed for the coated NCPs, we realized the important role of the coating allowing the protection of the NCPs from a fast degradation in biological conditions. In the case of coating NCPs, the time needed for the 50% of metal release was 21 h and 19 h for **In-NCP** and **Cu-NCP** at pH = 7.4, respectively (Table 4.16, Figure 4.57c-d)). In the same way, at acidic pH the release was faster but much slower than the uncoated NCPs at any pH. These results confirmed the gradual and controllable biodegradation of the synthesised NCPs in different physiological conditions.

Table 4.16 Percentage of In(III) and Cu(II) release for each NCP system at two different pHs.

NCP system	50% release of metal			
	Uncoated		Coated	
	pH = 7.4	pH = 5.2	pH = 7.4	pH = 5.2
In-NCP	7.5 h	4.5 h	21 h	12 h
Cu-NCP	6 h	4 h	19 h	10 h

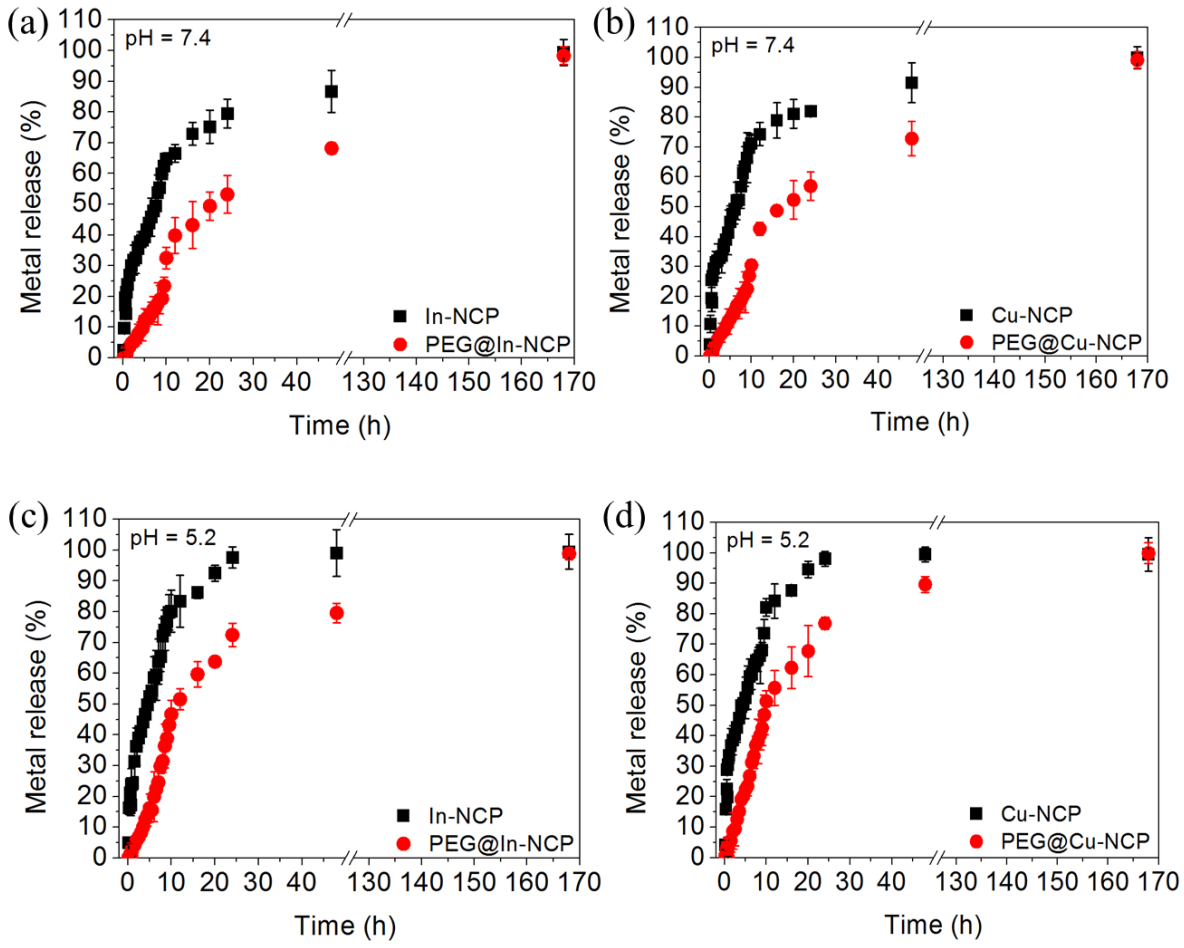

Figure 4.57 Stability of the NCPs systems at (a, b) pH = 7.4 and (c, d) pH = 5.2 in PBS-MSA-Plasma. Data is shown as mean ± standard deviation.

4.3.2.2.5 Biocompatibility: Cytotoxicity assays and in vitro uptake (Influence of folic acid)

To explore the applications of naked and PEG-coated NCPs in biomedicine, firstly we tested their potential toxicity on different cell lines (HeLa - cervical cancer cells, CT26 - mouse colon carcinoma cells and 3T3 - healthy fibroblasts cells) at different concentration for 24 and 72 h (Figure 4.58 and 4.59). The results demonstrated the effectiveness of the coating conferring more biocompatibility compared with the naked NCPs. As shown in Figure 4.58, after 24 h, coated **PEG@In-NCP** and **PEG@Cu-NCP** nanoparticles did not show significant toxicity at metal concentrations up to 100 µM.

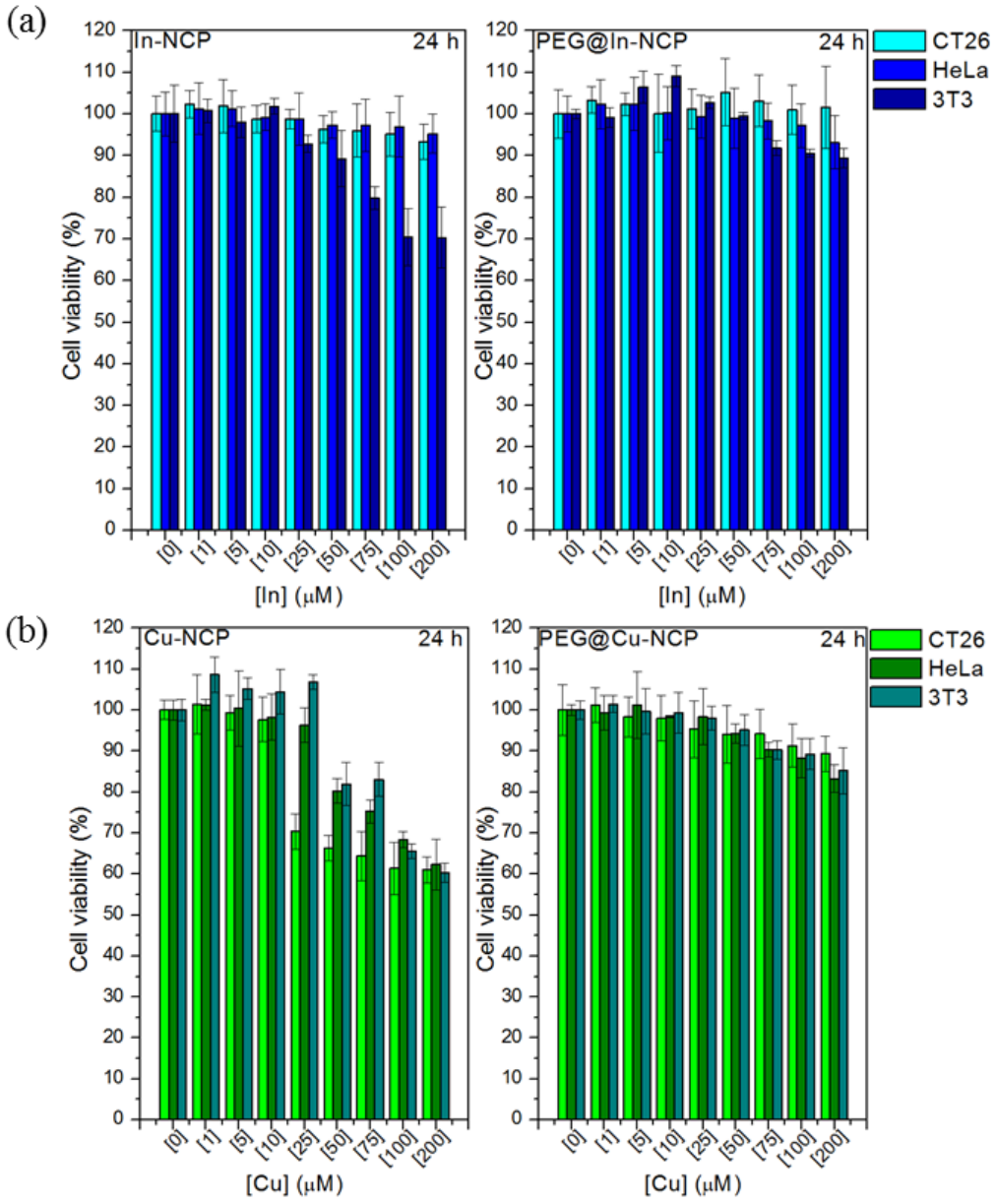

Figure 4.58 Effect of NCPs on cell viability in CT26, HeLA and 3T3 cells. Concentration-dependent cytotoxicity effects of NCPs were evaluated for 24 h incubating the different cell lines with (a) **In-NCP** and **PEG@In-NCP** and (b) **Cu-NCP** and **PEG@Cu-NCP**.

The effect of the PEG-catHMDA coating compared with the naked NCPs was clearly seen for concentrations higher than 75 µM and 25 µM for In-based and Cu-based NCPS, respectively. Once the NCPs were coated, the cell viability shown after 24 h of incubation was higher than 85% for both systems at the higher concentration tested (200 µM).

The positive effect of the PEG-catHMDA coating on the biocompatibility was also detected for 72 h of incubation with the three cell lines (Figure 4.59).

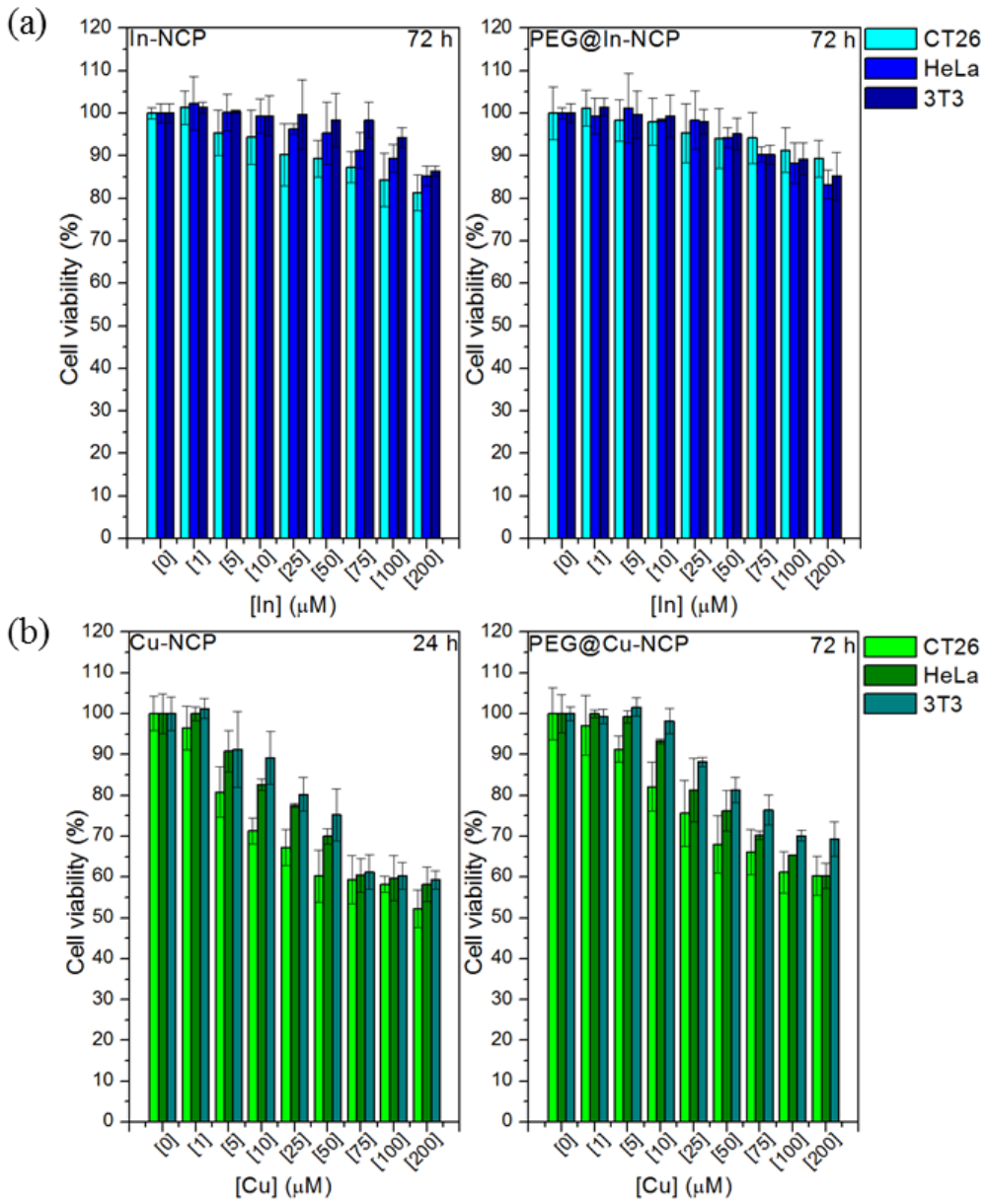

Figure 4.59 Effect of NCPs on cell viability in CT26, HeLA and 3T3 cells. Concentration-dependent cytotoxicity effects of NCPs were evaluated for 72 h incubating the different cell lines with (a) **In-NCP** and **PEG@In-NCP** and (b) **Cu-NCP** and **PEG@Cu-NCP**.

Although the Cu-based NCPs showed the higher toxicity compared with In-based NCPS, even for longer incubation times (72 h), the cell viability is maintained above 60% showing the low toxicity of the coated and PEGylated NCPs for concentrations up to 200 µM. These *in vitro* assays demonstrated the increase of the biocompatibility after the coating and subsequent PEGylation of the NCPs synthesised in addition to the very low toxicity detected.

Several images of the cells incubated with **PEG@NCPs** nanoparticles were recorded showing the normal cell growth during the incubation period without agglomeration or aggregation of the nanoparticles in the cell culture (Figure 4.60).

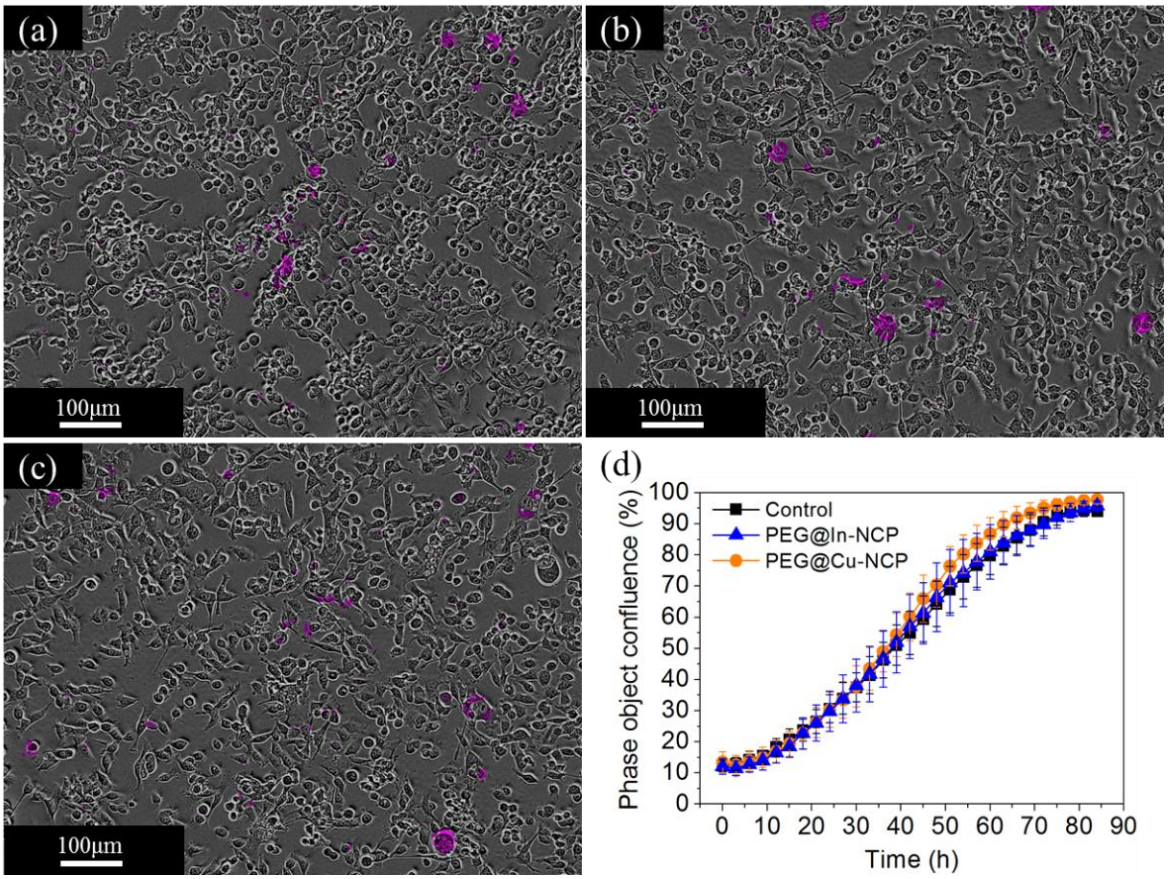

Figure 4.60 Incubation with cells after 24h. (a) Control, (b) **PEG@In-NCP** and (c) **PEG@Cu-NCP**. (d) Confluent cell growth after incubation with cells for24h. The concentration tested *in vitro* corresponds to the same tested for *in vivo*.

In order to optimize the pharmacokinetics, biocompatibility and targeting properties, FA molecules were attached chemically to the accessible amino-terminated PEG chains of the coated nanoparticles. The post-functionalisation of the PEGylated NCPs was preferred instead the pre-functionalisation of PEG chains to ensure the presence of FA on the surface of nanoparticles and maximize the interaction with folate receptors. Before to the *in vivo* experiments, the effect and the role of the folic acid was evaluated *in vitro* in CT26 cell line. The selected cell line presents an overexpression of folate

receptors allowing the *in vitro* evaluation of the uptake of functionalised NCPs. Thus, **PEG@NCPs** systems containing the specific radiotracer with folic acid (**FA-PEG@In-NCP**/**FA-PEG@Cu-NCP**) and without (**PEG@In-NCP**/**PEG@Cu-NCP**) were incubated for 24 h in the cell culture. The extracellular and intracellular fractions were measured by using a ɣ-counter and the last one was plotted over time (Figure 4.61).

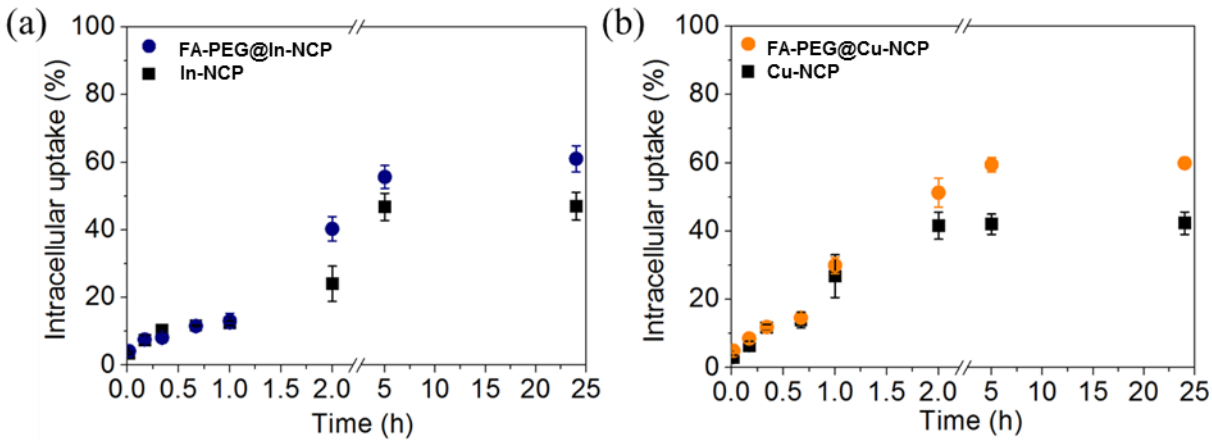

Figure 4.61 Role of the folic acid in CT26 cells. Intracellular uptake of nanoparticles with and without folic acid for (a) **In-NCP** (black) / **FA-PEG@In-NCP** (blue) and (b) **Cu-NCP** (black) / **FA-PEG@Cu-NCP** (orange).

In both cases, the uptake of the nanoparticles decorated with the folic acid was significantly increased in comparison with the nanoparticles without folic acid. At 24 h, **FA-PEG@In-NCP** and **FA-PEG@Cu-NCP** exhibited an uptake of 14% and 17% higher than the nanoparticles without FA, respectively. It was observed in all cases that after 5 h the cellular uptake kept slightly constant until 24 h when a plateau region was perceived (Table 4.17).

Table 4.17 Percentage of NCPs internalisation in CT26 cell line with folate receptors. Data is shown as mean ± standard deviation.

Time	Cell uptake (%)			
	In-NCP	**FA-PEG@In-NCP**	**Cu-NCP**	**FA-PEG@Cu-NCP**
1 min	3.54 ± 0.37	4.14 ± 1.55	2.99 ± 0.68	4.99 ± 0.53
10 min	7.45 ± 1.36	7.57 ± 0.12	6.47 ± 1.26	8.54 ± 0.28
20 min	10.28 ± 0.65	8.13 ± 0.51	11.74 ± 0.93	11.93 ± 1.24
40 min	11.74 ± 0.14	11.57 ± 0.69	13.97 ± 2.35	14.60 ± 1.09
1 h	12.45 ± 0.59	13.06 ± 2.27	26.77 ± 6.23	29.95 ± 2.35
2 h	24.04 ± 5.22	40.30 ± 3.62	41.55 ± 3.93	51.25 ± 4.24
5 h	46.78 ± 3.98	55.63 ± 3.38	42.01 ± 2.96	59.45 ± 2.09
24 h	47.00 ± 4.06	61.01 ± 3.85	42.31 ± 3.26	59.89 ± 1.32

These *in vitro* results validated the attachment of the folic acid on the NCPs surface and the increased uptake by the cells due to the active targeting properties of the resulting nanoparticles. The differences were more notable for periods longer than 2 h.

4.3.2.2.6 *In vivo* PET/SPECT: Biodistribution analysis

Three different systems were studied *in vivo* with different objectives (Figure 4.62). On the one hand, a complete *in vivo* biodistribution analysis was evaluated with the system containing ^{111}In as radiotracer, basically due to its high half-life what allows working more easily. The biodistribution was evaluated in detail for both **PEG@In-NCP** and **FA-PEG@In-NCP** for comparison purposes (Figure 4.62a,b). Additionally, as a first approximation for the potential use of ^{64}Cu-based NCPs as PET radiotracer, the **PEG@Cu-NCP** system was evaluated and compared with the previous ones (Figure 4.62c).

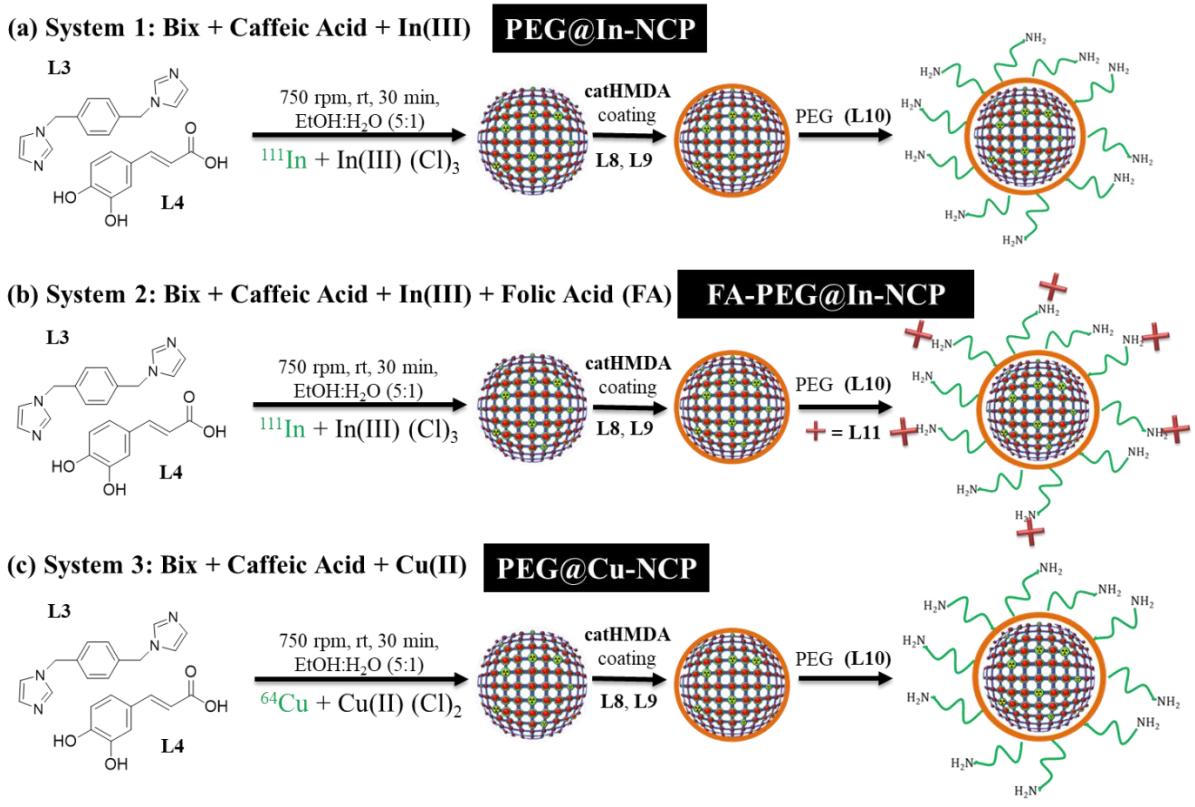

Figure 4.62 Systems studied for the *in vivo* assays. (a) **PEG@In-NCP**, (b) **PEG@In-NCP** and (c) **PEG@Cu-NCP**. The synthesis methodology and the procedure steps are summarised.

Thus, *in vivo* SPECT imaging were conducted to track ^{111}In-labelled NPs after i.v. injection into Balb/c CT26 tumour-bearing mice using a multimodal PET/SPECT/CT (VECTor/CT, MILabs, The Netherlands) rodent model scanner at various time points. After the induction of anaesthesia, 100 µL ± 2.5 µL of **PEG@In-NCP)** (~10.4 MBq) or **FA-PEG@In-NCP** (~34.4 MBq) were administered to mice through the tail vein. These nanoprobes, contained the specific activity 1.04 ± 0.11 MBq and 3.44 ± 0.08 MBq per mouse, respectively. Imaging contrast was observed after administration the nanoparticles and SPECT images were recorded at different time points as detailed in Figure 4.63. As shown, the **PEG@In-NCP** and **FA-PEG@In-NCP** nanoparticles initially presented a similar biodistribution with a main accumulation in the lungs in the first 15 min, which is a common behaviour for particles with hydrodynamic radios bigger that 100 nm.[44-46] Poor accumulation was observed in the liver, intestines, kidneys and spleen. The accumulation in lungs appears as preferential until 1 h. Interestingly, the levels of **PEG@In-NCP** nanoparticles retained in the lungs showed significant decrease after 1 h and gradually increasing levels were detected in liver and kidneys until 5 h after administration.

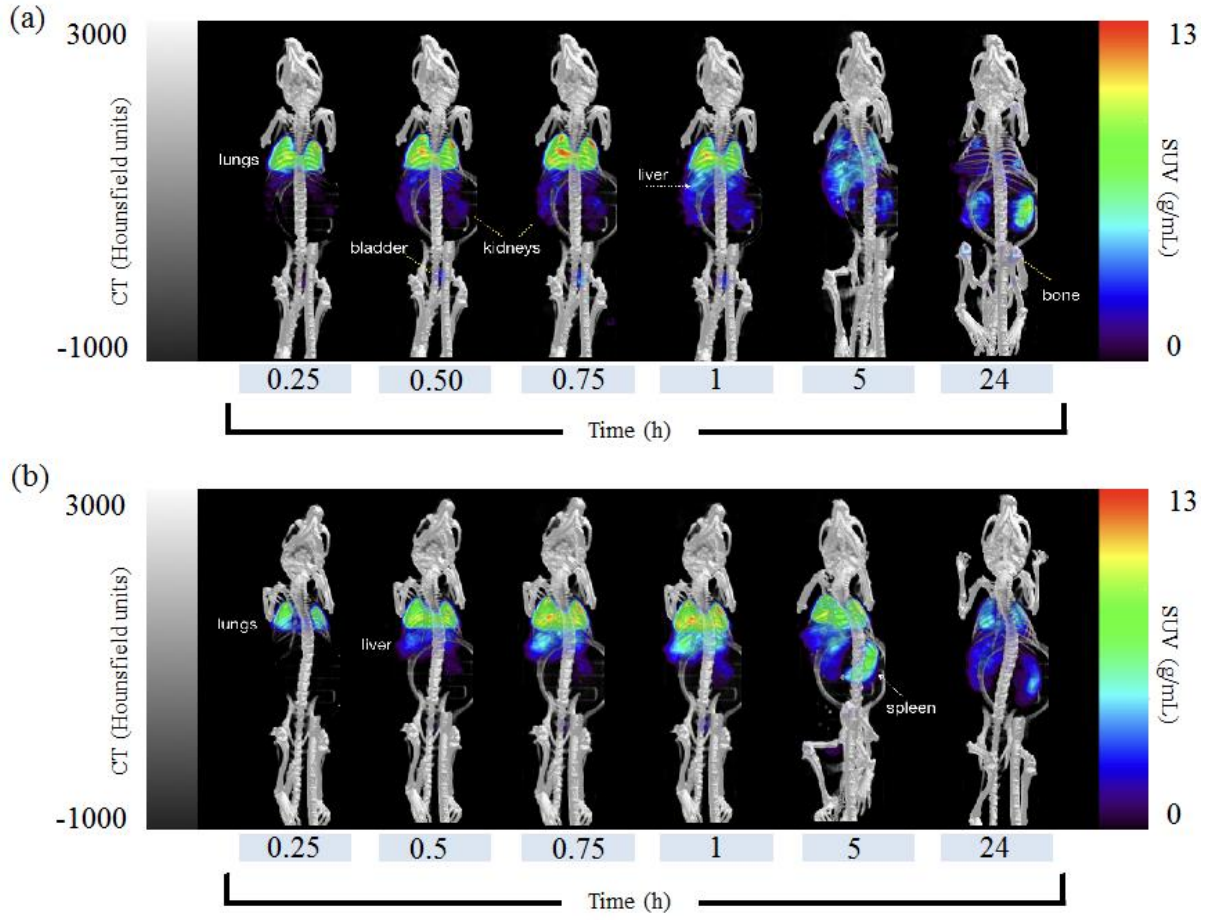

Figure 4.63 Top view maximum intensity projections (MIPs) on total body SPECT/CT scans at various time points after administration of **PEG@In-NCPs** (a) in the absence of folic acid in their structure and (b) functionalised with folic acid.

The average organ activity per volume obtained from the Standardised Uptake Values (SUVs) from each organ confirmed this tendency (Figure 4.64). After 5 h the levels of **PEG@In-NCP** retained in the liver showed notable decrease over time, while in kidneys still increase to reach high levels at 24 h, indicating a gradual and important clearance of the NCPs most likely via the renal pathway (Figure 4.64b). Interestingly, the nanoparticles decorated with FA showed an increased permanence in lungs and liver after 1h in comparison with the non-functionalised NCPs (Figure 4.64e).

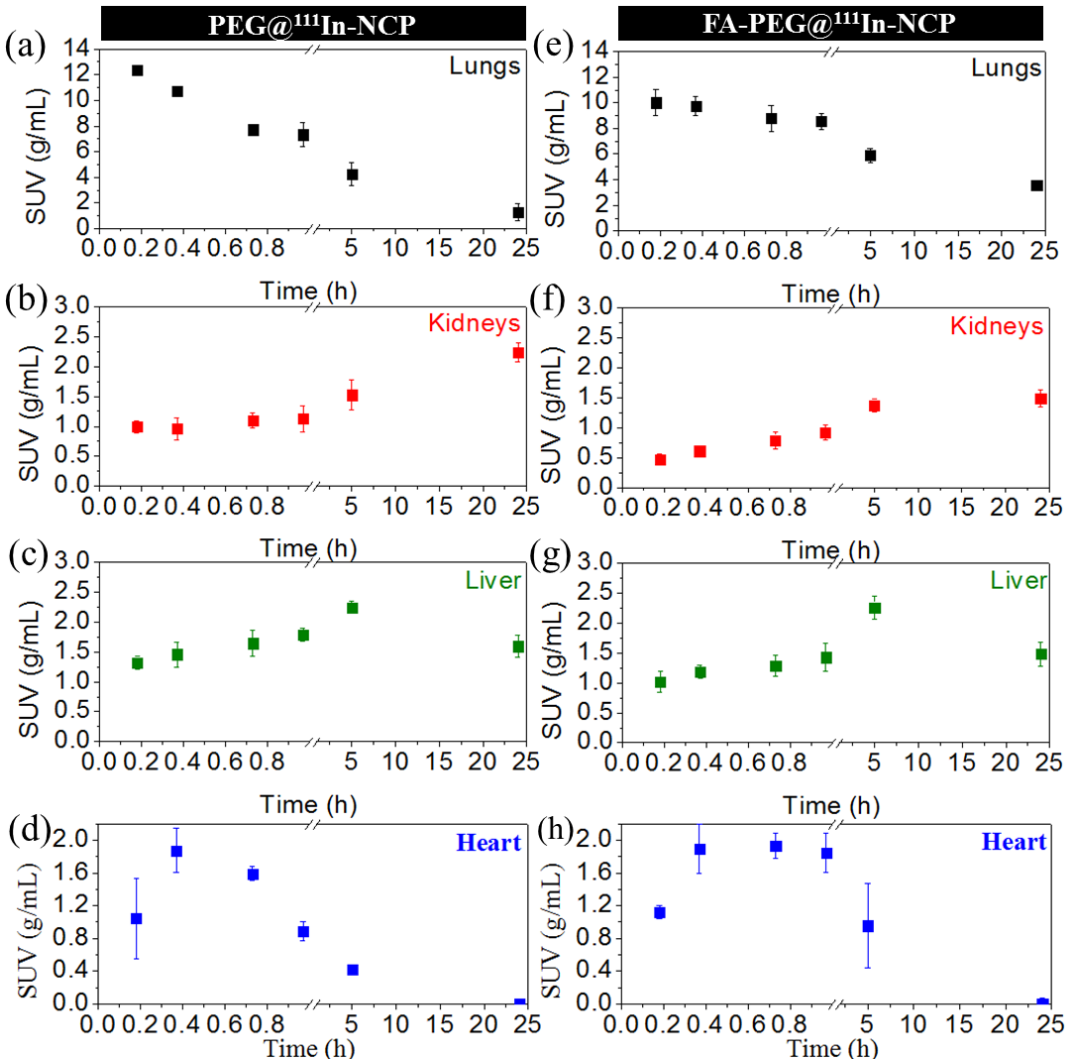

Figure 4.64 Standardized uptake vales (SUVs) for **PEG@In-NCP** and **FA-PEG@In-NCP**. (a, d) lungs, (b, e) kidneys, (c, f) liver.

In fact, the radiation levels in lungs remained at high levels for long time and the increase of residence time calculated for SUVs for **FA-PEG@In-NCP** versus **PEG@In-NCP** was around 30%. The present results corroborate the increased accumulation and permanence of NCPs in lungs and

liver in the first hour, permanence in lungs and accumulation in spleen observed at 5 h, and subsequently a slow clearance through the kidneys was observed in the next 20 h. The standardised values (Figure 4.64e) showed the decrease of the signal in the lungs with time while increase in the liver and kidneys. Finally, the SUVs obtained for the hearth showed how the NCPs circulate through the bloodstream after their i.v. injection. For the **PEG@In-NCP** system, the maximum value was measured after ~30 min p.i. and then a decrease was observed (Figure 4.64d). This behaviour was in agreement with the rapid accumulation of the NPs by the lungs. In the case of the functionalized NPs (**FA-PEG@In-NCP**), it was observed a longer circulation time reaching the maximum SUV after ~45 min p.i. From these values, the half-life circulation times were calculated, *vide infra*.

This different biodistribution behaviour between FA-contained and non-contained NCPs could be related to the specific binding ability of the FA-radiolabelling NCPs for detecting folic acid receptors in tissues. It was reported that the expression of folate receptors in healthy tissues is limited to the placenta, lungs, spleen, kidneys, and choroid plexus depending of the specie.[47] Then, this kind of approximations could provide a reliable and sensitive means for determining folate receptor expression in neoplastic tissues as well as non-neoplastic tissues, or for determining the expression of tumour markers. Knowing that folate-targeted therapeutics are currently being developed, this method could be useful for testing a wide variety of cancer and normal tissue specimens and establishing clinical trial eligibility (developing a reliable and comprehensive database of tissue folate receptor expression levels to supplement data that have been obtained by other methods). The post-mortem quantitative analysis of the organs indicated the biodistribution after 24 h p.i. The tumours and major organs were collected and the corresponding activity quantification of ^{111}In were acquired by a ɣ counter. The biodistribution of the levels of ^{111}In in the main organs (Figure 4.65) and tumour (Figure 4.67) is shown.

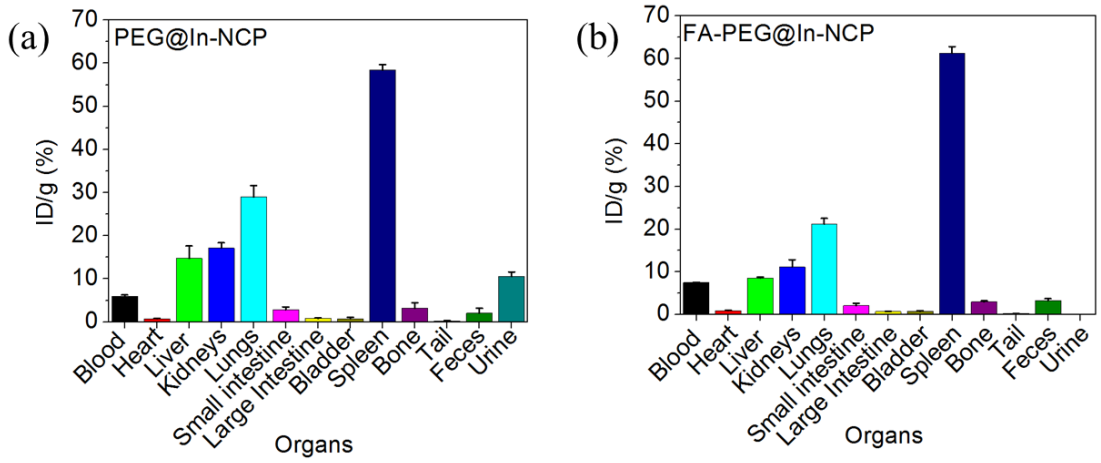

Figure 4.65 Biodistribution of (a) **PEG@In-NCP** and (b) **FA-PEG@In-NCP** euthanized after 24 h p.i. The results are shown in injected dose (ID) per gram of mice.

These results were based on the injected doses (ID) considering the activity at the moment of injection and the mouse weight (ID/g) after 24 h post-injection (p.i.). Thus, although the accumulation of the **PEG@In-NCP** nanoparticles in lungs was still notable (28.97 ± 2.63% ID/g), in kidneys (17.14 ± 1.21% ID/g) and liver (14.73 ± 2.87% ID/g) the values were quite low (Table 4.18). The amount of nanoparticles that remained in blood was also notably low, what corroborate the clearance from the blood stream at 24 h. The highest signal observed in the spleen (58.37 ± 1.31% ID/g) denoted their retention after 24 h. This was not surprising since various studies have concluded that many nanoparticles bigger than 100 nm are retained by the spleen.[48,49] For the **FA-PEG@In-NCP**, similar biodistribution was shown. In this case, the values were similar for lungs (21.20 ± 1.34% ID/g), kidneys (11.14 ± 1.70% ID/g), liver (8.53 ± 0.20% ID/g) and with higher retention in spleen (61.23 ± 1.57% ID/) after 24 h p.i. This large uptake in the spleen indicated that the clearance of the NCPs was mainly through MPS as previously reported for the similar type of NCPs in Chapter 4.2. As for **PEG@In-NCP,** after 24h p.i. nanoparticles were still detected circulating in the bloodstream (7.46 ± 0.09% ID/g). In the same way, notable differences between non-functionalised or functionalized nanoparticles with FA were observed also in the tumour uptake.

Although the tumour uptake of **PEG@In-NCP** and **FA-PEG@In-NCP** could not be well observed by time-dependent SPECT imaging data, the post-mortem quantitative analysis of the organs showed significant differences in tumour uptake comparing both groups of NCPs with and without folic acid (Figure 4.67). This observation denoted a clear accumulation of the NCPs targeted with folic acid at 24 h reaching the level of 10.39 ± 1.10 % ID/g in tumour cells, likely due to the EPR effect and the functionalization of the NCPs with the targeting molecule. On the other hand, the accumulation of **PEG@In-NCP** (without FA) reached a 0.92 ± 0.26 %ID/g which denoted notably the influence of FA targeting molecules in the tumour retention. The blood circulation half-lives of **PEG@In-NCP** and **FA-PEG@In-NCP** were determined to be 0.90 ± 0.15 h and 4.55 ± 0.22 h, respectively. This data indicates the high permanence of the NCPs in the bloodstream induced by the catechol-based coating containing PEG.

Additionally, PET imaging was conducted to track ^{64}Cu-labeled NCPs (**PEG@Cu-NCP**) after i.v. injection of 100 µL ± 2.5 µL into Balb/c mice, containing the equivalent 1.02 ± 0.69 MBq. Based on the results of the In-based NPs, the biodistribution *in vivo* imaging and post-mortem quantitative analysis of the organs, were recovered at 5 h after administration for comparison in an intermediate step of the pharmacokinetic evolution on the nanoparticles (Figure 4.66).

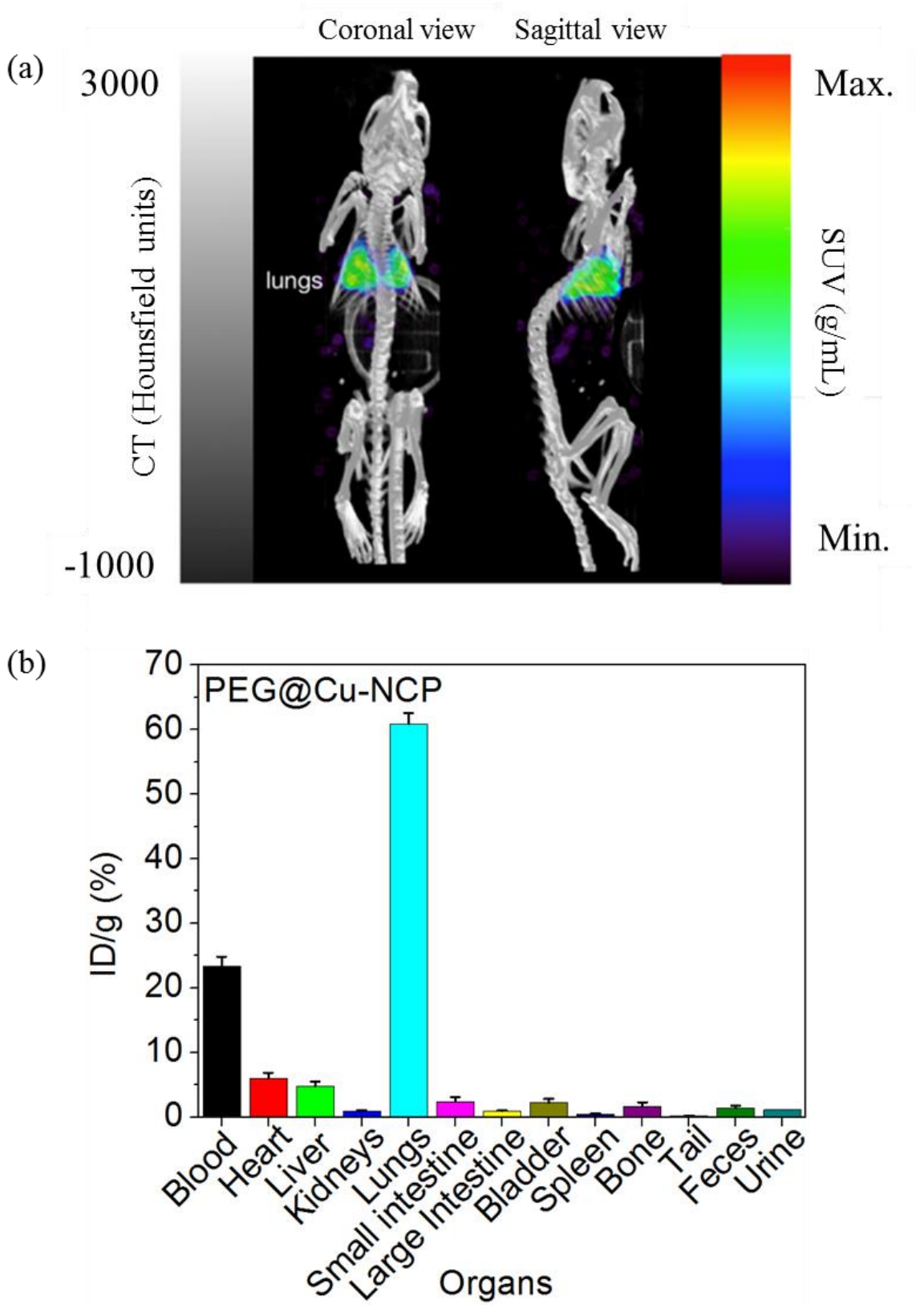

Figure 4.66 (a) Top view maximum intensity projections (MIPs) on total body PET/CT scans at 15 min after administration of **PEG@Cu-NCPs**. Coronal and sagittal views are presented. (b) Biodistribution of **PEG@Cu-NCP**. The biodistribution corresponds to after 5 h p.i. The results are shown in injected dose (ID) per gram of mice.

As in the case of the In-based NCP analogue, the results of PET imaging and SUVs are comparable to the SPECT images for (**PEG@Cu-NCP**) at 5 h. These results denoted a clear accumulation of the **PEG@Cu-NCP** nanoparticles in lungs (60.91±1.61 %ID/g) and blood (23.38±1.47 %ID/g). As in de case of **PEG@In-NCP** at 5 h, poor accumulation was observed in the liver (4.77±0.77 %ID/g), intestines (~3.40±0.70 %ID/g), kidneys (0.96±0.15 %ID/g), spleen (0.44±0.09 %ID/g) and tumour (1.33±0.36 %ID/g) (Table 4.18). Similar to **PEG@In-NCP,** the **PEG@Cu-NCP** system showed a very poor accumulation in tumour due to the non-targeting properties of the related NCPs, corroborating that the presence of FA increased notably the accumulation and retention in the tumour area (Figure 4.67). Thus, similar and extrapolable behaviour could be observed in both **PEG@Cu-NCP** and **PEG@In-NCP** nanoparticles. With this assay, we could corroborate the versatility of the present nanoconstruct for bearing different radionuclei and the suitability for performing SPECT or PET imaging. These preliminary results could open the door to the design of dual-mode PET/SPECT nanostructured radiotracers that would make feasible the use of combined radioimaging techniques and increasing the power of radionuclide-based imaging. The blood circulation half-lives of **PEG@Cu-NCP** at one time point (5 h) was determined to be 0.83 ± 0.19 h.

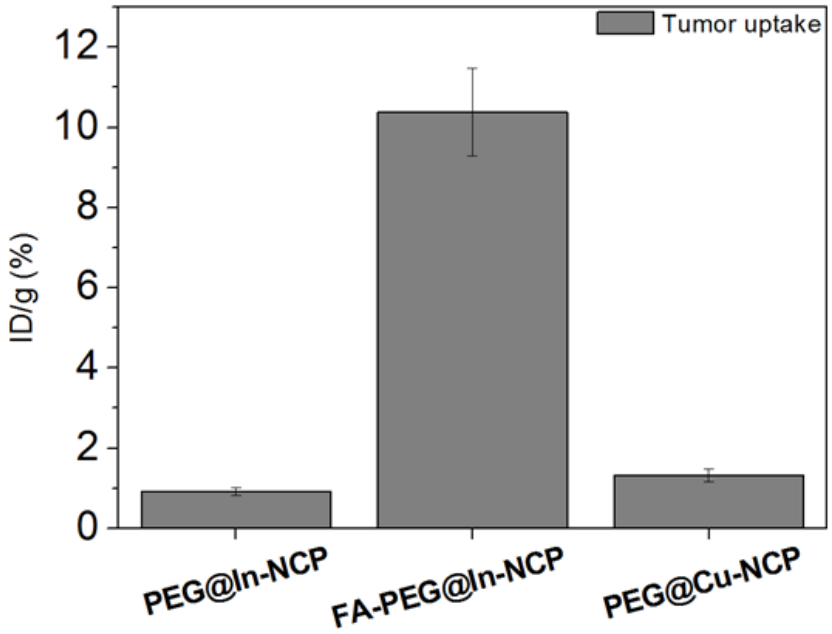

Figure 4.67 Tumour uptake for all the systems tested in vivo: **PEG@^{111}In-NCP**, **FA-PEG@In-NCP** and **PEG@Cu-NCP**. The results are shown in injected dose (ID) per gram of mice.

Table 4.18 Percentage of injected dose per gram of mouse (ID/g) for each NCP system. Data is shown as mean ± standard deviation. The data corresponding to the In-based NCPs (orange) are related with the mice euthanized after 24 p.i. The data corresponding to the Cu-based NCP (green) is related to the mice euthanized after 5 h p.i. The error is shown as ± standard deviation.

Organ	PEG@In-NCP	FA-PEG@In-NCP	PEG@Cu-NCP
	ID/g	ID/g	ID/g
Blood	5.94 ± 0.34	7.46 ± 0.09	23.38 ± 1.47
Heart	0.76 ± 0.08	0.91 ± 0.08	5.99 ± 0.91
Liver	14.73 ± 2.88	8.53 ± 0.20	4.77 ± 0.77
Kidneys	17.14 ± 1.22	11.14 ± 1.70	0.96 ± 0.15
Lungs	28.97 ± 2.63	21.20 ± 1.34	60.91 ± 1.61
Small intestine	2.83 ± 0.67	2.08 ± 0.53	2.43 ± 0.69
Large Intestine	0.80 ± 0.13	0.67 ± 0.13	0.97 ± 0.03
Bladder	0.73 ± 0.34	0.75 ± 0.15	2.23 ± 0.58
Spleen	58.37 ± 1.31	61.23 ± 1.57	0.44 ± 0.09
Bone	3.17 ± 1.29	2.95 ± 0.24	1.65 ± 0.66
Tail	0.23 ± 0.08	0.22 ± 0.04	0.19 ± 0.06
Tumour	0.92 ± 0.26	10.39 ± 1.10	1.33 ± 0.36
Feces	2.02 ± 1.14	3.25 ± 0.44	1.41 ± 0.39
Urine	10.59 ± 0.99	-	1.15 ± 0.12

In basis of the cumulative data from the experimental results we can establish that the present nanoparticles showed a quickly and preferential accumulation in lungs during the first hour. Although, for this time the biodistribution of NCPs containing and non-containing FA was comparable, notable differences were detected at 5 and 24 h. The presence of FA increased the retention time in lungs and spleen at 5 h reducing the clearance of the nanoparticles at long time, meanwhile non-FA functionalized NCPs was faster released from the body through the renal clearance. Thus, at 24 h the maximum signal for **PEG@In-NCP** was detected in kidneys meanwhile for **FA-PEG@In-NCP** the concentration of NCPs was distributed between lungs and kidneys. The low concentration of nanoparticles in blood stream during the study could be related to the high retention of NCPs in lungs. In any case, the quantitative analysis studies post-mortem of the organs 24h still indicated the presence of nanoparticles in blood stream, being more concentrated at 5 h (Figure 4.66b).

Knowing that folate-targeted therapeutics are currently being developed, this method could be clinically useful for testing specimens and establishing clinical trial eligibility for determining the expression of tumour markers by using the sensitivity of radioactive methods.

With this study, a complete pharmacokinetic behaviour of these NCPs was performed and explains much better the biodistribution a biodegradation of this kind of nanoparticles. In the previous work presented in Chapter 4.2, with the Fe-based NCPs (**Fe-NCP**), it had been indicated that these nanosystems resulted in a minimal tissue accumulation and gradual degradation/excretion without bioaccumulation, confirming the rapid excretion of the nanoparticles due to their intrinsic biodegradability. In fact, the biodegradability process was attributed to a gradual degradation of the

NCPs since the size needed to pass through the kidneys and reach the bladder should be smaller than 8 nm. Similarly, the large uptake of the NCPs observed in spleen indicated its important role in the nanoparticle pharmacokinetics based on their rapid clearance by MPS which is common for unmodified nanoparticles bigger than 40 nm.[50,51]

4.3.2.3 Preliminary results on dual In/Cu NCP system

4.3.2.3.1 Synthesis and characterization

As a forward step, the development of a dual system containing in the same structure the ^{111}In and ^{64}Cu radioisotopes was achieved (Figure 4.68). However, due to the lack of time, it was not possible to complete the corresponding *in vivo* studies. For doing such experiments, it was necessary to calibrate the equipment in order to detect at the same time both radionuclides and some issues were found during this process. Nevertheless, the main chemical characterization of the dual NCP system and the phantom study of the dual In-Cu for the equipment calibration is presented.

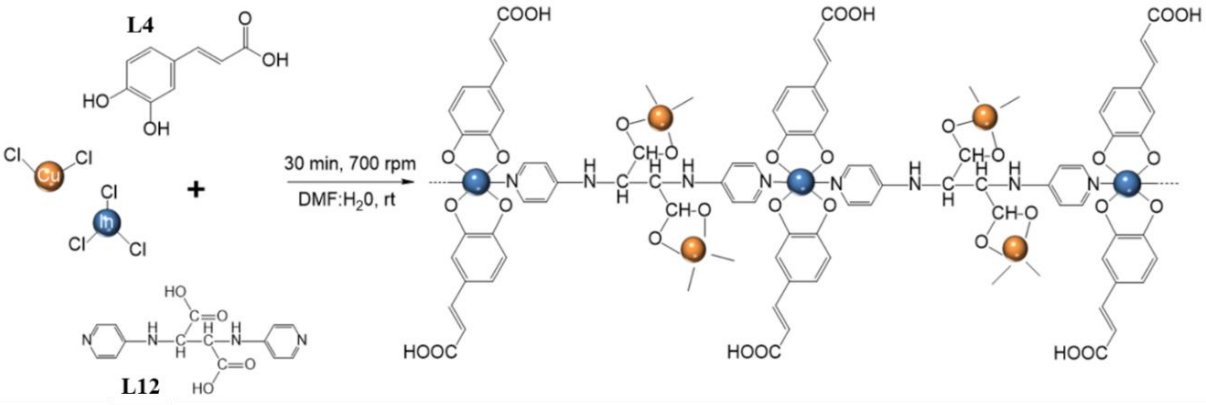

Figure 4.68 Synthesis of the dual NCPs complex. The metallic salts were mixed with its respective radiometal $^{111}InCl_3$ and $^{64}CuCl_2$ for the **InCu-NCP** system.

The protocol used for the synthesis of In-NCP and Cu-NCP was slightly modified. In this case, the reaction of $InCl_3$ and $[^{111}In]Cl_3$ together with $CuCl_2$ and $[^{64}Cu]Cl_2$ and 1,4-Bis(imidazole-1-ylmethil)-hexane (**L12**) and **L4** as a co-ligand in 1:1:2 molar ratio, yielded the formation of nanoparticles named as **InCu-NCP** (Figure 4.68). The mixture of metals (In(III) and Cu(II)) and their respective radioisotope (^{111}In(III) and ^{64}Cu(II)) was done in water and subsequently added to a dimethylformamide (DMF) solution containing the ligands (**L12** and **L4**). After addition of the metal salts, the fast precipitation of the resulting CP generated directly the nanostructuration of the material. Using this methodology NCPs of 75 ± 11 nm in size were obtained for the **InCu-NCP** system (Figure 4.69a,b).

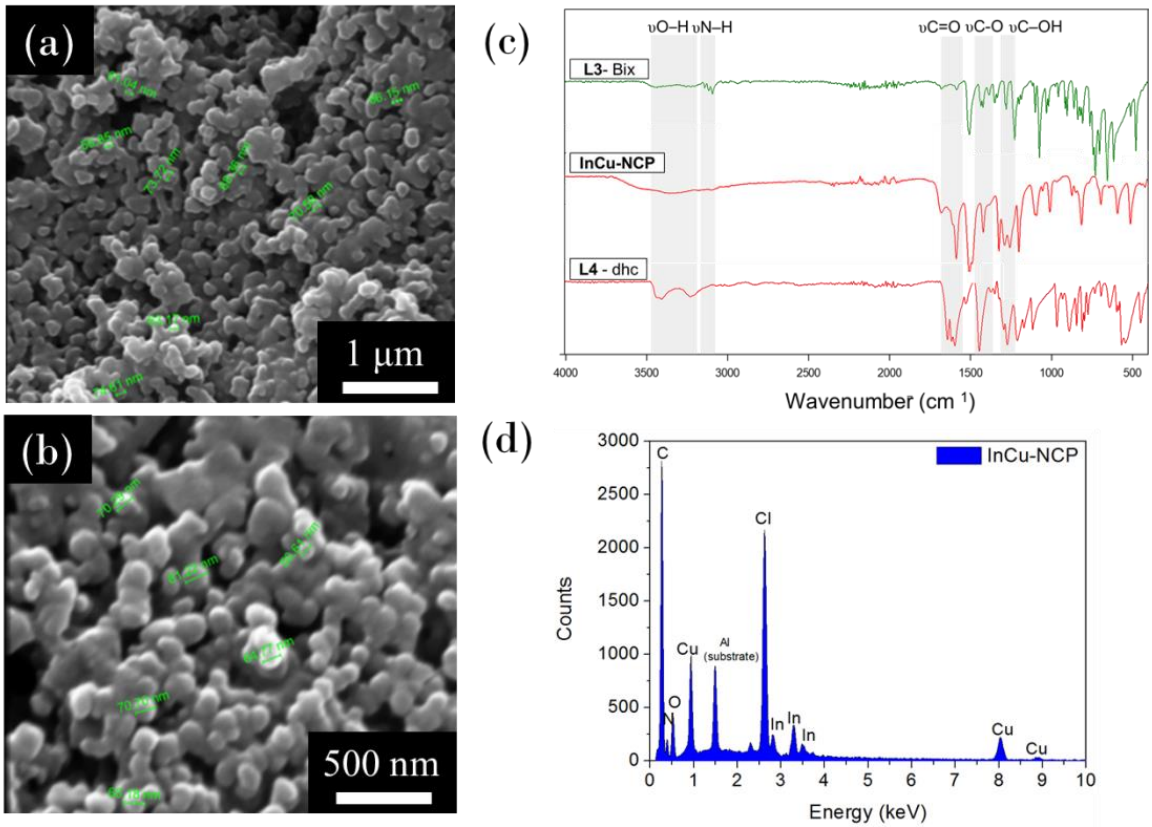

Figure 4.69 Physicochemical characterization of **InCu-NCP**. (a,b) SEM images of the dual **InCu-NCP** system. (c) FT-IR spectra for the **InCu-NCP**. The spectra of the ligands **L3** and **L11** are shown. (d) EDX measurements corroborating the presence of both In(III) and Cu(II) metal ions.

The FT-IR spectra revealed the coordination of the ligands with the metals (Figure 4.69c) and the presence of both In(III) and Cu(II) was confirmed by EDX (Figure 4.69d). Finally, the chemical stability of the coated InCu-NCP (**PEG@InCu-NCP**) was evaluated at two different pHs (Figure 4.70). The results showed a faster release of Cu(II) metal ions with time compared with In(III). As expected, the **PEG@InCu-NCP** was faster degraded at pH = 5.2.

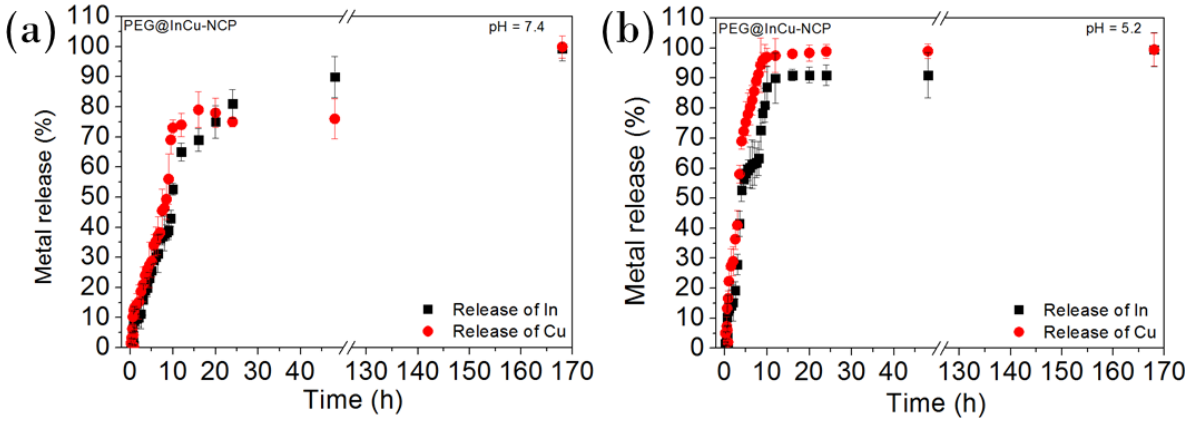

Figure 4.70 Stability of the **PEG@InCu-NCP** system at (a,) pH = 7.4 and (b) pH = 5.2 in PBS-MSA-Plasma. Data is shown as mean ± standard deviation.

4.3.2.3.2 Dual ^{111}In and ^{64}Cu phantoms study

These set of experiments were done for the first time in order to calibrate the equipment for doing the imaging of a system with a dual PET/SPECT-active radioisotope in the same structure (**InCu-NCP**). This study is important for accomplish the following objectives:

i. Evaluate the feasibility and quantitative accuracy of ^{64}Cu and simultaneous ^{64}Cu/^{111}In SPECT using a small-animal SPECT/PET/CT system.
ii. Determine the camera calibration factor (CF) of ^{64}Cu and ^{111}In using point-like sources (*Eppendorf* tubes) and extended sources (syringes)
iii. Determine the size of the smallest structure visible on ^{64}Cu and ^{64}Cu/^{111}In reconstructed images of a rod-phantom.
iv. Measure the time-activity curve (TAC) of ^{64}Cu using SPECT images (acquired at 0 h, 12 h, 24 h, 36 h and 48 h) of a phantom containing a mixture of ^{64}Cu and ^{111}In.

First of all, the ^{111}In and ^{64}Cu were evaluated separately (Figure 4.71a,b) and mixed (Figure 4.71c). for determining their calibration factor (especially for ^{64}Cu, which was measured for the first time in the equipment used). The radioisotopes were introduced in a device (Figure 4.71d) for its measurement at different time points. However, the ^{111}In content precipitated during the measurement due to the formation of a salt (Figure 4.71a). This precipitation did not allow the properly calculation of the calibration factors when mixing both radiotracers.

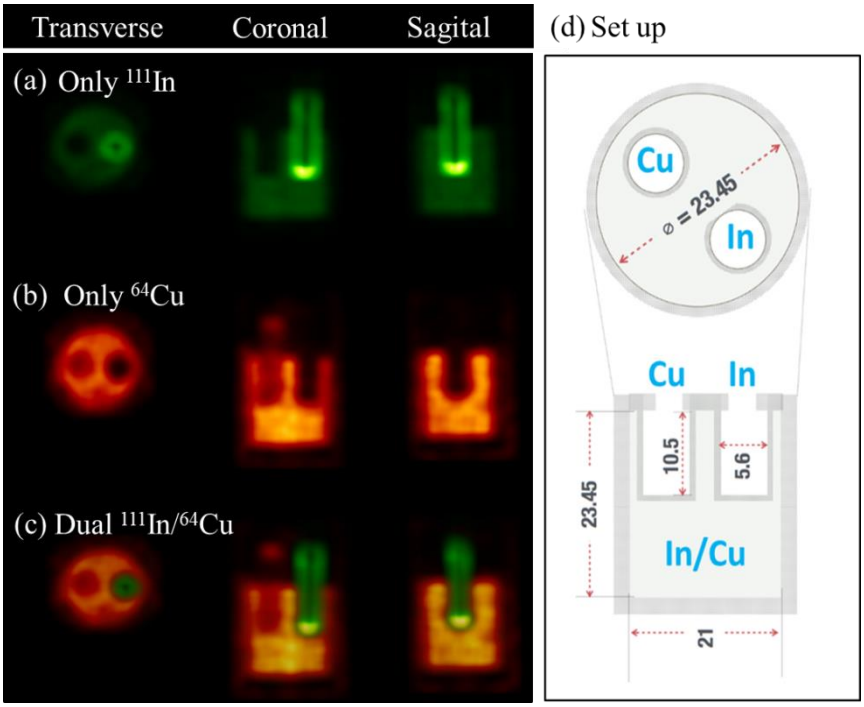

Figure 4.71 Results for the dual ^{111}In/^{64}Cu study. (a) Image obtained for the ^{111}In. The formation of a precipitate can be observed on the bottom (green brightness). (b) Image obtained for the 64Cu. (c) Image obtained for the mixture of ^{111}In/^{64}Cu. (d) The radioisotopes were introduced separately and mixed in the three-compartment device represented.

From the previous measurements, the energy spectra for the ^{111}In and ^{64}Cu radiotracers was obtained (Figure 4.72). These energy spectra are crucial for determining the energies which the signal from the ^{111}In and ^{64}Cu can be measured without overlapping or background noise.

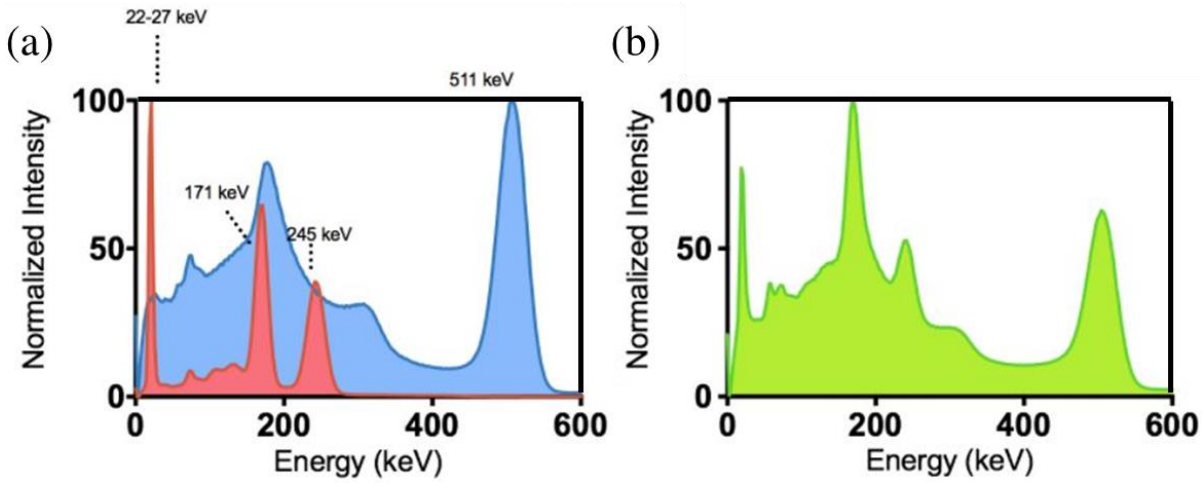

Figure 4.72 Energy spectra of ^{111}In (red) and ^{64}Cu (blue) acquired individually (a) and simultaneously (b) with VECTor equipment. In (a), the energy spectra were normalized by the intensity of the 22-27 keV peak and the 511 keV peak for ^{111}In and ^{64}Cu, respectively. In (b), the energy spectrum of the simultaneously acquired radionuclides was normalized by the intensity of the 173 keV peak.

The results showed in Figure 4.72 demonstrated that both radioisotopes could be measured simultaneously by acquiring the energies emitted at 22-27 keV and 511 keV for ^{111}In and ^{64}Cu, respectively. The reconstruction of the images obtained from the equipment can be performed at the mentioned energies in order to get in the same image the signal coming from each of the radioisotope separately. Due to problems originated form the precipitation of the 111In as a salt, the objectives iii) and iv) were not achieved. For this reason, as a future work, the study has to be properly finished.

In general, these studies were very preliminary and represent the potential of these systems to be used as dual radiotracers. However, its clinical translation is still difficult due to the costs and the low availability of dual PET/SPECT equipment. since there are currently only very few units that only have application in small animal research.

4.3.3 Summary and conclusions

Indium and Copper-based NCPs with uniform sizes were successfully synthesized via a one-pot chelator-free method. The NCPs could be labelled *in situ* with a ^{111}In and ^{64}Cu isotopes upon simple adding a fraction of radionuclei during synthesis, mixing them with non-radiolabelled metals and organic ligands, enabling *in vivo* SPECT and PET imaging. The resulting nanoparticles were coated with a catechol-based polymeric material that increased the chemical and colloidal stability and allowed functionalising the nanoparticles surface with PEG ligands and FA targeting molecules.

Radiolabelling nanoconstructs revealed low toxicity, high cellular uptake and targeting properties in vitro. After i.v. injection the nanoparticles showed:

i. No notable *in vivo* toxicity
ii. A preferential accumulation in lungs
iii. High persistence in blood and a gradual biodegradation process

The FA-decorated NCPs showed a notable modification of the biodistribution respect to the non-FA-functionalised NCPs. Thus FA-containing NCPs denoted an increasing permanence in lungs (for more than 5 h) in comparison with the non-functionalized ones (1 h). In the same way more accumulation in liver and spleen was observed. This increase in the residence time in organs determined their slow clearance through the kidneys in comparison with the non-functionalised in basis of the SPECT/CT images. The study determined the important clearance of this type of "soft" NCPs due to their inherently biodegradability after 24 h with no off-target accumulation in the liver and spleen.

Our work illustrates a kind of renal-clearable NCPs useful for chelator-free radiolabelling, *in vivo* SPECT and PET imaging, with improved efficacy and no additional side effects. NCPs may thus be a promising type of versatile nanoconstructs with great potential in clinical translation for lung diseases and tumour theranostic.

4.3.4 Experimental section

Materials Indium chloride and cupper chloride (Sigma-Aldrich, Merck, Madrid, Spain) were used as a metal salts for chelation together with ^{111}In chloride (^{111}In was provided as $^{111}InCl_3$ solutions in 0.05 M HCl (Nordion, Vancouver, Canada)) and ^{64}Cu chloride (TRIUMF, Vancouver, Canada) and used as received without further purification. 1,4-Bis(imidazol-1-ylmethyl)benzene (**L3**, Bix) was synthesized according to previously reported methodology[52] and the co-ligand and 3,4-dihydroxycinnamic acid (**L4**, dhc) was purchased from Sigma-Aldrich. Solvents were used as received without additional drying or degasification (Scharlab, Madrid, Spain).

Synthesis of ^{111}In-NCP and ^{64}Cu-NCP 1,4-Bis(imidazole-1-ylmethil)-benzene (**L3**, Bix – 6 mg, 0.25 mmol) and 3,4-dihydroxycinnamic acid (**L4**, dhc – 9 mg, 0.5 mmol) were dissolved in 0.8 mL of ethanol. Subsequently, the solution was treated with an aqueous solution containing metal salt either $InCl_3$ (7.3 mg, 0.25 mmol in 2 mL H_2O) and [^{111}In]Cl_3 (94.35 ± 36.26 MBq, 2-5 µL in 0.05 M HCl) for In-NCP; or $CuCl_2$ (5.2 mg, 0.25 mmol in 0.2 mL H_2O) and [^{64}Cu]Cl_2 (38.11 ± 5.92 MBq, 20 µL in 0.05 M HCl) for Cu-NCP. The reactions were carried out under

vigorous and homogeneous magnetic stirring (750 rpm). After 30 min, the resultant yellowish (In-NCP) and brownish (Cu-NCP) precipitates containing the nanoparticles were collected by centrifugation (7500 rpm, 1 min) and washed gently with ethanol and water.

^{111}In-NCP: ^{1}H NMR (250 MHz, MeOD, DCl, δ): 9.16 (d, 2H, C–$H_{imidazole}$ – **L3**), 7.68 (d, 2H, C–$H_{imidazole}$ – **L3**), 7.61 (d, 2H, C–$H_{imidazole}$ – **L3**), 7.56 (s, 4H, C–$H_{aromatic}$ – **L3**), 7.09 (dd, 1H, C–H_{ring} – **L4**), 6.96 (d, 1H, C–$H_{aliphatic}$ – **L4**), 6.83 (dd, 1H, C–H_{ring} – **L4**), 5.56 (s, 4H, C–H_2 – **L3**); IR (KBr): 3127 (m, δ(C–H_{ring})), 1625 (s, ν(C=C)), 1584 (m, δ(N–H)), 1519 (s, νC–H_{ring})), 1424 (s, ν(C–O)), 1400 (s), 1237 (s, ν(C–O)), 1106 (m), 1089 (s), 946 (m), 741 (s, δ(N–H_{ring})), 519 (w, In–O) cm^{-1}; Anal. Calcd (%): C 46.25, H 3.93, N 8.03; found: C 45.36, H 3.68, N 8.41. ICP-MS Calcd (%) for In-NCP: In 16.45; found: In 17.21. Compositional formula: In_1 $\mathbf{L3}_1$ $\mathbf{L4}_{1.43}$ $(Cl^-)_2(H_2O)_{0.9}$.

^{64}Cu-NCP: ^{1}H NMR (250 MHz, MeOD, DCl, δ): 9.06 (d, 2H, C–$H_{imidazole}$ – **L3**), 7.61 (d, 2H, C–$H_{imidazole}$ – **L3**), 7.53 (d, 2H, C–$H_{imidazole}$ – **L3**), 7.49 (s, 4H, C–$H_{aromatic}$ – **L3**), 6.98 (dd, 1H, C–H_{ring} – **L4**), 6.86 (d, 1H, C–$H_{aliphatic}$ – **L4**), 6.76 (dd, 1H, C–H_{ring} – **L4**), 5.47 (s, 4H, C–H_2 – **L3**); IR (KBr): 3132 (w, δ (C–H_{ring})), 1678 (w), 1625 (m, δ(N–H)), 1521 (s, νC–H_{ring})), 1394 (s, ν(C–O)), 1262 (s, ν(C–O)), 1109 (m), 980 (m), 723 (m, δ(N–H_{ring}), 467 (s, Cu–O) cm^{-1}; Anal. Calcd (%): C 50.01, H 4.95, N 6.93; found: C 49.65, H 4.29, N 6.88. ICP-MS Calcd (%) for Cu-NCP: Cu 7.87; found: Cu 8.35. Compositional formula: Cu_1 $\mathbf{L3}_1$ $\mathbf{L4}_{1.96}$ $(Cl^-)_{2.1}(H_2O)_2$

Synthesis of ^{111}In-^{64}Cu-NCP 1,4-Bis(imidazole-1-ylmethil)-hexane (**L11**, 0.25 mmol) and caffeic acid (**L4**, 0.5 mmol) were dissolved in 10 mL of dimethylformamide (DMF) under vigorous and homogenous magnetic stirring (700 rpm). Subsequently, the solution was mixed with an aqueous solution containing metal salt copper (II) acetate (0.25 mmol in 2.5 ml H_2O) and indium (III) chloride (0.25 mmol in 2.5 ml H2O) which turned the solution blueish. After 30 min reaction, the resultant precipitate blueish containing the nanoparticles was collected by centrifugation, washed gently with ethanol and water and lyophilized for long-term storage.

^{111}In^{64}Cu-NCP: 1H NMR (250 MHz, MeOD, DCl, δ): 9.36 (d, 2H, C-H_{hexane} –**L11**), 7.77 (d, 2H, C-H_{hexane} –**L11**), 7.41 (d, 2H, C-H_{hexane} –**L11**), 7.52 (s, 4H, C-$H_{aromatic}$ –L11), 6.91 (dd, 1H, C-H_{ring} –**L4**), 6.81 (d, 1H, C-$H_{aliphatic}$ –**L4**), 6.73 (dd, 1H, C-H_{ring} –**L4**), 5.41 (s, 4H, C-H2 –**L11**), 1.97 (Acetate); IR (KBr): 3130 (w, δ (C-H_{ring})), 1671 (w), 1619(m, δ(N-H)), 1518 (s, νC-H_{ring})), 1390 (s, ν(C-O)), 1259(s, ν(C-O)), 1100 (m), 921 (m), 719 (m, δ(N-H_{ring}), 468 (s, Cu-O) cm^{-1}; Anal. calcd: C 41.29, H 4.02, N 6.44; found: C 41.36, H 4.68, N 6.41

Primer coating and PEGylation of NCPs The NCPs synthesized where redispersed in a vial with PBS (1 mL, pH = 7.4). Subsequently, benzene–1,2–diol (1.7 mg, 10 mmol) and hexamethylenediamine (HMDA, 2.6 mg, 10 mmol) were added under homogenous stirring for

the formation of the primer coating. The vials were covered with a pierced Parafilm® (Labbox, Madrid, Spain) in order to allow the entrance of oxygen to the reaction mixture. After 60 min, 2 mg of poly(ethylene glycol) bis(amine) (3000 MW, Sigma-Aldrich), were added for the PEGylation of the primer coating the vial was closed and kept under magnetic stirring for 60 min. Finally, the nanoparticles were properly collected by centrifugation (7500 rpm, 1 min) and washed three times with Milli-Q water (Merck Chemicals & Life Science, Madrid, Spain)

Grafting the NCPs with folic acid The nanoparticles coated with primer coating and subsequently functionalized with PEG molecules, were mixed with 1 mL folic acid (10 mg/mL, PBS solution, pH = 7.4) containing n-Ethyl-N′-(3-dimethylaminopropyl)carbodiimide (EDC, 12 mg/mL) and n-hydroxysuccinimide (NHS, 13 mg/mL). This mixture was irradiated with ultrasounds for 30 min at room temperature, centrifuged (7500 rpm, 1 min) and washed with Milli-Q® water four times.

Characterization *To assess if PET/SPECT/CT-active metals could be chelated into nanoparticles, cold In(III) and Cu(II) salts were used and the nanoparticles characterized for comparison purposes. The nanoparticles with radiometal were led to complete decay previous its characterization.* Scanning electron microscopy (SEM) was performed for platinum-metallized samples on a FEI Quanta 650 FEG (Thermo Fisher Scientific, Eindhoven, The Netherlands) in mode operation of secondary electrons (SE) with a beam voltage between 5 and 20 kV. Fourier-transform infrared spectra (FT-IR) were recorded on a Tensor 27 FT-IR spectrometer (Bruker Optik GmbH, Berlin, Germany) with KBr pellets. All the measurements were taken under atmospheric conditions. Dynamic light scattering (DLS) measurements for obtaining size distribution and zeta potential (ζ-potential) of the nanostructures were performed using a Zetasizer Nano ZS 3600 (Malvern Instruments, U.K.). All analysed samples were diluted in order to obtain a concentration of nanoparticles suitable for the experimental calculation of size dispersion. The data reported are values coming from the mean of measurements for each sample which were measured per quadruplicate. Inductive coupled plasma-mass spectroscopy measurements (ICP-MS) were obtained using an ICP-MS NexION 300X (Perkin Elmer, San Francisco, CA, USA). All samples were measured in argon atmosphere. X-ray photoelectron spectroscopy (XPS) measurements were performed with a Phoibos 150 analyzer (SPECS GmbH, Berlin, Germany) in ultra-high vacuum conditions (based pressure 10^{-10} mbar). Monochromatic Al Kα was used as X-ray source (1486.6 eV). The electron energy analyzer was operated with pass energy of 50 eV. The analyzer was located perpendicular to the sample surface. The data was collected every eV with a dwell time of 0.5 s and treated with CasaXPS version 2.317PR1.1 /Casa Software LTD, Teignmouth, UK).

Radiochemistry yield (RCY) Radiochemistry efficiency was measured wit instant thin layer chromatographic (ITLC) using PBS as the mobile phase. The NCPs with higher molecular weight remain at the origin while free radioisotopes (^{111}In and ^{64}Cu) moves with the mobile phase.

Long-term in vitro stability The stability of both NCPs systems in mouse plasma was determined at different time intervals over 7 days. For this purpose, 200 μL of **PEG@In-NCP** or **PEG@Cu-NCP** was incubated with 1 mL of mouse plasma at 37 ºC (dialysis bag, 650 rpm). Different aliquots were taken at designed time points (5 min, 10 min, and every 10 min up to 1 h, every 30 min up to 10 h, 12 h, 16 h, 20 h, 1 day, 2 days, 3 days, 5 days and 7 days) and measured by ICP-MS. For comparison purposes, the nanoparticles without coating were analysed by following the same protocol.

Cell viability in vitro studies CT26, HeLa or 3T3 cells were added to a 96-well plate at a concentration of 5,000 cells per well. The plates were incubated at 37 °C for 24 hours, to allow cells to adhere to the wells. A serial dilution of nanoparticles was added to the wells in quadruplicate, ranging from a concentration of 5 - 200 μg metal/ml. Cells were incubated with the nanoparticles for 24 h and 72 h at 37 °C. Then 20 μL of 5 mg/ml MTT (thiazoyl blue tetrazolium bromide) solution was added to each well and incubated at 37 °C for two hours. The volume was slowly aspirated via pipette from the wells, to avoid disturbing the cells. Then 150 μL of DMSO was added to each well. The absorbance of each well was recorded at a wavelength of 540 nm using a plate reader.

In vitro cell uptake CT26 cells were added to a 24-well plate at a concentration of 50,000 cells per well and incubated at 37 °C for 48 hours to allow cells to adhere to the wells. Prior to addition to the wells, the nanoparticles were diluted in fresh cell media for a final activity of around 2 μCi per well. At 0, 0.08, 0.25, 0.5, 1, 2, 5 and 24 hours, the media was collected, and the cells were washed with ice-cold PBS 1X. Afterwards, SDS-NaOH lysis buffer (0.25% SDS, 0.05 N NaOH) was added to the cells to release the internalized nanoparticles and the solution was collected. Activity present in media (extracellular fraction) and lysis buffer (intracellular fraction) was then measured with a 2470 Wizard2™ gamma counter (PerkinElmer). Each time point was measured in triplicate.

In Vivo PET/SPECT Imaging The current study was performed in accordance with the Canadian Council on Animal Care (CCAC) and protocol approved by the Animal Care Committee (ACC) of the University of British Columbia (A16-0150). Three groups of 3 x Balb/c female mice (aged 6 to 8 weeks) were inoculated subcutaneously with 2.24 x 10^6 tumour cells suspended in PBS and tumours grew and were monitored for 3 weeks before mice were used for imaging. Mice were anaesthetized using isoflurane on a precision vaporizer (5% in

oxygen for induction, between 1.5 and 2.5% in oxygen for maintenance) and received a subcutaneous injection of lactated Ringer's solution (0.5 mL) for hydration prior to each imaging scan. After the induction of anaesthesia, an injection containing 100 μL of **PEG@In-NCP** (Group 1), **FA-PEG@In-NCP** (Group 2) or **PEG@Cu-NCP** (Group 3) in PBS were administered *via* tail vein for each group. Average injected activities were 1.04 ± 0.11 MBq, 3.44 ± 0.08 MBq and 1.02 ± 0.69 MBq for Group 1, 2 and 3, respectively. Immediately after injection, dynamic whole-body images were acquired during 60 min using a multimodal PET/SPECT/CT scanner (VECTor/CT, MILabs, The Netherlands) equipped with a high-energy UHR mouse pinhole collimator. For ^{111}In-NCPs, 4 frames of 15 min were acquired for the first hour scan. Thereafter, acquisitions were done at 5 and 24 h post-radiotracer injection using a single frame of 40 min. Throughout the entire scanning procedure, the mouse was kept under isoflurane anaesthesia and constant body temperature was maintained using a heating pad. Following each SPECT or PET acquisition, a whole-body CT scan was acquired to obtain anatomical information and both images were registered. The ^{111}In photopeak window was centred at 171 keV with a 20% energy window width. The ^{64}Cu photopeak window was centred at 511 keV with a 25% energy window width. For quantitative analysis, SPECT image reconstructions were carried out with a pixel-ordered subset expectation maximization (POSEM) algorithm that included resolution recovery and compensation for distance-dependent pinhole sensitivity. For the SPECT images, we used 16 subsets, 6 iterations and an isotropic 0.4 mm voxel grid. The images were decay corrected and after CT registration, attenuation correction was applied. For visual representation, the reconstructed volumes of SPECT scans were post-filtered with a 3D Gaussian filter. CT scans were acquired with a tube setting of 55 kV and 615 μA. In total 2 frames of 180 projections over 360 degrees were acquired in step and shoot rotation mode. The acquired projection data was reconstructed using SkyScan NRecon software to generate a 3D CT image on 0.169 mm^3 voxel size. Volumes of interest (VOIs) were manually defined using AMIDE (v.1.0.5) to determine the time activity pattern per target organ. Thus, the delineated regions were lungs, liver, bladder, and bone. The average organ activity per volume was obtained from the SPECT images and the Standardized Uptake Value (SUVs) was extracted from each organ. In order to relate the scanner units (counts/voxel) to radioactivity concentration, a calibration factor was determined scanning a source with a known concentration of ^{111}In or ^{64}Cu. Mice were sacrificed for *ex vivo* biodistribution and the radioactivity in diverse organs was determined by γ-counting.

Ex vivo BioD of PEG@^{111}In-NCPs*, *FA-PEG@^{111}In-NCPs and PEG@^{64}Cu-NCPs A full biodistribution was conducted (blood, heart, liver, kidneys, lungs, small intestine, large intestine, bladder, tumour, spleen, bone, tail, urine and feces) following the last scan at 24 h post-injection. Organs were cleaned from blood, weighed and the activity determined using a γ-

counter (Packard Cobra II auto-gamma counter, Perkin Elmer, Waltham, MA, USA). The calibration factor for 37 kBq of ^{111}In was 1.524.228 cpm (instrument specific). The calibration factor for 37 kBq of ^{64}Cu was 821.941 cpm (instrument specific) Total organ weights were used for the calculations of injected dose per organ (%ID/organ) except for blood bone where average literature values were used.

Statistical analysis All data is expressed as mean and standard deviation unless stated otherwise. Significance of the experimental data was assessed using one-way analysis of variance (ANOVA). The significance level was set to 0.05.

4.3.5 References

1. Hong, H.; Chen, F.; Zhang, Y.; Cai, W. *Adv. Drug Deliv. Rev.* **2014**, *76*, 2–20.
2. Pratt, E. C.; Shaffer, T. M.; Grimm, J. *WIREs Nanomed. Nanobiotechnol.* **2016**, *8*, 872–890.
3. Cutler, C. S.; Hennkens, H. M.; Sisay, N.; Huclier-Markai, S.; Jurisson, S. S. R. *Chem. Rev.* **2013**, *113*, 858–883.
4. Stockhofe, K.; Postema, J. M.; Schieferstein, H.; Ross, L. T. *Pharmaceuticals* **2014**, *7*, 392–418.
5. Polyak, A.; Ross, L. T. *Curr Med Chem*. **2017**, *24*, 1–26.
6. Li, N.; Yu, Z.; Pham, T. T.; Blower, P. J.; Yan, R. *Int. J. Nanomedicine* **2017**, *12*, 3281–3294.
7. Polyak, A.; Nagy, L. N.; Mihaly, J.; Görres, S.; Wittneben, A.; Leiter, I.; Bankstahl, J. P.; Sajti, L.; Kellermayer, M.; Zrínyi, M.; .Ross, T, L. *J Pharm Biomed Anal*. **2017**, *137*, 146–150.
8. Keinänen, O.; Mäkilä, E. M.; Lindgren, R.; Virtanen, H.; Liljenbäck, H.; Oikonen, V.; Sarparanta, M.; Molthoff, C.; Windhorst, A. D.; Roivainen, A.; Salonen, J. J.; Airaksinen, A. J. *ACS Omega* **2017**, *2*, 62–69.
9. Liang, L.; Zhang, X.; Su, X.; Li, J.; Tian, Y.; Xue, H.;Xu, H. *J Label. Compd. Radiopharm*. **2018**, *61*, 54–60.
10. Jokerst, J. V.; Lobovkina, T.; Zare, R. N.; Gambhir, S. S. *Nanomedicine* **2011**, *6*, 715–728.
11. Ernsting, M. J.; Murakami, M.; Roy, A.; Li, S.-D. *J. Control. Release* **2013**, *172*, 782–794.
12. Suk, J. S.; Xu, Q.; Kim, N.; Hanes, J.; Ensign, L. M. *Adv. Drug Deliv. Rev.* **2016**, *99*, 28–51.
13. Morales-Avila, E.; Ferro-Flores, G.; Ocampo-García, B. E.; De León-Rodríguez, L. M.; Santos-Cuevas, C. L.; García-Becerra, R.; Medina, L. A.; Gómez-Oliván L. *Bioconjugate Chem*. **2011**, *22*, 913–922.
14. Rainone, P.; Riva, B.; Belloli, S.; Sudati, S.; Ripamonti, M.; Verderio, P.; Colombo, M.; Colzani, B.; Gilardi, M. C.; Moresco, R. M.; Prosperi, D. *Int. J. Nanomedicine* **2017**, *12*, 3447–3461.

15. Oh, M. S.; Jung, S. H.; Choi, S. H. *Appl. Radiat. Isot.* **2014**, *85*, 19–22.
16. Oh, M. S.; Jung, S. H.; Choi, S. H. *J. Radioanal. Nucl. Chem.* **2014**, *302* (3), 1151–1158.
17. Shen, S.; Jiang, D.; Cheng, L.; Chao, Y.; Nie, K.; Dong, Z.; Kutyreff, C. J.; Engle, J. W.; Huang, P.; Cai, W.; Liu, Z. *ACS Nano* **2017**, *11*, 9103–9111.
18. Lu, H. D.; Wang, L. Z.; Wilson, B. K.; McManus, S. A.; Jumai'An, J.; Padakanti, P. K.; Alavi, A.; Mach, R. H.; Prud'Homme, R. K. *ACS Appl. Mater. Interfaces* **2018**, *10*, 3191–3199.
19. He, C.; Lin, W. *Chem. Rev.* **2015**, *115*, 11079–11108.
20. Lu, K.; Aung, T.; Guo, N.; Weichselbaum, R.; Lin, W. *Adv.Mater*. **2018**, *30*, 1707634.
21. Ding, Y. H.; Floren, M.; Tan, W. *Biosurf. Biotribol.* **2016**, *2*, 121–136.
22. Xu, L. Q.; Neo, K. -G.; Kang, E. -T. *Prog. Polym. Sci*. **2018**, *87*, 165–196.
23. Sedó, J.; Saiz-Poseu, J.; Busqué, F.; Ruiz-Molina, D. *Adv.Mater.* **2013**, *25*, 653–701.
24. Fure, E.; Falentin-Daudré, C.; Jérôme, C.; Lyskawa, J.; Fournier, D.; Woisel, P.; Detrembleur, C. *Prog. Polym. Sci.* **2013**, *28*, 236–270.
25. Poseu-Saiz, J.; Mancebo-Aracil, J.; Nador, F.; Busqué, F.; Ruiz-Molina, D. *Angew. Chem. Int. Ed*. **2019**, *58*, 696 –714.
26. Suárez-García, S.; Sedó, J.; Saiz-Poseu, J.; Ruiz-Molina, D. *Biomimetics* **2017**, *2*, 22.
27. Huynh, G. H.; Deen, D. F.; Szoka, Jr F. C.; *J. control Release* **2006**, *110*, 236–259.
28. Allen, T. M.; Cullis, P. R. *Adv. Drug Deliv. Rev.* **2013**, *65*, 36–48.
29. Wei, Y.; Zhao, L. Pharm. Dev. Technol. **2014**, *19*, 129–136.
30. Din, F.; Aman, W.; Ullah, I.; Qureshi, O. S.; Mustapha, O.; Shafique, S.; Zeb, A. *Int. J. Nanomedicine*. **2017**, *12*, 7291–7309.
31. Lim, Y. H.; Tiemann, K. M.; Hunstad, D. A.; Elsabahy, M.; Wooley, K. L. *WIREs Nanomed. Nanobiotechnol.* **2016**, *8*, 842–871.
32. Sung, J. C.; Pulliam, B. L.; Edwards, D. A. *Trends Biotechnol*. **2007**, *25*, 563–570.
33. Lai, S. K.; Wang, Y. -Y.; Hanes, J. *Adv. Drug. Deliv. Rev.* **2009**, *61*, 158–171.
34. Champion, J.; Walker, A.; Mitragotri, S. *Pharm. Res.* **2008**, *25*,1815–1821.
35. El-Sherbiny, I. M.; McGill, S.; Smyth, H. D. C. *J. Pharm. Sci.* **2010**, *99*, 2343–2356.
36. Sanders, N.; Rudolph, C.; Braeckmans, K.; De Smedt, S. C.; Demeester, J. *Adv. Drug Deliv. Rev*. **2009**, *61*, 115–127.
37. Novio, F.; Lorenzo, J.; Nador, F.; Wnuk, K.; Ruiz-Molina, D. *Chem. Eur. J.* **2014**, *20*, 15443–15450.
38. Assaraf, Y. G.; Leamon, C. P.; Reddy, J. A. *Drug Resist. Updat*. **2014**, *17*, 89-95.
39. Bazak, R.; Houri, M.; El Achy, S.; Kamel, S.; Refaat, T. *J Cancer Res Clin Oncol.* **2015**, *141*, 769–784.
40. Ramzy, L.; Nasr, M.; Metwally, A. A.; Awad, G. A. S. *Eur. J. Pharm. Sci.* **2017**, *104*, 273–292.

41. Nador, F.; Novio, F.; Ruiz-Molina, D. *Chem. Commun*. **2014**, *50*, 14570−14572
42. Amorín-Ferré, L.; Busqué, F.; Bourdelande, J. L.; Ruiz-Molina, D.; Hernando, J.; Novio, F. *Chem. Eur. J*. **2013**, *19*, 17508–17516
43. Jin, Q. Zhu, W., Jiang, D., Zhang, R. Kutyreff, C. J., Engle, J. W., Huang, P., Cai, W., Liu, Z. *Nanoscale* **2017**, *9*, 12609–12617.
44. Wei, Y.; Zhao, L. *Pharm. Dev. Technol.* **2014**, *50*, 129–136.
45. Sivarajakumar, R.; Mallukaraj, D.; Kadavakollu, M.; Neelakandan, N.; Chandran, S.; Bhojaraj, S.; Venkata, V.; Reddy Karri, S. *J. Young Pharm.* **2018**; *10*, 276–281.
46. Yu, J.; Yin, W.; Peng, T.; Chang, Y-n.; Zu, Y.; Li, J.; He, X.; Ma, X.; Gu, Z.; Zhao, Y. *Nansocale* **2017**, *9*, 4497–4507.
47. Parker, N.; Turk, M. J.; Wstrick, E.; Lewis, J. D.; Low, P. S.; Leamon, C. P. *Anal. Biochem.* **2005**, *338*, 284–293.
48. Moghimi, S.M.; Hunter, A.C.; Andresen, T.L. *Annu. Rev. Pharmacol. Toxicol*. **2012**, *52*, 481–503.
49. Lundy, D.J.; Chen, K.H.; Toh, E. K.; Hsieh, P. C. *Sci Rep*. **2016**, *6*, 25613.
50. Crayton, S. H.; Elias, A.; Al-Zaki, A.; Cheng, Z.; Tsourkas, A. *Biomaterials* **2012**, *33*, 1509−1519.
51. Yoo, J. W.; Chambers, E.; Mitragotri, S. *Curr. Pharm. Des.* **2010**, *16*, 2298−2307.
52. Adarsh, N. N.; Novio, F.; Ruiz-Molina, D. *Dalton Trans*. **2016**, *45*, 11233−11255.

Chapter 5

General Conclusions

In the present Thesis, the rational design of water-dispersible coordination nanostructures have been exploited for the development and study of functional materials for their application as thermochromic films and imaging probes. For achieving this challenging objective, the complete characterisation in a wide range of methodologies and functional validation was performed. The results are summarized next:

1. For the first time, 2D coordination nanosheets showing SCO were isolated from a Fe(II) layered crystal (**1**). The methodology applied consisted on a top-down approach through the liquid-phase exfoliation in water of the bulk (**1**) CP. The AFM and DLS measurements demonstrated the fine control over the time of the size of 2D flakes and their long-colloidal stability in water.
2. The 2D flakes were completely characterised in terms of physicochemical properties, showing the retention of the ST. Additionally, the thermal hysteresis associated was confirmed and measured. These results indicated that the top-down approach used for the delamination of complex (**1**) did not cancel the intrinsic magnetic properties.
3. The water-dispersible 2D coordination nanosheets were integrated in a PVA polymeric film as a proof-of-concept device for low-temperature thermochromics films. The ST was maintained after the embedding of the 2D flakes in the polymeric network thus indicating the feasibility for their use as thermochromic sensors.
4. For the first time, nanoparticles of complex (**2**) were obtained without using surfactants. The microfluidic nanoparticles (**MSCO**) were synthesized by the control of the reaction diffusion in microfluidic device. This bottom-up approach let the formation of unprecedented SCO nanoparticles with similar magnetic properties of its bulk counterpart.
5. The **MSCO** nanoparticles can be handled as colloidal suspensions in water by retaining its intrinsic ST. The complete physicochemical characterisation demonstrated the tuning of the final composition by the synthesis in mass control conditions.
6. As a proof-of-concept, the **MSCO** nanoparticles were integrated in PVA matrix for its potential application as a near-room temperature thermochromic film by retaining inalterable the ST.
7. A set of novel NCPs were developed by the rational combination of **L3** and **L4** as organic ligands and Fe(III), Gd(III), Mn(II), In(III) and Cu(II) as metal ions. Their reaction in one-pot synthesis allowed the formation of spherical nanoparticles with variable water-colloidal stability.

8. The cytotoxicity, biostability and biodegradability of the **Fe-NCP**, **Gd-NCP**, **GdDTPA-NCP** and **Mn-NCP** systems were studied *in vitro*. The results demonstrated the best performance for the **Fe-NCP** system which was selected as a candidate for pre-clinical *in vivo* studies.
9. Additionally, the *in vitro* and *ex vivo* relaxativity properties highlighted the dual-mode behaviour of **Fe-NCP** as T_1 and T_2 CA. Suggesting their potential use as DMCA for MRI. This was validated in the pre-clinical *in vivo* studies for the visualisation of glioblastoma by both T_1 and T_2 signals, demonstrating the enhanced imaging of the tumour.
10. The **In-NCP** and **Cu-NCP** were radiolabelled with its respective radioisotopes for their use in radioimaging. The water-stability was enhanced by the development of a new universal PDA-like coating synthesized by the crosslinking between **L8** and **L9**. Additionally, further PEGylation of **In-NCP** and **Cu-NCP** allowed the increase of the biostability.
11. The **In-NCP** and **Cu-NCP** were grafted with folic acid for the study of its influence in tumour and lung accumulation. The results were validated *in vivo* by measuring with PET and SPECT equipment.
12. Furthermore, a dual metal **In/Cu-NCP** was developed for their potential use as dual mode radiotracer for PET/SPECT.

The versatility and simplicity of the approaches used for the formation of the water-dispersible CPs nanostructures presented in this Thesis, demonstrated the potential applications offered by the rational design allowing the development of functional materials. The results presented in this Thesis represent new examples for the formation of nanostructured materials and its application that could lead to the improvement of current systems.